

Local Atomic Structure and Discommensurations in the Charge Density Wave of CeTe_3

H. J. Kim,¹ C. D. Malliakas,² A. T. Tomić,¹ S. H. Tessmer,¹ M. G. Kanatzidis,² and S. J. L. Billinge^{1,*}

¹*Department of Physics and Astronomy, Michigan State University, East Lansing, Michigan 48824, USA*

²*Department of Chemistry, Michigan State University, East Lansing, Michigan 48824, USA*

(Received 15 February 2006; published 5 June 2006)

The local structure of CeTe_3 in the incommensurate charge density wave (IC-CDW) state has been obtained using atomic pair distribution function analysis of x-ray diffraction data. Local atomic distortions in the Te nets due to the CDW are larger than observed crystallographically, resulting in distinct short and long Te-Te bonds. Observation of different distortion amplitudes in the local and average structures is explained by the discommensurated nature of the CDW, since the pair distribution function is sensitive to the local displacements within the commensurate regions, whereas the crystallographic result averages over many discommensurated domains. The result is supported by STM data. This is the first quantitative local structural study within the commensurate domains in an IC-CDW system.

DOI: [10.1103/PhysRevLett.96.226401](https://doi.org/10.1103/PhysRevLett.96.226401)

PACS numbers: 71.45.Lr, 61.10.Nz, 61.44.Fw

Incommensurate charge density waves (IC-CDWs) are a fundamental property of low-dimensional metals [1] and also underlie the novel properties of correlated electron oxides such as cuprates in the pseudogap state [2–4] and manganites at high doping [5]. Knowing the nature of local atomic displacements (Peierls distortions) in the IC-CDWs is crucial to understanding such factors as electron-lattice coupling [6], yet this information is difficult to obtain quantitatively. Here we solve this problem by taking the novel approach of using a local structural method, the atomic pair distribution function (PDF) technique [7], to determine the local atomic displacements with high precision in the system CeTe_3 . IC-CDWs, and the underlying atomic displacements, can be uniform incommensurate modulations or locally commensurate waves separated by narrow domain walls, known as discommensurations [8], where the phase of the wave changes rapidly. Here we show that the IC-CDW in CeTe_3 is discommensurated and obtain for the first time the quantitative local atomic displacements within the commensurate domains.

In the case of *incommensurate* CDWs, superlattice peaks observed crystallographically yield the average distorted structure. Except in the cases where the domains are periodically arranged, giving rise to satellite peaks [9], it is not possible to determine whether the underlying CDW is truly incommensurate or forms a discommensurated structure with commensurate regions separated by domain walls [8]. A number of techniques have been successful at differentiating between the truly incommensurate and discommensurated cases. The earliest verification of a discommensurated phase came from photoemission spectroscopy evidence that the Ta $4f$ states in $1T\text{-TaS}_2$ had the same splitting in the commensurate and nearly commensurate states [10]. Photoemission is a local probe and found distinct Ta environments rather than a broad continuum expected from a purely incommensurate state. Similarly, another local probe, nuclear magnetic resonance (NMR), found distinct Knight shifts for three Se sites in the in-

commensurate state of $2H\text{-TaSe}_2$, similar to the commensurate phase [11,12]. High resolution atomic imaging methods have also contributed to this debate. The strain fields due to the domain walls were observed in dark field transmission electron microscopy measurements [13]. Interestingly, atomic resolution images in real space have difficulty in resolving discommensurated domains [14–17]. However, Fourier analysis of scanning tunneling microscopy (STM) images can be a reliable measure, as discussed in detail by Thomson *et al.* [18].

As in the case of the NMR and photoemission studies, the PDF approach described here makes use of the fact that the local structure deviates from the average in the discommensurated case. By comparing atomic displacements determined from the PDF with those determined crystallographically, we establish the presence of commensurate domains but, crucially, also obtain quantitatively the atomic structure within these domains. This novel approach is applied here to the incommensurate phase of CeTe_3 .

In its undistorted form, CeTe_3 takes the NdTe_3 structure type with space group $Cmcm$ [19]. It forms a layered structure with ionic $[\text{Ce}_2^{3+}\text{Te}_2^{2-}]^{2+}$ layers sandwiched between two Te^- layers. These sandwich layers stack together with weak van der Waals forces to form the three-dimensional structure. Te ions in the Te^- layers form a square net with 3.1 Å Te-Te bonds. The structure is shown in Fig. 1(a). The electronic bands crossing the Fermi level are Te p bands from the 2D square nets [20], and the CDW forms in these metallic layers. In the CDW state, an incommensurate superlattice is observed [20,21], with a wave vector characteristic of a strong Fermi-surface nesting vector in the electronic structure [22–25]. This is a surprisingly stable and simple single- q IC-CDW state in an easily cleavable 2D square net, making the $R\text{Te}_3$ (R denotes rare earth metal) systems ideal for studying the IC-CDW state [20]. The atomic distortions giving rise to the superlattice have been solved crystallographically from

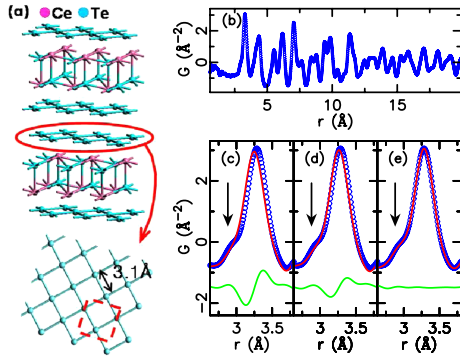


FIG. 1 (color online). (a) The crystal structure of CeTe_3 with the square Te net that supports the CDW highlighted. The reduced unit cell on the Te net is indicated by the red dashed box. (b) The PDF of CeTe_3 at room temperature. In (c)–(e), the first peak of the experimental PDF of CeTe_3 (blue circles) is plotted with the calculated PDF (red line) from various models: (c) the undistorted crystal structure model ($Cmcm$), (d) the distorted-crystallographic model, and (e) the local structural model determined from a PDF refinement over the range $2.5 < r < 6.37 \text{ \AA}$. The difference between the experimental and calculated PDFs (green line) is plotted below the data in each panel. The shoulder due to the Peierls distortions in the Te nets is indicated by an arrow.

single crystal x-ray diffraction data [21]. The incommensurate wavelength of the distortion is close to $25a/7$, where a is the lattice parameter of the undistorted phase. The distorted structure is in the $Ama2$ space group [21]. From the crystallography alone, it is not possible to determine whether this distorted structure is truly incommensurate or whether discommensurations form between short-range commensurate domains.

The x-ray PDF experiment was conducted on a fine powder of CeTe_3 prepared as described in Ref. [21]. CeTe_3 powder was loosely packed in a flat plate with thickness of 1.0 mm sealed with kapton tape. Care must be taken when grinding this material or turbostratic disorder is introduced, significantly modifying the stacking of the layers. Diffraction data were collected at 300 K using the rapid acquisition pair distribution function technique [26]. Standard corrections [7,26] were made using the program PDFGETX2 [27] to obtain the properly normalized total scattering function $S(Q)$ [7], which was truncated at Q_{max} of 25 \AA^{-1} before Fourier transforming to obtain the PDF $G(r) = \frac{2}{\pi} \int_0^\infty Q[S(Q) - 1] \sin(Qr) dQ$. Structural models are fit to the data using the program PDFFIT [28].

The PDF of CeTe_3 , measured at room temperature, is shown in Fig. 1(b). The PDF gives the probability of finding an atom at a distance r away from another atom. The nearest neighbor peak around 3.1 \AA comes from the Te-Te bond in the nets and the Ce-Te bond in the intergrowth layers. This is shown on an expanded scale in Figs. 1(c)–1(e). A shoulder is evident on the low- r side of the peak. This feature is robust; it is much larger than the

statistical and systematic errors and is reproduced in measurements of isostructural compounds NdTe_3 and PrTe_3 . Figure 1(c) shows the fit to this peak of the undistorted crystal structure model ($Cmcm$), where only symmetry allowed atomic positions and isotropic thermal factors were refined. The result clearly does not explain this shoulder which originates from short Te-Te bonds in the Te net. Surprisingly, however, the PDF calculated from the *distorted* structure determined crystallographically [21] also does not explain this shoulder well. In this case, the atoms were fixed at the crystallographically determined positions and isotropic thermal factors were refined. This resulted in a better fit to the first peak [Fig. 1(d)]; however, the fit is not ideal and required a large value of U_{iso} for the Te atoms in the nets [$U_{\text{iso}} = 0.0152(2) \text{ \AA}^2$]. The value was 2 times larger than U_{iso} of the Ce and Te atoms in the ionic $[\text{Ce}_2^{3+}\text{Te}_2^{2-}]^{2+}$ layers [$0.0077(2)$ and $0.0080(2) \text{ \AA}^2$ for U_{iso} of Ce and Te atoms, respectively].

The large fluctuation in the difference curve in Fig. 1(c) arises because the real distribution of Te-Te bond lengths in the data is broader than in the undistorted model. This fluctuation in the difference curve is smaller in Fig. 1(d) because the distortions of the Te net in the $Ama2$ crystallographic model result in a broader Te-Te bond-length distribution. However, clearly the distorted-crystallographic model still has a Te-Te bond-length distribution that is narrower than in the data. We therefore refined the Te-net distortions directly in the PDF by allowing the atomic positions in the model to vary. The model was constrained to have the $Ama2$ symmetry, and the same unit cell was used as in the distorted-crystallographic model. The refinement result for $2.5 < r < 6.37 \text{ \AA}$ is shown in Fig. 1(e). As well as giving a significantly better fit to the low- r region of the PDF, this refinement resulted in much smaller and more physical thermal factors on the planar Te ions.

The model of the local structure refined from the PDF gives a broader range of Te-Te bond lengths (from 2.83 to 3.36 \AA) than the crystallographic distorted model (from 2.94 to 3.26 \AA). It is also interesting to see the shape of the bond-length *distributions* for the Te-Te bonds in the Te nets from these two models. These are shown in Fig. 2. The dark (blue) solid line shows the bond-length distribution refined from the PDF, and the light (red) line is the distribution from the crystallographic model [21]. For direct comparison, the distributions are plotted using the same thermal broadening of 0.007 \AA^2 . The distorted-crystallographic model has broad but symmetric and Gaussian bond-length distribution coming from the continuous distribution of Te-Te bond lengths in the *average* IC-CDW. On the other hand, the local structure refinement ($r_{\text{max}} = 6.37 \text{ \AA}$) yields a bond-length distribution that is clearly bimodal and is separated into distinct “short” and “long” Te-Te distances. This is emphasized in Fig. 2(b), where we show a fit of two, well separated, Gaussian curves to the PDF-refined bond-length distribution. This behavior is charac-

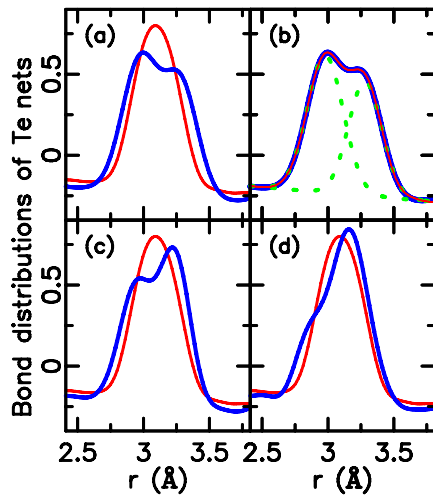


FIG. 2 (color online). Bond-length distributions in the Te nets refined from the PDF over various r ranges [dark (blue) line]: (a) $r_{\max} = 6.37$ Å, (b) $r_{\max} = 6.37$ Å, (c) $r_{\max} = 14.5$ Å, (d) $r_{\max} = 27.1$ Å. The r_{\min} value was fixed to 2.5 Å for all the cases. The bond distribution from the distorted-crystallographic model [light (red) line] is plotted in (a), (c), and (d) for comparison. In (b), the bond distribution of the local structural model ($r_{\max} = 6.37$ Å) is fit with two Gaussians. The fit is shown as a light (red) line and the two Gaussian subcomponents as a dotted (green) line.

teristic of oligomerization with Te forming bonded and nonbonded interactions with its neighbors in the net [29] that would be expected in a commensurate structure. Since we know that the modulation is incommensurate on average, this is strong evidence that the structure consists of commensurate domains separated by discommensurations. As r_{\max} in the PDF refinements is increased, the PDF-refined distribution crosses over towards the crystallographic result and by $r_{\max} = 27.1$ Å, resembles it rather closely [Fig. 2(d)].

We have applied STM on the exposed Te net of a cleaved single crystal of CeTe_3 , grown according to the method described in Ref. [21]. Measurements were done at 300 K in the constant current mode of the STM. Data were acquired with a bias voltage of 100 mV and with a tunneling current of 0.6 nA. Figure 3(a) shows a representative atomic resolution image with the CDW modulation clearly visible oriented at 45° to the net. To investigate the images for discommensurations, we examine the corresponding two-dimensional Fourier transform, shown in Fig. 3(b). As indicated by the labels, in addition to the fundamental CDW peak (1), four more peaks lie along the CDW direction (2)–(5). Although the transforms of real-space images resemble diffraction data, symmetry requirements intrinsic to diffraction data do not apply. As demonstrated by Thomson and co-workers, the Fourier transforms of STM images that exhibit true discommensurations always have extra peaks in proximity to the fundamental CDW peak

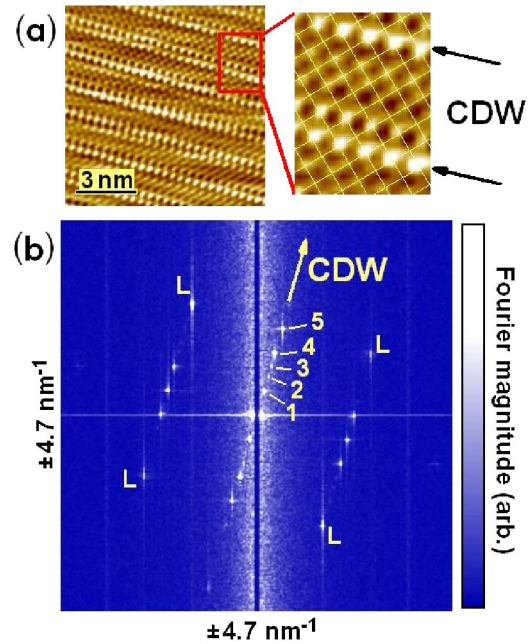


FIG. 3 (color online). (a) A representative STM image from the Te net showing the CDW. On the expanded image, the network of Te bonds is superimposed. (b) The Fourier transform of the STM data. To achieve a high signal-to-noise ratio, the transform represents the average of 24 images (each image was 27×27 nm). The unprocessed transform image shows enhanced noise along the vertical axis, an artifact due to the scan direction. This noise was removed to better resolve the peaks near the origin. The square Te net gives rise to four distinct peaks (L), with peaks related to the CDW oriented at 45° , as indicated by the arrow. The fundamental CDW peak (corresponding to a wavelength of ≈ 15 Å) and the $\lambda/2$ harmonic are labeled 1 and 3, respectively. Peaks 2 and 4 are in close proximity to 3, implying a characteristic discommensuration length of 38 Å, as described in the text. Peak 5 corresponds to the diagonal of the Te net. This component may be enhanced due to the underlying crystal structure; the CDW-lattice interaction may also enhance this peak.

[18]. This arises from the fact that a discommensurate CDW can be expressed as the product of a uniformly incommensurate CDW and a modulation envelope [18]. The wavelengths of the envelope are given by the differences in the wave vectors of closely spaced peaks. The longest such wavelength in our images is 38 Å, corresponding to peaks 2–3 and 3–4 in the Fourier transform, indicating that a discommensuration separation of this length scale exists. This is consistent with the refined PDF behavior, which crosses over from the local to the average behavior for a refinement range of around 27 Å (Fig. 2), which would be expected to occur at around, or a little above, the *radius* of the local domains.

As well as the bond-length distributions, the local and average structure refinements allow us to study the patterns of atomic displacements due to the IC-CDW. The average structure refinement [21] results in an almost perfectly

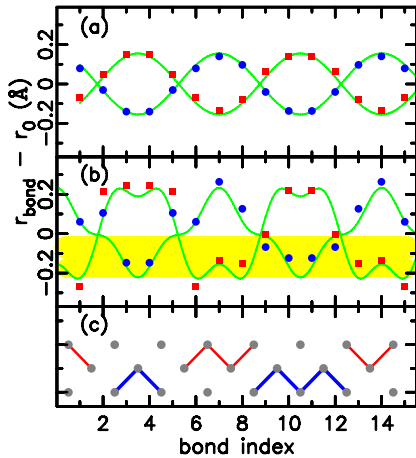


FIG. 4 (color online). Te-Te bond-length deviation from the average value as refined (a) crystallographically and (b) from the PDF. The deviation $r_{\text{bond}} - r_0$ is defined such that r_i is the Te-Te bond length of the i th bond (bond index i) in the unit cell and $r_0 = 3.1$ Å. (c) Schematic of the arrangements of short Te-Te bonds within the unit cell coming from the PDF refinements and highlighting the formation of oligomers. Light (dark) lines and square (circular) markers are “short bonds” lying in the top (bottom) row of the unit cell. Short bonds are defined as those whose length lies within the shaded (yellow) band in (b). This shaded (yellow) band is centered at the position of the *first* Gaussian of the bimodal distribution in Fig. 2(b) and has a width of one standard deviation of that Gaussian.

sinusoidal pattern of bond lengths, with the wavelength of the CDW [Fig. 4(a)], clearly identifying these as Peierls distortions. The local structural model was refined in the same unit cell and space group but results in a much more square-wave-like distribution, consistent with the distinct short and long Te-Te distances described above [Fig. 4(b)]. Figure 4(c) shows the pattern of Te-Te short bonds, as defined in the figure caption, that results when the short distances determined from the PDF data are plotted in the unit cell. In this way, the Peierls distortions are seen to result in oligomers, or short segments of bonded Te atoms, in the Te net. In this picture, the discommensurations occur when the pattern of oligomers has defects. This is a common picture in the chemistry literature [21,30], though we note that this picture is not supported by the crystallographic results shown in Fig. 4(a) and needed the application of a local structural method to show that it has a physical reality beyond its heuristic value.

The refined parameters of the low- r_{max} PDF refinements yield quantitatively the atomic displacements within the commensurate domains. This is the first demonstration of the use of the PDF to obtain quantitatively the atomic displacements (Peierls distortion) within the commensurate domains of a discommensurated IC-CDW. This opens the way to a quantitative first-principles calculations and a better microscopic understanding of the IC-CDW state.

We gratefully acknowledge P.M. Duxbury, S.D. Mahanti, and D.I. Bilec for discussions and D. Robinson and D. Wermeille for help with collecting data. Work was supported by the National Science Foundation through Grants No. DMR-0304391, No. DMR-0443785, and No. DMR-0305461. MUCAT is supported by the U.S. Department of Energy through Contract No. W-7405-Eng-82 and the APS by Contract No. W-31-109-Eng-38.

*Electronic address: billinge@pa.msu.edu

- [1] G. Grüner, *Density Waves in Solids* (Addison-Wesley, New York, 1994).
- [2] M. Vershinin *et al.*, *Science* **303**, 1995 (2004).
- [3] J.E. Hoffman *et al.*, *Science* **295**, 466 (2002).
- [4] T. Hanaguri *et al.*, *Nature* (London) **430**, 1001 (2004).
- [5] J.C. Loudon *et al.*, *Phys. Rev. Lett.* **94**, 097202 (2005).
- [6] G.C. Milward, M.J. Calderón, and P.B. Littlewood, *Nature* (London) **433**, 607 (2005).
- [7] T. Egami and S.J.L. Billinge, *Underneath the Bragg Peaks: Structural Analysis of Complex Materials* (Pergamon, Oxford, England, 2003).
- [8] W.L. McMillan, *Phys. Rev. B* **14**, 1496 (1976).
- [9] D.E. Moncton, J.D. Axe, and F.J. DiSalvo, *Phys. Rev. B* **16**, 801 (1977).
- [10] H.P. Hughes and R.A. Pollack, *Commun. Phys.* **1**, 61 (1976).
- [11] B.H. Suits, S. Couturie, and C.P. Slichter, *Phys. Rev. Lett.* **45**, 194 (1980).
- [12] B.H. Suits, S. Couturie, and C.P. Slichter, *Phys. Rev. B* **23**, 5142 (1981).
- [13] C.H. Chen, J.M. Gibson, and R.M. Fleming, *Phys. Rev. Lett.* **47**, 723 (1981).
- [14] J.M. Gibson, C.H. Chen, and M.L. McDonald, *Phys. Rev. Lett.* **50**, 1403 (1983).
- [15] T. Ishiguro and H. Sato, *Phys. Rev. B* **44**, 2046 (1991).
- [16] M. Kuwabara *et al.*, *Phys. Status Solidi A* **96**, 39 (1986).
- [17] J.W. Steeds *et al.*, *Ultramicroscopy* **18**, 97 (1985).
- [18] R.E. Thomson *et al.*, *Phys. Rev. B* **49**, 16 899 (1994).
- [19] W. Lin, H. Steinfink, and E.J. Weiss, *Inorg. Chem.* **4**, 877 (1965).
- [20] E. DiMasi *et al.*, *Phys. Rev. B* **52**, 14 516 (1995).
- [21] C. Malliakas *et al.*, *J. Am. Chem. Soc.* **127**, 6510 (2005).
- [22] G.H. Gweon *et al.*, *Phys. Rev. Lett.* **81**, 886 (1998).
- [23] V. Brouet *et al.*, *Phys. Rev. Lett.* **93**, 126405 (2004).
- [24] H. Komoda *et al.*, *Phys. Rev. B* **70**, 195101 (2004).
- [25] J. Laverock *et al.*, *Phys. Rev. B* **71**, 085114 (2005).
- [26] P.J. Chupas *et al.*, *J. Appl. Crystallogr.* **36**, 1342 (2003).
- [27] X. Qiu, J.W. Thompson, and S.J.L. Billinge, *J. Appl. Crystallogr.* **37**, 678 (2004).
- [28] T. Proffen and S.J.L. Billinge, *J. Appl. Crystallogr.* **32**, 572 (1999).
- [29] R. Patschke and M.G. Kanatzidis, *Phys. Chem. Chem. Phys.* **4**, 3266 (2002).
- [30] R. Patschke *et al.*, *J. Am. Chem. Soc.* **123**, 4755 (2001).

Scanning tunneling microscopy study of the CeTe₃ charge density waveA. Tomic,¹ Zs. Rak,¹ J. P. Veazey,¹ C. D. Malliakas,² S. D. Mahanti,¹ M. G. Kanatzidis,² and S. H. Tessmer^{1,*}¹Department of Physics and Astronomy, Michigan State University, East Lansing, Michigan 48824, USA²Department of Chemistry, Northwestern University, Evanston, Illinois 60208, USA

(Received 15 August 2008; revised manuscript received 19 January 2009; published 20 February 2009)

We have studied the nature of the surface charge distribution in CeTe₃. This is a simple cleavable layered material with a robust one-dimensional incommensurate charge density wave (CDW). Scanning tunneling microscopy (STM) has been applied on the exposed surface of a cleaved single crystal. At 77 K, the STM images show both the atomic lattice of surface Te atoms arranged in a square net and the CDW modulations oriented at 45° with respect to the Te net. Fourier transform of the STM data shows Te square lattice peaks and peaks related to the CDW oriented at 45° to the lattice peaks. In addition, clear peaks are present, consistent with subsurface structure and wave-vector mixing effects. These data are supported by electronic structure calculations, which show that the subsurface signal most likely arises from a lattice of Ce atoms situated 2.53 Å below the surface Te net.

DOI: 10.1103/PhysRevB.79.085422

PACS number(s): 71.45.Lr, 61.44.Fw, 71.15.Mb, 73.20.-r

I. INTRODUCTION

The metallic compound CeTe₃ belongs to a family of layered RETe₃ materials, where RE is a rare-earth element, which have received much attention as a model system to study incommensurate charge density waves (CDWs).¹⁻³ This class of materials features two-dimensional square-net motifs composed of Te atoms. Such square-net arrangements have been considered theoretically performing electronic band-structure calculations and were found to be susceptible to CDW formation driven by Fermi-surface nesting.⁴ On the experimental side, measurements have shown rather weak coupling between the layers and large energy gaps as high as 400 meV for CeTe₃.⁵⁻⁷ The CDW is well formed in CeTe₃ at room temperature, and no transition to a non-CDW state has been observed for temperatures as high as 500 K.⁸ Although it is well established that the CDW forms in the RETe₃ family has not been resolved to date. For example, there is an ongoing debate regarding whether the CDW is uniformly incommensurate or locally commensurate within domains, with phase slips, i.e., discommensurations, occurring at the domain walls.^{9,10}

In this paper we present scanning tunneling microscopy (STM) measurements obtained at a temperature of 77 K and theoretical calculations of the CeTe₃ surface, with the main focus on understanding the surprisingly large subsurface contribution to the tunneling signal. This study can be compared to room-temperature STM data presented in Ref. 9. Reference 9 also included pair distribution function analysis of x-ray diffraction data that showed clear evidence for discommensurations; moreover, peaks in the Fourier transform (FT) of the STM images were identified as satellite structures, consistent with the discommensuration picture. Compared to the previous study, the data presented here are of higher quality due to an increase in the signal-to-noise ratio. This was achieved by operating the microscope at low temperature, which yields higher normal-mode mechanical frequencies. The data are compared to a compelling wave-vector-mixing analysis, which does not involve discommensurations, originally suggested by Fisher *et al.*^{10,11}

The undistorted crystal structure of CeTe₃ is shown in Fig. 1. It is of NdTe₃ (Refs. 12 and 13) type, weakly orthorhombic, and described within the space group *Cmcm*. It is a layered structure that consists of two building blocks: double layers of [Te]⁻ square nets and puckered ionic [Ce³⁺Te₂²⁻]²⁺ double layers that are placed between the nets. The three-dimensional structure is composed of slabs of these structural motifs. The atoms within slabs are covalently bonded, while bonds between the slabs are weak van der Waals type, allowing the crystals to cleave easily between the Te layers. Hence the exposed surface is the Te net, ideal for STM studies of the CDW.

The existence of a unidirectional CDW in tritellurides was first reported in a transmission electron microscopy study of

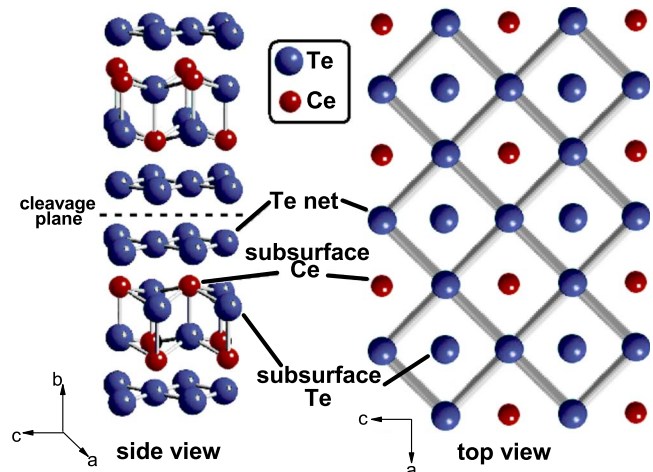


FIG. 1. (Color online) The average (undistorted) crystal structure of CeTe₃ consisting of corrugated CeTe slabs and Te layers, where Te atoms are separated by 3.1 Å in a square net. The side view shows two complete unit cells, with the unit repeated along the *b* axis. The top view shows the surface Te net exposed upon cleaving the crystal. The first subsurface layers of Ce and Te atoms are indicated. Taking into account atomic relaxation, with respect to the *b* direction (perpendicular to the layers), the subsurface Ce lattice is 2.53 Å below the surface Te net and the subsurface Te lattice is 3.44 Å below the Te net.

a series of RETe_3 crystals by DiMasi *et al.*¹ They identified superlattice reflections in the electron diffraction pattern corresponding to a single incommensurate modulation wave vector with a magnitude of $q_{\text{CDW}} \approx 2/7 \times 2\pi/c$, where $c = \sqrt{2}a_0$ and a_0 is the Te-Te separation of 3.1 Å. This indicated the presence of incommensurate distortions in the Te layer planes. The incommensurate superstructure was solved within space group $C2cm(00\gamma)000$ for RE=Ce, Pr, and Nd by Malliakas *et al.*³ using single-crystal x-ray diffraction. This study quantified distortions in the Te net and revealed that a distribution of planar Te-Te distances exists, with a minimum value of ~ 2.95 Å and a maximum value of ~ 3.24 Å.

Due to the large lattice constant along the b direction (~ 25 Å), as shown in Fig. 1, the Brillouin zone of RETe_3 is compressed (platelike) and slightly orthorhombic.¹⁴ Strong anisotropy has been observed in their transport properties,^{1,6} which reflects the nearly two-dimensional nature of the system originating from the weak hybridization between the Te layers and the RETe slabs. The electronic structure for tellurium planes is rather simple. The electronically active valence band consists predominantly of $5p$ orbitals of the Te atoms from the Te planes. The only significant role in the formation of the CDW is played by the perpendicular chains of in-plane $5p_x$ and $5p_y$ orbitals since the energy of completely filled $5p_z$ is pushed below the Fermi level as indicated by the first-principles band-structure calculations.^{15,16}

II. STM MEASUREMENTS

We have performed low-temperature STM topography and spectroscopy of CeTe_3 at 77 K to characterize the CDW state. CeTe_3 crystals were grown by a halide flux method, as described in Ref. 17. The crystals were carefully cleaved with adhesive tape and quickly placed in a vacuum system for subsequent STM measurements at a temperature of 77 K. A representative unfiltered real-space image is shown in Fig. 2(a). The image was taken at a sample bias of 100 mV and a tunneling current of 0.6 nA. Both the net of Te atoms and the CDW modulation—oriented at 45° to the net—are clearly visible, as indicated. The gray lines on the left mark the locations of the CDW maxima. The locations were determined by extracting the phase of the CDW signal using SPIR image analysis software.¹⁸ The apparent irregular spacing of the CDW is addressed by the STM simulation in Fig. 2(b). The top image shows a square two-dimensional lattice of wavelength $a_0 = 0.31$ nm to represent the Te net. The pixelization of the simulation is rather coarse (one wavelength $= 3$ pixels). It is superimposed with a larger lattice, scaled by $\sqrt{2}$ and rotated by 45° to account for the subsurface structure. The middle panel shows a one-dimensional sine wave of wavelength 1.60 nm representing the CDW. Finally, the bottom panel gives the sum of the simulated lattice and the CDW. We see a qualitatively different pattern for each stripe, similar to the measured STM images. Although none of the patterns are identical to those seen in the images, it must be noted that this simple approach lacks significant effects discussed below that give rise to multiple peaks in the Fourier transform. Specifically, the subtleties in the subsurface lattice

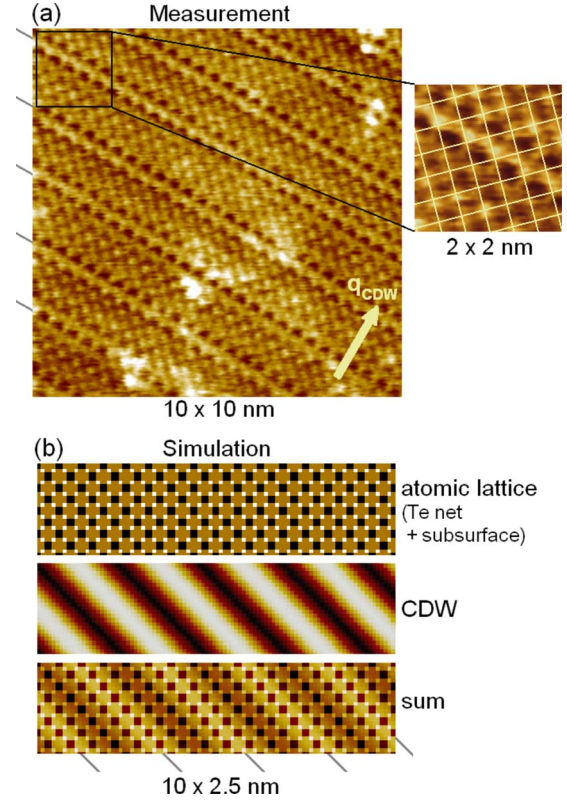


FIG. 2. (Color online) (a) A 10×10 nm real-space STM image of the Te net obtained at 77 K, showing both Te atoms and CDW modulations oriented at 45° to the net. The image is the average of four images that were obtained consecutively, in constant-current mode, at a sample bias of 100 mV and tunneling current of 0.6 nA; no image processing or filtering of the data was performed. The bright irregular features indicate surface contamination. The expanded image on the right includes a square grid as a guide to the eyes; a Te atom is located at each intersection. The gray lines on the left mark the locations of the CDW maxima. (b) A simple simulation of the STM image intended to address the apparent irregular spacing of the CDW feature. Top: a square two-dimensional sinusoidal lattice of wavelength $a_0 = 0.31$ nm to represent the Te net. It is superimposed with a larger lattice, scaled by $\sqrt{2}$ and rotated by 45° to account for the subsurface structure. Middle: a one-dimensional sine wave of wavelength 1.60 nm to represent the CDW. Bottom: the sum of the simulated lattice and the CDW. We see that each CDW wavelength forms a distinct pattern which is qualitatively different from the neighboring stripes. The gray lines mark the actual CDW maxima.

are neglected by this simple simulation (see below).

Figure 3(a) shows the Fourier transform of the 77 K real-space data obtained from 16 24×24 nm images— ~ 2.4 times the area shown in Fig. 2—using a straightforward averaging procedure.¹⁹ The Te square lattice peaks are labeled L. The nearest-neighbor distance of the Te lattice is well established to be $a_0 = 0.31$ nm, corresponding to a lattice wave vector of $2\pi/a_0 = 20.3$ nm $^{-1}$. This information is used to calibrate the scan range of the real-space images and the wave-vector axes of the Fourier transform data. Peaks related to the CDW are oriented 45° clockwise to the square lattice peaks. To examine the peaks carefully, we take a line cut along the CDW direction in Fig. 3(b). We expect the CDW

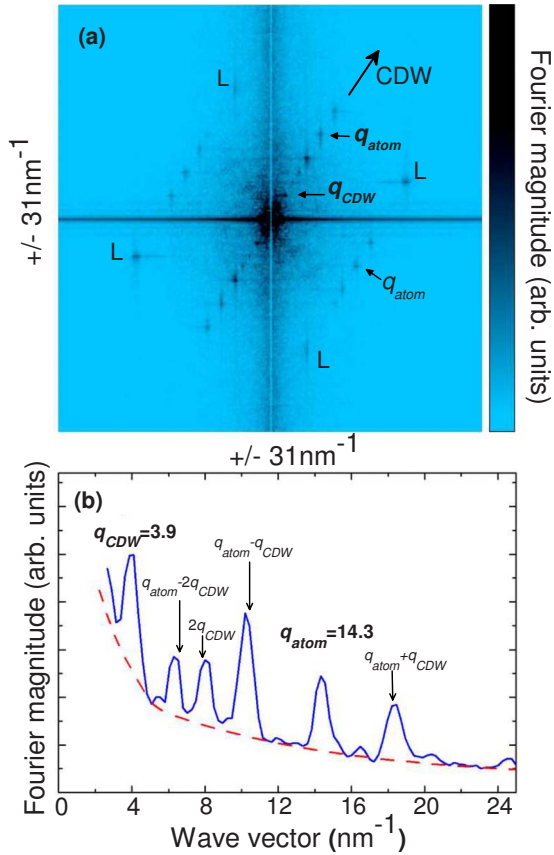


FIG. 3. (Color online) (a) The Fourier transform of the low temperature STM data. Enhanced noise along the vertical axis is an artifact due to the scan direction. Horizontal and vertical axes are wave-vector components k_x and k_y . The square Te net gives rise to four distinct peaks (L). Peaks at 45° to Te net are consistent with the CDW peaks. The CDW peak q_{CDW} , as well as peak q_{atom} , which is consistent with underlying atomic structure, are labeled. (b) Subset of the data from the Fourier transform along a path in the direction of the CDW. Noise in the Fourier transform becomes significantly larger near the origin. This is due to the impurities present in the real-space data. As the guide to the eyes, the dashed line indicates the background noise.

peak to be located near $q_{\text{CDW}} \approx 2/7 \times 2\pi/c = 4.1 \text{ nm}^{-1}$. Indeed, we find a prominent peak at 3.9 nm^{-1} , which we label q_{CDW} in bold. The peak at $2\pi/c = 14.3 \text{ nm}^{-1}$, labeled q_{atom} , also appears in the direction perpendicular to the CDW. Hence it is consistent with a larger square lattice oriented at 45° to the surface Te net. As seen in Fig. 1, this pattern is consistent with either the first subsurface Ce layer or the first subsurface Te layer. A similar Fourier transform peak was observed by Fang *et al.*,¹⁰ while working with the related material TbTe_3 , who also attributed it to sensitivity to the subsurface structure. Surprisingly, q_{atom} and q_{CDW} have roughly the same magnitude, which is approximately equal to the magnitude of the Te-net Fourier peaks, labeled L in Fig. 3(a). Theoretical calculations given in Sec. V will address the relative magnitudes of the contributions of the tunneling current from the surface Te net and subsurface Ce and Te atoms.

Because the Fourier transform lacks phase information, the square lattice corresponding to peak q_{atom} could possibly

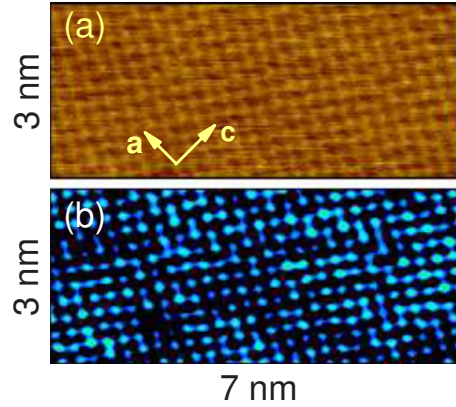


FIG. 4. (Color online) (a) STM topography of CeTe_3 at room temperature in ambient conditions with a sample bias of -800 mV , the same used in Fig. 2(a) of Ref. 10. The current set point was -0.14 nA , which was necessary to achieve quality comparable to that of Ref. 10. We do not observe evidence of dimerizations, in contrast to the work of Fang *et al.* with the related material, TbTe_3 . Lower quality images at -0.05 nA (the reported current for Ref. 10) also lacked evidence of dimerizations. The image shown is raw data, aside from line by line subtraction and the manual removal of an artifact caused by the controller software. (b) Low-pass Fourier filtered image of the same data in (a). Data shown are those below $|k|=26 \text{ nm}^{-1}$. The image is given in high contrast for comparison with Ref. 10.

be attributed to the apparent dimerizations of the surface Te net reported by Fang *et al.*¹⁰ while working with the related material TbTe_3 . However, we observe no evidence of dimers in topographic images of CeTe_3 when reproducing the same tunneling conditions (Fig. 4). Moreover, we have not seen evidence for dimers in the hundreds of images we have taken of CeTe_3 over a broad set of bias voltages in the range of $\pm 800 \text{ mV}$. To the naked eye, the subsurface structure is less apparent in this topographic image compared to Fig. 2(a); however, the Fourier transform is similar to that of Fig. 3(a) with regard to peaks q_{atom} . In addition, the topographic CDW contrast is less apparent. This is not surprising, given that the absolute value of the bias voltage times the electron charge is 800 meV , well above the characteristic CDW energy.

III. WAVE-VECTOR MIXING

Returning to Fig. 3(b), four peaks are present in addition to q_{CDW} and q_{atom} . In our original study, we interpreted similar structure as satellite peaks, which supported the interpretation of a discommensurated CDW.⁹ However, Fisher¹¹ suggested an alternative wave-vector-mixing explanation, which we explore here in detail.

Consider an STM signal acquired on a surface with a uniformly incommensurate CDW and lattice modulation, both of which are described by sinusoidal waves with wave vectors k_{CDW} and k_{atom} along the x direction. The Fourier transform along this direction would ideally exhibit exactly two peaks, one at k_{CDW} and one at k_{atom} . Implicit in the ideal case is the assumption that the STM signal is proportional to the sum of the two sine waves. However, in reality the signal

may have a significant component that resembles the product of the two waves. In Ref. 19, Tomic showed explicitly that this is indeed the case if an asymmetry existed in the way the CDW couples to the peaks of the atomic signal compared to the troughs. In other words, the signal will exhibit a contribution similar to the product of the two waves if the CDW signal is stronger at the atomic lattice sites and weaker at the locations between atoms or vice versa. Algebraically, the product of two sine waves can be expressed as a sum and a difference: $\sin(k_{\text{CDW}}x)\sin(k_{\text{atom}}x) = \frac{1}{2}\cos(k_{\text{CDW}}x - k_{\text{atom}}x) - \frac{1}{2}\cos(k_{\text{CDW}}x + k_{\text{atom}}x)$. Hence we expect this effect to give extra peaks in the Fourier transform at $k_{\text{CDW}} + k_{\text{atom}}$ and $k_{\text{CDW}} - k_{\text{atom}}$. More generally, Tomic showed that such a peak-trough asymmetry leads to wave-vector mixing, additional Fourier peaks at linear combinations of the two wave vectors.

With this in mind, we interpret the additional peaks in the FT of our STM data as linear combinations of q_{CDW} and q_{atom} . In Fig. 3(b), the additional peaks are labeled as $q_{\text{atom}} - 2q_{\text{CDW}}$, $2q_{\text{CDW}}$, $q_{\text{atom}} - q_{\text{CDW}}$, and $q_{\text{atom}} + q_{\text{CDW}}$. The arrows mark the precise wave-vector value at which we would expect each mixed peak to occur; indeed we see excellent agreement between the arrows and the actual peak locations. This analysis is similar to the analysis presented by Fang *et al.*¹⁰ to describe the TbTe₃ data.

As all of the clear Fourier peaks are accounted for without invoking discommensurations, our STM data of CeTe₃ are consistent with a uniformly incommensurate CDW. However, this analysis does not preclude the presence of discommensurations. It is possible that some of the unlabeled features such as the small peaks near 16.5 nm^{-1} and 20 nm^{-1} are satellite peaks indicative of discommensurations.⁹ However these features are just above the noise level of the data.

Given that CDW and lattice modulations are typically well described by undistorted sinusoidal waves, it is surprising that the wave-vector-mixing effect is so large. In light of the analysis by Tomic¹⁹ and our assertion that the lattice signal in this case corresponds to the subsurface Ce or Te, we conjecture the following. The CDW modulates the amplitude of the tunneling signal of the surface Te atoms; these are located at trough positions with respect to the subsurface lattice. But the CDW is expected to only weakly couple to the subsurface atoms themselves. We believe that this is the source of the peak-trough asymmetry. Unfortunately, the effect is rather subtle with respect to the real-space patterns; given the noise in the measurement, it is difficult to confirm this conjecture by examining the direct images.

IV. SPECTROSCOPY

Formation of the CDW state is expected to be accompanied by an energy gap opening up at the Fermi level. Using the point spectroscopy mode we can probe the CDW gap at different locations of the sample surface and estimate its size. Spectra were acquired at a temperature of 77 K at various locations of the tip above the exposed Te plane on the surface of CeTe₃.

Figure 5 shows the characteristic density of states (DOS) as obtained when the tip is above a Te atom. The data have

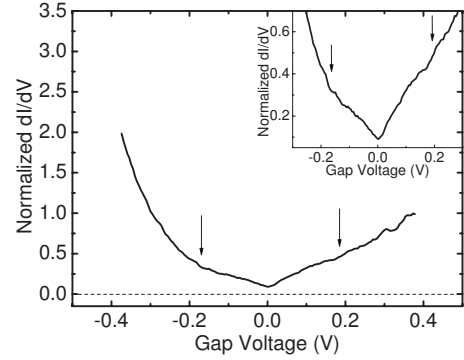


FIG. 5. Local DOS around the Fermi level for CeTe₃. The Fermi level corresponds to zero bias voltage. The estimated CDW gap size in CeTe₃ is about 360 meV, as indicated by vertical arrows. The spectroscopy was carried out when the tip was located directly above a Te atom. The effect of thermal smearing of the data is approximately $3.5 k_B T \approx 25 \text{ meV}$ at 77 K temperature; hence it is not significant over the plotted range. Inset: expanded view of dI/dV near the Fermi level is shown to enhance the visibility of the subtle edges we identify as the CDW energy gap (again indicated by vertical arrows).

been normalized to the value at 0.3 V and represent an average of 168 measurements performed consecutively. Designation of the CDW gap is difficult because the variations in the dI/dV at the edges are subtle. To illustrate how we chose the locations of the arrows, we zoom in on the dI/dV curve near the Fermi level (inset of Fig. 5). There are small shifts in the slope of dI/dV at $\pm 0.18 \text{ V}$, leading to an estimated width of 360 meV. The magnitude and shape of the dI/dV curves are remarkably similar to the previous TbTe₃ measurements by Fang and co-workers^{7,10} and may be compared to the angle resolved photoemission spectroscopy results of 400 meV. The local density of states has a shape that is suggestive of subgap states, characterized by the nonzero V-shaped structure within the gap.

V. THEORETICAL STUDIES

A. Method of calculation

The STM data obtained for CeTe₃ were simulated using electronic structure calculations within density-functional theory (DFT).^{20,21} It is well known that the local (spin) density approximation [L(S)DA] fails to describe the correct ground state of a system containing transition-metal or rare-earth metal atoms. L(S)DA always puts the partially filled d or f band right at the Fermi level (E_F), predicting metallic character with itinerant d or f electrons, which is obviously not correct. Strong Coulomb repulsion between localized d (or f) electrons suppresses the charge fluctuations inherent in a metallic system. In order to describe correctly the ground state of such systems, one has to go beyond standard L(S)DA and take into account the strong electron-electron correlations. One of the successful approaches is the L(S)DA+U method,^{22–25} in which the localized d or f electrons and the delocalized s and p electrons are treated differently. The orbital-dependent Coulomb potential is only taken into ac-

count for localized states, while the delocalized states are treated by orbital-independent L(S)DA type potential. For CeTe₃ the LSDA+U approach was used based on full potential linearized augmented plane wave+local orbital (FP-LAPW+lo) method^{26,27} as implemented in the WIEN2K package.²⁸ The on-site electron correlation was taken into account for the Ce *f* states with $U_{\text{eff}}(\text{Ce})=6.8$ eV. For the exchange and correlation functional the LSDA (Ref. 29) was used. The value of the convergence parameter RK_{max} , which is defined as the product of the minimal atomic sphere radius (R) and the largest reciprocal lattice vector (K_{max}) of the plane-wave basis, was chosen as $RK_{\text{max}}=7$. We use 2.5 a.u. for the muffin-tin radii of all Ce and Te atoms. The Brillouin zone (BZ) was sampled by a dense mesh of 625 irreducible k points in the $k_z=0$ plane. Spin-orbit (SO) interaction was included using the second variational treatment.^{30,31}

B. STM simulation

The CeTe₃ surface was modeled by a periodic slab geometry separated by a vacuum region of 14 Å. The slabs consisted of repeating supercells, each containing two unit cells along the crystallographic long axis (b axis for CeTe₃). The supercell was constructed using the theoretical lattice constants of the bulk CeTe₃. The thickness of the slab constructed this way is 47.5 Å, which is sufficient to eliminate the spurious surface-surface interaction. Geometry optimization was performed on the surface Te square lattice and on the Ce and Te layers closest to the surface. The calculations were carried out on the high-symmetry structure. Since calculations using supercell models for the incommensurate CDW are not feasible, we focus on the nature of the electronic wave functions near E_F , on the undistorted structure, with the goal of elucidating the contributions from the subsurface atoms to these wave functions.

According to the theory of tunneling between a real solid surface and model probe tip, the tunneling current in the first-order perturbation theory is given by^{32,33}

$$I = \frac{2\pi e}{\hbar} \sum_{\mu\nu} f(E_\mu)[1 - f(E_\nu + eV)] \times |M_{\mu\nu}|^2 \delta(E_\mu - E_\nu), \quad (1)$$

where $f(E)$ is the Fermi function, V is the applied voltage, and E_μ and E_ν are the energies of the states ψ_μ and ψ_ν of the probe tip and the surface, respectively. $M_{\mu\nu}$ is the tunneling matrix element between ψ_μ and ψ_ν . Taking the limit of small voltage (100 mV) and low temperature (77 K) and approximating the tip with a spherical wave function, the tunneling current can be written as

$$I \propto \sum_{\nu} |\psi_\nu(r_0)|^2 \delta(E_\nu - E_F), \quad (2)$$

where E_F is the Fermi energy. When $E_\nu=E_F$, the tunneling current is proportional to the local density of states (LDOS) at the position of the tip (r_0), as given by Eq. (2). Using the slab geometry described above we simulate a constant-height-mode STM image by calculating the charge density in an energy range of 0.0–0.1 eV around E_F taken at a distance

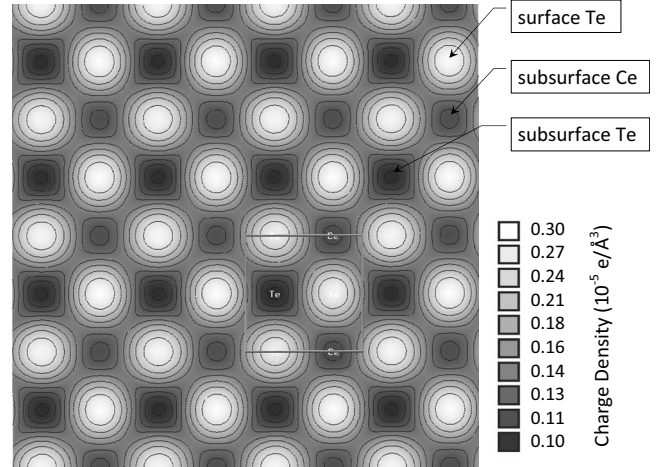


FIG. 6. To simulate the STM image, we give the contour plot of the charge density projected onto a plane at 3.0 Å above the surface, in the energy range of 0.0–0.1 eV. The brighter (white) spots come from the surface Te. The subsurface Ce atoms contribute more to the charge density than the subsurface Te atoms. The Fermi level (E_F) corresponds to 0.0 eV. Moreover, the subsurface modulation, considering only the regions between surface Te, is of comparable magnitude to the signal from the surface Te net.

of 3.0 Å above the surface Te net, where 0.0 eV is the Fermi energy. Figure 6 shows the contour plot of this charge density. The main contribution comes from the surface Te atoms arranged in a square lattice. The subsurface Ce and Te atoms are arranged in puckered double layers in which the Ce and Te atoms form square lattices oriented at 45° to the surface Te net. As shown in Fig. 6, the subsurface Ce contributes more to the charge density than the subsurface Te, suggesting that tunneling is more likely to appear from the Ce sites than from the subsurface Te sites. This is consistent with the experimental finding that the peak q at 14.3 nm⁻¹ in Fig. 3 corresponds to the underlying structure closest to the surface, namely, to the square lattice of Ce atoms.

We have obtained similar results when we calculated the LDOS in an energy range of ± 0.08 eV, at distances of 2.5 Å and 3.0 Å above the surface Te net.

C. Electronic structure

Figure 7 shows the calculated partial density of states (PDOS) associated with the p orbitals of the surface and subsurface Te atoms. Since the spin-up and spin-down DOS associated with the Te atoms are identical, we only show the spin-up channel. As pointed out by DiMasi *et al.*^{5,34} in RETe₃ compounds the rare earth is trivalent; it provides two electrons for bonding to the puckered double-layer of RE-Te and one electron to the Te square net. Therefore we expect the p -states of the subsurface Te atoms (which are part of the RE-Te slabs) to be completely occupied, while the p -state surface Te atoms (which form the square net) should be partially filled. As shown in Fig. 7, our electronic structure calculation agrees with this observation and with the earlier theoretical results:^{15,16} the only significant contribution to the DOS at E_F comes from the p_x and p_y orbitals of the surface

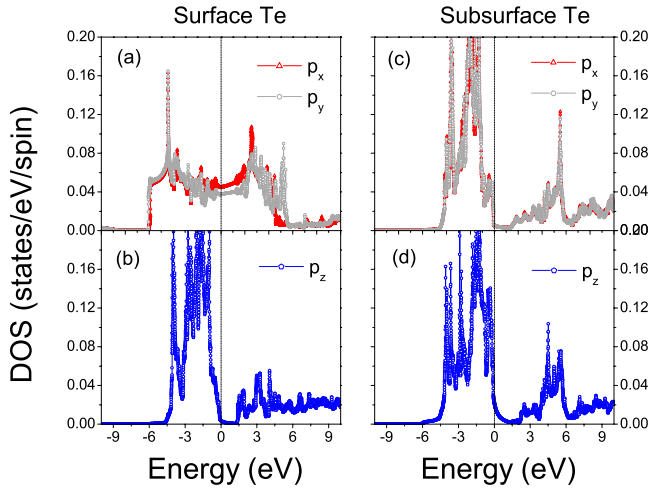


FIG. 7. (Color online) The only significant contribution to the DOS near E_F comes from the surface Te p_x and p_y states. (a) Partial DOS associated with the p_x and p_y orbitals of the surface Te atoms. The flat DOS near E_F is characteristic to the CDW systems. (b) The p_z orbital of the surface Te is occupied and located mostly below E_F . [(c) and (d)] The p -states of the subsurface Te atoms are occupied because the trivalent Ce provides two electrons within the Ce-Te slab.

Te. The partial DOS associated with these two orbitals [Fig. 7(a)] are rather flat at E_F , which is a characteristic of the CDW systems in the high-symmetry phase. The p_z orbital of the surface Te atom [Fig. 7(b)] and the p states of the subsurface Te atoms [Figs. 7(c) and 7(d)] are nearly fully occupied and located mostly below E_F .

In order to understand why the subsurface Ce atoms contribute so much to the STM charge density calculation, we give the spin-polarized DOS associated with the subsurface Ce atom in Fig. 8. The spin-up states are represented in the positive (upper) region, while the spin-down states are shown in the negative (lower) region of the graph. The main contribution to the DOS comes from the Ce f states: the narrow, sharp peak in the spin-up DOS located at ~ 2.5 eV below E_F represents the only one occupied Ce f level. The broader peaks located between 3.0 and 5.0 eV above E_F , in both the spin-up and spin-down DOS, come from the rest of the 13 empty Ce f states (6 spin-up and 7 spin-down states). The splitting between the occupied and empty states is approximately equal to the chosen value of the Coulomb repulsion within the f shell $U_{\text{eff}}(\text{Ce})=6.8$ eV. The inset of Fig. 8 gives the DOS associated with the Ce orbitals near E_F . There is a small but finite contribution coming from both the hybridization of f states with Te p bands and Ce d states. These states will contribute to tunneling measurements above the Ce sites.

Now let us discuss the tunneling results in the light of our theoretical calculations. As discussed in Sec. VB, the STM tunneling current is proportional to the LDOS at the position of the tip. In reality however there is a matrix element between the states from which the tunneling occurs (host) and the tip state. Assuming that the tip state can be approximated by a smooth s -like function, the symmetry of the host state will determine the strength of the tunneling current. For ex-

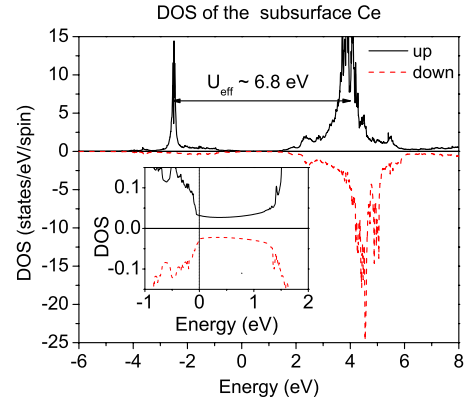


FIG. 8. (Color online) Spin-polarized partial DOS associated with the subsurface Ce atom. The peak at -2.5 eV in the spin-up DOS corresponds to one occupied f level while the peaks between 3.0–5.0 eV (spin-up and spin-down) represent the 13 unoccupied f states. The inset shows that the DOS near E_F is nonzero.

ample, for the surface Te, p_x and p_y states that make dominant contribution to the DOS near E_F will have zero (very small) contribution to the tunneling current. As discussed above, the intensity of the FT of the STM signal as a function of q along the direction of the CDW wave vector (which is rotated by 45° with respect to the direction of the square lattice peaks) gives peaks at $q_{\text{CDW}}=3.9$ nm^{-1} and at $q_{\text{atom}}=14.3$ nm^{-1} , the latter is ascribed to the subsurface Ce or Te lattice. From our PDOS calculations we find that for the subsurface Te, the p_x and p_y orbitals contribute ~ 0.004 states/eV/spin near E_F , whereas the p_z orbital contributes ~ 0.02 states/eV/spin. Thus both due to symmetry and small PDOS, the p_x and p_y states will not contribute to the tunneling current, only the p_z orbital will contribute. The PDOS associated with the Ce orbitals are ~ 0.03 states/eV/spin comparable to the subsurface Te p_z . However the lattice of Ce atoms is a distance of 2.53 \AA from the surface Te net, whereas the subsurface Te lattice is a distance of 3.44 \AA . Hence the Ce atoms are nearly 1 \AA closer to the STM tip; it is therefore likely that the tunneling current above Ce sites is larger than that above the subsurface Te sites. Furthermore, since the surface Te p_z contribution to the DOS near E_F is rather small (~ 0.004 states/eV/spin) our charge density analysis suggests that the tunneling currents above the Ce sites and the surface Te net sites are comparable. This is the origin of the surprisingly high sensitivity to the subsurface Ce, consistent with both the experiment (Fig. 3) and theoretical simulation (Fig. 6). This result is significant because it may be possible to probe the nature of Ce f states through careful tunneling measurements.

VI. SUMMARY

STM constant-current-mode images and spectroscopy measurements of CeTe_3 were acquired at 77 K. The effects of the CDW were clearly resolved in both the images and the spectroscopy curves. In addition to the CDW, the images show the expected signal from the surface net of Te atoms

and a large contribution from subsurface structure of approximately the same magnitude. Contrary to a study by Fang *et al.*,¹⁰ no evidence of dimerization of the surface Te net was observed.

Fourier transform analysis of the STM images showed two principal peaks along the direction of the charge density wave, one from the CDW at $q_{\text{CDW}}=3.9 \text{ nm}^{-1}$ and the other from a subsurface lattice at $q_{\text{atom}}=14.3 \text{ nm}^{-1}$. In addition to these peaks four others were observed which we show are well described by a wave-vector-mixing effect of the principal wave vectors. We believe the high degree of wave-vector mixing is caused essentially by the fact that the CDW, which exists in the surface layer, distorts preferentially the troughs between the subsurface atoms. With regard to the uniformity of the CDW, our present study does not provide support for discommensurations, in contrast to the interpretation of our earlier STM work.⁹ However, the data presented here do not rule out discommensurations and the issue remains an open question.

To better understand the nature of the tunneling signal and the large contribution from subsurface atoms, we theoretically considered the symmetry of the tunneling matrix elements and performed density-functional theory calculations. We concluded that the dominant contribution to the subsurface signal is from a lattice of Ce atoms 2.53 \AA below the surface Te net. Moreover a simulated STM image constructed from our calculations confirms that the modulation of the signal arising from this lattice is comparable in magnitude to the signal from the surface Te net.

ACKNOWLEDGMENTS

We gratefully acknowledge helpful comments and advice from S. J. L. Billinge, H. J. Kim, and E. S. Bozin. Theoretical calculations were performed at the High Performance Computing Center at Michigan State University. This work was supported by the National Science Foundation under Grants No. DMR-0305461, No. DMR-0703940, and No. DMR-0801855.

*Corresponding author: tessmer@pa.msu.edu

¹E. DiMasi, M. C. Aronson, J. F. Mansfield, B. Foran, and S. Lee, *Phys. Rev. B* **52**, 14516 (1995).

²R. Patschke and M. G. Kanatzidis, *Phys. Chem. Chem. Phys.* **4**, 3266 (2002).

³C. Malliakas, S. J. L. Billinge, H. J. Kim, and M. G. Kanatzidis, *J. Am. Chem. Soc.* **127**, 6510 (2005).

⁴W. Tremel and R. Hoffmann, *J. Am. Chem. Soc.* **109**, 124 (1987).

⁵E. DiMasi, B. Foran, M. C. Aronson, and S. Lee, *Chem. Mater.* **6**, 1867 (1994).

⁶N. Ru and I. R. Fisher, *Phys. Rev. B* **73**, 033101 (2006).

⁷V. Brouet, W. L. Yang, X. J. Zhou, Z. Hussain, N. Ru, K. Y. Shin, I. R. Fisher, and Z. X. Shen, *Phys. Rev. Lett.* **93**, 126405 (2004).

⁸C. Malliakas and M. G. Kanatzidis, *J. Am. Chem. Soc.* **128**, 12612 (2006).

⁹H. J. Kim, C. D. Malliakas, A. T. Tomić, S. H. Tessmer, M. G. Kanatzidis, and S. J. L. Billinge, *Phys. Rev. Lett.* **96**, 226401 (2006).

¹⁰A. Fang, N. Ru, I. R. Fisher, and A. Kapitulnik, *Phys. Rev. Lett.* **99**, 046401 (2007).

¹¹I. R. Fisher (private communication).

¹²W. Lin, H. Steinfink, and E. J. Weiss, *Inorg. Chem.* **4**, 877 (1965).

¹³B. K. Norling and H. Steinfink, *Inorg. Chem.* **5**, 1488 (1966).

¹⁴H. Komoda, T. Sato, S. Souma, T. Takahashi, Y. Ito, and K. Suzuki, *Phys. Rev. B* **70**, 195101 (2004).

¹⁵A. Kikuchi, *J. Phys. Soc. Jpn.* **67**, 1308 (1998).

¹⁶J. Laverock, S. B. Dugdale, Z. Major, M. A. Alam, N. Ru, I. R. Fisher, G. Santi, and E. Bruno, *Phys. Rev. B* **71**, 085114 (2005).

¹⁷Y. Iyeiri, T. Okumura, C. Michioka, and K. Suzuki, *Phys. Rev. B* **67**, 144417 (2003).

¹⁸Image Metrology SPIP, www.imagemet.com.

¹⁹A. Tomic, Ph.D. thesis, Michigan State University, 2008.

²⁰S. Urzhadin, D. Bilc, S. H. Tessmer, S. D. Mahanti, T. Kyratsi, and M. G. Kanatzidis, *Phys. Rev. B* **66**, 161306(R) (2002).

²¹P. Hohenberg and W. Kohn, *Phys. Rev.* **136**, B864 (1964); W. Kohn and L. Sham, *ibid.* **140**, A1133 (1965).

²²V. I. Anisimov, J. Zaanen, and O. K. Andersen, *Phys. Rev. B* **44**, 943 (1991).

²³V. I. Anisimov, I. V. Solovyev, M. A. Korotin, M. T. Czyżyk, and G. A. Sawatzky, *Phys. Rev. B* **48**, 16929 (1993).

²⁴M. T. Czyżyk and G. A. Sawatzky, *Phys. Rev. B* **49**, 14211 (1994).

²⁵V. I. Anisimov, F. Aryasetiawan, and A. I. Liechtenstein, *J. Phys.: Condens. Matter* **9**, 767 (1997).

²⁶D. J. Singh, *Planewaves, Pseudopotentials, and the LAPW Method* (Kluwer Academic, Boston, 1994).

²⁷S. Cottenier, *Density Functional Theory and the Family of (L)APW Methods: A Step by Step Introduction* (Institut voor Kern- en Stralingsfysica, Belgium, 2002).

²⁸P. Blaha, K. Schwartz, G. Madsen, D. Kvasnicka, and J. Luitz, *WIEN2K: An Augmented Plane Wave+Local Orbitals Program for Calculating Crystal Properties* (Techn. Universitat Wien, Austria, 2001).

²⁹J. P. Perdew and Y. Wang, *Phys. Rev. B* **45**, 13244 (1992).

³⁰D. D. Koelling and B. N. Harmon, *J. Phys. C* **10**, 3107 (1977).

³¹A. H. MacDonald, W. E. Pickett, and D. D. Koelling, *J. Phys. C* **13**, 2675 (1980).

³²J. Bardeen, *Phys. Rev. Lett.* **6**, 57 (1961).

³³J. Tersoff and D. R. Hamann, *Phys. Rev. Lett.* **50**, 1998 (1983).

³⁴E. DiMasi, M. C. Aronson, J. F. Mansfield, B. Foran, and S. Lee, *Phys. Rev. B* **52**, 14516 (1995).

Role of K/Bi disorder in the electronic structure of β -K₂Bi₈Se₁₃

Khang Hoang,¹ Aleksandra Tomic,² S. D. Mahanti,^{2,*} Theodora Kyratsi,³
Duck-Young Chung,⁴ S. H. Tessmer,² and Mercouri G. Kanatzidis^{4,5}

¹Materials Department, University of California, Santa Barbara, California 93106, USA

²Department of Physics and Astronomy, Michigan State University, East Lansing, Michigan 48824, USA

³Department of Mechanical and Manufacturing Engineering, University of Cyprus, Nicosia 1678, Cyprus

⁴Materials Science Division, Argonne National Laboratory, Argonne, Illinois 60439, USA

⁵Department of Chemistry, Northwestern University, Evanston, Illinois 60208, USA

(Received 30 March 2009; revised manuscript received 29 June 2009; published 15 September 2009)

We have carried out tunneling spectroscopy and first-principles studies for β -K₂Bi₈Se₁₃, a promising thermoelectric material with partially disordered mixed K/Bi sites. The tunneling data, obtained with a scanning tunneling microscope (STM), show that the system is a semiconductor with a band gap of ~ 0.4 eV and band-tail states near the valence-band top and the conduction-band bottom. First-principles calculations, on the other hand, show that β -K₂Bi₈Se₁₃ can be semimetallic or semiconducting depending on the arrangements of the K and Bi atoms in the mixed sites. The electronic structure of β -K₂Bi₈Se₁₃ near the band-gap region is largely determined by unbonded Se *p* states and states associated with strained bonds which are present due to K/Bi disorder and by the Bi *p*-Se *p* hybridization which tends to drive the system toward metallicity. Among the different K/Bi arrangements investigated, we have identified a structural model (quasidisordered structure) that is able to satisfactorily reproduce the atomic and electronic structures of β -K₂Bi₈Se₁₃; i.e., the local composition in the mixed channels as observed experimentally and the band gap and tails as seen in the STM measurements. We argue that transport properties of β -K₂Bi₈Se₁₃ can be qualitatively understood in terms of the electronic structure obtained in calculations using the above structural model.

DOI: [10.1103/PhysRevB.80.125112](https://doi.org/10.1103/PhysRevB.80.125112)

PACS number(s): 71.20.Nr, 71.23.An, 72.15.Jf

I. INTRODUCTION

In the last several decades, significant efforts have been focused on finding efficient materials for thermoelectric applications. Many different classes of materials have been explored; some examples are complex chalcogenides, skutterudites, half-Heusler alloys, metal oxides, and intermetallic clathrates.¹ Among the complex chalcogenides, β -K₂Bi₈Se₁₃, a narrow band gap and partially disordered semiconductor, has been found to be a promising thermoelectric material at room temperature. The compound exhibits very low thermal conductivity (~ 1.3 W/m K) and relatively high power factor (~ 12 μ W/cm K²).²

β -K₂Bi₈Se₁₃ crystallizes in the monoclinic *P*2₁/*m* space group with $a=17.492(3)$ Å, $b=4.205(1)$ Å, $c=18.461(4)$ Å, $\beta=90.49(2)^\circ$. This structure possesses a three-dimensional architecture made up of Bi₂Te₃⁻, NaCl-, and CdI₂-type infinite rod-shaped blocks. Alternately, it can be described as having one-dimensional channels running along the crystallographic *b* axis each containing K, Bi, Se, or K and Bi atoms. There are one inequivalent channel (per unit cell) fully occupied with K atoms denoted as K(2) and two inequivalent channels denoted as K(1)/Bi(9) and Bi(8)/K(3) containing mixtures of K and Bi atoms. The Bi(8)/K(3) channel contains 62% Bi and 38% K, whereas the K(1)/Bi(9) channel contains 62% K and 38% Bi.² The enhanced thermoelectric property of this system is believed to arise from the unusually low thermal conductivity resulting from a large unit cell with low symmetry, the weakly bound K⁺ ions, and the disorder associated with the mixed-occupancy K/Bi channels.

Low thermal conductivity is only a part of the thermoelectric physics of this system. In order to understand the

physical reason behind the observed large power factor one has to look at the electronic structure of this complex material. It is well known that transport and optical properties of semiconductors depend sensitively on the nature of the electronic states near the band gap.³ Thus, it is necessary to understand the nature of these states in β -K₂Bi₈Se₁₃ and how they are affected by the K/Bi disorder. In this work, we carry out detailed studies of the electronic structure of β -K₂Bi₈Se₁₃ using both tunneling spectroscopy measurements and first-principles calculations. The tunneling measurements were acquired with a cryogenic scanning tunneling microscope (STM), allowing us to investigate the electronic structure of the system in the neighborhood of the chemical potential at low temperature. These measurements provide an important experimental reference which allows for a critical evaluation of different theoretical structural models that take into account the observed disorder in the system.

First-principles calculations have become an important tool to investigate different types of structural disorder and how they impact the electronic properties. Although in principle the disorder effects can be studied using realistic models for disorder, in practice one makes use of supercells that model different configurations for the K/Bi mixed sites in β -K₂Bi₈Se₁₃ to make such calculations feasible. This investigation serves two purposes, one is to understand the interplay between atomic and electronic structures and the role played by the K/Bi disorder, and two is to identify model(s) that best reproduces the atomic and electronic structures of β -K₂Bi₈Se₁₃ as seen in experiments.

Earlier first-principles studies carried out by Bilc *et al.*⁴ using supercell models have provided limited information on the atomic and electronic structures of β -K₂Bi₈Se₁₃. As we

will discuss in Sec. III, the models proposed in Ref. 4 do not correctly reproduce the observed local composition of the mixed channels and hence the fine details of the electronic structure of the system. In this paper, we propose a structural model that better describes the atomic and electronic structures of β -K₂Bi₈Se₁₃. Some of the supercell models proposed earlier by Bilc *et al.* will also be reinvestigated and comparison between different models will be made.

The arrangement of this paper is as follows: in Sec. II, we provide some details on the β -K₂Bi₈Se₁₃ sample preparation and results of the tunneling measurements. Several supercell models designed for first-principles calculations and the calculational details are presented in Sec. III. In Sec. IV, we discuss our results of the energetics, atomic and electronic structures for different models of β -K₂Bi₈Se₁₃. We conclude this paper with a summary in Sec. V.

II. STM MEASUREMENTS

The β -K₂Bi₈Se₁₃ samples used in this study were grown by reacting stoichiometric combination of elemental K, Bi, and Se. All manipulations were carried out under a dry nitrogen atmosphere in a Vacuum Atmospheres Dri-Laboratory glove-box. A mixture of 0.282 g of K, 6.021 g of elemental Bi, and 3.697 g of elemental Se was loaded into silica tube, which was subsequently flame-sealed at a residual pressure of $<10^{-4}$ Torr. The mixture was heated to 850 °C over 12 h and kept there for 1 h, followed by cooling to 450 °C and kept there for 48 h, and cooling to 50 °C at a rate of -15 °C/h. We find that the electronic grade of the material is very high; all samples for measurements discussed here were selected randomly.^{5,6} There is no composition variation or segregation as concluded from x-ray diffraction and energy dispersive x-ray analysis measurements (within the techniques' accuracy). Regarding thermoelectric properties, we have measured the Seebeck coefficient on a sample from the same ingot as the STM measurement, shown below; we find a value of -120 ± 15 μ V/K at 300 K, where the uncertainty is due to limitations of the measurement method. Seebeck measurements on samples from different ingots agree with this value to within the uncertainty.

Transport measurements indicate that β -K₂Bi₈Se₁₃ and related samples are at relatively high doping level as prepared, and that they remain good conductors at low temperature.⁷ As discussed in Ref. 7, the system is well described by a finite-gap semiconductor model, with the addition of a significant concentration of charge carriers originating from the disorder. Further investigation of this issue is the major focus of the present paper.

For the STM measurements, the crystals were cleaved on a laboratory bench top with a razor blade parallel to *b*-axis, and then quickly placed in a high-vacuum environment of a cryogenic STM system, similar to the system described in Ref. 8. The tunneling signals we observed were robust and stable; moreover, high-quality reproducible tunneling spectroscopy curves were observed, as described below. Hence we believe that surface contamination and oxide were minimal. However, attempts to obtain atomically resolved images at room-temperature and low-temperature were unsuccessful.

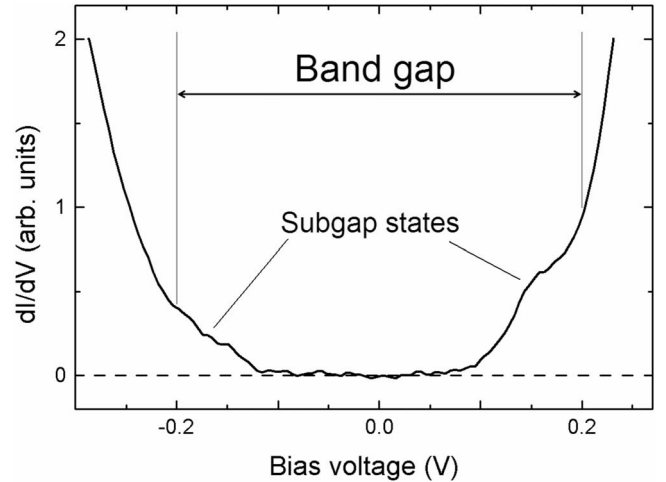


FIG. 1. Local density of states of β -K₂Bi₈Se₁₃ as obtained by STM spectroscopic measurements at 1.6 K. The labels on the horizontal axis give the voltage applied to the sample, relative to the tip (there is no shift or effective zero voltage introduced). The dI/dV curve shows two basic features: a gap and band tails, which we label as subgap states. The gap size has been estimated to be approximately ~ 0.4 eV, by linear extrapolation of the dI/dV curve before it changes slope at the subgap states. The assigned size of the gap is then the approximate voltage between the two intercepts of extrapolated lines with the zero dI/dV baseline.

Tunneling spectroscopy measurements on a cleaved surface of β -K₂Bi₈Se₁₃ were performed at 1.6 K for various positions of the probing tip above the surface of the sample. Sweeping the bias voltage V over a range of ± 300 mV, we have measured tunneling current I as a function of the ramped voltage. Differentiation of $I(V)$ data with respect to V gives the thermally broadened local density of states. The measurements for a given tip position were repeated 100 times, and averaged, in order to improve signal-to-noise ratio.

A representative measurement of the density of states of β -K₂Bi₈Se₁₃ is shown in Fig. 1. Because atomic resolution was not achieved, we do not know which part of the unit cell was probed. However, data were acquired at several tip positions, all of which show nearly identical spectroscopic features. Hence we do not have evidence of significant spectroscopic variations from atom to atom. The thermal smearing of the density of states is $3.5 k_B T$, where k_B is the Boltzmann constant and T is temperature; this results in a voltage smearing of 5×10^{-4} V, which is negligible over the displayed range of data. The data clearly indicate the presence of a band gap. The magnitude of the observed gap is ~ 0.4 eV.⁹ As can be seen in Fig. 1, the spectroscopy data also shows the presence of band-tail states (subgap states), seen as finite density of states in the gap region both near the top of the valence band and near the bottom of the conduction band. Possible explanations of the origin of these states are surface states, defects, and/or the presence of disorder. In the following, we will show that the band tails can indeed be understood in terms of the K/Bi disorder that exists in the system.

III. THEORETICAL MODELING

A. Supercell models

As discussed earlier, β -K₂Bi₈Se₁₃ contains channels with mixed K/Bi occupancy, perhaps in a disordered fashion. Although mixed occupancy as well as disorder can be treated using, for example, coherent potential approximation,^{10,11} they cannot be handled in a realistic fashion by our current first-principles calculations based on density functional theory (DFT). We have therefore used different ordered configurations for the K(1)/Bi(9) and Bi(8)/K(3) channels, using large supercells, to model the mixed sites. This approach can help us understand how the arrangement of the different atoms in the mixed channels and their local geometry affect the electronic structure of β -K₂Bi₈Se₁₃, particularly near the band-gap region. Based on our understanding of the interplay between atomic and electronic structures, we can then identify a supercell model with minimum size that can mimic the crystal structure of partially disordered β -K₂Bi₈Se₁₃.

Several supercell models have been proposed earlier by Bilc *et al.*⁴ to understand the electronic structure of β -K₂Bi₈Se₁₃. Among the proposed configurations for the K(1)/Bi(9) and Bi(8)/K(3) mixed channels there was one with extreme occupancy, hereafter called model M1, that contains 100% Bi on the Bi(8)/K(3) site and 100% K on the K(1)/Bi(9) site. This model (which has 46 atoms/cell) clearly does not reproduce the observed local composition of the mixed channels, i.e., 62% Bi and 38% K on the Bi(8)/K(3) site and 62% K and 38% Bi on the K(1)/Bi(9) site. In order to incorporate the mixed occupancy, a (1 × 2 × 1) supercell with 92 atoms was also proposed.⁴ This model (M2) requires doubling of the unit cell with respect to the unit cell given by the experiment (average occupancy picture). It has K and Bi atoms alternatively occupying the mixed sites along the channels. Each mixed channel has 50% Bi and 50% K. In Ref. 4, models M1 and M2 were referred to as “configuration I” and “configuration III,” respectively.

As we will show later, these two models do not satisfactorily reproduce the electronic structure of β -K₂Bi₈Se₁₃ as seen in our spectroscopy measurements. We, therefore, introduce a new structural model (M3) that can take into account the local composition in the K(1)/Bi(9) and Bi(8)/K(3) channels more accurately. This model requires unit cell tripling along the *b* axis with respect to the unit cell given by experiment, resulting in a (1 × 3 × 1) supercell with 138 atoms. The mixed channels, K(1)/Bi(9) and Bi(8)/K(3), are modeled by repeating (K-Bi-K) unit (67% K and 33% Bi) and (Bi-K-Bi) unit (67% Bi and 33% K), respectively, along the *b* axis.

B. Computational details

Structural optimization, total energy and electronic structure calculations were performed within the DFT formalism, using the generalized-gradient approximation (GGA) (Ref. 12) and the projector-augmented wave (PAW) (Refs. 13 and 14) method as implemented in the VASP code.^{15–17} We used the standard PAW potentials in the VASP database. Scalar relativistic effects (mass-velocity and Darwin terms) and spin-orbit interaction (SOI) were included, except in ionic optimization where only scalar relativistic effects were taken

into account. Each calculation begins with volume optimization and ionic position relaxations of a chosen structure, the relaxed structure was then used to calculate energy and single-particle electronic density of states (DOS).

For the calculations of models M1, M2, and M3, we used 3 × 14 × 3 (35 **k** points in the irreducible Brillouin zone), 3 × 7 × 3 (32 **k** points), and 3 × 5 × 3 (23 **k** points) Monkhorst-Pack¹⁸ **k**-point meshes, respectively, for the self-consistent run to calculate charge densities. More **k** points (~50% larger) were used to produce high-quality electronic DOSs. In all the calculations, the energy cutoff was set to 220 eV and the convergence was assumed when the total energy between cycles was less than 10⁻⁴ eV. A choice of denser **k**-point meshes and/or larger energy cutoff does not change the physics of what we are presenting.

IV. RESULTS AND DISCUSSION

A. Atomic relaxations and energetics

We find remarkable changes in the local geometry of β -K₂Bi₈Se₁₃ in all the three models. The optimized volumes of the supercells are larger compared to the experimental value by ~3%. This is expected since it is known that DFT-GGA tends to overestimate the lattice constants.¹⁹ Regarding internal relaxations, the displacements from the initial positions are largest for the Bi atoms in the mixed channels, i.e., Bi(8) and Bi(9), and for their neighboring Se atoms. This is a result of the strong hybridization between trivalent cation (Bi)*p* and divalent anion (Se)*p* states as seen in many chalcogenides,^{20,21} and the initial positions of the Bi atoms in the mixed channels being far from equilibrium. Note that, in the initial structures (models M1, M2, and M3), K and Bi are treated equally in the mixed channels, i.e., without taking into account the fact that they bond differently to the neighboring Se atoms. The large geometric relaxations also result in large (internal) relaxation energies, measured as the difference between the total energy of the fully relaxed (volume, cell shape, and positions of ions) supercell and that of the partially relaxed (only volume optimization) supercell; -802, -722, and -720 meV/f.u. for M1, M2, and M3, respectively, where f.u. = K₂Bi₈Se₁₃.

Figure 2 shows the relaxed structure of β -K₂Bi₈Se₁₃ in model M1 where the mixed sites are occupied by 100% K or 100% Bi. The most notable feature in this structure is the presence of onefold coordinated Se atoms, Se(9). Se(9) channels are sandwiched between K(1) and K(2) channels; Se(9) atoms only bond to their nearest neighbor Bi(3) atoms with the Se(9)-Bi(3) distance being 2.62 Å. This relaxation pattern is clearly caused by the deficit of Bi in the local environment of the Se(9) atoms. Besides having Se(9) as the nearest neighbor, Bi(3) in model M1 has two Se(10) atoms as the second nearest neighbors with the bond lengths being 2.79 Å.

Figure 3 shows the relaxed structure of β -K₂Bi₈Se₁₃ in model M2. Unlike M1, there is no onefold coordinated Se atoms in M2 which has 50% K and 50% Bi in the mixed channels. Both Se(9) and Se(4) are twofold coordinated. Bi(8) and Bi(9) in the mixed channels relax appreciably to-

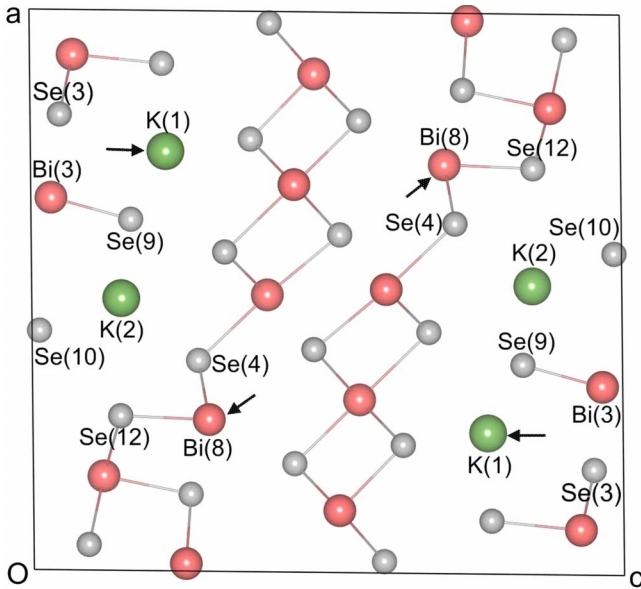


FIG. 2. (Color online) Relaxed structure of β - $K_2Bi_8Se_{13}$ in model M1 (46 atoms/cell). The view is along the b axis. Potassium is represented by large (green) spheres, bismuth is medium (red), and selenium is small (gray). This model contains 100% K and 100% Bi, respectively, on the K(1)/Bi(9) and Bi(8)/K(3) mixed sites (marked by arrows). After relaxations, Se(9) is onefold coordinated, with the Se(9)-Bi(3) bond length being 2.62 Å. Bi(8) has one Se(12) atom as its nearest neighbor (bond length: 2.81 Å) and two Se(4) atoms as its second-nearest neighbors (bond lengths: 2.84 Å). Only bonds with bond length smaller than 3.1 Å are shown.

ward their respective neighboring Se atoms, Se(4) and Se(9), respectively.

Model M3, on the other hand, has one third of the Se(9) atoms that are onefold coordinated, two-third of the atoms in the Se(9) channels are twofold coordinated; see Fig. 4. This is because of the deficit of Bi in the K(1)/Bi(9) mixed chains where one has only 33% Bi. In this model, we also find that Bi(8) and Bi(9) strongly relax toward, respectively, Se(4) and Se(9). As we will discuss below, the onefold coordinated Se atoms seen in some of these models play a very important role in determining the electronic structure of the system near the band gap.

Energetically, model M2 has the lowest energy, lower than models M1 and M3 by 299 and 92 meV/f.u., respectively. One can understand this trend in terms of the presence (or absence) of undercoordinated Se atoms. In M1 there is a channel containing Se atoms in which each Se atom has only one Bi atom as a neighbor to bond and stabilize its p orbitals. In M2 each Se atom is bonded to two Bi atoms whereas in M3 there is a mixture of one- and twofold coordinated Se atoms. These differences in bonding and their impact on the electronic structure of β - $K_2Bi_8Se_{13}$ will be discussed in detail later. What is interesting and surprising is that although on energetic grounds the ordered 50-50 mixture of K and Bi channels (model M2) is most favorable, it is likely that the presence of quasisordered 33-67 mixture (model M3) makes that system kinetically more favorable, given the experimentally observed structure.

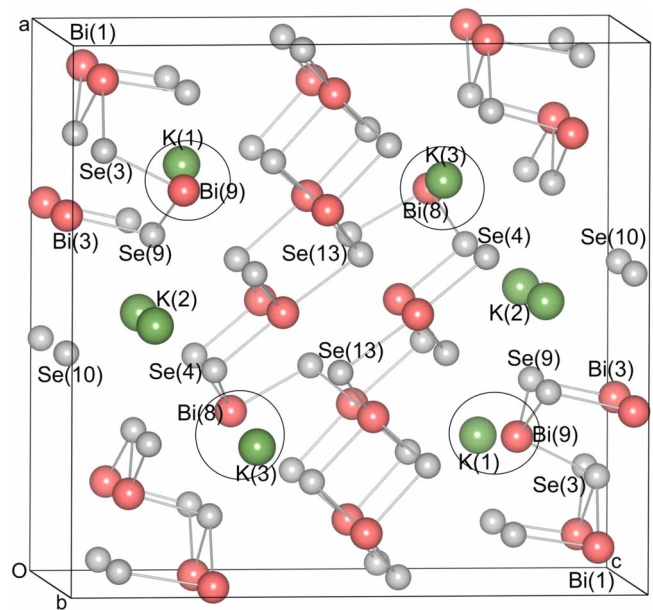


FIG. 3. (Color online) Relaxed structure of β - $K_2Bi_8Se_{13}$ in model M2 (92 atoms/cell). The viewing direction is approximately parallel to the b axis. Potassium is represented by large (green) spheres, bismuth is medium (red), and selenium is small (gray). This model requires unit cell doubling along the b axis with respect to the unit cell given by experiment. The mixed sites, K(1)/Bi(9) and Bi(8)/K(3) [marked by circles], are modeled by K-Bi-... and Bi-K-... channels, respectively, along the b axis; both channels have 50% K and 50% Bi. After relaxations, the Bi(9) atom in the K(1)/Bi(9) channel moves closer and forms bonds with two Se(9) atoms (bond lengths: 2.70 and 2.73 Å) and one Se(3) atom (bond length: 2.90 Å). The Bi(9) atom in the Bi(8)/K(3) channel, on the other hand, moves closer and forms bonds with two Se(9) atoms (bond lengths: 2.70 and 2.76 Å) and one Se(13) atom (bond length: 2.94 Å). Only bonds with bond length smaller than 3.1 Å are shown.

B. Electronic structure

Figure 5 shows the total DOS of β - $K_2Bi_8Se_{13}$ in model M1 focusing on the electronic structure near the band-gap region. Model M1 shows semimetallic feature, consistent with results reported by Bilc *et al.*⁴ In the earlier calculations, where only partial internal relaxations were performed, the band structure did not appear to change appreciably due to internal relaxation. In the present calculations, we have carried out full internal relaxation and have monitored the DOS in the neighborhood of the Fermi level. We find that atomic relaxations reduce the DOS in the region near the Fermi level considerably by pushing some states toward lower and some states toward higher energies. An analysis of the wave functions shows that the region below and near the Fermi level is predominantly Se(9) p states, which are unbonded, and a small contribution from the Se(10) p states; whereas the region above and near the Fermi level is predominantly hybridized Bi(8) p and Se(4) p states.

The above results can be understood in terms of the observed relaxed structure of β - $K_2Bi_8Se_{13}$ in model M1 (see also Fig. 2) where Se(9) is onefold coordinated and Bi(8) and Se(4) are the nearest neighbors of one another. The electronic

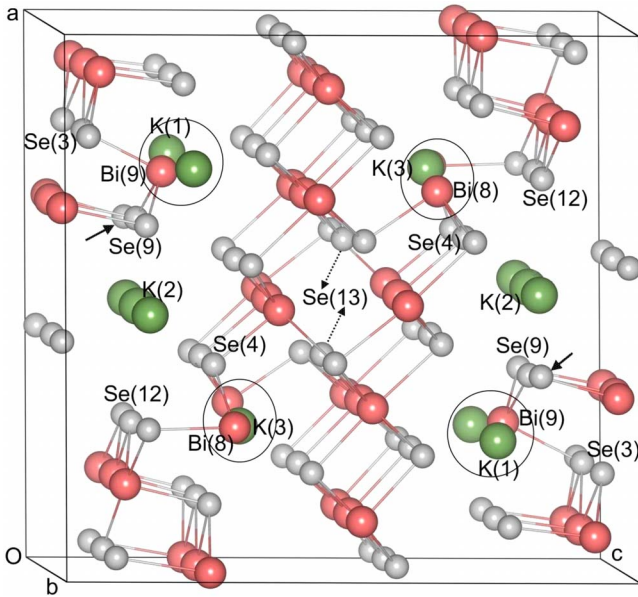


FIG. 4. (Color online) Relaxed structure of $\beta\text{-K}_2\text{Bi}_8\text{Se}_{13}$ in model M3 (138 atoms/cell). The viewing direction is approximately parallel to the b axis. Potassium is represented by large (green) spheres, bismuth is medium (red), and selenium is small (gray). This model requires unit cell tripling along the b -axis with respect to the unit cell given by experiment. The mixed sites, K(1)/Bi(9) and Bi(8)/K(3) [marked by circles], are modeled by K-Bi-K... (67% K and 33% Bi) and Bi-K-Bi... (67% Bi and 33% K) channels, respectively, along the b axis. After relaxations, the Bi(9) atom in the K(1)/Bi(9) channel moves closer and forms bonds with two Se(9) atoms (bond lengths: 2.69 and 2.71 Å) and one Se(3) atom (bond length: 2.89 Å). There are two Bi(8) atoms in the K(3)/Bi(8) channel which relax toward different directions. One Bi(8) atom moves closer and forms bonds with two Se(4) atoms (bond lengths: 2.77 and 2.80 Å) and one Se(12) atom (bond length: 2.81 Å). The other Bi(8) atom moves closer and forms bonds with two Se(4) atoms (bond lengths: 2.72 and 2.83 Å) and one Se(13) atom (bond length: 2.87 Å). One-third of the Se(9) atoms is onefold coordinated [marked by arrows] because of the deficit of Bi in the K(1)/Bi(9) channels. Only bonds with bond length smaller than 3.1 Å are shown.

structure near the band-gap region in model M1 is, therefore, determined by the onefold coordinated Se(9) atoms and the hybridization between Bi(8) p and Se(4) p states. The latter introduces hybridized p states into the band-gap region from the conduction-band bottom and reduces (or even closes) the band gap. This is consistent with the observations in many chalcogenides where the hybridization between trivalent cation p states and divalent anion p states tends to drive the system toward metallicity.^{20,21}

Figure 6 shows the total DOS of $\beta\text{-K}_2\text{Bi}_8\text{Se}_{13}$ in model M2. In this model, both the valence- and conduction-band edges are sharp for both the relaxed and the unrelaxed structures. This indicates that the electronic states coming from Se(4), Se(9), Bi(8), and Bi(9) are completely stabilized, consistent with our analysis of the relaxed structure of model M2 and also the fact that this model gives the lowest energy. An analysis of the wave functions indeed shows that the top of the valence band is predominantly Se(10) p states with

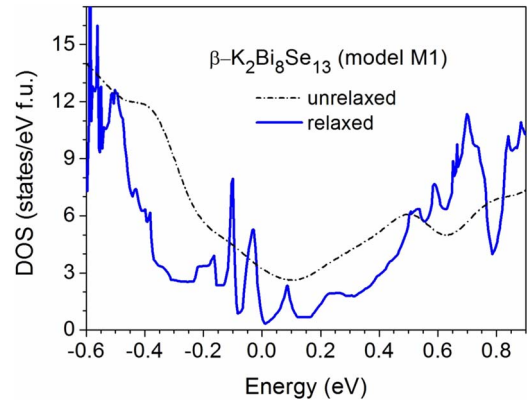


FIG. 5. (Color online) Total DOS of $\beta\text{-K}_2\text{Bi}_8\text{Se}_{13}$ (model M1) obtained in calculations using unrelaxed (dash dotted curve) and relaxed (solid curve) structures; SOI was included. The Fermi level (at 0 eV) is set to the highest occupied state; f.u. = $\text{K}_2\text{Bi}_8\text{Se}_{13}$. This model shows semimetallic character.

very small contribution from hybridized states of Se(9) p and Bi p ; the conduction-band bottom consists predominantly of Bi(1) p states with small contribution from Bi(3) p states. There are no unbonded Se p states (as seen in model M1) and the hybridized states coming from Bi(9) p -Se(9) p and Bi(8) p -Se(4) p hybridizations are stabilized by, respectively, the monovalent cation K(1) and K(3) in the K(1)/Bi(9) and Bi(8)/K(3) mixed channels. The relaxed structure gives a band gap of ~ 0.52 eV, slightly larger than the unrelaxed one (by 0.10 eV). The calculated band gap in the unrelaxed structure is in good agreement with the earlier results of Bilc *et al.*⁴ (~ 0.41 eV), where only the supercell volume was optimized. This indicates that the internal atomic relaxations are important and can significantly affect the electronic structure of the system near the band gap. We note that SOI has strong effects on the electronic structure of $\beta\text{-K}_2\text{Bi}_8\text{Se}_{13}$, reducing the band gap by a significant amount (from 0.75 to 0.52 eV for model M2).

The total DOS of $\beta\text{-K}_2\text{Bi}_8\text{Se}_{13}$ for model M3, which gives a more accurate partial occupancy of the K/Bi channels, is

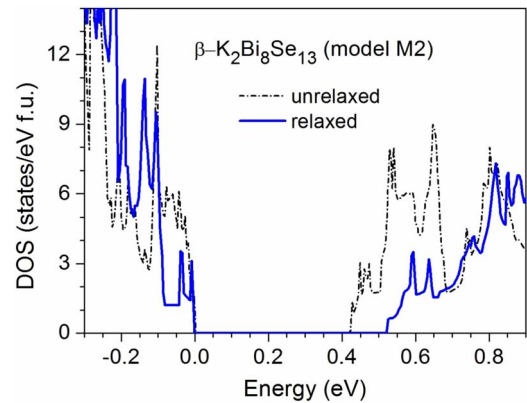


FIG. 6. (Color online) Total DOS of $\beta\text{-K}_2\text{Bi}_8\text{Se}_{13}$ (model M2) obtained in calculations using unrelaxed (dash dotted curve) and relaxed (solid curve) structures; SOI was included. The Fermi level (at 0 eV) is set to the highest occupied state; f.u. = $\text{K}_2\text{Bi}_8\text{Se}_{13}$. The band gap is ~ 0.52 eV (relaxed) and the band edges are sharp (no band tails) in this model.

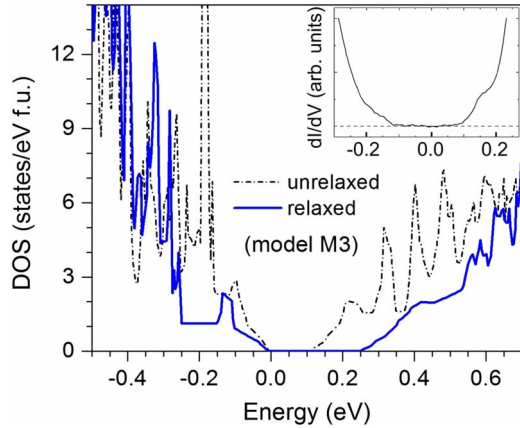


FIG. 7. (Color online) Total DOS of β - $\text{K}_2\text{Bi}_8\text{Se}_{13}$ (model M3) obtained in calculations using unrelaxed (dash dotted curve) and relaxed (solid curve) structures; SOI was included. The Fermi level is set to the highest occupied state; f.u. = $\text{K}_2\text{Bi}_8\text{Se}_{13}$. There are band-tail states in this model formed by the unbonded states associated with the onefold coordinated Se(9) atoms, the hybridized Bi p -Se p states near the mixed channels, and those coming from strained bonds associated with a wide range of Bi and Se atoms. The local density of states of β - $\text{K}_2\text{Bi}_8\text{Se}_{13}$ obtained by STM spectroscopic measurements (Fig. 1) is shown in the inset for comparison.

shown in Fig. 7. This model gives a semiconducting gap of ~ 0.25 eV, much smaller than seen in M2. However there is a different way to interpret the DOS for this model, namely a band gap of ~ 0.4 eV (> 0.25 eV) with a large band-tail density of states both below the conduction band and above the valence band. An examination of the wave functions shows that the states associated with the valence band tail are

predominantly Se(10) p states with contribution from the p states of the onefold coordinated Se(9) atoms and a small contribution from the Bi(3) p states. The conduction band tail states are primarily Bi(1) p states and contributions from a wide range of other Bi and Se atoms including the hybridized Bi p -Se p states that are not fully stabilized by the monovalent K because of the deficit of K atoms in the Bi(8)/K(3) channels. This is shown clearly in Fig. 8, where we plot the partial charge densities associated with the valence-band top and the conduction-band bottom of β - $\text{K}_2\text{Bi}_8\text{Se}_{13}$.

Clearly, the unbonded p states of the onefold coordinated Se(9) atoms, which account for one third of the total number of atoms in the Se(9) channels, play a crucial role in forming the valence band-tail states in model M3. There are possibly other contributions from the strained bonds associated with a variety of Bi and Se atoms to the valence band tail (and to the conduction band tail), given the complexities of the relaxed structure where atoms in the neighboring region of the mixed sites are strongly perturbed from their average positions. We note that studies on defective crystalline Si and amorphous Si by Pan *et al.*²² also showed that band tails existed in these systems and there were correlations between the band-tail states and the long and short bonds in the lattice.

C. Comparison with experiment

Let us now make comparison between the results obtained in first-principles studies and those from experiments. The computed DOS for model M3 and the results of STM measurements for β - $\text{K}_2\text{Bi}_8\text{Se}_{13}$ show remarkable similarities (see Fig. 7). The gap between the subgap states is ~ 0.2 eV whereas the calculated band gap is ~ 0.25 eV. The values of

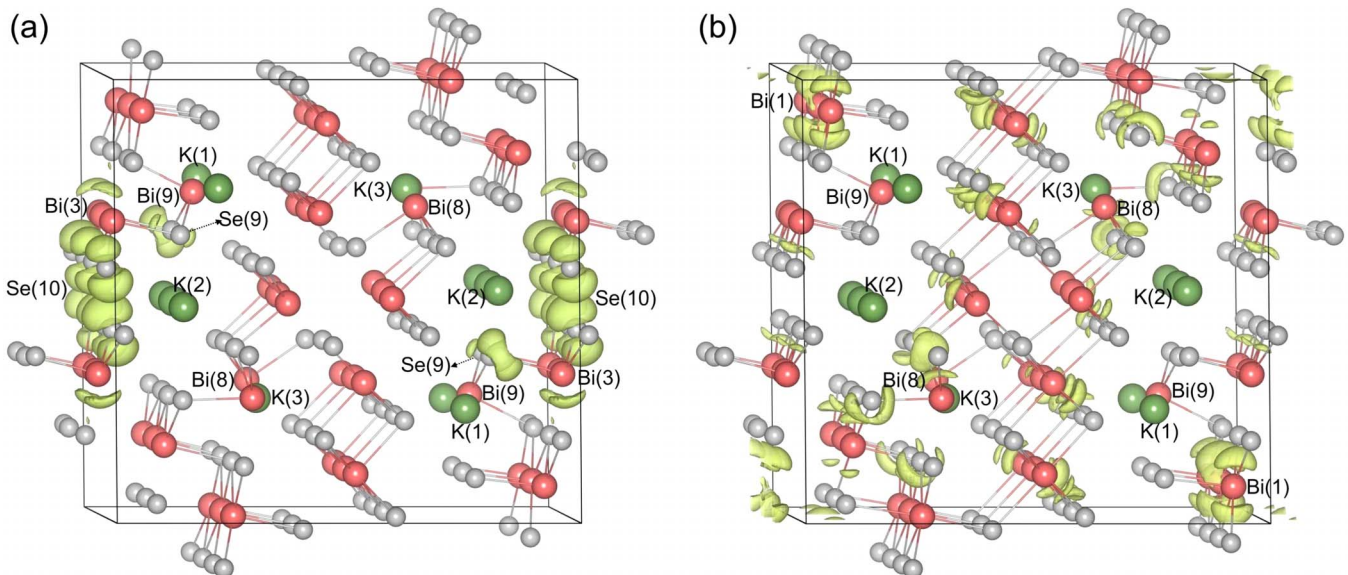


FIG. 8. (Color online) Partial charge density associated with (a) the valence-band top (in the energy range -0.2 to 0 eV) and (b) the conduction-band bottom (in the energy range $+0.2$ to $+0.4$ eV) as illustrated by electron clouds around the atoms; the energy ranges are with respect to the total DOS of β - $\text{K}_2\text{Bi}_8\text{Se}_{13}$ (model M3) shown in Fig. 7. The isosurface corresponds to (charge density) \times (supercell volume) = 10.5 in (a) and 1.5 in (b). Potassium is represented by large (green) spheres, bismuth is medium (red), and selenium is small (gray). In (a), the visualized charge density is predominantly Se(10) with contribution from the onefold coordinated Se(9) atoms and a small contribution from Bi(3), whereas in (b) it is Bi(1) and contributions from a wide range of other Bi and Se atoms.

the band gap between the valence-band maximum and the conduction-band minimum (disregarding the subgap or band-tail states) in spectroscopy measurements and in theoretical calculations are comparable and are estimated to be of ~ 0.4 eV.

The overall agreement between the density of states obtained for model M3 and the STM measurements appears to be quite good; however, one should consider this agreement with some caution because of the usual band gap underestimation by DFT-GGA,¹⁹ and the close agreement is perhaps fortuitous. What is important is that the DFT calculations give a physical picture of the electronic states near the top of the valence band and the bottom of the conduction band, referred to as the “subgap” states in the description of our STM results. These states are present only when the K/Bi mixed channels have stoichiometry consistent with experiment.

Although there may be limitations associated with DFT-GGA calculations and the simplicity of the model to capture the mixed occupancy along K/Bi channels, the ability of model M3 to reproduce band-tail states as seen in the spectroscopy measurements provides strong validation for this model, making it an excellent candidate that can be used for further theoretical studies and analyses of partially disordered β -K₂Bi₈Se₁₃, such as in structural analysis and in first-principles calculations of the transport properties. Among the three models that we have presented, model M3 is also closest to the experimental crystal structure of β -K₂Bi₈Se₁₃ in terms of the local composition of the mixed sites. Careful PDF measurements²³ can validate some of our theoretical predictions in terms of different bond lengths due to internal relaxations.

Finally, our results for the electronic structure of β -K₂Bi₈Se₁₃ are consistent with measured transport properties of β -K₂Bi₈Se₁₃ (and its alloys with the Sb analog),⁷ where the experimental data were successfully interpreted by using a narrow band-gap semiconductor model. In addition,

the band tails observed in first-principles calculations (using model M3) and in the spectroscopy measurements may explain why β -K₂Bi₈Se₁₃ has higher electrical conductivity without much loss of thermoelectric power, compared to its allotropic kin α -K₂Bi₈Se₁₃ which does not contain channels with mixed occupancy.^{2,24}

V. SUMMARY

In summary, the electronic density of states in the neighborhood of the Fermi energy of β -K₂Bi₈Se₁₃, a partially disordered narrow band-gap semiconductor with mixed occupancy on two K/Bi sites, was studied using scanning tunneling spectroscopy. The STM spectroscopic data showed that this material is a narrow band-gap semiconductor with a band gap of ~ 0.4 eV. The spectroscopy measurements also revealed the presence of band tail (subgap) states.

First-principles calculations using different supercell models (M1, M2, and M3) showed that β -K₂Bi₈Se₁₃ can either be a semimetal or a semiconductor depending on how the K and Bi atoms are arranged in the mixed-occupancy channels. Among these models, M3 was found to satisfactorily reproduce the atomic and electronic structures of partially disordered β -K₂Bi₈Se₁₃, including the local composition in the mixed channels as observed experimentally and the band gap and band tails as seen in the spectroscopy measurements. The transport properties of β -K₂Bi₈Se₁₃ can be qualitatively understood in terms of the electronic structure obtained in our studies.

ACKNOWLEDGMENTS

This work was supported in part by the Office of Naval Research and NSF Grant No. 0305461, and made use of the computing facilities of Michigan State University High Performance Computing Center.

*Corresponding author; mahanti@pa.msu.edu

¹G. S. Nolas, J. Poon, and M. G. Kanatzidis, *MRS Bull.* **31**, 199 (2006), and references therein.

²D. Y. Chung, K. S. Choi, L. Iordanidis, J. L. Schindler, P. W. Brazis, C. R. Kannewurf, B. Chen, S. Hu, C. Uher, and M. G. Kanatzidis, *Chem. Mater.* **9**, 3060 (1997).

³G. D. Mahan and J. O. Sofo, *Proc. Natl. Acad. Sci. U.S.A.* **93**, 7436 (1996).

⁴D. I. Bilc, S. D. Mahanti, T. Kyratsi, D.-Y. Chung, M. G. Kanatzidis, and P. Larson, *Phys. Rev. B* **71**, 085116 (2005).

⁵Th. Kyratsi, J. S. Dyck, W. Chen, D.-Y. Chung, C. Uher, K. M. Paraskevopoulos, and M. G. Kanatzidis, *J. Appl. Phys.* **92**, 965 (2002).

⁶Th. Kyratsi, D.-Y. Chung, and M. G. Kanatzidis, *J. Alloys Compd.* **338**, 36 (2002).

⁷Th. Kyratsi, E. Hatzikraniotis, K. M. Paraskevopoulos, C. D. Malliakas, J. S. Dyck, C. Uher, and M. G. Kanatzidis, *J. Appl. Phys.* **100**, 123704 (2006).

⁸S. H. Tessmer, D. J. Van Harlingen, and J. W. Lyding, *Rev. Sci. Instrum.* **65**, 2855 (1994).

⁹Diffuse reflectance spectroscopy measurements of β -K₂Bi₈Se₁₃ at room temperature suggested an apparent band gap of ~ 0.59 eV (Ref. 2). The key difference between the optical and tunneling measurements of the band gap is that optical measurements are sensitive to wave vector \mathbf{k} and optical matrix element connecting the valence and conduction band states. In contrast, the tunneling measurements are sensitive to the matrix element between the states of the system and the tip. This difference may be the reason for observed difference in the values of the band gap seen in tunneling and reflectance spectroscopy measurement.

¹⁰P. Soven, *Phys. Rev.* **156**, 809 (1967).

¹¹B. L. Gyorffy, *Phys. Rev. B* **5**, 2382 (1972).


¹²J. P. Perdew, K. Burke, and M. Ernzerhof, *Phys. Rev. Lett.* **77**, 3865 (1996).

¹³P. E. Blöchl, *Phys. Rev. B* **50**, 17953 (1994).

- ¹⁴G. Kresse and D. Joubert, *Phys. Rev. B* **59**, 1758 (1999).
- ¹⁵G. Kresse and J. Hafner, *Phys. Rev. B* **47**, 558 (1993).
- ¹⁶G. Kresse and J. Furthmüller, *Phys. Rev. B* **54**, 11169 (1996).
- ¹⁷G. Kresse and J. Furthmüller, *Comput. Mater. Sci.* **6**, 15 (1996).
- ¹⁸H. J. Monkhorst and J. D. Pack, *Phys. Rev. B* **13**, 5188 (1976).
- ¹⁹W. G. Aulber, L. Jönsson, and J. W. Wilkins, *Solid State Phys.* **54**, 1 (2000).
- ²⁰K. Hoang, S. D. Mahanti, J. R. Salvador, and M. G. Kanatzidis, *Phys. Rev. Lett.* **99**, 156403 (2007).
- ²¹K. Hoang and S. D. Mahanti, *Phys. Rev. B* **77**, 205107 (2008).
- ²²Y. Pan, F. Inam, M. Zhang, and D. A. Drabold, *Phys. Rev. Lett.* **100**, 206403 (2008).
- ²³S. J. L. Billinge and I. Levin, *Science* **316**, 561 (2007).
- ²⁴T. J. McCarthy, S. P. Ngeyi, J. H. Liao, D. C. DeGroot, T. Hogan, C. R. Kannewurf, and M. G. Kanatzidis, *Chem. Mater.* **5**, 331 (1993).

RESEARCH ARTICLE | MARCH 03 2015

Enhanced thermoelectric power and electronic correlations in RuSe₂

Kefeng Wang ; Aifeng Wang; A. Tomic; Limin Wang; A. M. Milinda Abeykoon; E. Dooryhee; S. J. L. Billinge; C. Petrovic



APL Mater. 3, 041513 (2015)

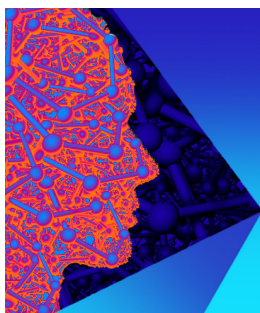
<https://doi.org/10.1063/1.4913919>



View
Online



Export
Citation



APL Materials
Special Topic: 2D Materials
for Biomedical Applications

Submit Today



Enhanced thermoelectric power and electronic correlations in RuSe₂

Kefeng Wang,^{1,a} Aifeng Wang,¹ A. Tomic,¹ Limin Wang,¹
 A. M. Milinda Abeykoon,³ E. Dooryhee,³ S. J. L. Billinge,^{1,2} and C. Petrovic^{1,b}
¹Condensed Matter Physics and Materials Science Department, Brookhaven National
 Laboratory, Upton, New York 11973, USA
²Department of Applied Physics and Applied Mathematics, Columbia University, New York,
 New York 10027, USA
³Photon Sciences Directorate, Brookhaven National Laboratory, Upton,
 New York 11973, USA

(Received 31 December 2014; accepted 19 February 2015; published online 3 March 2015)

We report the electronic structure, electric and thermal transport properties of Ru_{1-x}Ir_xSe₂ ($x \leq 0.2$). RuSe₂ is a semiconductor that crystallizes in a cubic pyrite unit cell. The Seebeck coefficient of RuSe₂ exceeds $-200 \mu\text{V/K}$ around 730 K. Ir substitution results in the suppression of the resistivity and the Seebeck coefficient, suggesting the removal of the peaks in density of states near the Fermi level. Ru_{0.8}Ir_{0.2}Se₂ shows a semiconductor-metal crossover at about 30 K. The magnetic field restores the semiconducting behavior. Our results indicate the importance of the electronic correlations in enhanced thermoelectricity of RuSb₂. © 2015 Author(s). All article content, except where otherwise noted, is licensed under a Creative Commons Attribution 3.0 Unported License. [<http://dx.doi.org/10.1063/1.4913919>]

Recent interest in thermoelectric energy conversion induces a wide interest in the materials with high thermoelectric performance.^{1,2} A narrow distribution or a large peak in the electronic density of states (DOS) close to the Fermi level has long been considered favorable for a high Seebeck coefficient (S).^{3,4} Such peak could be induced by the resonant level dopants in semiconductors^{5,6} or by the magnetic interaction between the local magnetic moment and itinerant electrons in many f - and d -electron based materials.^{7,8} It has been reported that some strongly correlated metals (such as heavy fermion metals) and correlated semiconductors (such as Kondo insulators) show significant enhanced Seebeck coefficient and power factor. For example, large peaks in Seebeck coefficient up to $800 \mu\text{V/K}$ were observed in heavy fermion metal CePd₃,^{9,10} Kondo insulator FeSi,¹¹⁻¹³ Ce₃Pt₃Sb₄,¹⁴ and CeFe₄P₁₂.¹⁵

More recently, a very large Seebeck coefficient ($\sim 4 \times 10^4 \mu\text{V/K}$) and huge power factor ($\sim 2 \times 10^3 \mu\text{W/K}^2 \text{cm}$)¹⁶⁻¹⁹ were observed in FeSb₂.²⁰ This makes the mechanism of thermopower enhancement in FeSb₂ of high interest.²¹⁻²⁶ The results from density functional theory without electron correlation effect can only qualitatively reproduce the temperature dependence of the Seebeck coefficient. The predicted peak value of S is only one tenth of the experimental value, suggesting the importance of strong electronic correlations.^{13,23,26}

Pyrite FeS₂ is a semiconductor with a band gap of (0.8–0.95) eV and a high light absorption.^{27,28} FeS₂ shows a Seebeck coefficient up to $\sim -300 \mu\text{V/K}$ at 300 K.²⁹ The Seebeck coefficient of iron dichalcogenides FeX₂ [$X = (\text{S}, \text{Se}, \text{Te})$] decreases for heavier chalcogens due to decreasing energy gap but retains relatively large values of $\sim |(2-3)| \cdot 10^2 \mu\text{V/K}$ above 200 K.³⁰

Here, we report the detailed electronic structure, electric and thermal transport properties of pure and Ir-doped RuSe₂ pyrite. RuSe₂ shows a semiconducting behavior with an indirect gap from

^aPresent address: Department of Physics, University of Maryland, College Park, Maryland 20742-4111, USA. Electronic mail: wangkf@umd.edu.

^bpetrovic@bnl.gov

resistivity ~ 1.5 eV. The band structure calculation shows a pileup of states near the Fermi level suggesting correlation effects. The Seebeck coefficient of RuSe₂ exceeds -200 $\mu\text{V}/\text{K}$ at 730 K, showing the electron-type carriers. Ir doping introduces lattice expansion and extra electrons, which results in the significant suppression of the resistivity and the Seebeck coefficient. The sample with 20% Ir doping shows a semiconductor-metal transition at about 20 K, while the magnetic field restores the semiconducting behavior.

(Ru_{1-x}Ir_x)Se₂ (with $x = 0, 0.1, 0.2$) polycrystals were made using a high-temperature solid state reaction method. Stoichiometric Ru (99.99%), Ir (99.99%), and Se (99.9999%) were ground, pelletized, sealed in a quartz tube, heated to 1000 °C, kept for about 20 h, and then the furnace was turned off. Next, the material was ground, pelletized again, and heated with the similar temperature profile at 1100 °C. Medium resolution room temperature X-ray diffraction measurements were carried out using a (0.25-0.25) mm² 48 keV ($\lambda = 0.02487$ nm) focused (on the detector) X-ray beam at 28-ID-C beam line at National Synchrotron Light Source II at Brookhaven National Laboratory. The X-ray energy was selected using a horizontally focused double crystal Laue monochromator, with vertical focusing achieved using 1 m long Si mirror. Finely pulverized samples were filled into 1 mm diameter cylindrical polyimide capillaries, and the data collection was carried out in transmission geometry using Perkin Elmer amorphous silicon area detector mounted orthogonal to the beam path 1272.6 mm away from the sample. The raw 2D data were integrated and converted to intensity versus scattering angle using the software Fit2D.³¹ The average structure was assessed through Rietveld refinements³² to the raw diffraction data using the General Structure Analysis System (GSAS)³³ operated under EXPGUI (a graphical user interface for GSAS),³⁴ utilizing Pa-3 model from the literature.³⁵ Electrical transport measurements were conducted on polished samples in Quantum Design Physical Properties Measurement System PPMS-9 with conventional four-wire method. Thermal transport properties were measured in Quantum Design PPMS-9 from 2 K to 350 K, and in Ulvac ZEM-3 system at higher temperatures, both using one-heater-two-thermometer method. The relative error of each measurement was $\frac{\Delta\kappa}{\kappa} \sim 5\%$ and $\frac{\Delta S}{S} \sim 10\%$ based on standard; however, at 350 K, the discrepancy in measured values was 25%. As opposed to ULVAC ZEM-3, PPMS S , and ρ were obtained in separate measurements using TTO (thermal transport option) and ACT (alternating current transport) option on the same sample. Hence, ULVAC ZEM-3 data were normalized to PPMS values at 300 K. First principle electronic structure calculation was performed using experimental lattice parameters within the full-potential linearized augmented plane wave (LAPW) method³⁶ implemented in WIEN2k package.³⁷ The general gradient approximation (GGA) of Perdew *et al.*,³⁸ was used for exchange-correlation potential. The LAPW sphere radius was set to 2.5 Bohr for all atoms. The converged basis corresponding to $R_{min}k_{max} = 7$ with additional local orbital was used, where R_{min} is the minimum LAPW sphere radius and k_{max} is the plane wave cutoff.

Diffraction data for all three compositions are well explained within pyrite-type *Pa-3* structure, comprised of 3D network of distorted (squashed) Se6 octahedra that coordinate Ru/Ir. Irregularity of the octahedra is reflected in principal axes deviating from 90° (see Figure 1). Refined structural parameters are summarized in Table I. Lattice parameter increases on substituting Ru with larger Ir. Average Ru-Se near neighbor distance decreases slightly with doping, whereas departure for regularity in octahedral angles increases slightly. Debye-Waller factors increase slightly with doping as well, consistent with presence of quenched disorder introduced by chemical substitution. The Ir doping limit is 20% and above that the synthesis resulted in mixed phases of *Pa-3* space group of pure RuSe₂ and *Pnma* space group of pure IrSe₂.

Fig. 2 shows the electrical and thermal transport properties. The resistivity of RuSe₂ [Fig. 2(a)] shows typical semiconducting behavior. The fitting for thermal activation conductivity [the solid line in Fig. 2(b)] estimates that the main band gap is ~ 1.5 eV. The slope of the resistivity or the energy gap changes in the low temperature range, possibly due to the native *d*-states or impurity states within the main band gap, similar to Fe_{1-x}Ru_xSb₂.³⁹ The Seebeck coefficient [Fig. 2(c)] approaches 180 $\mu\text{V}/\text{K}$ at 350 K and shows a peak of about 247 $\mu\text{V}/\text{K}$ at about 730 K. The thermal conductivity of RuSe₂ [Fig. 2(d)] is rather high in the whole range of measured temperatures.

The semiconducting behavior of RuSe₂ is consistent with the first principle calculation results (Fig. 3). The density of states [Fig. 3(a)] shows a gap with size of 0.4 eV, whereas the band structure [Fig. 3(b)] indicates that RuSe₂ is an indirect-gap semiconductor. However, the gap size from the

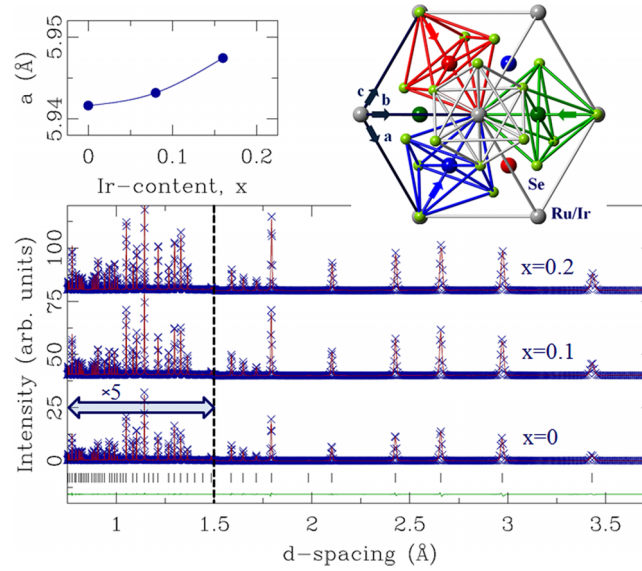


FIG. 1. $\text{Ru}_{1-x}\text{Ir}_x\text{Se}_2$ crystal structure considerations. Main panel shows 300 K experimental x-ray diffraction patterns (cross symbols) and refined structural model $Pu-3$ (solid red line), with difference curve (green solid line) offset for clarity for $x = 0$. Vertical ticks mark reflections. Data and model profiles for samples with $x = 0.1$ and 0.2 nominal composition are included and offset for clarity. Top left: evolution of lattice parameter with refined Ir content, solid line is guide for the eyes. Top right: pyrite-type crystal structure as seen along (111) direction, and distorted RuSe_6 corner shared octahedra representing basic building blocks of the structure.

density functional theory (0.4 eV) is much smaller than the transport gap (about 1.5 eV), suggesting that the electron correlations may be important. There are several narrow bands just below the Fermi level with Ru $4d$ orbital character [the heavy lines in Fig 3(b)]. This is confirmed by the large pileup of states [Fig. 3(a)]. But there is also significant hybridization between Ru $4d$ and Se p orbitals indicated by the overlap between the peaks from Ru and Se below and above the Fermi level.

The high Seebeck coefficient of RuSe_2 should come from the peaks in density of states just below the Fermi level [Fig. 3(a)], with major contribution from the narrow d -bands. Although the Seebeck coefficient of RuSe_2 is high, its power factor is small because of the high resistivity.

Ir doping introduces carriers and is effective in enhancing the conductivity; however, it also significantly suppresses Seebeck coefficient [Figs. 2(a) and 2(c)]. The 10% Ir doped sample still shows semiconducting behavior but the residual resistivity decreases by two orders of magnitude at 2 K and in half at 200 K when compared to pure RuSe_2 . Further increase in Ir substitution suppresses the resistivity even more. The sample with 20% Ir doping shows a semiconductor-metal crossover at ~ 30 K; below that temperature, the resistivity begins decreasing with decreasing temperature [Figs. 2(a) and 4(a)]. The thermal conductivity is also suppressed by Ir doping [Fig. 2(d)], possibly due to the lattice disorder introduced by the doping. The 10% Ir doping reduces the Seebeck coefficient to only about $2 \mu\text{V}/\text{K}$ at 300 K [inset in Fig. 2(c)].

TABLE I. Lattice parameters for Ir-doped RuSe_2 .

Nominal composition	Lattice (Å)	x_{Se}	Uiso-Ru (Å)	Uiso-Se (Å)	Refined composition	R (°)
RuSe_2	5.941 64(3)	0.3807(2)	0.0039(3)	0.0051(3)	$\text{Ru}_{0.99(1)}\text{Se}_2$	7.3
$\text{Ru}_{0.9}\text{Ir}_{0.1}\text{Se}_2$	5.943 19(7)	0.3794(2)	0.0042(3)	0.0058(3)	$\text{Ru}_{0.92(1)}\text{Ir}_{0.08(1)}\text{Se}_2$	5.6
$\text{Ru}_{0.8}\text{Ir}_{0.2}\text{Se}_2$	5.947 40(7)	0.3784(2)	0.0045(3)	0.0061(3)	$\text{Ru}_{0.84(1)}\text{Ir}_{0.16(1)}\text{Se}_2$	4.5
Nominal composition	Se-Ru (Å)	Se-Ru-Se (°)	Se-Ru-Se (°)			
RuSe_2	2.4742(3)	94.71(2)	85.29(2)			
$\text{Ru}_{0.9}\text{Ir}_{0.1}\text{Se}_2$	2.4722(3)	94.82(2)	85.18(2)			
$\text{Ru}_{0.8}\text{Ir}_{0.2}\text{Se}_2$	2.4720(3)	94.91(2)	85.09(2)			

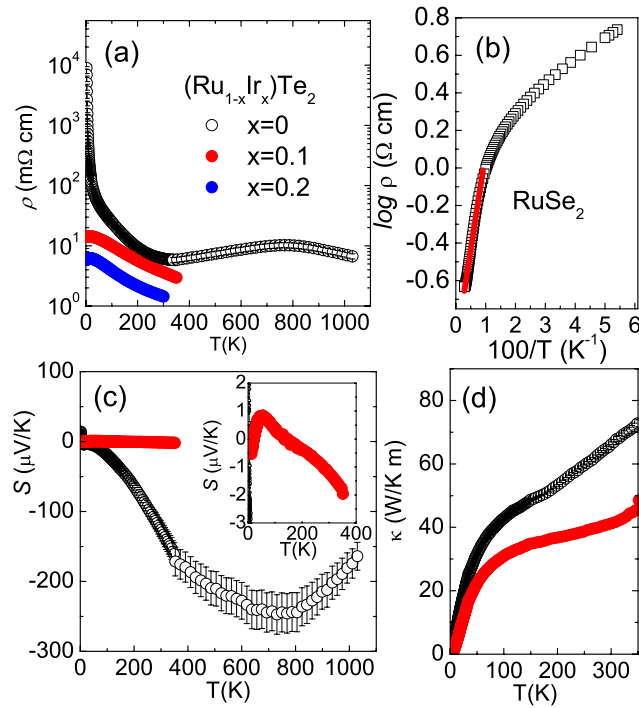


FIG. 2. The Resistivity ρ (a), the $\log \rho$ vs $1/T$ relationship for pure RuSe₂ and the solid line is the linear fitting result using thermal activation theory (b), Seebeck coefficient S (c), and thermal conductivity κ (d) for (Ru_{1-x}Ir_x)Se₂ with $x = 0, 0.1,$ and 0.2 .

The magnetic field has significant influence on the transport of Ru_{0.8}Ir_{0.2}Se₂ in the low temperature range [Fig. 4(a)]. Above the semiconductor-metal crossover at ~ 30 K, the application of magnetic field has minute effect on the resistivity. But below it, in the metallic regime, the magnetic field enhances the value of resistivity and changes its temperature dependence. In 4 T field, the $\rho(T)$ still undergoes the semiconductor-metal transition at the same temperature but then changes to semiconducting behavior below 4 K. The 9 T magnetic field totally smears out the semiconductor-metal transition and restores the semiconducting behavior. The magnetoresistance ratio (MR) is always positive at 2 K and tends to saturate in higher fields [Fig. 4(b)].

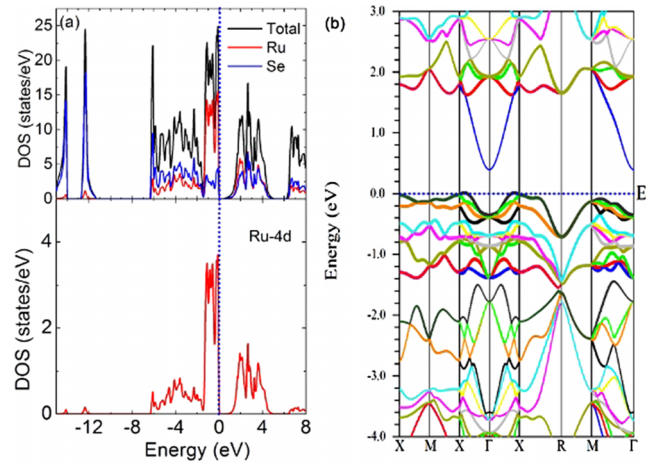


FIG. 3. (a) The density of states and (b) the band structure of RuSe₂. The different colors in band structure indicate different bands and the thickness of the bands represents the weight of Ru 4d orbitals.

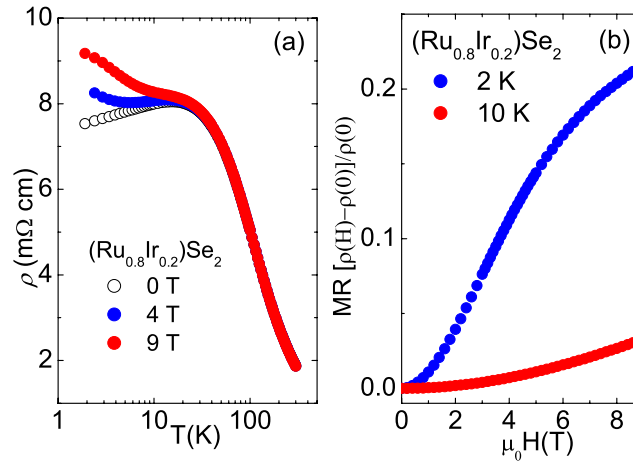


FIG. 4. (a) Temperature dependence of the resistivity ρ of $(\text{Ru}_{0.8}\text{Ir}_{0.2})\text{Se}_2$ in different magnetic fields. (b) The magnetoresistance ratio $MR = (\rho(H) - \rho(0)) / \rho(0)$ as the function of the magnetic field for $(\text{Ru}_{0.8}\text{Ir}_{0.2})\text{Se}_2$ with $T = 2 \text{ K}$ and 10 K , respectively.

The clear suppression of the value and the slope of the resistivity indicate that the Ir-doping induces the decrease of the band gap. The 10% Ir doping only introduces 0.1 electrons per unit cell. This will result in a slight shift of the Fermi level toward higher energy direction [Fig. 3(a)], within the framework of the density functional theory. Since 10% Ir-doped RuSe_2 is still a semiconductor, it is reasonable to believe that the Fermi level is still in the gap. If so, this slight shift of the Fermi level could not induce the huge suppression of the Seebeck coefficient [Fig. 2(c)]. Since the Seebeck coefficient is related to the energy slope of the density of states near the Fermi level, this implies the effect of electronic correlations. The $5d$ electrons of Iridium feature less localized (i.e., more extended) wave functions when compared to $4d$ electrons of Ruthenium. Hence, Iridium substitution not only introduces extra carriers but also reduces the electronic correlations. Furthermore, since the magnetic field restores the semiconducting behavior in sample with 20% Ir level, the original semiconducting behavior in pure RuSe_2 could be related to some extent to the magnetic mechanism. Taken together with enhanced thermopower, our results suggest that physical properties of RuSe_2 may share some similarity with the correlated electron semiconductor FeSb_2 .^{19,20} The comparison of the electronic structure, electronic and magnetic correlations of pyrite RuSe_2 to marcasite FeSb_2 could be important for studies of structural effects on correlated electron thermoelectricity and deserves further studies.

Electronic structure of pyrites, such as $\text{NiS}_{2-x}\text{Se}_x$, is related to the occupation of d orbitals which have significant influence on the band filling and correlation effect.⁴⁰ Pyrites and marcasites both feature distorted octahedral coordination of transition metals (e.g., Fe or Ru) in the local structure.⁴¹ Whereas the octahedra share common corners in the cubic pyrite unit cell and the resulting crystal field at Ru in RuSe_2 has trigonal symmetry, the orthorhombic marcasite unit cell features linear chains of edge-sharing octahedra parallel to orthorhombic c -axis. In both cases, d -electrons dominate the electronic states near the Fermi level. In RuSe_2 , the t_{2g} orbitals are completely filled as opposed to t_{2g} orbitals in marcasite FeSb_2 .^{41,42} This inhibits a possibility for thermally induced anisotropic metallic states and thermally induced enhanced Pauli susceptibility.^{19,20,43} On the other hand, when comparing RuSe_2 to RuSb_2 , Se($4p4$) has an extra electron when compared to Sb ($5p3$). So it is expected that the occupation of d orbitals in RuSe_2 is different from RuSb_2 which would change correlation strength. This is reflected in the density of states: Ru d -states in RuSe_2 (Fig. 3) are more enhanced near the Fermi level when compared to RuSb_2 .³⁹ Triangular arrangement of metal (i.e., Ru) atoms in pyrite lattice of RuSe_2 (Fig. 1) could enhance the correlation effects in RuSe_2 even further via geometric frustration. This has been theoretically considered⁴⁴ and experimentally verified in pyrite NiS_2 .⁴⁵ Since geometrical frustration coupled with strong Coulomb

interaction may enhance thermoelectric power,^{46,47} putative antiferromagnetic states in RuSe₂ materials are of interest. The figure of merit $ZT = S^2/\rho\kappa$ value at 300 K (730 K) is only about 0.003 (0.005 assuming about 100 W/Km). Thermal conductivity is rather high and very far away from the amorphous limit. Nanoengineering of RuSe₂ objects may reduce thermal conductivity and could lead to much larger values of ZT .^{48–51}

In conclusion, we report enhanced thermoelectric power and electronic correlations in RuSe₂. RuSe₂ show a semiconducting behavior with a thermally activated gap. The band structure calculation confirmed the semiconducting characteristic, albeit with significantly underestimated gap implying the importance of the electron correlation effect. The Seebeck coefficient of RuSe₂ approaches $-250 \mu\text{V/K}$ near 730 K, showing the electron-type carriers. Small Ir doping results in the significant suppression of the resistivity and the Seebeck coefficient. The sample with 20% Ir doping shows a semiconductor-metal transition at about 20 K, while the magnetic field restores the semiconducting behavior at low temperature. Our results shows the large Seebeck coefficient of RuSe₂ and implies the important role of electron and magnetic correlations.

Work at Brookhaven is supported by the U.S. DOE under Contract No. DE-AC02-98CH10886. X-ray scattering data were collected at 28-ID-C x-ray powder diffraction beam line at National Synchrotron Light Source II at Brookhaven National Laboratory. Use of the National Synchrotron Light Source II, Brookhaven National Laboratory, was supported by the U.S. Department of Energy, Office of Science, Office of Basic Energy Sciences, under Contract No. DE-SC0012704.

- ¹ G. D. Mahan and J. O. Sofo, "The best thermoelectric," *Proc. Natl. Acad. Sci. U. S. A.* **93**, 7436-7439 (1996).
- ² G. J. Snyder and E. S. Toberer, "Complex thermoelectric materials," *Nat. Mater.* **7**, 105-114 (2008).
- ³ Y. Pei, X. Shi, A. LaLonde, H. Wang, L. Chen, and G. J. Snyder, "Convergence of electronic bands for high performance bulk thermoelectrics," *Nature* **473**, 66-69 (2011).
- ⁴ L. E. Bell, "Cooling, heating, generating power and recovering waste heat with thermoelectric system," *Science* **321**, 1457-1461 (2008).
- ⁵ J. P. Heremans, V. Jovovic, E. S. Toberer, A. Sarmat, K. Kurosaki, A. Charoenphakdee, S. Yamanaka, and G. J. Snyder, "Enhancement of thermoelectric efficiency in PbTe by distortion of the electronic density of states," *Science* **321**, 554-557 (2008).
- ⁶ J. P. Heremans, B. Wiendlocha, and A. M. Chamoire, "Resonant levels in bulk thermoelectric semiconductors," *Energy Environ. Sci.* **5**, 5510-5530 (2012).
- ⁷ G. D. Mahan, *Solid State Phys.* **51**, 81 (1998).
- ⁸ J. Kondo, "Giant thermo-electric power of dilute magnetic alloys," *Prog. Theor. Phys.* **34**, 372-382 (1965).
- ⁹ G. D. Mahan, B. Sales, and J. Sharp, "Thermoelectric materials: New approaches to an old problem," *Phys. Today* **50**(3), 42 (1997).
- ¹⁰ Y. Ijiri and F. J. DiSalvo, "Thermoelectric properties of R_xCe_{1-x}Pd₃ (R=Y, La_{0.5}Y_{0.5}, Nd)," *Phys. Rev. B* **55**, 1283 (1998).
- ¹¹ R. Wolfe, J. H. Wernick, and S. E. Haszko, "Thermoelectric properties of FeSi," *Phys. Lett.* **19**, 449-450 (1965).
- ¹² B. C. Sales, O. Delaire, M. A. McGuire, and A. F. May, "Thermoelectric properties of Co-, Ir-, and Os-doped FeSi alloys: Evidence for strong electron-phonon coupling," *Phys. Rev. B* **83**, 125209 (2011).
- ¹³ J. M. Tomczak, K. Haule, and G. Kotliar, "Signatures of electronic correlations in iron silicide," *Proc. Natl. Acad. Sci. U. S. A.* **109**, 3243-3246 (2012).
- ¹⁴ C. D. W. Jones, K. A. Regan, and F. J. DiSalvo, "Thermoelectric properties of the doped Kondo insulator: Nd_xCe_{3-x}Pt₃Sb₄," *Phys. Rev. B* **58**, 16057 (1998).
- ¹⁵ H. Sato *et al.*, "Anomalous transport properties of RFe₄P₁₂ (R = La, Ce, Pr, and Nd)," *Phys. Rev. B* **62**, 15125 (2000).
- ¹⁶ A. Bentien, S. Johnsen, G. K. H. Madsen, B. B. Iversen, and F. Steglich, "Colossal Seebeck coefficient in strongly correlated semiconductor FeSb₂," *Europhys. Lett.* **80**, 17008 (2007).
- ¹⁷ P. Sun, N. Oeschler, S. Johnsen, B. B. Iversen, and F. Steglich, "FeSb₂: Prototype of huge electron-diffusion thermoelectricity," *Phys. Rev. B* **79**, 153308 (2009).
- ¹⁸ P. Sun, N. Oeschler, S. Johnsen, B. B. Iversen, and F. Steglich, "Huge thermoelectric power factor: FeSb₂ versus FeAs₂ and RuSb₂," *Appl. Phys. Express* **2**, 091102 (2009).
- ¹⁹ Q. Jie, R. Hu, E. Bozin, A. Llobet, I. Zaliznyak, C. Petrovic, and Q. Li, "Electronic thermoelectric power factor and metal-insulator transition in FeSb₂," *Phys. Rev. B* **86**, 115121 (2012).
- ²⁰ C. Petrovic, Y. Lee, T. Vogt, N. Dj. Lazarov, S. L. Bud'ko, and P. C. Canfield, "Kondo insulator description of spin state transition in FeSb₂," *Phys. Rev. B* **72**, 045103 (2005).
- ²¹ H. Z. M. Pokharel, G. Zhu, S. Chen, K. Lukas, Q. Jie, C. Opeil, G. Chen, and Z. Ren, "Dramatic thermal conductivity reduction by nanostructures for large increase in thermoelectric figure-of-merit of FeSb₂," *Appl. Phys. Lett.* **99**, 163101 (2011).
- ²² K. Wang, R. Hu, J. Warren, and C. Petrovic, "Enhancement of the thermoelectric properties in doped FeSb₂ bulk crystals," *J. Appl. Phys.* **112**, 013703 (2012).
- ²³ M. K. H. Zhao, M. Pokharel, S. Chen, T. Dahal, C. Opeil, G. Chen, and Z. Ren, "Thermoelectric property enhancement by Cu nanoparticles in nanostructured FeSb₂," *Appl. Phys. Lett.* **102**, 213111 (2013).
- ²⁴ A. Bentien, G. K. H. Madsen, S. Johnsen, and B. B. Iversen, "Experimental and theoretical investigations of strongly correlated FeSb_{2-x}Sn_x," *Phys. Rev. B* **74**, 205105 (2006).

- ²⁵ P. Sun, N. Oeschler, S. Johansen, B. B. Iversen, and F. Steglich, "Narrow band gap and enhanced thermoelectricity in FeSb₂," *Dalton Trans.* **39**, 1012-1019 (2010).
- ²⁶ J. Tomczak, K. Haule, A. Georges, and G. Kotliar, "Thermopower of correlated semiconductors: Application to FeAs₂ and FeSb₂," *Phys. Rev. B* **82**, 085104 (2010).
- ²⁷ M. S. Seehra and S. S. Seehra, "Temperature dependence of the band gap of FeS₂," *Phys. Rev. B* **12**, 6620 (1979).
- ²⁸ A. Ennaoui, S. Fiechter, Ch. Pettenkofer, N. Alonso-Vante, K. Buker, M. Bronold, Ch. Hopfner, and H. Tributsch, "Iron disulfide for solar energy conversion," *Sol. Energy Mater. Sol. Cells* **29**, 085104 (1993).
- ²⁹ G. Willeke, O. Blenk, Ch. Kloc, and E. Bucher, "Preparation and electrical transport of pyrite (FeS₂) single crystals," *J. Alloys Compd.* **178**, 181 (1992).
- ³⁰ T. Harada, "Transport properties of iron dichalcogenides FeX₂ (X=S,Se and Te)," *J. Phys. Soc. Jpn.* **67**, 1352 (1998).
- ³¹ A. P. Hammersley, S. O. Svenson, M. Hanfland, and D. Hauserman, "Two-dimensional detector software: From real detector to idealised image of two-theta scan," *High Pressure Res.* **14**, 235 (1996).
- ³² H. M. Rietveld, "Line profiles of neutron powder-diffraction peaks for structure refinement," *Acta Crystallogr.* **22**, 151 (1967).
- ³³ A. C. Larson and R. B. Von Dreele, "General structure analysis system," Report No. LAUR-86-748, Los Alamos National Laboratory, Los Alamos, NM 87545, 1987.
- ³⁴ B. H. Toby, "EXPGUI, a graphical user interface for GSAS," *J. Appl. Crystallogr.* **34**, 210 (2001).
- ³⁵ H. D. Lutz, B. Muller, T. Schmidt, and T. Stingl, "Structure refinement of pyrite-type ruthenium disulfide, RuS₂, and ruthenium diselenide RuSe₂," *Acta Crystallogr., Sect. C: Cryst. Struct. Commun.* **46**, 2003 (1990).
- ³⁶ M. Weinert, E. Wimmer, and A. J. Freeman, "Total-energy all-electron density functional method for bulk solids and surfaces," *Phys. Rev. B* **26**, 4571 (1982).
- ³⁷ P. Blaha, K. Schwarz, G. K. H. Madsen, D. Kvasnicka, and J. Luitz, *WIEN2k, An Augmented Plane Wave 1 Local Orbitals Program for Calculating Crystal Properties* (Karlheinz Schwarz, Technische Universitat Wien, Austria, 2001). ISBN 3-9501031-1-2.
- ³⁸ J. P. Perdew, K. Burke, and M. Ernzerhof, "Generalized gradient approximation made simple," *Phys. Rev. Lett.* **77**, 3865 (1996).
- ³⁹ M. K. Fuccillo, Q. D. Gibson, M. N. Ali, L. M. Schoop, and R. J. Cava, "Correlated evolution of colossal thermoelectric effect and Kondo insulating behavior," *APL Mater.* **1**, 062102 (2013).
- ⁴⁰ M. Imada, A. Fujimori, and Y. Tokura, "Metal-insulator transitions," *Rev. Mod. Phys.* **70**, 1039 (1998).
- ⁴¹ J. B. Goodenough, "Energy bands in TX₂ compounds with pyrite, marcasite and arsenopyrite structures," *J. Solid State Chem.* **5**, 144 (1972).
- ⁴² G. Brostigen and A. Kjekhus, "Bonding schemes for compounds with the pyrite, marcasite and arsenopyrite type structures," *Acta Chem. Scand.* **24**, 2993 (1970).
- ⁴³ C. Petrovic, J. W. Kim, S. L. Bud'ko, A. I. Goldman, P. C. Canfield, W. Choe, and G. J. Miller, "Anisotropy and large magnetoresistance in the narrow-gap semiconductor FeSb₂," *Phys. Rev. B* **67**, 155205 (2003).
- ⁴⁴ S. Katsura and T. Imaizumi, "Annealed ising bond-mixture on the pyrite lattices," *Prog. Theor. Phys.* **67**, 434 (1982).
- ⁴⁵ M. Matsuura, Y. Endoh, H. Hiraka, K. Yamada, A. S. Mishchenko, N. Nagaosa, and I. V. Solovyev, "Classical and quantum spin dynamics in the fcc antiferromagnet NiS₂ with frustration," *Phys. Rev. B* **68**, 094409 (2003).
- ⁴⁶ X.-L. Gu, F. Lu, D.-Y. Liu, and L.-J. Zou, "Thermoelectric power of single-orbital and two-orbital Hubbard models on triangular lattices," *Physica B* **405**, 4145 (2010).
- ⁴⁷ L.-F. Arsenault, B. S. Shastry, P. Semon, and A.-M. S. Tremblay, "Entropy, frustration and large thermopower of doped Mott insulators on the fcc lattice," *Phys. Rev. B* **87**, 035126 (2013).
- ⁴⁸ A. I. Hochbaum, R. Chen, R. D. Delgado, W. Liang, E. C. Garnett, M. Najarian, A. Majumdar, and P. Yang, "Enhanced thermoelectric performance of rough silicon nanowires," *Nature* **451**, 163 (2007).
- ⁴⁹ B. Poudel, Q. Hao, Y. Ma, Y. Lan, A. Minnich, B. Yu, X. Yan, D. Wang, A. Muto, D. Vashaee, X. Chen, J. Liu, M. Dresselhaus, G. Chen, and Z. F. Ren, "High thermoelectric performance of nanostructured bismuth antimony telluride bulk alloys," *Science* **320**, 634 (2008).
- ⁵⁰ M. G. Kanatzidis, "Nanostructured thermoelectrics: The new paradigm," *Chem. Mater.* **22**, 648 (2010).
- ⁵¹ L.-F. C. Wan, Y. Wang, N. Wang, W. Norimatsu, M. Kusunoki, and K. Koumoto, "Development of novel thermoelectric materials by reduction of lattice thermal conductivity," *Sci. Technol. Adv. Mater.* **11**, 044306 (2010).



ZnFe₂O₄ antiferromagnetic structure redetermination

Aleksandar Kremenović^{a,*}, Bratislav Antić^b, Predrag Vulić^a, Jovan Blanuša^b, Aleksandra Tomic^{b,c}



^a Laboratory for Crystallography, Faculty of Mining and Geology, University of Belgrade, Dušina 7, Belgrade 11000, Serbia

^b Condensed Matter Physics Laboratory, Institute of Nuclear Sciences "Vinča", University of Belgrade, P.O. Box 522, Belgrade 11001, Serbia

^c Department of Applied Physics and Applied Mathematics, Columbia University, New York, NY, 10027, USA

ARTICLE INFO

Keywords:

Antiferromagnetic structure
Normal spinel
Non-collinear model

ABSTRACT

Magnetic structure of ZnFe₂O₄ normal spinel is re-examined. Antiferromagnetic structure non-collinear model is established within C_{2v} space group having four different crystallographic/magnetic sites for 32 Fe³⁺ spins within magnetic unit cell.

1. Introduction

Zinc ferrite ZnFe₂O₄ crystallizes in spinel type structure, represented by general formula AB₂X₄, nuclear space group (S.G.) $Fd\bar{3}m$. Cations occupy tetrahedral 8a (A), and octahedral 16d (B) sites, while oxygen is in the 32e crystallographic position. Crystalline ZnFe₂O₄ could have a mixed, metastable, cation distribution with some percentage of Zn²⁺ residing at 16d sites instead of 8a sites, and corresponding concentration of Fe³⁺ then occupies 8a sites. This is often described as inverted spinel with formula (Zn_{1-α}Fe_α)A[Zn_αFe_{2-α}]B, where inversion parameter α depends on the sample preparation method and on the thermal treatment. It is well-known that three kinds of interactions, AA, B-B, and A-B superexchange interactions, exist in spinel ferrites, in which A-B interaction is much stronger than the others. In ZnFe₂O₄ having normal spinel structure, the absence of Fe at A sites (populated by nonmagnetic Zn) results in weak antiferromagnetic exchange interactions within Fe at B sites, making ZnFe₂O₄ antiferromagnetic below 9 K. The B site is octahedrally coordinated with edge-sharing connectivity and the B-B distances are rather short. Therefore, the supremacy of the nearest neighbour interaction will be much reduced and ZnFe₂O₄ exhibits long range ordering and quite complex ground states.

In the literature there are a few descriptions of the magnetic structure of normal ZnFe₂O₄. However, the existing references don't give precise data on all elements of the magnetic structure i.e. atomic coordinates with corresponding magnetic moment projections and magnetic symmetry space group. For example Szytuła gave only a graphical presentation of the magnetic structure (Figure 8 in [8]) while Greedan point that "ZnFe₂O₄ for example, adopt very complex spin orderings with large magnetic unit cells" and suggest the existence of geometric frustration in it [3]. The magnetic structure model for

normal ZnFe₂O₄ presented by König et al. (Figures 3 and 4) and Boucher et al. (Figures 2–5) both in 1970 is only schematically presented. They did not report numeric values of atomic coordinates and corresponding magnetic moment projections. As a potential solution for normal ZnFe₂O₄ magnetic structure description they discussed different magnetic structure space groups; $P1\bar{4}$ in reference [4] and $I\bar{4}2d$, $I\bar{4}22$ or even lower symmetry space groups in reference [1]. Consequently, the exact magnetic structure space group for normal ZnFe₂O₄ is still missing. Without this information magnetic structure description of normal ZnFe₂O₄ is exclusively in space group $P1$, i.e. for all 32 Fe atoms that are within the unit cell numeric values for atomic coordinates and corresponding magnetic moment projections are symmetrically independent. The main goal of our work is to find symmetry relations between different Fe atoms with corresponding magnetic moments within unit cell, i.e. find the normal ZnFe₂O₄ magnetic structure space group other than $P1$.

2. Results and discussion

It is now well established that ZnFe₂O₄ normal spinel magnetically orders (long range order – LRO) at a rather low temperature of 9 K into a ground state. However, the magnetic structure description so far has been incomplete and not well understood [3]. Particularly, neither the collinearity/noncollinearity of the spin ordering has been confirmed, nor has the magnetic space group been deduced unquestionably. The magnetic structure model used at present is the one proposed by König [4] and Boucher [1], defined as a non-collinear model that can be described by ordering vector $\mathbf{k}=(0\ 0\ 1/2)$ applied to a cubic spinel structure and involves 32 Fe spins. In both references rather low values of magnetic moments are reported, 3.9 μ_B[4] and 4.0 μ_B[1] respectively at 4.2 K, as compared to expected 5 μ_B. Furthermore, the consensus

* Corresponding author.

E-mail address: akremenovic@rgf.bg.ac.rs (A. Kremenović).

Table 1

Atom labels, symmetry multiplicities, Wyckoff labels, fractional coordinates x,y and z, site occupancy, moment crystal axes x, y and z for magnetic structure model in S.G. $P1$ and unit cell parameters $a=8.43961 \text{ \AA}$, $b=8.43961 \text{ \AA}$, $c=16.87923 \text{ \AA}$, $\alpha=\beta=\gamma=90^\circ$.

label	Symm mult.	Wyck label	x	y	z	occ	moment x μ_B	moment y μ_B	moment z μ_B	net moment μ_B
Fe1	1	a	0.500	0.500	0.250	1	-2.609	0.000	-3.758	4.575
Fe2	1	a	0.250	0.750	0.000	1	0.000	2.609	3.758	4.575
Fe3	1	a	0.750	0.000	0.125	1	0.000	-2.609	3.758	4.575
Fe4	1	a	0.000	0.250	0.375	1	-2.609	0.000	-3.758	4.575
Fe5	1	a	0.500	0.000	0.000	1	0.000	-2.609	3.758	4.575
Fe6	1	a	0.250	0.250	0.250	1	2.609	0.000	-3.758	4.575
Fe7	1	a	0.750	0.500	0.375	1	2.609	0.000	-3.758	4.575
Fe8	1	a	0.000	0.750	0.125	1	0.000	2.609	3.758	4.575
Fe9	1	a	0.000	0.500	0.000	1	0.000	2.609	-3.758	4.575
Fe10	1	a	0.750	0.750	0.250	1	-2.609	0.000	3.758	4.575
Fe11	1	a	0.250	0.000	0.375	1	-2.609	0.000	3.758	4.575
Fe12	1	a	0.500	0.250	0.125	1	0.000	-2.609	-3.758	4.575
Fe13	1	a	0.000	0.000	0.250	1	2.609	0.000	3.758	4.575
Fe14	1	a	0.750	0.250	0.000	1	0.000	-2.609	-3.758	4.575
Fe15	1	a	0.250	0.500	0.125	1	0.000	2.609	-3.758	4.575
Fe16	1	a	0.500	0.750	0.375	1	2.609	0.000	3.758	4.575
Fe17	1	a	0.500	0.500	0.750	1	2.609	0.000	3.758	4.575
Fe18	1	a	0.250	0.750	0.500	1	0.000	-2.609	-3.758	4.575
Fe19	1	a	0.750	0.000	0.625	1	0.000	2.609	-3.758	4.575
Fe20	1	a	0.000	0.250	0.875	1	2.609	0.000	3.758	4.575
Fe21	1	a	0.500	0.000	0.500	1	0.000	2.609	-3.758	4.575
Fe22	1	a	0.250	0.250	0.750	1	-2.609	0.000	3.758	4.575
Fe23	1	a	0.750	0.500	0.875	1	-2.609	0.000	3.758	4.575
Fe24	1	a	0.000	0.750	0.625	1	0.000	-2.609	-3.758	4.575
Fe25	1	a	0.000	0.500	0.500	1	0.000	-2.609	3.758	4.575
Fe26	1	a	0.750	0.750	0.750	1	2.609	0.000	-3.758	4.575
Fe27	1	a	0.250	0.000	0.875	1	2.609	0.000	-3.758	4.575
Fe28	1	a	0.500	0.250	0.625	1	0.000	2.609	3.758	4.575
Fe29	1	a	0.000	0.000	0.750	1	-2.609	0.000	-3.758	4.575
Fe30	1	a	0.750	0.250	0.500	1	0.000	2.609	3.758	4.575
Fe31	1	a	0.250	0.500	0.625	1	0.000	-2.609	3.758	4.575
Fe32	1	a	0.500	0.750	0.875	1	-2.609	0.000	-3.758	4.575

Table 2

Atom labels, symmetry multiplicities, Wyckoff labels, fractional coordinates x,y and z, site occupancy, moment crystal axes x, y and z for magnetic structure model in S.G. C_{2v} and unit cell parameters $a=11.93541 \text{ \AA}$, $b=16.87923 \text{ \AA}$, $c=8.43961 \text{ \AA}$, $\alpha=90^\circ$, $\beta=135.0^\circ$, $\gamma=90^\circ$.

Label	Symm Mult.	Wyck label	x	y	z	occ.	moment x μ_B	moment y μ_B	moment z μ_B	net moment μ_B
Fe1	8	e	0.375	0.000	0.000	1	0.000	3.758	-2.609	4.575
Fe2	8	e	0.125	0.250	0.500	1	-3.690	-3.758	-2.609	4.549
Fe3	8	e	0.875	0.125	0.750	1	3.690	-3.758	2.609	4.549
Fe4	8	e	0.125	0.375	0.750	1	0.000	3.758	-2.609	4.575

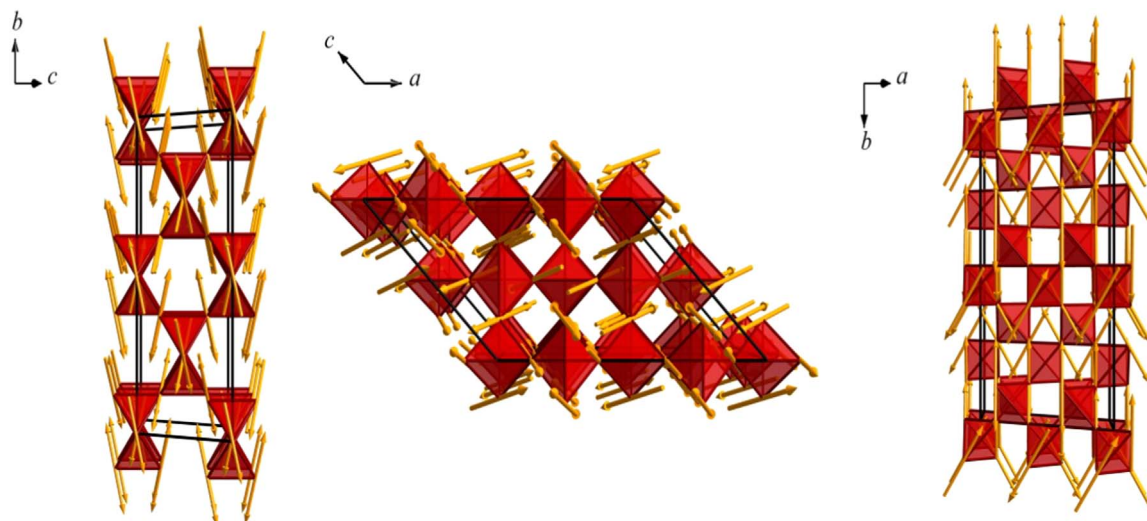


Fig. 1. Polyhedral representation of magnetic structure model in projection normal to [100], normal to [010] and normal to [001].

about the exact symmetry of magnetic ordering has also not been reached to date: P_4 in reference [4] and I_42d , I_422 or even lower symmetry in reference [1]. Evidently, the final symmetry model for the LRO component of the magnetic structure has not been established to date. Based on results of König [4] and Boucher [1], e.g. Figure 4 in [4], we established non-collinear magnetic structure model ($P1$ space group having all 32 Fe^{3+} spins independent and propagation vector $\mathbf{k}=(0\ 0\ 1/2)$), Table 1.

Magnetic moment of $4.575\ \mu_B$ for Fe^{3+} is established where the two projections on unit cell axes, are determined to be $\pm 3.758\ \mu_B$ and $\pm 2.609\ \mu_B$ respectively. The third projection is always zero. The corresponding angle between the magnetic moment and the four fold axis is established to be 55° . Magnetic structure model symmetry was then checked by computer program FINDSYM [7] which revealed higher magnetic symmetry, than described in S.G. $P1$, which can be described within S.G. C_2 (BNS setting; #5.17) [5]. The monoclinic model within S.G. C_2 that possesses four different crystallographic/magnetic sites was obtained, Table 2.

The monoclinic lattice vectors \mathbf{a} , \mathbf{b} and \mathbf{c} are related to the pseudo cubic lattice vectors \mathbf{a}' , \mathbf{b}' and \mathbf{c}' reported by König [4] and Boucher [1] through the transformation:

$$\begin{bmatrix} \mathbf{a} \\ \mathbf{b} \\ \mathbf{c} \end{bmatrix} = \begin{bmatrix} -1 & -1 & 0 \\ 0 & 0 & -1 \\ 1 & 0 & 0 \end{bmatrix} \begin{bmatrix} \mathbf{a}' \\ \mathbf{b}' \\ \mathbf{c}' \end{bmatrix}.$$

The final magnetic structure model is depicted in Fig. 1. Perpendicular to \mathbf{b} -axis in the magnetic unit cell eight layers composed from Fe^{3+} tetrahedra could be recognized in the magnetic structure, Fig. 1 and Table 2. The Fe^{3+} magnetic spins are inverted over $\mathbf{b}/2$.

Here presented magnetic structure description of normal ZnFe_2O_4 in space group C_2 could help in all calculations that take into account coordinates and corresponding magnetic moment projections of Fe atoms. Due to 4 instead of 32 independent Fe atoms and corresponding magnetic moments savings in all calculation are important. Interpretation of different physical properties of normal ZnFe_2O_4 that take into account Fe magnetic moments could contain discussion about the symmetry of the magnetic structure. Here presented magnetic structure model of normal ZnFe_2O_4 is candidate for new addition into the magnetic structure database MAGNDATA (contains more than 420

magnetic structures) that contains portable cif files [2,6].

3. Conclusion

Antiferromagnetic structure ZnFe_2O_4 normal spinel is re-examined. Non-collinear antiferromagnetic model within C_2 space group having four different crystallographic/magnetic sites for 32 Fe^{3+} spins within magnetic unit cell is established. Perpendicular to \mathbf{b} -axis in the magnetic unit cell eight layers composed from Fe^{3+} tetrahedra could be recognized in the magnetic structure. The Fe^{3+} magnetic spins are inverted over $\mathbf{b}/2$.

Acknowledgements

The Serbian Ministry of Education and Science has financially supported this work under contract No. III 45015. We greatly appreciate Emil S. Bozin efforts helpful comments during manuscript preparation.

Appendix A. Supporting information

Supplementary data associated with this article can be found in the online version at doi:10.1016/j.jmmm.2016.11.071.

References

- [1] B. Boucher, R. Buhl, M. Perrin, Phys. Stat. Sol. 40 (1970) 171–182.
- [2] S.V. Gallego, J.M. Perez-Mato, L. Elcoro, E.S. Tasci, R.M. Hanson, K. Momma, I. Mois, M.I. Aroyo, G. Madariaga, J. Appl. Cryst. 49 (2016) 1750–1776.
- [3] J.E. Greedan, J. Mater. Chem. 11 (2001) 37–53.
- [4] U. König, E.F. Bertaut, Y. Gros, M. Mitrikov, G. Chol, Solid State Commun. 8 (1970) 759–764.
- [5] D.B. Litvin, Magnetic Group Tables, ISBN 978-0-9553602-2-0, International Union of Crystallography; (http://www.iucr.org/__data/assets/pdf_file/0010/76915/Intro_to_the_MGT_N12.pdf), 2013.
- [6] J.M. Perez-Mato, S.V. Gallego, E.S. Tasci, L. Elcoro, G. de la Flor, M.I. Aroyo, Annu. Rev. Mater. Res. 45 (2015) 217–248 (http://webdcrista1.ehu.es/magndata/index.php?show_db=1).
- [7] H.T. Stokes, D.M. Hatch, J. Appl. Cryst. 38 (2005) 237–238.
- [8] A. Szytuła, L. Gondek, B. Penc, J. Hernandez-Velasco, Acta Physica Pol. A 106 (2004) 583–591.

ARTICLE OPEN

Superconducting order from disorder in 2H-TaSe_{2-x}S_xLijun Li^{1,2}, Xiaoyu Deng³, Zhen Wang¹, Yu Liu¹, Milinda Abeykoon⁴, Eric Dooryhee⁴, Aleksandra Tomic⁵, Yanan Huang^{1,8}, John B. Warren⁶, Emil S. Bozin¹, Simon J. L. Billinge^{1,5}, Yuping Sun^{2,7}, Yimei Zhu¹, Gabriel Kotliar^{1,3} and Cedomir Petrovic¹

We report on the emergence of robust superconducting order in single crystal alloys of TaSe_{2-x}S_x ($0 \leq x \leq 2$). The critical temperature of the alloy is surprisingly higher than that of the two end compounds TaSe₂ and TaS₂. The evolution of superconducting critical temperature $T_c(x)$ correlates with the full width at half maximum of the Bragg peaks and with the linear term of the high-temperature resistivity. The conductivity of the crystals near the middle of the alloy series is higher or similar than that of either one of the end members 2H-TaSe₂ and/or 2H-TaS₂. It is known that in these materials superconductivity is in close competition with charge density wave order. We interpret our experimental findings in a picture where disorder tilts this balance in favor of superconductivity by destroying the charge density wave order.

npj Quantum Materials (2017)2:11; doi:10.1038/s41535-017-0016-9

INTRODUCTION

The interplay of disorder and interactions is a fruitful area of investigation. In the absence of electron–electron interactions, disorder can turn a metallic system into an Anderson insulator,¹ but can remain metallic when interactions are important. The additional complexity of competing orders such as superconductivity with charge density wave (CDW) or magnetism makes this problem one of the most challenging frontiers in physics.^{2–5} A large body of literature is devoted to this interplay in nearly magnetic materials.⁶ The interplay of disorder and superconductivity in CDW materials have been less explored than its magnetic analog.

Superconductivity and CDW are traditionally viewed as weak-coupling Fermi surface instabilities due to electron–phonon coupling.⁷ Arguments have been made both for their cooperation and competition.^{8, 9} Hexagonal transition metal dichalcogenide 2H-TaSe₂ (*P63/mmc* space group) undergoes a second-order transition to an incommensurate CDW at 122 K followed by a first-order lock-in transition to a commensurate CDW (CCDW) phase at 90 K, eventually becoming superconducting below 0.14 K upon cooling.^{10, 11} 2H-TaS₂ has $T_c = 0.8$ K below an in-plane CCDW at 78 K.^{10, 12} The CDW mechanism in 2H-TaSe₂ involves an electron instability in the bands nested away from the Fermi surface, whereas 2H-TaS₂ features a polar charge and orbital order.^{13, 14} CDW in 2H-TaSe₂ is dominated by hopping between next-nearest neighbors that creates three weakly coupled triangular sublattices.¹⁵ It is of interest to note that the 2H-TaSe₂ is quasi-two-dimensional (2D) metal with pseudogap and with *c*-axis resistivity 25–50 times higher than the in-plane resistivity, i.e., $\rho_c(T) \gg \rho_{ab}(T)$.^{10, 13, 16–18}

Here, we report that in the 2H-TaSe_{2-x}S_x alloy series the CDW is suppressed and the superconductivity is maximized with

crystallographic disorder. The $T_c(x)$ evolution is correlated with the high-temperature linear resistivity $\rho(T) = aT + b$. The constant term b can be attributed to impurity-like carrier scattering of the local CDW fluctuations, and it also appears in dynamical mean field theory (DMFT) of bad metals at high temperature.^{19–22} On very general grounds (Anderson theorem) *s*-wave superconductivity is immune to weak disorder,²³ on the other hand disorder is detrimental to CDW. We argue that the increase in superconducting T_c in the alloy is a direct result of disorder-induced suppression of CDW order. In a weak coupling picture, CDW suppression results in an increase in number of carriers available for superconductivity pairing at Fermi surface, thus enhancing T_c . The physical scenario that in systems where CDW competes with superconductivity disorder promotes the latter is very general and extends to a strongly coupled situation as long as disorder remains weak (see Supplementary Information).

RESULTS

Powder patterns for all samples have been successfully indexed within the *P63/mmc* space group. Representative refinement is shown in Fig. 1a and the unit cell is shown in Fig. 1b. Single crystal X-ray diffraction (XRD) patterns for a subset of single crystals used in this study (Fig. 1c) show (00l) reflections. Reflections shift to higher scattering angles with increasing *S*, indicating decrease of the unit cell volume. Evolution of unit cell parameters with *S*, obtained from fits to the powder patterns (Fig. 1d, e), is consistent with the single crystal data.

The resistivity of all single crystals (Fig. 2a) is metallic. The curves for $0 \leq x \leq 0.25$ show a change of slope in $\rho(T)/\rho(200\text{ K})$ (Fig. 2b). As opposed to commonly observed increase in $\rho(T)$ at T_{CDW} the slope change is attributed to CDW transition that leaves the bands

¹Condensed Matter Physics and Materials Science Department, Brookhaven National Laboratory, Upton, NY 11973, USA; ²Key Laboratory of Materials Physics, Institute of Solid State Physics Chinese Academy of Sciences, Hefei 230031, China; ³Department of Physics & Astronomy, Rutgers, The State University of New Jersey—Piscataway, Piscataway, NJ 08854, USA; ⁴Photon Sciences Directorate, Brookhaven National Laboratory, Upton, NY 11973, USA; ⁵Department of Applied Physics and Applied Mathematics, Columbia University, New York 10027, USA; ⁶Instrumentation Division, Brookhaven National Laboratory, Upton, NY 11973, USA and ⁷High Magnetic Field Laboratory, Chinese Academy of Sciences, Hefei 230031, China

Correspondence: Lijun Li (lijun@issp.ac.cn) or Cedomir Petrovic (petrovic@bnl.gov)

⁸Present address: Key Laboratory of Materials Physics, Institute of Solid State Physics, Chinese Academy of Sciences, Hefei 230031, China

Received: 15 August 2016 Revised: 3 January 2017 Accepted: 24 January 2017

Published online: 24 February 2017

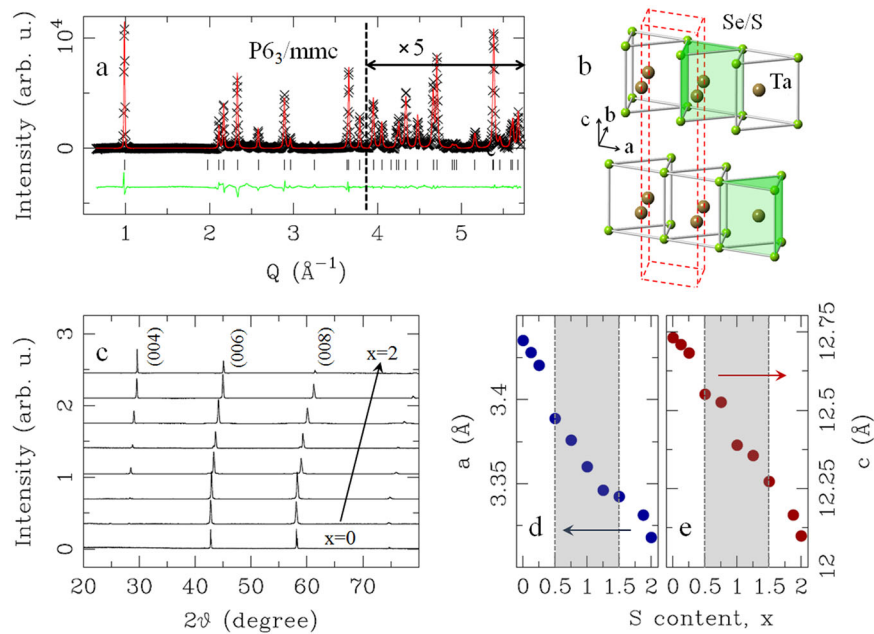


Fig. 1 Crystal structure aspects of 2H-TaSe_{2-x}S_x ($0 \leq x \leq 2$) **a** Powder XRD pattern for 2H-TaSe₂ at 300 K, shown as scattering intensity vs. momentum transfer Q , indexed within $P6_3/mmc$ space group. Crosses are data, solid red line is the model, green solid line is the difference (offset for clarity), and vertical ticks mark are the reflections. **b** Structural motif of the $P6_3/mmc$ model. Red dashed box depicts the unit cell. **c** Single crystal XRD patterns at the room temperature. Patterns are offset for clarity. **d, e** Room temperature evolution of a and c lattice parameters, respectively, as obtained from powder diffraction data. Shaded is the range where CDW cannot be detected in resistivity

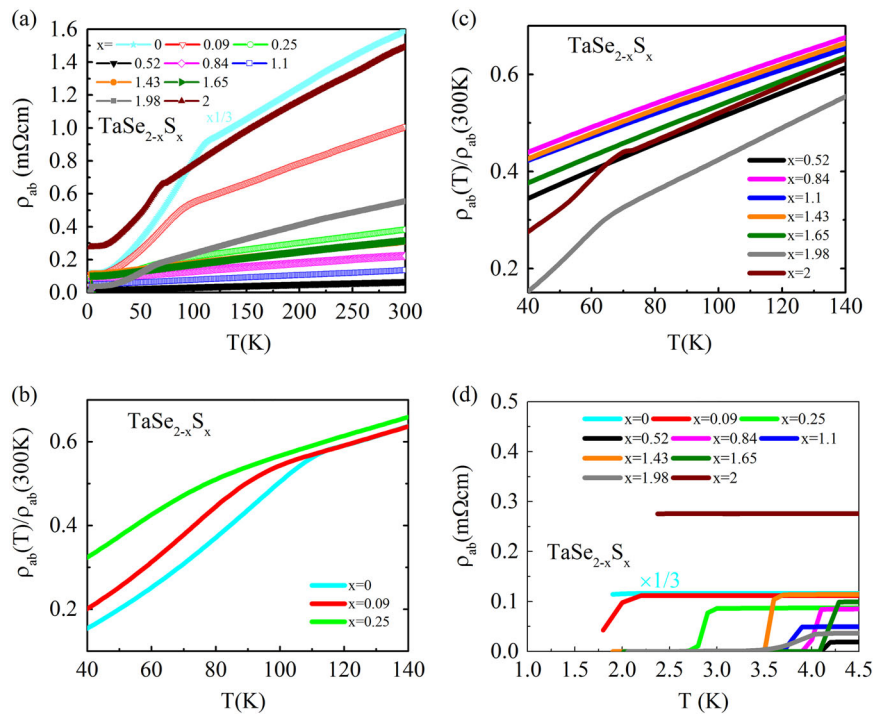


Fig. 2 Electrical resistivity of 2H-TaSe_{2-x}S_x ($0 \leq x \leq 2$) **a** Temperature dependence of the resistivity for single crystals in the absence of magnetic field. **b, c** Temperature dependence of $\rho(T)/\rho(300\text{K})$ near CDW transitions. **d** $\rho(T)$ curves near superconducting transitions, indicating large enhancement of superconductivity

associated with the undistorted sublattice ungapped.^{14–17} The hump shifts to lower temperature with S doping and vanishes for $x \geq 0.52$, but appears again for $x = 1.98$ at about 70 K, somewhat below the $T_{\text{CDW}} = 75$ K for pure 2H-TaS₂ (Fig. 2c). The

resistivity decreases to zero at lower temperatures, implying superconductivity (Fig. 2d). The magnetic susceptibility transitions and the large values of $-4\pi\chi$ at 1.9 K imply bulk superconductivity (Fig. 3a).

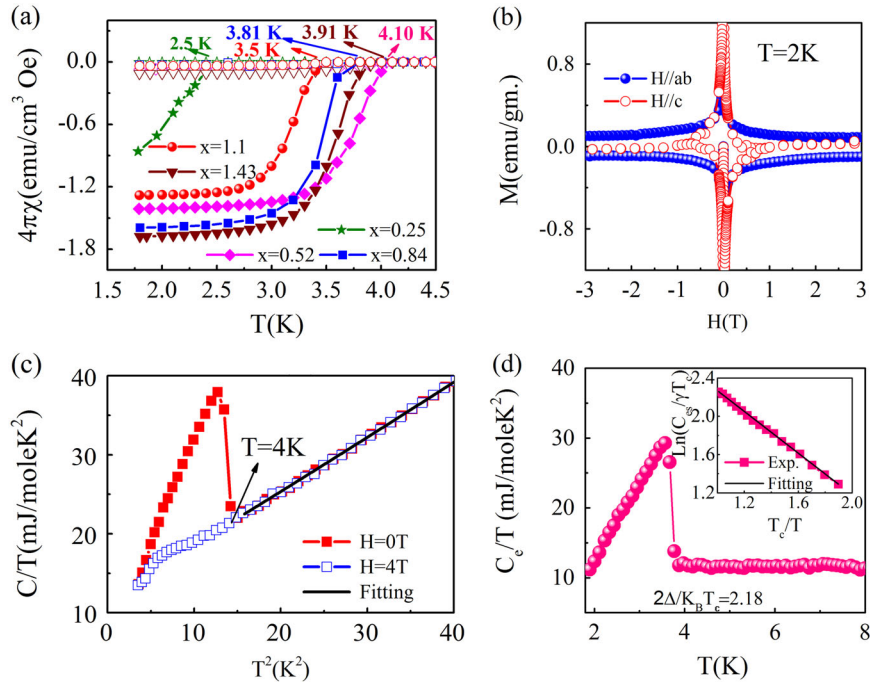


Fig. 3 Magnetic and thermodynamic properties of 2H-TaSe_{2-x}S_x ($0 \leq x \leq 2$) **a** Magnetic susceptibility after zero-field-cooling (*filled*) and field-cooling (FC, *open symbols*). The smaller magnetization value for FC is likely due to the complex magnetic flux pinning effects. **b** Magnetization hysteresis loops $M(H)$ of TaSe_{1.48}S_{0.52} for $H \parallel ab$ (*solid*) and $H \parallel c$ (*open symbols*). **c** Low-temperature specific heat of TaSe_{1.48}S_{0.52} measured at $H = 0$ (*solid*) and in 4 T (*open symbols*). **d** The electronic-specific heat in the superconducting state C_e for 2H-TaSe_{1.48}S_{0.52} is obtained by subtracting the lattice contribution from the total specific heat: $C_e = C - C_{ph} = \gamma T$, where $C_{ph}(T) = \beta T^3 + \delta T^5$ and $\theta_D = [(n-1.944 \times 10^6)/\beta]^{1/3}$, where n is the number of elements per formula unit. *Inset*: below the superconducting transition temperature, electronic-specific heat temperature dependence follows an exponential decay, as $C_e \sim \exp[-\Delta(T)/k_B T]$. The *solid line* shows C_e/T calculated by assuming an isotropic s -wave BCS gap with $2\Delta = k_B T_c = 2.17$

Table 1. Superconducting parameters of 2H-TaSe₂, 2H-TaSe_{1.48}S_{0.52}, and 2H-TaS₂

Parameters	2H-TaSe ₂	2H-TaSe _{1.48} S _{0.52}	2H-TaS ₂
T_c (K)	0.14	4.20(1)	0.8
γ (mJ/mol K ²)	4.5	12.0(3)	7.5
β (mJ/mol K ⁴)	0.72	0.65(2)	0.44
δ (mJ/mol K ⁶)	–	$6(1) \cdot 10^{-4}$	–
λ_{e-ph}	0.397	0.73(1)	0.486
θ_D (K)	202	207(1)	236
$2\Delta/k_B T_c$	–	2.18(2)	–
Reported by	Ref 12	This work	Ref 12

Specifically, the anisotropic $M(H)$ curves (Fig. 3b) confirm type-2 superconductivity for TaSe_{1.48}S_{0.52} and imply anisotropic critical current density. The lambda anomaly in the specific heat jump around $T = 4$ K (Fig. 3c) is suppressed significantly in 4 T. A rough estimate of the average electron–phonon coupling $\lambda_{e-ph} \sim 0.73$ can be obtained from the McMillan equation, assuming the empirical value of the Coulomb pseudopotential $\mu^* = 0.15$ and taking the Debye frequency as the relevant phonon energy:²⁴

$$\lambda = \frac{\mu^* \ln\left(\frac{1.45T_c}{\theta_D}\right) - 1.04}{1.04 + \ln\left(\frac{1.45T_c}{\theta_D}\right)(1 - 0.62\mu^*)}. \quad (1)$$

When compared with the parent 2H-TaSe₂ with electronic-specific heat coefficient $\gamma = 4.5$ mJ mol⁻¹ K⁻², γ is larger for 50% S-doped sample (Fig. 3d, Table 1). The electron–phonon coupling $\lambda_{e-ph} = 0.73$ is somewhat larger than for 2H-TaSe₂ and 2H-TaS₂

(Table 1). The ratio of the gap at the critical temperature $2\Delta/k_B T_c = 2.17$ can be obtained by linear fitting $\ln(C_e/\gamma T_c) - T_c/T$ data (Fig. 3d inset).

In a multiband electronic system with local CDW fluctuations^{15–17, 20} above T_{CDW} , such as 2H-Ta(S₂Se)₂, the carrier scattering mechanism arises from collective excitations below the CDW and from local CDW fluctuations above the CDW.¹⁹ Above T_{CDW} $\rho(T) \sim aT + b$, immediately below T_{CDW} $\rho(T) \sim dT^2$ and at temperatures below about 15–20 K $\rho(T) \sim cT^3$. The T^5 is due to normal electron–phonon scattering, whereas the T^2 arises due to scattering of electrons by collective excitations of CDW; the rapid drop just below CDW is due to CDW phase ordering. The linear terms a, b above T_{CDW} arise due to electron–phonon scattering and phase disorder impurity-like scattering due to local CDW fluctuations. The fits of resistivity for the entire single crystal alloy series of 2H-TaSe_{2-x}S_x ($0 \leq x \leq 2$) are satisfactory (Fig. 4a–c, Table 2). In all samples resistivity is linear at high temperatures. Just above the superconducting T_c interband scattering is negligible and individual s -band and d -band normal electron–phonon scattering dominates.¹⁹ The constant term b for such crystals is much smaller than for CDW samples, because disorder suppresses the CDW therefore increases the number of carriers and thus the conductivity.

We present the evolution of superconducting T_c in 2H-TaSe₂ with S substitution x (normalized to T_c value for $x = 0$) in Fig. 4d. The T_c shows 30-fold increase and anticorrelation with the evolution of the high-temperature local charge fluctuation parameter $b(x)$ (also normalized to b value for $x = 0$) (Fig. 4d). Note that weak decrease of T_c near $x = 1$ coincides with weak increase in normalized $b(x)$ near the same S content. It appears that the considerable increase and evolution of $T_c(x)$ is related to an increase in available carrier concentration or mobility. These changes are matched (Fig. 4d) with the nearly identical evolution

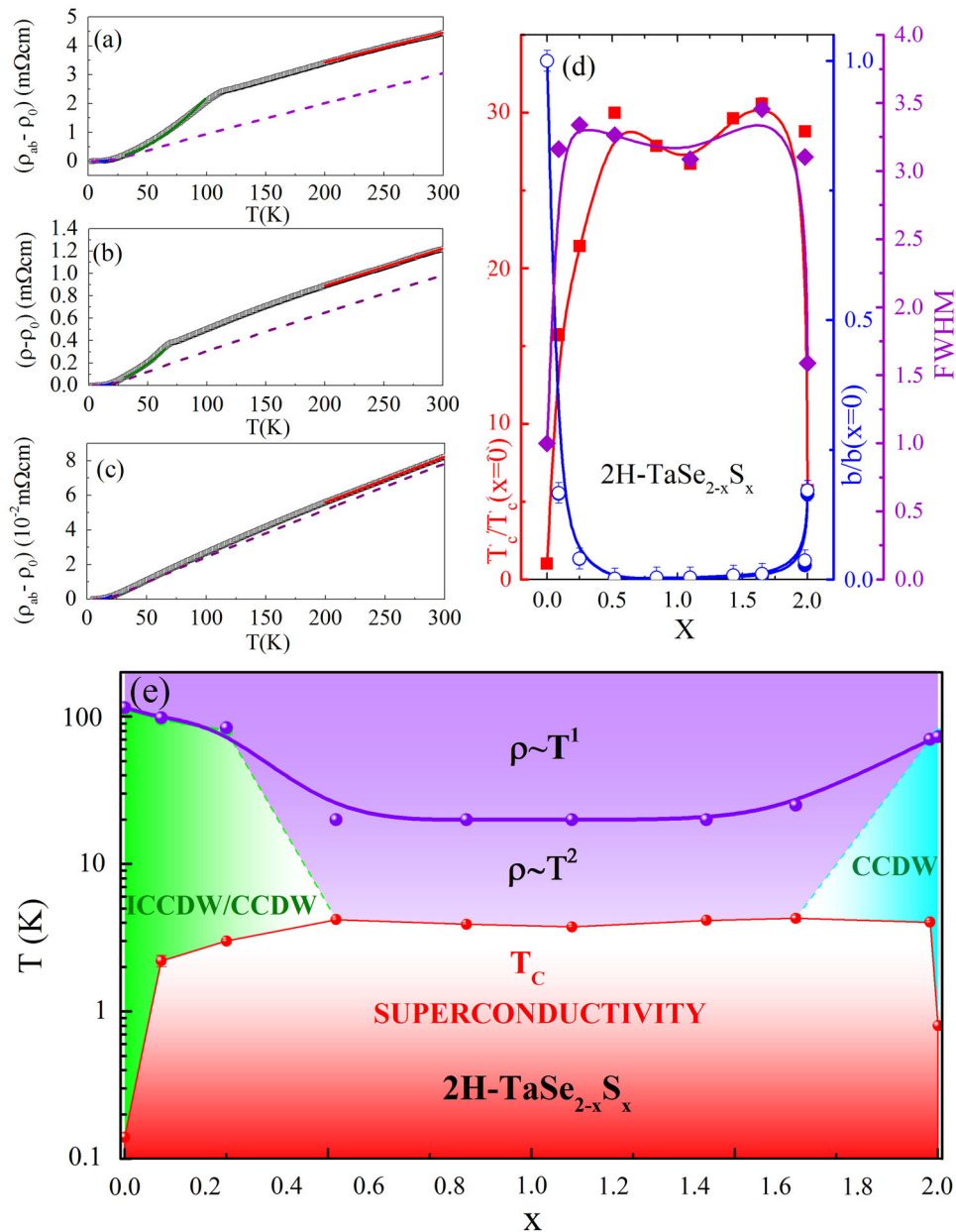


Fig. 4 Electronic phase diagram of 2H-TaSe_{2-x}S_x ($0 \leq x \leq 2$) **a–c** Electronic scattering mechanism for **a** 2H-TaSe₂, **b** 2H-TaSe₂, and **c** 2H-TaSe_{0.9}S_{1.1}. Low-temperature phonon scattering, scattering of collective excitations of CDW and high-temperature scattering of the local CDW fluctuations are shown by blue, green, and red solid lines, respectively. Dashed violet line shows the phonon resistivity approximated by the Bloch–Grüneisen formula (see text and Supplementary Information). **d** Note that the weak double dome evolution of superconducting $T_c(x)$ coincides with similar evolution of crystallographic disorder with sulfur content as revealed by FWHM of [006] Bragg peak in Fig. 1c. The intensity was normalized to 1 for each value of x . Moreover, $T_c(x)$ is in close correlation with disorder-induced changes in the high-temperature local charge fluctuations as seen by the changes in parameter b ; all normalized to values of 2H-TaSe₂ ($x=0$). The parameter b is shown from fits without (open) and with phonon subtraction from Bloch–Grüneisen formula (full symbols) (Supplementary Information). The error bars are about 0.01 for x , up to 0.04 for normalized T_c , and up to 0.01 for the normalized parameter b and FWHM (also see Table 1). **e** Phase diagram indicating the evolution of CDW (incommensurate ICCDW and commensurate CCDW) and superconductivity states with the change of x

of the crystallographic disorder as shown by the width of diffraction peaks taken on single crystals full width at half maximum (FWHM) normalized to width of $x=0$ crystal. The linear resistivity $aT + b$ in the high- T_c crystals without CDW is rather close to the Bloch–Grüneisen phonon resistivity (Fig. 4c, Supplementary Information), suggesting that the strong suppression of parameter $b(x)$ in 2H-TaSe_{2-x}S_x can be attributed to suppression of local CDW fluctuations for high- T_c crystals.

Figure 4e presents the electronic phase diagram. With the increase in x , the CDW transition of 2H-TaSe₂ is suppressed, whereas the superconducting transition temperature T_c increases up to 4.2 K for $x=0.52$ where CDW disappears. Further sulfur increase shows weak but well resolved minimum in $T_c(x)$ for $x=1.10$ up to the second maximal value of 4.28 K for $x=1.65$ sulfur content in 2H-TaSe_{1-x}S_x. Signature of a CDW state, most probably CDW of the pure 2H-TaSe₂, appears in $\rho(T)$ for higher S content up

Table 2. Superconducting T_c (defined as 90% of normal state resistivity; Fig. 2d), charge density wave T_{CDW} transition temperatures (defined as peak in resistivity; Fig. 2b, c), and fitting parameters of the CDW phase fluctuations scattering model for resistivity (see text)

x	T_c (K)	T_{CDW} (K)	c	c_{range} (K)	d	d_{range} (K)	a	b	L_{range} (K)	ρ_0
0	0.14	112(1)	2.12(7)	3–20	22.1(2)	30–100	102.8(1)	1.37(1)	200–300	3.4(5)
0.09(1)	2.2(1)	96(3)	0.52(2)	3–20	5.43(5)	34–86	22.4(3)	0.226(7)	200–300	1.1(2)
0.25(1)	3.0(5)	80(3)	0.27(2)	5–20	2.17(3)	34–65	8.08(1)	0.054(1)	200–300	0.9(1)
0.52(1)	4.2(1)	–	0.04(1)	5–20	–	–	1.6(1)	0.0004(1)	200–300	0.19(3)
0.84(1)	3.9(1)	–	0.10(1)	5–20	–	–	4.64(1)	0.0015(1)	200–300	0.8(1)
1.10(1)	3.7(2)	–	0.030(3)	5–20	–	–	2.64(1)	0.0031(1)	200–300	0.48(7)
1.43(1)	4.1(2)	–	0.20(1)	5–20	–	–	6.32(1)	0.0066(1)	200–300	1.1(1)
1.65(1)	4.3(1)	–	0.14(1)	5–20	–	–	6.82(1)	0.0099(3)	200–300	1.0(1)
1.98(1)	4.0 (1)	70(3)	0.20(1)	5–20	3.19(4)	30–60	16.8(1)	0.037(1)	200–300	0.36(5)
2.00(1)	0.8	75(1)	0.79(3)	3–20	7.78(3)	30–64	34.3(2)	0.225(1)	200–300	2.7(4)

Note: Considerable change in local CDW fluctuation scattering for crystals without CDW strives to increase conduction and is concomitant with the greatly enhanced superconducting T_c values. The units for c , d and a are in (10^{-8} m Ω cm/K⁵), (10^{-5} m Ω cm/K²), (10^{-4} m Ω cm/K), respectively. The units for b and ρ_0 are in (m Ω cm) and (10^{-1} m Ω cm). For crystals near the middle of the alloy series where CDW cannot be detected in resistivity, the highest crystallographic disorder and consequently a substantial increase of ρ_0 (i.e., total $\rho(T)$ when $T \rightarrow 0$) are expected. However, the impurity-like scattering due to local CDW fluctuations (phase disorder scattering) term b becomes small for that range of x , making the overall resistivity ρ_0 smaller or similar to $x=0$ and $x=2$ crystals (Table 2, Columns b and ρ_0). L_{range} denotes the temperature range of linear $aT+b$ fit

to $x=2$. The two T_c maxima in the double-dome appear at the critical doping, where CDW orders vanish similar to 1T-Se₂ and 2H-NbSe₂.^{25, 26}

DISCUSSION

It should be noted that electron-irradiated 2H-TaSe₂ shows enhancement of superconducting T_c up to about 2.5 K.²⁷ Irradiation introduces defects, i.e., changes in stoichiometry similar to chemical substitutions. Cu-intercalated 2H-TaS₂ shows enhancement of T_c up to 4.7 K.²⁸ Copper behaves as n -type dopant and therefore its intercalation brings both disorder and charge transfer.²⁹ Similar doping and disorder interplay is expected with Na intercalation in 2H-TaS₂, where T_c was raised up to 4.4 K.³⁰ In contrast, isoelectronic substitution in 2H-TaSe_{2-x}S_x single crystal alloy series allows for clear separation of disorder from doping-induced changes. The basic electronic structure of 2H-TaSe₂, 2H-TaSeS, and 2H-TaS₂ is quite similar as shown in the Local Density Approximation (LDA) calculations (Supplementary Material), leaving disorder as the origin of the increase in T_c . The intense variation of physical properties at low energy is a prime example of emergent phenomena.

Below the CDW transition temperature, a gap opens in 2H-TaSe₂ on two distorted sublattices in contrast to undistorted sublattice.¹⁵ This makes for a small density of states at the Fermi level and consequently low superconducting T_c .¹⁰ Sulfur substitution could introduce different Ta–S and Ta–Se bond lengths, disorder and puckering of metal plane. This would suppress CDW and increase density of electronic states, electron–phonon coupling, and superconducting T_c .³¹ The lattice defect disorder increases superconducting T_c in CDW superconductor ZrTe₃ by factor of only 2–3.³² Furthermore, $T_c(x)$ (Fig. 4e) cannot be explained by the f -wave model of CDW that predicts linear $T_c(x)$ in 2H-TaSe_{2-x}S_x ($0 \leq x \leq 2$), whereas increased conductivity in high- T_c crystals argues against the change of the amplitude of ionic vibrations as in disordered films or amorphous lattices.^{33, 34}

The normal state properties of this material are not well understood theoretically. Our experimental results indicate that the low-temperature specific heat coefficient of the alloy is very close to that computed in LDA (please see Supplementary Material), suggesting that the correlations due to Coulomb

interactions are weak, while the electron–phonon coupling couples strongly to a few states not too close to the Fermi surface, which is consistent with the results of ref. 35. Alternatively, strong correlations are invoked in the exciton liquid model of 2H-TaSe₂. This model of CDW in 2H-TaSe₂ provides an explanation of some anomalous normal state properties such as linear resistivity above CDW transition, pseudogap, optical conductivity $\sigma(\omega, T)$, and incoherent metal features.^{20, 36} Within that model and in contrast to ZrTe₃,³² emergence of CDW reduces incoherent scattering, i.e., CDW-related bump in $\rho(T)$ is a coherence restoring transition that enables higher conductivity below T_{CDW} . The reduction in interband mixing dispersion that mixes the small number of d_{z^2} electrons and p_z holes should remove the CDW, maximizing strong scattering of preformed incoherent excitons and enabling linear resistivity to progress to lower temperatures.²⁰ The observation of wide temperature range of linear resistivity in high- T_c crystals (Fig. 2a) suggests the rapid reduction in conduction and valence band mixing within that model. This calls for photoemission studies of newly synthesized alloy to test these theoretical models and to clarify the measure of the correlation strength.

Pressure should bring phonon hardening following the contraction of lattice parameters from 2H-TaSe₂ to 2H-TaS₂ (Fig. 1).^{23, 37, 38} Assuming similar bulk modulus to WSe₂ (72 GPa),³⁹ the estimated chemical pressure differences of 2H-TaSeS ($T_c = 3.7$ K) when compared with 2H-TaSe₂ ($T_c = 0.14$ K) and 2H-TaS₂ ($T_c = 0.8$ K) are 6 GPa (positive pressure/contraction) and 2.8 GPa (negative pressure/expansion). Positive pressure increases considerably superconducting T_c in both 2H-TaS₂ and 2H-TaSe₂; 6 GPa brings T_c in 2H-TaSe₂ up to about 3 K.⁴⁰ CDW is robust, surviving up to 20 GPa (2H-TaSe₂) and up to 16 GPa (2H-TaS₂). Clearly, chemical pressure may influence the rise of superconducting T_c in S-doped 2H-TaSe₂, but it cannot explain the absence of CDW in high- T_c samples in the phase diagram (Fig. 4e), the increase of superconducting T_c with lattice expansion in 2H-TaS₂ or the $T_c(x)$ evolution in 2H-TaSe_{2-x}S_x ($0 \leq x \leq 2$) (Fig. 4e). The reduction in conduction and valence band mixing within DMFT framework facilitates not only the reduction of incoherence and stabilization of pseudogap characterized by linear $\rho(T)$, but also an increase in density of states at the Fermi level, thus highlighting

the effect of disorder, incoherent states, and the importance of local dynamical correlations.²⁰

In summary, we show that disorder-induced superconducting states arise by isoelectronic substitution in 2H-TaSe₂. In contrast to all known CDW superconductors that have hitherto featured only a single dome of T_c with variation of any external parameter, the electronic phase diagram we present features a weak double dome in $T_c(x)$. The increase in superconducting T_c and changes in $T_c(x)$ are directly correlated with crystallographic disorder and disorder-induced scattering of the local CDW fluctuations. Our experimental findings can be understood on more general grounds without relying on a specific microscopic theory. For a given band structure, weak disorder does not affect the superconductivity of an *s*-wave superconductor (Anderson's theorem, Supplementary Information),^{1, 23} but it is detrimental to the competing CDW order. The combination of these effects results in an enhanced superconducting critical temperature and a reduction of the CDW.

METHODS

Single crystals of 2H-TaSe_{2-x}S_x ($0 \leq x \leq 2$) were grown via iodine vapor transport method. The source and growth zone were set at 900 °C for 3 days and then kept at 900 and 800 °C, respectively, for 10 days. Black plate-like single crystals with a typical size of $3 \cdot 3 \cdot 0.2$ mm³ were obtained. The element analysis was performed using an energy-dispersive X-ray spectroscopy in a JEOL LSM-6500 scanning electron microscope. Electrical resistivity, specific heat, and magnetization measurements were performed in a Quantum Design PPMS-9 and MPMS XL-5. XRD patterns on single crystals were taken using a Rigaku Miniflex. Room temperature powder XRD measurements were carried out at the X-ray powder diffraction (28-ID-C) beam line at National Synchrotron Light Source II. The raw room temperature powder X-ray 2D data were integrated and converted to intensity vs. scattering angle using the software Fit2D.⁴¹ The average structure was assessed from raw diffraction data using the General Structure Analysis System operated under EXPGUI utilizing *P63/mmc* model from the literature.^{42–44}

ACKNOWLEDGEMENTS

Work at Brookhaven is supported by the U.S. DOE under Contract No. DE-SC00112704. Work at Institute of Solid State Physics of CAS is supported by the National Natural Science Foundation of China, Grant No. 11404342. Use of the National Synchrotron Light Source II, Brookhaven National Laboratory, was supported by the U.S. Department of Energy, Office of Science, Office of Basic Energy Sciences, under Contract No. DE-SC0012704. X.D. is supported by AFOSR MURI program. Y.L. and G.K. are supported by U.S. Department of energy, Office of Science, Basic Energy Sciences as a part of the Computational Materials Science Program.

AUTHOR CONTRIBUTIONS

C.P. designed research. L.L. and Y.L. made crystals and carried out transport, magnetization, and thermal measurements. L.L. and Y.S. contributed single crystal X-ray diffraction data. Y.L., Y.H., and J.W. performed SEM measurements. Z.W. and Y.Z. performed TEM measurements. M.A., E.D., A.T., E.S.B., and S.J.L.B. carried out and analyzed crystal powder X-ray diffraction data. C.P. supervised the project, analyzed the transport data with Y.L. and single crystal data with L. L. and wrote the paper with L.L. and with contributions from G.K. and Y.S. X.D. performed the LDA calculations and contributed to the theoretical interpretation of results. The manuscript reflects contribution and ideas of all authors.

COMPETING INTERESTS

The authors declare no competing interest.

REFERENCES

- Anderson, P. Absence of diffusion in certain random lattices. *Phys. Rev.* **109**, 1492–1505 (1958).
- Belitz, D. & Kirkpatrick, T. R. The Anderson-Mott transition. *Rev. Mod. Phys.* **66**, 261–380 (1994).
- Zeljko, I. et al. Imaging the impact of single oxygen atoms on superconducting Bi_{2+y}Sr_{2-y}CaCu₂O_{8+x}. *Science* **337**, 320–323 (2012).

- Seo, S. et al. Disorder in quantum critical superconductors. *Nat. Phys.* **10**, 120–125 (2014).
- Mizykami, Y. et al. Disorder-induced topological change of the superconducting gap structure in iron pnictides. *Nat. Commun.* **5**, 5657 (2014).
- Alloul, H. et al. Defects in correlated metals and superconductors. *Rev. Mod. Phys.* **81**, 45–108 (2009).
- Grüner, G. The dynamics of charge-density waves. *Rev. Mod. Phys.* **60**, 1129–1181 (1988).
- Kiss, T. et al. Charge-order-maximized momentum dependent superconductivity. *Nat. Phys.* **3**, 720–725 (2007).
- Borisenko, S. V. et al. Two energy gaps and Fermi-surface “arcs” in NbSe₂. *Phys. Rev. Lett.* **102**, 166402 (2009).
- Harper, J. M., Geballe, T. E. & Disalvo, F. J. Thermal properties of layered transition-metal dichalcogenides at charge-density-wave transitions. *Phys. Rev. B* **15**, 2943–2951 (1977).
- Moncton, D. E., Axe, J. D. & DiSalvo, F. J. Study of superlattice formation in 2H-NbSe₂ and 2H-TaSe₂ by neutron scattering. *Phys. Rev. Lett.* **34**, 734–737 (1975).
- Nishihara, H., Scholz, G. A., Naito, M., Frindt, R. F. & Tanaka, S. NMR of ¹⁸¹Ta in 2H-TaS₂ and 2H-TaSe₂, observation of locally commensurate CDW. *J. Magn. Magn. Mater.* **31**, 717–718 (1983).
- Laverock, J. et al. k-resolved susceptibility function of 2H-TaSe₂ from angle-resolved photoemission. *Phys. Rev. B* **88**, 035108 (2013).
- Van Wezel, J. Polar charge and orbital order in 2H-TaS₂. *Phys. Rev. B* **85**, 035131 (2012).
- Barnett, R. L., Polkovnikov, A., Demler, E., Yin, Wei-Guo & Ku, Wei Coexistence of gapless excitations and commensurate charge-density wave in the 2H transition metal dichalcogenides. *Phys. Rev. Lett.* **96**, 026406 (2006).
- Vescoli, V., Degiorgi, L., Berger, H. & Forró, L. Dynamics of correlated two-dimensional materials: the 2H-TaSe₂ case. *Phys. Rev. Lett.* **81**, 453–456 (1998).
- Ruzicka, B., Degiorgi, L., Berger, H., Gaál, R. & Forró, L. Charge dynamics of 2H-TaSe₂ along the less conducting *c*-axis. *Phys. Rev. Lett.* **86**, 4136–4139 (2001).
- Yokota, K. I., Kurata, G., Matsui, T. & Fukuyama, H. Superconductivity in the quasi-two-dimensional conductor 2H-TaSe₂. *Phys. B* **284–288**, 551–552 (2000).
- Naito, M. & Tanaka, S. Electrical transport properties in 2H-NbS₂, -NbSe₂, -TaS₂ and -TaSe₂. *J. Phys. Soc. Jpn.* **51**, 219–227 (1982).
- Taraphder, A., Koley, S., Vidhyadhiraja, N. S. & Laad, M. S. Preformed excitonic liquid route to a charge density wave in 2H-TaSe₂. *Phys. Rev. Lett.* **106**, 236405 (2011).
- Xu, W., Haule, K. & Kotliar, G. Hidden Fermi liquid, scattering rate saturation and Nernst effect: a dynamical mean field theory perspective. *Phys. Rev. Lett.* **111**, 036401 (2013).
- Deng, X., Mravlje, J., Zitko, R., Ferrero, M., Kotliar, G. & Georges, A. How bad metals turn good: spectroscopic signatures of resilient quasiparticles. *Phys. Rev. Lett.* **110**, 086401 (2013).
- Anderson, P. W. Theory of dirty superconductors. *J. Phys. Chem. Solids* **11**, 26–30 (1959).
- McMillan, W. L. Transition temperature of strong-coupled superconductors. *Phys. Rev.* **167**, 331–344 (1968).
- Kusmartseva, A. F., Sipo, B., Berger, H., Forró, L. & Tutiš, E. Pressure induced superconductivity in pristine 1T-TaSe₂. *Phys. Rev. Lett.* **103**, 236401 (2009).
- Feng, Y. et al. Order parameter fluctuations at a buried quantum critical point. *Proc. Natl. Acad. Sci.* **109**, 7224–7229 (2012).
- Mutka, H. Superconductivity in irradiated charge-density-wave compounds 2H-NbSe₂, 2H-TaS₂, and 2H-TaSe₂. *Phys. Rev. B* **28**, 2855–2858 (1983).
- Wagner, K. E. et al. Tuning the charge density wave and superconductivity in Cu_xTaS₂. *Phys. Rev. B* **78**, 104520 (2008).
- Zhao, J. F. et al. Evolution of the electronic structure of 1T-Cu_xTiSe₂. *Phys. Rev. B* **99**, 146401 (2007).
- Fang, L. et al. Fabrication and superconductivity of Na_xTaS₂ crystals. *Phys. Rev. B* **72**, 014534 (2005).
- Liu, Y. et al. Nature of charge-density-wave and superconductivity in 1T-TaSe_{2-x}Te_x. *Phys. Rev. B* **94**, 041531 (2016).
- Zhu, X. et al. Disorder-induced bulk superconductivity in ZrTe₃ single crystals via growth control. *Phys. Rev. B* **87**, 024508 (2013).
- Castro Neto, A. H. Charge density wave, superconductivity, and anomalous metallic behavior in 2D transition metal dichalcogenides. *Phys. Rev. Lett.* **86**, 4382–4385 (2001).
- Garland, J. W., Bennemann, K. H. & Mueller, F. M. Effect of lattice disorder on the superconducting transition temperature. *Phys. Rev. Lett.* **21**, 1315–1319 (1968).
- Varma, C. M. & Simons, A. L. Strong coupling theory of charge-density-wave transitions. *Phys. Rev. Lett.* **51**, 138–141 (1983).
- Borisenko, S. V. et al. Pseudogap and charge density waves in two dimensions. *Phys. Rev. B* **100**, 196402 (2008).
- Loa, I. & Syassen, K. Calculated elastic and electronic properties of MgB₂ at high pressures. *Solid State Comm.* **118**, 279–282 (2001).

38. Smith, T. F., Shelton, R. N. & Schwall, R. E. Superconductivity of $\text{TaSe}_{2-x}\text{Se}_x$ layer compounds at high pressure. *J. Phys. F: Metal. Phys.* **5**, 1713–1725 (1975).
39. Selvi, E., Aksoy, R., Knudson, R. & Ma, Y. High-pressure X-ray diffraction study of tungsten diselenide. *J. Phys. Chem. Solids* **69**, 2311–2314 (2008).
40. Freitas, D. C. *et al.* Strong enhancement of superconductivity at high pressures within the charge-density-wave states of 2H-TaS_2 and 2H-TaSe_2 . *Phys. Rev. B* **93**, 184512 (2016).
41. Hammersley, A. P., Svensson, S. O., Hanfland, M., Fitch, A. N. & Hausermann, A. Two-dimensional detector software: from real detector to idealised image or two-theta scan. *High Pressure Res.* **14**, 235–248 (1996).
42. Larson, A., C. and Von Dreele, R., B. Report No. LAUR-86-748, Los Alamos National Laboratory, Los Alamos, NM 87545 (2004).
43. Toby, B. H. EXPGUI, a graphical user interface for GSAS. *J. Appl. Crystallogr.* **34**, 210–213 (2001).
44. Brixner, L. H. Preparation and properties of the single crystalline AB_2 -type selenides and tellurides of niobium, tantalum, molybdenum and tungsten. *J. Inorg. Nucl. Chem.* **24**, 257–263 (1962).



This work is licensed under a Creative Commons Attribution 4.0 International License. The images or other third party material in this article are included in the article's Creative Commons license, unless indicated otherwise in the credit line; if the material is not included under the Creative Commons license, users will need to obtain permission from the license holder to reproduce the material. To view a copy of this license, visit <http://creativecommons.org/licenses/by/4.0/>

© The Author(s) 2017

Supplementary Information accompanies the paper on the *npj Quantum Materials* website (doi:[10.1038/s41535-017-0016-9](https://doi.org/10.1038/s41535-017-0016-9)).

Bulletin of the American Physical Society

2006 APS March Meeting

Monday–Friday, March 13–17, 2006; Baltimore, MD

Session A15: Metals: 1D, 2D, 3D

8:00 AM–11:00 AM, Monday, March 13, 2006
Baltimore Convention Center Room: 311

Sponsoring Unit: DCMP

Chair: Duane Johnson, University of Illinois, Urbana-Champaign

Abstract ID: BAPS.2006.MAR.A15.7

Abstract: A15.00007 : Scanning tunneling microscopy study of the charge density wave in rare-earth tritellurides*

9:12 AM–9:24 AM

[Preview Abstract](#)

← Abstract →

Authors:

Aleksandra Tomic
Christos Malliakas
Hyun-Jeong Kim
Mercouri Kanatzidis
Simon Billinge
Stuart Tessmer
(Michigan State University)

A number of correlated electron oxides exhibit surprisingly intricate ordered density modulations which underlie their novel properties. These modulations arise from incommensurate charge density waves (IC-CDWs). We have applied scanning tunneling microscopy (STM) to study the nature of IC-CDWs in the rare-earth tritellurides -- simple, cleavable, layered materials. In particular, for CeTe₃ we have observed both the atomic lattice of surface Te atoms and the CDW modulations oriented at 45 degrees with respect to the Te net. Two-dimensional Fourier transforms of the STM images were obtained to search for discommensurations. These are essentially domain walls whose presence has been strongly suggested by atomic pair distribution function studies. We observe satellite peaks in addition to the principal CDW peaks. These represent strong evidence for the presence of discommensurations with a characteristic length scale of about 38 angstroms.

*Research supported by the National Science Foundation grant No DMR03-05461.

To cite this abstract, use the following reference: <http://meetings.aps.org/link/BAPS.2006.MAR.A15.7>

This site uses cookies. To find out more, read our [Privacy Policy](#).

I Agree

2
2003



This is to certify that the
dissertation entitled

Scanning tunneling microscopy of complex electronic
materials

presented by

Aleksandra T. Tomic

has been accepted towards fulfillment
of the requirements for the

Ph.D. degree in Physics and Astronomy

Stuart Jessup
Major Professor's Signature

3/4/08
Date

PLACE IN RETURN BOX to remove this checkout from your record.
TO AVOID FINES return on or before date due.
MAY BE RECALLED with earlier due date if requested.

DATE DUE	DATE DUE	DATE DUE

SCANNING TUNNELING MICROSCOPY OF COMPLEX ELECTRONIC
MATERIALS

By

Aleksandra T. Tomic

A DISSERTATION

Submitted to
Michigan State University
in partial fulfillment of the requirements
for the Degree of

DOCTOR OF PHILOSOPHY

Department of Physics and Astronomy

2008

ABSTRACT

SCANNING TUNNELING MICROSCOPY OF COMPLEX ELECTRONIC MATERIALS

By

Aleksandra T. Tomic

I present results of experiments aimed at investigating two complex electronic systems, CeTe_3 and $\beta\text{-K}_2\text{Bi}_8\text{Se}_{13}$, utilizing scanning tunneling microscopy (STM) and scanning tunneling spectroscopy (STS) methods. In these systems, the electronic properties of interest are a charge density wave (CDW) state and thermoelectricity, respectively.

STM and STS measurements of CeTe_3 at room temperature and 77 K were performed, resulting in the first atomically resolved images of the material. Clear patterns showing the superposition of the atomic lattice and the charge density wave were resolved. The CDW wave length is incommensurate with the atomic lattice. The nature of this incommensurate state is a key question. It may be that the incommensurate CDW state is uniformly incommensurate, or that it is locally commensurate within domains and undergoes phase slips at the domain walls. The phase slips are called discommensurations. We have analyzed the Fourier transform of the STM images to test for signatures of discommensurations. Some Fourier peaks may be interpreted as evidence for discommensurations. However, a more compelling interpretation leads to the conclusion that the STM data is insufficient to discern discommensurations. In contrast, the atomic pair distribution function analysis gives evidence for discommensurations. The local density of states using the STS mode was measured at 77 K, and the CDW gap was observed at various places on the surface of the sample. The gap size measured directly above the Te atoms is ~ 360 meV. The CDW gap of YTe_3 was obtained from room temperature STS, and was estimated to be roughly ~ 320 meV.

$\text{K}_2\text{Bi}_8\text{Se}_{13}$ is a narrow band gap semiconductor and a promising thermoelectric material. The local electronic structure near the Fermi level of $\beta\text{-K}_2\text{Bi}_8\text{Se}_{13}$ was studied in STS mode. This crystal has a needle-like structure; in particular four chains of atoms form within the unit cell along the c direction. These are structural features of interest in this material, that significantly influence the electronic structure and narrow the band gap. STS measurements at 1.6 K temperature revealed a gap of approximately 0.4 eV, in good agreement with results of theoretical calculations. Further, the STS study revealed the presence of subgap states that, according to recent electronic band structure calculations exploring several K/Bi chain configurations, occur due to disorder along the chains. The disorder in $\beta\text{-K}_2\text{Bi}_8\text{Se}_{13}$ could play an important role for its thermoelectric properties, by changing the density of states near the band gap and potentially increasing the thermopower.

To my family

Acknowledgments

I would like to express my utmost gratefulness to my thesis adviser, Professor Stuart H. Tessmer, for all his help, guidance, patience, as well as for financial support during my graduate studies.

Unreserved gratitude and thanks to my thesis committee members, Professors S. D. Mahanti, Simon J. L. Billinge, Michael Thoennessen, and Carl Schmidt for their help during my studies and for their time and effort while being on the committee.

Significant contributions of Professor Mercouri G. Kanatzidis in various segments of the project presented here are acknowledged and greatly appreciated. Samples used in this study were provided by Kanatzidis group, and were synthesized by Christos Malliakas and Theodora Kyratsi. I thank them for their kind help.

Collaboration and discussions with HyunJeong Kim, Khang Hoang, and Zsolt Rak, are greatly appreciated, and I thank them for their kind help.

Many thanks to my dear friend and colleague Irma Kuljanishvili, and colleagues Morewell Gasseller, Cemil Kayis, and Josh Veazey for their companionship in the lab and their kind help.

I would like to thank my husband Emil Bozin for support and encouragement throughout the course of my graduate studies.

Finally, I thank my family for all the support, understanding and love, especially to my mother Vera Tomic for all her motherly help and support.

This work was supported by the National Science Foundation through Grant No. DMR-0305461, and by the Center for Fundamental Materials Research at Michigan State University.

Contents

List of Tables	viii
List of Figures	ix
1 Introduction and Motivation	1
1.1 Thesis outline	3
2 Scanning Tunneling Microscopy	5
2.1 Basic principles of STM	5
2.1.1 Introduction	5
2.1.2 Tunneling in STM	6
2.1.3 STM resolution	8
2.2 Frequently used STM methods	9
2.2.1 Surface topographic imaging mode	9
2.2.2 Scanning tunneling spectroscopy	10
2.3 STM design	12
2.4 Cryogenic system	17
2.5 Mechanical stability of STM	19
2.6 System testing and calibration	22
3 Charge density waves	24
3.1 Introduction	24
3.2 Basics of the physics of CDWs	25
3.2.1 The Peierls transition	26
3.2.2 Fermi surface nesting	28
3.3 CDW types	30
3.4 Methods of detection of CDWs in materials	32
3.5 Examples of CDW materials	36
4 Study of the charge density wave in CeTe₃	38
4.1 Introduction	38
4.2 CDW and structure of CeTe ₃	40
4.2.1 Ideal crystallographic structure of CeTe ₃	40
4.2.2 CDW detection and revised structure of CeTe ₃	41
4.3 Electronic properties of RETe ₃	43
4.4 Sample synthesis and experimental details	47
4.5 Results of STM measurements on CeTe ₃	49

4.5.1	Room temperature data and the nature of the CDW	49
4.5.2	Results of STM at 77 K	58
4.5.3	Wave vector mixing	60
4.6	Scanning tunneling spectroscopy of CeTe ₃	65
4.7	STM and STS measurements on other RETe ₃	68
4.8	Summary	70
5	Characterizing electronic structure of β-K₂Bi₈Se₁₃ thermoelectric using STS	72
5.1	Introduction	72
5.2	Fundamentals of thermoelectrics	73
5.2.1	Historic highlights	73
5.2.2	Thermoelectric figure of merit and good thermoelectric materials	75
5.3	K ₂ Bi ₈ Se ₁₃	77
5.3.1	Properties	77
5.3.2	Crystal and electronic structure of β -K ₂ Bi ₈ Se ₁₃	79
5.4	Scanning tunneling spectroscopy of β -K ₂ Bi ₈ Se ₁₃	83
5.4.1	Sample synthesis	83
5.4.2	Results and discussion	84
5.5	Summary	90
6	Concluding remarks	91
6.1	Summary	91
6.1.1	CeTe ₃ and YTe ₃	91
6.1.2	β -K ₂ Bi ₈ Se ₁₃	92
6.2	Future work	93
	Bibliography	95

List of Tables

4.1	Characteristics of some of the rare-earth tritellurides. The table shows q_{CDW} component, approximate maximum size of the CDW gap, and the CDW transition temperature. q_{CDW} components were measured by C. Malliakas. CDW gap values are based on ARPES measurements. CDW transition temperature values are based on resistivity measurements.	47
-----	---	----

List of Figures

2.1	(Images in this dissertation are presented in color.) Conducting electrodes (1) and (2) in close proximity: when unbiased, the Fermi levels equilibrate and take the same value E_F (a). When bias voltage V is applied the Fermi levels split by eV and become E_F^L and E_F^R (b). . .	6
2.2	The vacuum barrier of width d between the sample and the tip, shown with the electronic wavefunction. Bias voltage V is applied, and the Fermi levels E_F of the sample and the tip are separated by eV . The electronic wavefunctions are periodic in the sample and the tip, and decay exponentially in the vacuum region.	7
2.3	Scheme and photograph of the scanning tunneling microscope, based on a design by K. Besocke. The sample holder is resting on three piezoelectric tubes. The central piezotube is holding the tip. The sample is located above the tip (dark square).	13
2.4	(a) Schematic representation of a typical STM piezotube with four quadrants. (b) The top view: the quadrants denoted with +X, +Y, -X, and -Y are used for the electromechanical control. (c) Schematic of the three carrier piezotubes indicating motion in rotational sense. .	14
2.5	Schematic representation of the STM feedback circuit.	16
2.6	Schematic representation of our STM cryogenic setup.	18
2.7	(This figure is presented in color.) (a) Carbon atoms in the STM image of graphite surface at the scan range of $24.4 \text{ \AA} \times 25.8 \text{ \AA}$, obtained at the tunneling current of 0.5 nA and the bias voltage of 100 mV . The image is cleared with Fourier filtering. (b) The STM image of platinum sample at the scan range of $5.8 \mu\text{m} \times 5.7 \mu\text{m}$, obtained at the tunneling current of 80 pA and the bias voltage of 180 mV	23
3.1	The conduction band of a one-dimensional crystal. One-electron states with energy $E(\mathbf{k}) < E(\mathbf{k}_F)$ are filled, while states with $E(\mathbf{k}) > E(\mathbf{k}_F)$ are empty. (a) Periodic crystal with $\pm\pi/a$ describing the boundary of the first Brillouin zone. 1D crystal with a PLD with period $\mathbf{q} = 2\mathbf{k}_F$, showing an energy gap, Δ , in the dispersion at $\mathbf{k} = \pm\mathbf{k}_F$	27

3.2	Fermi surface nesting in a free electron model. (a) In the case of a single 1D chain, the Fermi surface consists of two points. (b) In the 2D case of non-interacting parallel chains, the Fermi surface consists of two sets of colinear points along two parallel lines perpendicular to the direction of chains. (c) In 3D periodic distribution of non-interacting parallel chains, the Fermi surface consists of two planes perpendicular to the direction of the chains. (d) In 3D isotropic crystals, nesting is fulfilled for a single point on the spherical Fermi surface.	29
3.3	(a) For an undistorted one-dimensional metal with a half-filled band, the lattice is a periodic array of atoms with lattice constant a . (b) One-dimensional metal with a half-filled band, with introduced periodic lattice deformation and associated CDW with period $2a$	30
3.4	The normalized resistance $R/R_0 = (1/R_0)dV/dI$, versus applied external electric field, E , in NbSe ₃ . V represents voltage, I is current, and R_0 is the value of R at $V = 0$. For the low values of E the system obeys Ohm's law, $R/R_0 = 1$. Above certain threshold field ($E_0 = 117mV/cm$ in case of NbSe ₃), the incommensurate CDW starts sliding, thus opening a second conduction channel, resulting in a decreased resistance $R/R_0 < 1$	31
3.5	Anomalous transport properties of NbSe ₃ , as observed by Ong and Monceau. Large increases of the dc resistivity appear at 144 K and 59 K, indicating the formation of two independent CDWs in this system.	34
4.1	Schematic illustration of charge density waves along one-dimensional chains of atoms (circles and dots). The shading of each atom indicates its apparent magnitude with respect to an STM measurement, with white corresponding to a relatively high signal and black indicating a relatively low signal. Depending on the ratio of the CDW wavelength λ and atomic lattice a , the CDW can be (a) commensurate with λ/a rational, or (b) incommensurate with λ/a irrational. Part (c) shows the discommensurate case, for which an incommensurate CDW is locally commensurate - or locked in with the atomic lattice - with discommensurations (domain walls) preserving the average CDW wavelength. . .	39
4.2	(This figure is presented in color.) The average crystal structure of CeTe ₃ consisting of corrugated CeTe slabs, and Te layers, where Te atoms are separated by 3.1 Å in a square-net. The figure is courtesy of H. J. Kim	41
4.3	(a) Selected area electron diffraction pattern of CeTe ₃ , and (b) selected intensity scan along the c^* direction of the electron diffraction pattern marked with a box in (a). The arrows indicate the positions of the observed superlattice reflections.	42

4.4	The experimental atomic PDF of CeTe ₃ (symbols) up to 3.7 Å, featuring a shoulder that corresponds to ~ 2.9 Å Te-Te distance, indicated by the arrow. The solid line represents the <i>Cmcm</i> model that assumes an undistorted Te net, and the difference curve is offset below. This model clearly does not explain the data.	43
4.5	Low-T resistivity of CeTe ₃ , as obtained by Ru and Fisher, for current flowing within Te layers and along the direction perpendicular to it. Arrows indicate corresponding ordinates. Note the degree of anisotropy: at ~ 45 K the in-plane resistivity is about 50 times smaller than that corresponding to the out-of-plane direction.	44
4.6	Contour plot in reciprocal space of ARPES spectral weight for CeTe ₃ at 25 K, representing a Fermi energy intensity map, as obtained by Brouet and collaborators. The arrow indicates characteristic nesting vector \mathbf{q}_{CDW}	45
4.7	Temperature dependence of the anisotropic resistivity for TbTe ₃ , as measured by Ru and co-workers. Arrows indicate corresponding ordinates for the in-plane and perpendicular directions. A characteristic change in resistivity is present around $T_{CDW} = 336$ K, as indicated by the vertical dashed line.	46
4.8	(This figure is presented in color.) A representative room temperature STM image of the Te net, showing both Te atoms and the CDW modulations oriented at 45° to the net. The image, obtained at a scan range of 27 nm x 27 nm, has been Fourier filtered. On the expanded image, the network of Te distances is superimposed. Lines indicate locations of high charge density due to the CDW, while the arrow marks the CDW direction.	50
4.9	(This figure is presented in color.) The two-dimensional Fourier transform of the room temperature STM data. The unprocessed transform image shows enhanced noise along the vertical axis, an artifact due to the scan direction. To better resolve the peaks near the origin, we applied a line-by-line correction to remove this noise. This creates the dark line along the y axis. Horizontal and vertical axes are wave vector components k_x and k_y . The square Te net gives rise to four distinct peaks (L). Peaks related to the CDW are oriented at 45° to Te net peaks, as indicated by the arrow. The fundamental CDW peak and the first harmonic are labeled 1 and 3, respectively. Peaks 2 and 4 are in close proximity to peak 3, and peak 5 corresponds to the underlying structure.	53

4.10	Simulated STM image of CeTe ₃ from theoretical calculations. The image is simulated by calculating the charge density in the plane 3 Å above the surface Te layer, obtained for an energy range between 0.05 eV and 0.1 eV above the Fermi level. The first atomic layer below the surface Te layer is Ce layer. The color scale denotes charge density changes: light color denotes large charge density, while dark color denotes small charge density. The square marks one unit cell along the <i>a</i> and <i>c</i> directions, with a lattice parameter of 4.4 Å. Simulation courtesy of Z. Rak.	55
4.11	(This figure is presented in color.) Part (a) shows a line cut of the FT data starting from the origin in the direction of the CDW. Part (b) shows the same data with an expanded scale. The red arrow indicates where we would expect to find a 2 nd satellite peak, given our interpretation of peak 2.	57
4.12	(This figure is presented in color.) A real-space STM image of the Te net obtained at 77 K, showing both Te atoms and CDW modulations oriented at 45° to the net. The image is the average of four images that were obtained consecutively at a scan range of 10.2 nm x 10.2 nm, with just a line-by-line correction. Here we show the biggest area without substantial contamination, although some contamination is present as seen in the upper left corner. The approximate size of the displayed area is 6.5 nm x 6.5 nm. Lines indicate locations of high charge density due to CDW, while the arrow marks the CDW direction.	59
4.13	(This figure is presented in color.) The Fourier transform of the low temperature STM data. Enhanced noise along the vertical axis is an artifact due to the scan direction. Horizontal and vertical axes are wave vector components <i>k_x</i> and <i>k_y</i> . The square Te net gives rise to four distinct peaks (L). Peaks at 45° to Te net are consistent with the CDW peaks. The CDW peak <i>q_{CDW}</i> , as well as peak <i>q</i> related to underlying Ce atoms, are labeled.	60
4.14	(This figure is presented in color.) Subset of the data from the Fourier transform along a path from the origin in the direction of the CDW. Noise in the Fourier transform becomes significantly larger near the origin. This is due to the impurities present in the real-space data. As the guide to the eye, the red dashed line indicates the background noise.	61

4.15	(a) Simulated one-dimensional STM signal representing the superposition of two sine waves: the short wavelength represents lattice effects, while the long wavelength represents CDW. The corresponding Fourier transform is shown in panel (e). Non-sinusoidal distortions to the simulated STM signal of various magnitudes were considered in (b)-(d), with the original signal shown as a gray curve for comparison. The corresponding Fourier transforms are given in panels (f)-(h). Additional peaks appear at special positions in the Fourier transform as the distortion is introduced. See text for details.	62
4.16	Fourier transform of the distorted signal from Figure 4.15(h). While in the Fourier transform of undistorted signal only peaks labeled with q_1 and q_2 appear, as they correspond to the two superposed waves in the direct space, additional peaks are observed in the case when distortions are present. These additional peaks occur at q_2-q_1 , q_2+q_1 , $2q_2$, $2q_2-q_1$, $2q_2+q_1$, and other linear combinations.	63
4.17	(This figure is presented in color.) Subset of the data from Fourier transform along path from the origin in the direction of the CDW. Noise in the Fourier transform becomes significantly larger near the origin. This is due to the impurities present in the real-space data. As the guide to the eye, the red dashed line indicates the background noise.	64
4.18	Local DOS around the Fermi level for CeTe_3 . The Fermi level corresponds to zero bias voltage. The estimated CDW gap size in CeTe_3 is about 360 meV, as indicated by vertical arrows. The spectroscopy was carried out when the tip was located directly above a Te atom (a), and when the tip position was above the center of a Te plaquette (b). In the later case the data were collected above two adjacent plaquettes, shown as two curves, one above Ce and another above Te subsurface atoms. See text for details.	66
4.19	(This figure is presented in color.) (a) STM real-space image and (b) Fourier transform of YTe_3 . STM data are obtained at the scan range of $5.2 \text{ nm} \times 5.1 \text{ nm}$, with bias voltage of 100 mV and tunneling current of 0.6 nA. The Fourier transform shown is that of the STM data with scan range $8.4 \text{ nm} \times 8.1 \text{ nm}$, obtained at bias voltage of 100 mV and tunneling current of 0.6 nA. These data are of poor quality, hence no conclusions related to the CDWs could be made.	69
4.20	Local DOS around Fermi level for YTe_3 . dI/dV curve was obtained from I vs. V data measured by sweeping the bias voltage in range $\pm 300\text{mV}$. The data is very noisy, but it gives hints on the size of CDW gap. Dashed vertical lines are guides for the eyes. Our estimate for the CDW gap size in YTe_3 is about 320 meV.	70
5.1	Electrical conductivity of single crystal $\beta\text{-K}_2\text{Bi}_8\text{Se}_{13}$ sample.	77

5.2	Seebeck coefficient of β -K ₂ Bi ₈ Se ₁₃ for single crystal (open circles) and powder (open squares) samples.	78
5.3	ZT of a single crystal β -K ₂ Bi ₈ Se ₁₃ sample.	79
5.4	(This figure is presented in color.) Crystal structure of β -K ₂ Bi ₈ Se ₁₃ . The structure shown represents the unit cell doubled in the <i>c</i> direction. Large blue spheres represent K atoms, large gray spheres denote Bi atoms, while small green spheres show Se atoms. K/Bi sites of interest for this study that form chains in the structure along <i>c</i> direction are circled. See text for details.	80
5.5	Band structure of β -K ₂ Bi ₈ Se ₁₃ as obtained from theoretical considerations for three different configurations of atoms along K/Bi chains. See text for details. Figure after D. Bilc <i>et al.</i>	82
5.6	SEM image of needle-like structure of β -K ₂ Bi ₈ Se ₁₃ . Figure courtesy of T. Kyratsi.	83
5.7	Local density of states of β -K ₂ Bi ₈ Se ₁₃ as obtained by the STS measurements at 1.6 K. From the data, a band-gap of ~ 0.4 eV is estimated, in agreement with theoretical prediction based on configuration III that assumes alternating K/Bi chains. In addition, subgap states are observed. See text for details.	84
5.8	Schematic representation of various configurations of the K/Bi chains considered in theoretical calculations. K atoms are represented with solid circles, while Bi atoms are represented with cross-marks. There are four K/Bi chains of interest in the original unit cell, however there are only two inequivalent chain types, K1/Bi9 and Bi8/K3. Configuration III requires unit cell doubling along the chain direction and assumes chains of alternating K and Bi, such that two inequivalent chains have opposite ordering phase. Configuration IV requires unit cell tripling along the chain direction, with K1/Bi9 chain type having K-Bi-K sequence, while Bi8/K3 type features Bi-K-Bi sequence. Configuration V also requires tripling of the unit cell, and is closely related to configuration IV, except that all four chains are now made inequivalent, by offsetting the phase along the equivalent chains. . . .	86
5.9	DOS obtained from the electronic band structure calculations considering three different configurations along the K/Bi chains: configuration III (dotted line), configuration IV (dashed line), and configuration V (solid line). Arrows indicate specific features discussed in the text. . .	88

- 5.10 (a) STS data for DOS near the Fermi level of β -K₂Bi₈Se₁₃, at 1.6 K.
(b) DOS obtained from the electronic band structure calculations considering three different configurations along the K/Bi chains: configuration III (dotted line), configuration IV (dashed line), and configuration V (solid line). The arrows in both panels indicate features of interest discussed in text. 89

Chapter 1

Introduction and Motivation

Solid state physics has been challenged by the discovery of new classes of complex materials in the past two decades. The degree of structural complexity and the delicate interplay between structural, electronic and magnetic effects yield fascinating physical properties such as high-temperature superconductivity in doped copper oxides [1], colossal magnetoresistance in manganites at high doping [2], and enhanced thermoelectric properties in novel thermoelectric materials [3]. Although these materials are important for potential technological applications, much of the physics behind corresponding phenomena is still not fully understood. It has recently been realized that features such as nanoscale inhomogeneities [4, 5, 6, 7, 8] and charge density waves [9, 10, 11, 12, 13] could play an important role in the physics of these important materials.

The degree of complexity of these materials and associated phenomena requires an approach that involves multiple experimental techniques probing different aspects of these phenomena, such as scanning tunneling microscopy (STM), which probes local electronic structure, and diffraction based techniques, that provide structural information. In addition, comparison of the experimental results with theoretical calculations is crucial for better understanding of the physics of these materials.

The STM technique is a powerful tool for studies of the nanoscale electronic

structure of novel complex materials. Although STM is still a relatively new technique [14, 15], it has revolutionized surface science, and has been successfully employed in resolving local structure and spectroscopy of many materials of interest. In STM, atomic-scale spatial resolution can be achieved allowing for detailed studies of crystal surface topography, as well as local probing of the electronic structure. It is based on the quantum mechanical effect of electron tunneling through a vacuum barrier between two conductive electrodes.

In this work, I present results of experiments utilizing scanning tunneling microscopy in two specific complex systems. In these systems, electronic properties are of interest in the context of charge density wave states and thermoelectric properties, respectively.

The charge density wave (CDW) state, which is one of the fundamental broken-symmetry ground-states of metals [16], is most common in systems with reduced dimensionality. The CDW represents a spontaneous periodic spatial modulation of charge density across a material, with an associated deformation of the crystal lattice. The CDW state in materials is characterized by a gapped Fermi surface. A CDW is said to be incommensurate when the ratio of the CDW wavelength to the atomic lattice is an irrational number. Incommensurate CDWs exhibit nonlinear transport properties that can be utilized for potential applications [17]. It is very important to characterize the precise nature of the CDW in systems in which they occur. We employed STM in the surface topographic imaging mode and point spectroscopy mode to study the charge density wave state in CeTe_3 at various temperatures. Although CeTe_3 is a simple, layered system with a one-dimensional incommensurate CDW, the exact nature of the incommensurability in this material is not fully understood, as the CDW could either be uniformly incommensurate, or could be locally commensurate with discommensurations. In this work, STM is used to observe the CDW, to determine the CDW gap size, and to address the nature of the incommensurate

CDW.

Thermoelectric materials are those materials that can be utilized for conversion of temperature gradient to electric potential difference and vice versa. Good thermoelectric materials require large electrical conductivity, large thermopower, and small thermal conductivity [18]. Optimization of these parameters is often difficult [19]. Narrow band-gap semiconductors show great promise for future thermoelectric materials, as their properties can be tuned by doping. Electrical conductivity and thermopower are determined by the details of the electronic properties including the size and structure of the semiconductor band gap and scattering of charge carriers by defects and impurities, while thermal conductivity is affected by scattering of phonons. Therefore, resolving the electronic structure of thermoelectric materials is key to understanding their properties. We used scanning tunneling spectroscopy to study the electronic structure of β -K₂Bi₈Se₁₃, which is a promising thermoelectric material. In particular, the band gap of β -K₂Bi₈Se₁₃ obtained using optical measurements in the infrared regime at room temperature [20] showed marked disagreement with the results of theoretical calculations [21]. In order to resolve this issue, I measured the band gap of this important material using STM. The observed electronic structure is also considered in relation to the nature of structural disorder on specific atomic sites that is believed to play an important role for its thermoelectric properties.

1.1 Thesis outline

The thesis is organized as follows. Chapter 2 represents a description of the STM experimental technique, including explanations of different modes used to carry out experiments and various experimental details. Chapter 3 reviews relevant physics related to the CDW phenomenon, with an overview of CDW types and of typical experimental methods sensitive to the CDW state. Chapter 4 brings the detailed results of the STM characterization of the CDW state in CeTe₃ at room temperature

and 77 K. The basics of the physics of thermoelectric materials is given in Chapter 5, as well as the STM results of the electronic structure of β -K₂Bi₈Se₁₃ at 1.6 K temperature. Concluding remarks and possible directions for further work are given in Chapter 6.

Chapter 2

Scanning Tunneling Microscopy

2.1 Basic principles of STM

2.1.1 Introduction

Scanning tunneling microscopy (STM) is a technique developed in the early 1980s, after the first tunneling signal through a controllable vacuum gap had been achieved by Binnig, Rohrer and collaborators [14]. This was followed by the demonstration of successful surface microscopy using vacuum tunneling, producing the first topographic pictures of surfaces on an atomic scale. Examples of resolved monoatomic steps and surface reconstructions were shown by the same group for surfaces of Si, CaIrSn_4 and Au [15]. STM is now routinely used for surface imaging as well as for local probing of the electronic structure of materials.

The operation of the STM is based on the quantum mechanical effect of electron tunneling through a vacuum barrier between two conductive electrodes. The tunneling current starts to flow when a sharp tip of the STM probe is brought in proximity of a conducting surface, at a distance of approximately 0.5 nm. A polarity of a voltage applied between the tip and the sample surface determines the direction of the tunneling current. The magnitude of the tunneling current decays exponentially as the tip-sample separation increases. The STM technique can only be applied to study

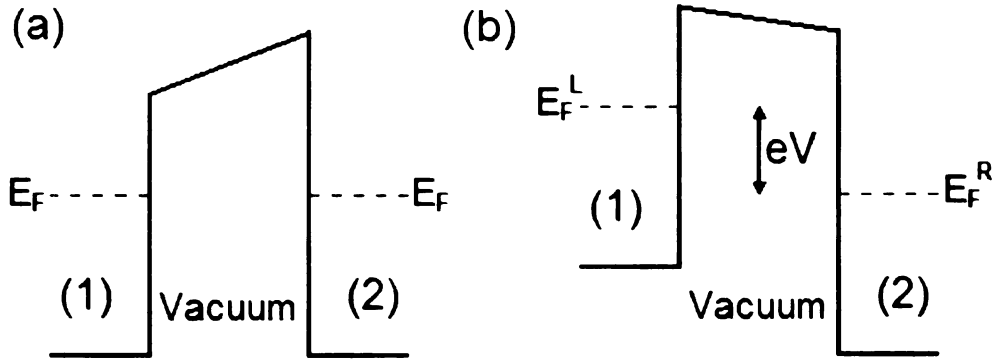


Figure 2.1: Conducting electrodes (1) and (2) in close proximity: when unbiased, the Fermi levels equilibrate and take the same value E_F (a). When bias voltage V is applied the Fermi levels split by eV and become E_F^L and E_F^R (b).

conducting or semiconducting samples, as for the insulating samples the electrons have no available energy states to tunnel into or out of due to the insulating band gap.

2.1.2 Tunneling in STM

Consider two conducting electrodes (1) and (2) at a temperature of absolute zero. When the separation between the two electrodes is small enough to allow tunneling, the electrodes come into an electrical equilibrium, such that there is a unique Fermi level for both of them, as shown in Figure 2.1(a). When a bias voltage V is applied across the two electrodes, the Fermi levels split by energy eV , where e is the electron charge, as shown in Figure 2.1(b), and directed quantum tunneling can occur. States within an energy interval eV separating the two Fermi levels contribute to the tunneling, with electrons occupying filled states within eV below the higher Fermi level of one electrode tunneling into the empty states within eV above the lower Fermi level in the other electrode [22]. At finite temperatures transient tunneling can occur even when no voltage is applied as some of the electrons in the electrodes will be thermally excited above the Fermi level. On average, this effect cancels as tunneling occurs in both directions between the electrodes.

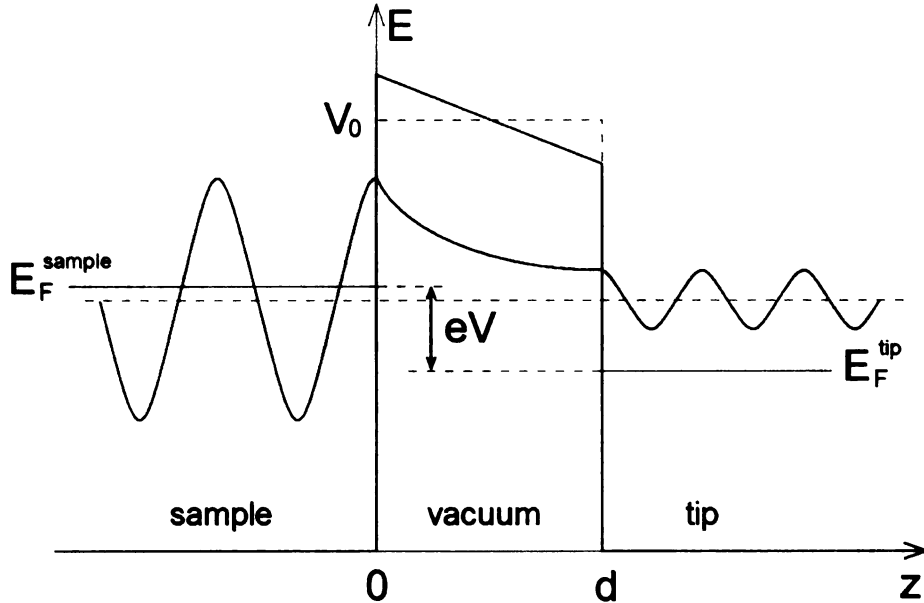


Figure 2.2: The vacuum barrier of width d between the sample and the tip, shown with the electronic wavefunction. Bias voltage V is applied, and the Fermi levels E_F of the sample and the tip are separated by eV . The electronic wavefunctions are periodic in the sample and the tip, and decay exponentially in the vacuum region.

Here I provide a simple illustration of the quantum tunneling effect which is a basis of the STM operation. Consider a rectangular barrier, such as that shown in Figure 2.2, which is a reasonable approximation if the bias voltage is small compared to the work functions of the tip and the sample. The work function is defined as $\phi = V_0 - E_F$, where V_0 is the potential in the barrier. For simplicity I will assume a one dimensional tunneling barrier, with the dimension denoted z . For such a barrier the electron motion is governed by the time independent Schrödinger equation

$$-\frac{\hbar^2}{2m} \frac{d^2\psi}{dz^2} + V_0\psi = E\psi. \quad (2.1)$$

If the electrons are incident on the barrier from the left, then there are three branches for the solution to the Schrödinger equation as follows:

$$\psi(z) = \begin{cases} A \exp(\frac{ipz}{\hbar}) + B \exp(\frac{-ipz}{\hbar}), & z < 0 \\ C \exp(-kz) + D \exp(kz), & 0 \leq z \leq d \\ \tau \exp(\frac{ip(z-d)}{\hbar}), & z > d \end{cases} \quad (2.2)$$

where $p = \sqrt{2mE}$ and $\hbar k = \sqrt{2m(V_0 - E)}$. At the boundaries of the three regions these functions and their first derivatives must be continuous, which sets constraints on the choice of constants. Furthermore, the value of constant D is exponentially suppressed, to avoid the unphysical solution of the wave function diverging in the case of a thick barrier.

In the STM system the two electrodes are the tip and the surface of the sample, where the separation between them is less than 1 nm. As implied from Eq. 2.2, the electron wavefunction is sinusoidal in the sample and the tip, but *decays exponentially* inside the barrier as $\psi(z) = C \exp(-kz)$. The wavefunction of the transmitted electrons is $\psi(z) = \tau \exp(\frac{ip(z-d)}{\hbar})$, where τ is the transmission coefficient. If the barrier is sufficiently thick, the slope of the exponentially decaying function $\psi(z)$ is close to zero at the vacuum-tip interface. Due to continuity conditions of ψ and $\frac{d\psi}{dz}$, it follows that the value of the wavefunction at $z = d$ is $\psi(d) = C \exp(-kd) = |\tau|$. As the tunneling current I is proportional to the transmission probability $|\tau|^2$ [23], it follows that

$$I \propto \exp(-2kd). \quad (2.3)$$

2.1.3 STM resolution

As the tunneling current depends exponentially on separation between the tip and the sample, one readily sees that the STM is extremely sensitive to small variations in the tip-sample spacing. This is called z-sensitivity. When the separation between the tip and the sample changes by Δd , then the tunneling current changes by a factor of $\exp(-2k\Delta d)$, as seen from Equation 2.3. For example, for the typical value of

work function of $\phi=4$ eV, the value of $k = \frac{\sqrt{2m(V_0-E)}}{\hbar}$ for states at Fermi level is 1.03 \AA^{-1} . An increase of $\Delta d=1 \text{ \AA}$ in the separation between the tip and the sample would cause the tunneling current to drop by factor of $\exp(-2k\Delta d) = 0.127$, i.e., an *order of magnitude*. Atomic resolution of STM is a direct consequence of the z-sensitivity: if one atom at the apex of the tip is 1 \AA closer to the sample than the other atoms, most of the tunneling current will flow through that apex atom. As it is shown by Stoll *et al.*, most of the tunneling current is typically confined to a small area with a radius of approximately 3 \AA on the sample surface, which is sufficient to detect the corrugation of individual atoms [24].

2.2 Frequently used STM methods

The STM technique was initially developed to investigate the surface topography properties of materials on the atomic scale. However, fairly soon after it was established, STM was employed for probing of the local electronic structure as well. Essentially, there are three parameters that can be varied: the applied bias voltage between the tip and the sample, the tunneling current, and the tip position with respect to the sample. The ability to vary these parameters enables the STM probe to be useful for characterization of different properties. There are two common modes of STM operation. One mode is the *constant current mode*, also referred to as the *surface topographic imaging*. The second mode of operation is *scanning tunneling spectroscopy* (STS) in *point spectroscopy mode*.

2.2.1 Surface topographic imaging mode

In the surface topographic imaging mode, the tip is scanned over the surface of the sample while the tunneling current is maintained constant. A fixed bias voltage is applied and the desired tunneling current is set. As the tip is scanned across the

surface of the sample, variations in the topography of the sample and the underlying electronic structure affect the tunneling current. In order to keep the preselected value of the tunneling current constant, a feedback circuit is used to adjust the position of the tip above the sample surface. Feedback voltage, corresponding to the vertical position of the tip is recorded, reflecting the surface topography. Details are described in Section 2.3.

2.2.2 Scanning tunneling spectroscopy

In the point spectroscopy mode, the position of the STM tip is kept fixed with respect to the sample surface, over a single point of the sample. The bias voltage V is ramped, typically from -300 mV to +300 mV, and the tunneling current I is measured as a function of the ramped voltage V . Differentiation of $I(V)$ with respect to V provides a direct measure of the sample's *density of states* at a temperature of absolute zero. At finite temperatures, the measurements are *smearred* by $3.5 k_B T$, where k_B is the Boltzmann constant, and T is the measurement temperature. To minimize the smear out of the data, the STM spectroscopy is typically operated cryogenically. At liquid ^4He temperature, 4.2 K, we can resolve details of the electronic structure of the sample on a sub-meV energy scale. Since materials that are subject of this study are expected to have band gaps of the order of hundreds of meV, the energy resolution of the measurements allows for the energy band structure to be determined with exceptional quality.

To illustrate the principle behind the electronic structure measurements in the spectroscopic mode of STM, we will follow a simple set of equations. In order to obtain an expression relating tunneling current to the electronic structure, we assume that all tunneling transitions occur at constant energy where states within an energy interval eV separating the two Fermi levels contribute to the tunneling [23]. We can calculate the total tunneling current by adding up all contributions from each energy

level. For temperatures $T > 0$, the number of occupied states in the sample electrode at the given energy E is $N_s(E)f(E)$, where $N_s(E)$ is the density of states of the sample electrode and $f(E)$ is the Fermi function. The number of empty states in the tip electrode, at the same energy E , is given by $N_t(E - eV)(1 - f(E - eV))$, where $N_t(E - eV)$ is the density of states of the tip electrode. As electrons from the occupied states can tunnel only into empty states, the tunneling current from the sample to the tip can be written as

$$I_{s \rightarrow t} \propto \int_{-\infty}^{\infty} |\tau|^2 N_s(E) f(E) N_t(E - eV) [1 - f(E - eV)] dE, \quad (2.4)$$

where

$$f(E) = \frac{1}{\exp(\frac{E}{k_B T}) + 1} \quad (2.5)$$

represents the Fermi function for a state with energy E . For temperatures $T > 0$, thermal excitations bring electrons into states above the Fermi energy. Thermally excited electrons in the sample electrode leave the empty states. Thermally excited electrons in the tip electrode can tunnel into these emptied states, creating the tunneling current from the tip to the sample

$$I_{t \rightarrow s} \propto \int_{-\infty}^{\infty} |\tau|^2 N_t(E - eV) f(E - eV) N_s(E) [1 - f(E)] dE. \quad (2.6)$$

The quantity $|\tau|^2$ is the transmission probability for tunneling from the initial to a final state. We can approximate that the transmission probability is independent of energy E if only energies close to the Fermi energy are considered. Therefore $|\tau|^2$ can be immersed into the constant of proportionality. The total tunneling current is the difference between the current from the sample to the tip and the current from the

tip to the sample:

$$I \propto \int_{-\infty}^{\infty} N_s(E)N_t(E - eV)[f(E) - f(E - eV)]dE, \quad (2.7)$$

To simplify the equation we will assume that the STM tips, typically made of noble metals such as *Au* or *Pt*, have *constant* density of states near the Fermi level, i.e., N_t is independent of E . Differentiation of I with respect to V then gives

$$\frac{dI(V)}{dV} \propto \int_{-\infty}^{\infty} N_s(E)\left[-\frac{\partial f(E - eV)}{\partial(eV)}\right]dE. \quad (2.8)$$

When $k_B T \rightarrow 0$, then

$$\frac{\partial f(E - eV)}{\partial(eV)} \rightarrow \delta(E - eV) \quad (2.9)$$

leading to

$$\frac{dI(V)}{dV} \propto N_s(eV) \quad (2.10)$$

when $T \rightarrow 0$. Thus at low temperatures, differentiation of I with respect to V gives a direct measure of the sample's density of states.

2.3 STM design

An important aspect of the exponential decay of the tunneling current with increased sample-tip separation is that it sets spatial limitations to the tunneling range of the microscope. If the tip is too far away from the sample, no tunneling can occur, as the tunneling probability will be negligible. Therefore, bringing the tip into tunneling range and scanning it over the sample surface requires extremely precise control. Since the invention of scanning tunneling microscopy, the issue of tip and sample control was part of the design, and significant improvements of stability and performance of the STM have been achieved over the years.

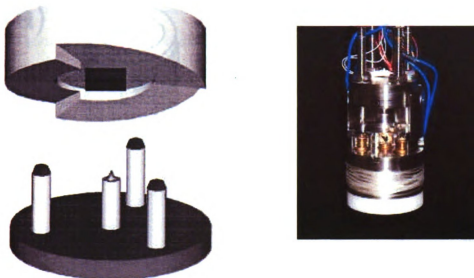


Figure 2.3: Scheme and photograph of the scanning tunneling microscope, based on a design by K. Besocke [25]. The sample holder is resting on three piezoelectric tubes. The central piezotube is holding the tip. The sample is located above the tip (dark square).

The control of the sample-tip separation is typically achieved by using a series of electrically controlled piezo-tubes. These materials utilize the piezoelectric effect, which represents the ability of crystals and certain ceramic compounds to generate a voltage in response to applied mechanical stress. Conversely, piezoelectric crystals, when subjected to an externally applied voltage, can change their shape by a small amount. The piezoelectric effect has numerous applications, such as high voltage and power generation, sensors, actuators, reduction of vibrations, production and detection of sound, electronic frequency generation, micro-balances, and ultra fine focusing of optical or electronic assemblies, such as STM.

The design of the scanning tunneling microscope used in this study (Figure 2.3) is based on the design developed by K. Besocke [25], which provides excellent stability utilizing a compact assembly. Moreover, the design achieves very small thermal drift by using a thermally compensated geometry. Figure 2.3 shows a schematic of the design and a photograph of the microscope. The position of the tip with respect to

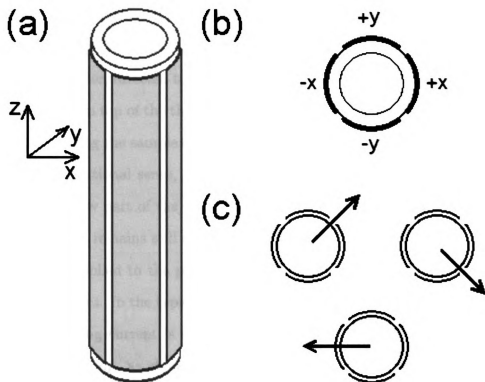


Figure 2.4: (a) Schematic representation of a typical STM piezotube with four quadrants. (b) The top view: the quadrants denoted with +X, +Y, -X, and -Y are used for the electromechanical control. (c) Schematic of the three carrier piezotubes indicating motion in rotational sense.

the sample is controlled by small piezoelectric tubes. The sample holder is resting on three carrier piezoelectric tubes in a triangular configuration. The carrier piezotubes have smooth stainless steel balls on the top, used for contact with the sample holder. These piezotubes bring the sample into tunneling range of the tip. The tip is attached to the central piezotube (also called scanning tube), which is used to scan the tip over the surface. Each of the piezotubes is metallized to form four quadrants, as shown in Figure 2.4(a) and Figure 2.4(b), that can each change dimensions independently. The tube is lengthened or shortened by applying a positive or negative voltage on all the quadrants simultaneously, providing the motion in the z direction. For motion in the lateral direction, one quadrant is lengthened while the opposite one is shortened, causing the tube to bend in the x or y direction. For our microscope at room

temperature the sensitivity of the piezoelectric ceramics is $200 \text{ \AA}/\text{V}$, providing the maximum scan range of about $5 \mu\text{m}$ in the x and y directions.

The sample holder, directed toward the tip, contains three sloped ramps (see Figure 2.3) that slide on top of the three piezotubes, as controlled by the electromechanical system, and bring the sample closer to or away from the tip. This is accomplished by motion in a rotational sense, as seen in Figure 2.4(c), using a sawtooth-like signal. During the slow part of the signal, the sample holder rotates together with the piezotubes, while it remains still during the fast part of the signal.

The voltages applied to the piezotube quadrants are controlled by commercially purchased electronics. In the typical mode of STM operation, *constant current mode*, the desired tunneling current is maintained by controlling tip-to-sample separation by using feedback loop, as shown in Figure 2.5. An amplifier with 10^9 V/A gain is used to convert the low tunneling current between the tip and the sample to a voltage signal. This is compared to the preset voltage corresponding to the desired value of the tunneling current. The difference between these two voltages is used to create a feedback voltage as follows. The difference signal, or error signal, is sent into a feedback circuit. The feedback voltage is generated as a combination of two components: the first is called gain, and is directly proportional to the error signal; the second one, called time constant, is proportional to the integral of the error signal. The feedback voltage is sent to the piezoelement controlling the z position of the tip, resulting in an adjustment of the tip position to correspond to the preset tunneling current. The tunneling current is typically set to a range of $0.1\text{-}1 \text{ nA}$.

A high value of the gain results in a faster response of the feedback loop, while a low gain would result in a relatively slow response. However, if the value of the gain is set too high and the integrator too low, the system may over correct, which will cause the current to oscillate around the set value. This phenomenon is known as feedback oscillation. It can be particularly troublesome if too much noise is present

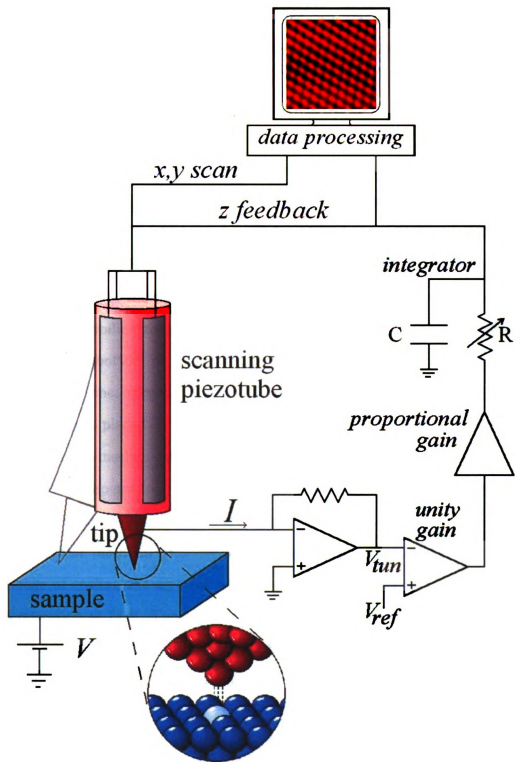


Figure 2.5: Schematic representation of the STM feedback circuit.

in the signal. This undesirable mode is corrected by resetting the values of the gain and time constant. The typical gain varies between the values of 0 and 2. Typical value of the feedback time constant varies between 1 and 20 ms.

2.4 Cryogenic system

The STM experiments can be performed at room temperature as well as at selected low temperatures using a cryogenic system. In this project we employed a ^3He cryogenic system, Figure 2.6, which operates at liquid nitrogen temperature (77 K), liquid ^4He temperature (4.2 K), at the temperature of liquid ^3He around 1.2 K, which could be further lowered to the base temperature of 0.270 K by lowering the vapor pressure to decrease the boiling temperature of ^3He . The scanning tunneling microscope is mounted to the bottom of a long stainless steel probe which is used to lower the microscope into the cryogenic system. To prepare for a data run at room temperature, the probe is placed on the top of the cryostat and the sample area is evacuated by using a turbo-mechanical pump to achieve high vacuum. Cooling the cryostat to liquid helium temperature of 4.2 K is done in stages. In the first stage, the cryostat is cooled down to 77 K with liquid nitrogen. The liquid nitrogen is then completely evacuated from the main reservoir, and the cryostat is filled with liquid ^4He . The first stage of cooling the cryostat with liquid nitrogen could be maintained for the STM operation at 77 K. The probe is lowered into the sample space of the cryostat, which is kept in vacuum. After lowering into the sample space, the probe requires approximately 10-15 hours for thermal equilibration.

The base temperature of the cryogenic system operation of 0.270 K is achieved by reducing the vapor pressure of the liquid ^3He which is initially at temperature of 1.2 K. Before proceeding to the base temperature, the cryogenic system has to be cooled to liquid ^4He temperature. Gaseous ^3He is then allowed to enter the sample space from the ^3He storage dump, but it is trapped inside the sorb, a cold massive

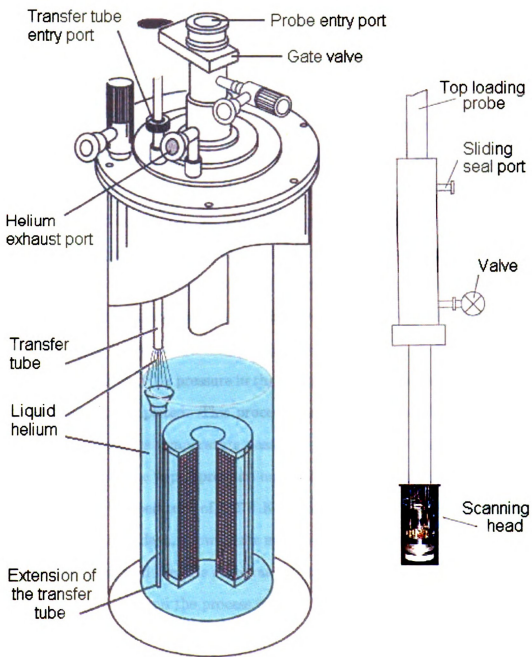


Figure 2.6: Schematic representation of our STM cryogenic setup.

charcoal pump in the sample space. By warming up the sorb slightly, a few mbar of ^3He gas is introduced into the sample space as a heat exchange gas. The scanning tunneling microscope, mounted to the probe, is then lowered to the bottom of the sample space. Lowering the microscope needs to be done slowly in order to protect the piezoelements from thermal stress. Outside of the sample space, attached to its walls, is a donut shaped chamber called 1 K pot. The 1 K pot is used for condensation of ^3He and for keeping the measuring system cold. The pot is not in the direct contact with the main liquid ^4He reservoir, the connection is achieved only through a thin tube for ^4He delivery, so the pot could be run at varying temperatures. With a flow of about 2 l/min of liquid ^4He through the pot and by lowering the pressure in the pot to about 20 mbar, the 1 K pot temperature lowers to a minimum of 1.2 K.

When the sorb is warmed to about 30 K temperature, gaseous ^3He is released from the sorb. This ^3He hits the cold copper piece of the probe (which is in a contact with the 1 K pot), condenses on it and drips into the ^3He pot at the bottom of the sample space. When the ^3He pressure in the sample space reaches its minimum value, the condensation is completed. This procedure requires about 1 hour. The sorb is then cooled down. As its temperature passes 15 K it starts to pump the remaining ^3He gas, and reduces the vapor pressure and boiling temperature of the liquid ^3He . This way the base temperature of 0.270 K is achieved. The base temperature can be maintained for three days, allowing for measurements at cryogenic temperature to take place, after which all the ^3He evaporates. At that moment all ^3He molecules are trapped inside the sorb, and the process can be repeated.

2.5 Mechanical stability of STM

It has been shown in Sections 2.1.2 and 2.1.3 that the tunneling current changes by almost an order of magnitude for a change in tip-sample separation as small as 1 Å. Considering the sensitivity of the STM, good mechanical isolation of the microscope

from all external vibrations is a critical issue. The surrounding environment of the STM probe, such as the building, the people and the machinery, are all common sources of noise, with amplitude of mechanical vibrations of the order of a few thousand angstroms. Keeping the tunneling current stable requires tip-sample mechanical vibrations to be limited to amplitudes less than 0.1 \AA . Such mechanical stability is achieved by use of compact STM design and an efficient dual-stage isolation system. The compact STM design, discussed in Section 2.3, gives high normal-mode vibration frequencies $\sim 1 \text{ kHz}$, which are not easily excited by room vibrations ($\sim 10\text{-}20 \text{ Hz}$).

Mechanical decoupling of the STM probe from the ambient vibrations is achieved with the dual-stage external vibration isolation system. The first stage of the isolation consists of four donut shaped rubber air springs, and the second stage consists of four specialized hydraulic shock-absorbing legs, frequently used to support tables with delicate optical measurement setups. These two stages may be modeled as a dual stage oscillating system of simple springs which results in an increase of the damping factor, important for achieving necessary stability of STM. Acoustic vibrations are also observed to have the effect on stability of the tunneling current. In addition to the system assigned to dampen mechanical vibrations from the experimental floor, our laboratory STM room is cushioned with sound absorption padding on the walls, to cut down on acoustic reverberation. The cushion contains patterned sheets of sound-insulating material arranged in checkerboard pattern, to most efficiently dampen all the sounds propagating through the experimental room.

Other dominating sources of noise are STM tip instabilities and various defects and impurities on the sample surface. The STM tips used in this study were commercially purchased from Materials Analytical Services, Inc.

The experiments were performed with fresh chemically etched tips, as well as with in-house mechanically cut tips. In both cases, the tips are made of alloyed platinum and iridium in a 80/20 ratio. These tips do not oxidize, which is important for

stability of the experiment when tunneling is performed in the air. Typical length of the tip is 1.0(1) cm, with the wire diameter of 0.25 mm. The top part of the STM tip is tapered. It is about 200 μm long with the radius of curvature of the very end of 50 nm. Although the tips are prepared in the same way, using the same method, not all of the tips perform equally well. There is no simple method of evaluating and predicting the performance of the tip other than to test its performance once it is mounted on the STM. The tip stability is one of the first parameters to ensure successful experimental performance. In the cases when the tip is unstable, due to a tunneling through a loose atom on a tip, or because some particles are attached to it, the STM images are usually streaky. Unstable tip conditions could sometimes be improved by a process of 'shaking' the tip, which is a fast scanning with a maximum possible scan range, for about 10 minutes. Another commonly used process is field emission where a sudden increase in bias voltage causes the electric field to eject loose particles on the tip. Of course, if these measures are unsuccessful, the tip has to be exchanged with a new one.

Cleanness of the surface of the sample is another important issue influencing the stability, as the tip can interact with impurities and become unstable. Samples to be studied are therefore carefully cleaved with scotch tape or a razor blade, such that layers are tightly packed without loose flakes, allowing for a fresh surface to be probed. If weakly attached layers are present on the sample surface, the tunneling current is unstable due to electric field forces acting on them. The samples used in this study were prepared in the air, and then transferred into a loading chamber and evacuated with a turbo-mechanical pump. Although the samples were exposed to air for about 5 minutes, the experimental tests that were carried out indicated that the surfaces were sufficiently inert such that the contamination is negligible.

2.6 System testing and calibration

After the new STM tip is mounted on the probe and before experiments are conducted, routine tests have to be performed. These tests are required to ensure good performance of the tip as there is no other special way to evaluate it. The typical sample to use in the tests is graphite. Obtaining atomic resolution images of graphite demonstrate that the tip is acceptable. Graphite crystals consist of the layers of carbon atoms. In each layer, carbon atoms are covalently bonded into hexagons, while different layers are connected together by weak van der Waals forces. Carbon atoms on the graphite surface appear in the STM images as a triangular lattice which contains every other atom, not as honeycomb rings as it would be expected. Figure 2.7(a) is the STM image of graphite surface where triangles of three carbon atoms are visible, while the other three atoms are missing. This asymmetry was explained by Tomanek *et al.* as a purely electronic effect due to the interlayer interactions [26]. It was explained as having two nonequivalent carbon atom types in each layer. Carbon atoms of one type have neighbors directly beneath them in the underlying atomic layer. Carbon atoms of the second type do not have neighbors directly beneath them. Band structure calculations predict that atoms visible in the STM image are ones that do not have the subsurface atom beneath them.

The sensitivity of piezo material in the scanning tube depends on the geometry and polarization. We use graphite samples and a structured platinum sample to properly calibrate our piezotubes. Graphite is used for getting lateral sensitivity: the STM image of graphite with good atomic resolution is used to obtain correct value of the scan range, knowing that graphite plane lattice constant is 2.46 \AA . For the particular STM image, the applied voltage to the scanning piezotube for motion in the lateral direction is known. The lateral sensitivity of the piezotube is then determined as a measure of lateral displacement per one volt. The platinum sample is useful for z -calibration. This sample is patterned into a mesh of squared pits. A value used for

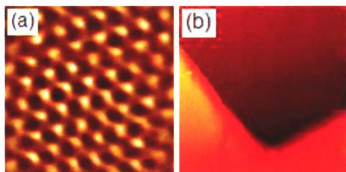


Figure 2.7: (This figure is presented in color.) (a) Carbon atoms in the STM image of graphite surface at the scan range of $24.4 \text{ \AA} \times 25.8 \text{ \AA}$, obtained at the tunneling current of 0.5 nA and the bias voltage of 100 mV . The image is cleared with Fourier filtering. (b) The STM image of platinum sample at the scan range of $5.8 \text{ \mu m} \times 5.7 \text{ \mu m}$, obtained at the tunneling current of 80 pA and the bias voltage of 180 mV .

z -calibration is the actual depth of the platinum pits of 180 nm . As the squared pits are 5 \mu m in size, with the same size of separation between them, there is an excellent chance of finding an edge, as it can be seen in Figure 2.7(b). Using the same method as for the lateral calibration, the z sensitivity of the piezotubes can be obtained.

Chapter 3

Charge density waves

3.1 Introduction

The charge density wave (CDW) state is one of the competing ground states in anisotropic, low-dimensional materials. Among the phenomena that can occur in such materials are superconductivity, ferromagnetism, antiferromagnetism, and spin density wave states. The physics of charge density wave formation involves pronounced nesting vectors in the Fermi surfaces of these materials [22, 27], accompanied with the gapping of parts of the Fermi surfaces. The conduction electron density in nearly free-electron-like three-dimensional metals can be considered as highly uniform, while the equilibrium positions of the atoms in the underlying lattice form a perfectly periodic arrangement. Spatial variations of the electron density are strongly suppressed in these systems, as they require large Coulomb energy penalty. On the other hand, in systems with reduced dimensions static modulations of the electronic density are possible. In such materials, when the temperature decreases below a certain critical temperature, the crystal lattice spontaneously develops a periodic deformation due to electron-lattice coupling. In a self consistent manner, this results in a modulation in electron density with the same periodicity, which is accompanied by a rearrangement of the electronic bands such that the total energy of the system is lowered. Such

modulation of the electron density is called a charge density wave [16].

The CDW phenomenon is usually observed in crystals of reduced dimensions, such as quasi-two-dimensional [28] and quasi-one-dimensional [16] materials. Well-known examples include inorganic layered materials like NbSe₃, TaSe₃, and K_{0.3}MoO₃, and quasi-one-dimensional organic conductors like tetramethyl-tetraselenafulvalene (TMTSF) or tetrathiafulvalene-tetracyanoquinodimethane (TTF-TCNQ). Periodic arrangements of charges have also been observed in various oxide systems, such as charge stripes in nickelates [29, 30], superconducting cuprates [12] and colossal magnetoresistive manganites [31], and checkerboard charge arrangements in cuprates [32, 33]. In the late 1990's the stripe phase observed in cuprate high temperature superconductors attracted considerable attention as long-range ordered charge stripes were found to correlate with the suppression of superconductivity [12]. Moreover, dynamically fluctuating stripe phases have been considered to be of central importance for an understanding of the physics of high-temperature superconductors [12, 34].

Compared with other conducting materials studied in bulk form, CDW conductors show an extremely rich variety of properties, like nonlinear and anisotropic electrical properties, unusual elastic properties, and gigantic dielectric constants. These properties make them interesting for potential applications such as CDW memory devices, switches, rectifiers, mixers, and optical detectors [35]. The organic CDW materials are of particular importance for studies of electrons in solids because their properties can be tuned at the synthesis stage [36].

3.2 Basics of the physics of CDWs

More than 50 years ago, R. E. Peierls introduced the theory of CDWs [37]. Peierls showed that the one-dimensional electron gas coupled to the phonon system becomes unstable at low temperature and undergoes a phase transition to an insulating state. The basic concept of this phenomenon resurfaced when the first anisotropic, low-

dimensional materials became available. This was at the time when various organic materials were synthesized [38], starting with TTF-TCNQ [39], in which a set of long molecules donated electrons to another set leaving one-dimensional conductors with partially filled bands, presumably good candidates for superconductivity [40]. Surprisingly, with cooling, these materials became insulators rather than superconductors. That was the first experimental observation of this phenomenon, called the Peierls transition.

While all materials are three-dimensional by definition, in certain classes of materials, electrons are limited to moving easily along one direction in the structure, and are much less mobile perpendicular to it. In such a case the electron conductivity might be from 10 to 1000 times greater in the preferred direction [36]. Such materials are said to have quasi-one-dimensional character. Prerequisite for CDW formation is existence of such reduction of dimensionality, hence reduced dimensionality represents a common feature of all CDW materials [35].

3.2.1 The Peierls transition

The charge density wave represents a cooperative state in which both the crystal lattice and the electron gas exhibit a distortion to lower the total energy of the system. The periodic distortion of the lattice creates a supercell which reduces the kinetic energy of the highest energy occupied electrons of the conduction band. This energy gain, however, becomes relevant as the temperature is lowered below some critical temperature, T_{CDW} , where the effect of thermal excitations is reduced. If the total energy gain is sufficiently large to surpass the cost of distorting the lattice and the Coulomb energy, the charge density wave will form.

To illustrate the underlying physics behind the CDW formation, I will consider a one-dimensional metal at temperature $T = 0$. If electron-phonon interaction is not present, the ground state corresponds to the one shown in Figure 3.1(a). The

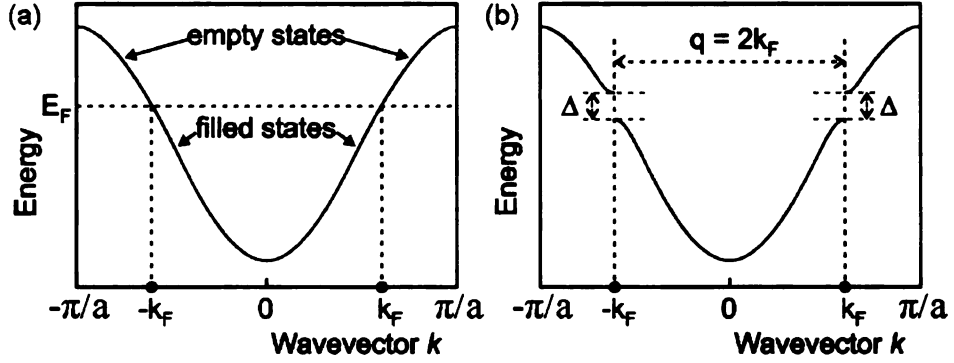


Figure 3.1: The conduction band of a one-one-dimensional crystal [42]. One-electron states with energy $E(\mathbf{k}) < E(\mathbf{k}_F)$ are filled, while states with $E(\mathbf{k}) > E(\mathbf{k}_F)$ are empty. (a) Periodic crystal with $\pm\pi/a$ describing the boundary of the first Brillouin zone. (b) 1D crystal with a PLD with period $\mathbf{q} = 2\mathbf{k}_F$, showing an energy gap, Δ , in the dispersion at $\mathbf{k} = \pm\mathbf{k}_F$.

one-electron states of the conduction band are occupied up to the Fermi level E_F , while states above the Fermi level are empty. In the presence of electron-phonon interaction, the metal becomes unstable. Peierls showed that it was energetically favorable to introduce a periodic deformation of the lattice, with the period λ related to the Fermi wavevector \mathbf{k}_F by $\lambda = \pi/\mathbf{k}_F$, corresponding to the wavevector \mathbf{q} which is twice the Fermi wavevector, $\mathbf{q} = 2\mathbf{k}_F$ [37]. The periodic lattice deformation (PLD) is responsible for opening up a gap at the Fermi level, as shown in Figure 3.1(b). The energies of the occupied states below the Fermi energy E_F are lowered, while the empty states are raised in energy. The gain in electron energy is proportional to $u^2 \ln(u)$ for small lattice distortions u , while the cost of strain energy is proportional to u^2 [41], thus explaining the stability of the deformed state.

As shown by Peierls [37], the CDW state is the preferred ground state in quasi-one-dimensional and quasi-two-dimensional metals at low temperature. This comes about as the cost in elastic energy to modulate the atomic lattice is smaller than the gain in conduction electron energy. At sufficiently high temperature the metallic state is stable, as the electronic energy gain competes with the thermal excitation of electrons across the gap. The second order phase transition that occurs between the

metallic and CDW state at T_{CDW} is known as Peierls transition.

3.2.2 Fermi surface nesting

The Peierls instability is induced by strong electron-phonon interaction, which can develop due to the characteristic topology of the Fermi surface. In quasi-two dimensional or quasi-one-dimensional free-electron-like metals the Fermi surface is cylindrical or planar, and large areas of the Fermi surface can be separated by the same wavevector. The CDW state becomes most favorable when there are large number of states connected by the same $2\mathbf{k}_F$ vector. Such a vector of constant momentum transfer connecting parallel segments of Fermi surface is called a nesting vector [27]; similarly, the overlap of parts of the Fermi surface as a result of a translation of parts of the surface by a nesting vector is called Fermi surface nesting. The more the Fermi surface is nested, the more stable the CDW state is. To better understand this concept, consider a system of electrons in a single one-dimensional chain of atoms at $T = 0$. The Fermi surface for such a system consists of two points $\mathbf{k} = -\mathbf{k}_F$ and $\mathbf{k} = +\mathbf{k}_F$, and involves two states each due to spin. These are the states that would lower their energy when the CDW gap opens. If we have a two-dimensional system of n non-interacting parallel chains in a plane, this system can be considered quasi-one-dimensional and its Fermi surface comprises of two sets of colinear points along two parallel lines perpendicular to the direction of chains, $2\mathbf{k}_F$ apart. In such a case we have $4n$ states subject to lowering their energy by the gap opening, for the same expense in the elastic energy, thus lowering the total energy of the system. Similarly, for a three-dimensional, periodic distribution of non-interacting chains, the Fermi surface is made of two flat parallel planes perpendicular to $(0, 0, \pm k_F)$, where the z -direction is the direction of the chains. In this case every point of the plane $(0, 0, -k_F)$ of the Fermi surface is connected with a point of the plane $(0, 0, k_F)$ by the vector $\mathbf{q} = (0, 0, q_z)$ with $q_z = 2k_F$, which is called perfect nesting. In such a case

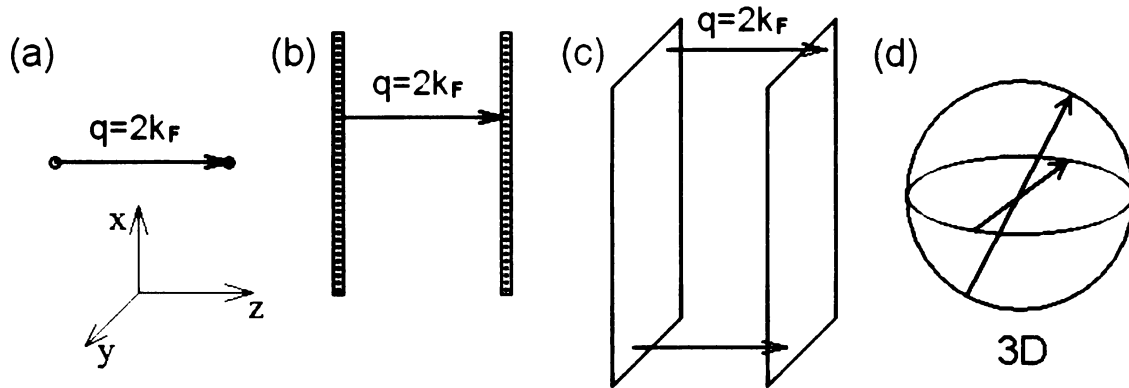


Figure 3.2: Fermi surface nesting in a free electron model. (a) In the case of a single 1D chain, the Fermi surface consists of two points. (b) In the 2D case of non-interacting parallel chains, the Fermi surface consists of two sets of colinear points along two parallel lines perpendicular to the direction of chains. (c) In 3D periodic distribution of non-interacting parallel chains, the Fermi surface consists of two planes perpendicular to the direction of the chains. (d) In 3D isotropic crystals, nesting is fulfilled for a single point on the spherical Fermi surface.

periodic lattice deformation with modulation wavevector \mathbf{q} will lower the energy of all one-electron states below the Fermi surface. Then the CDW state, characterized by \mathbf{q} , will have lower energy than the normal state. All three cases are illustrated in Figure 3.2 (a)-(c). On the other hand, in three-dimensional crystals, as shown in Figure 3.2(d), the nesting condition for each prospective vector \mathbf{q} can be fulfilled only for a single point on the Fermi surface, and the gain in electronic energy for the few states near this point is *insufficient* to overcome the elastic energy cost.

In real systems containing one-dimensional metallic chains, there are always weak interactions between them, and the electron bands have a small dispersion in the directions perpendicular to the chains. The characteristic one-dimensional dispersion still remains parallel to the direction of chains. Any given vector \mathbf{q} will then be a good nesting vector for only part of the Fermi surface. Only the nested fraction of the Fermi surface will become gapped, while the remaining part will keep the compound metallic [42].

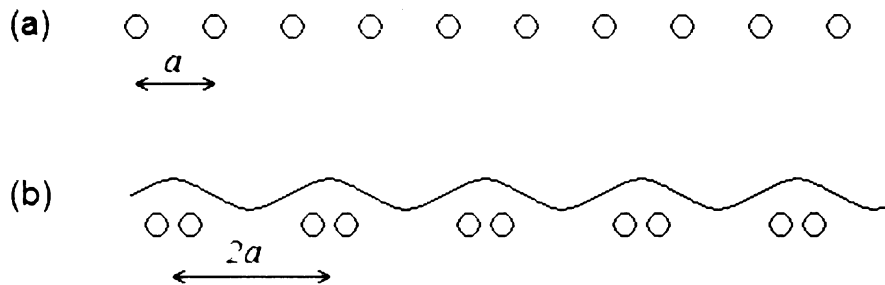


Figure 3.3: (a) For an undistorted one-dimensional metal with a half-filled band, the lattice is a periodic array of atoms with lattice constant a . (b) One-dimensional metal with a half-filled band, with introduced periodic lattice deformation and associated CDW with period $2a$.

3.3 CDW types

The character of a CDW depends on how its wavelength λ relates to the original lattice periodicity a , hence CDW is often characterized by the ratio λ/a . The CDW wavelength $\lambda = 2\pi/q_{CDW} = 2\pi/2\mathbf{k}_F = \pi/\mathbf{k}_F$ depends on the number of electrons in the conduction band: if there are more electrons, the value of \mathbf{k}_F increases and the CDW wavelength becomes smaller, and vice versa. For a crystal with a half-filled band, the CDW state corresponds to a periodic structure with a period that is twice as large as the periodicity of the crystal lattice, as seen in Figure 3.3. In general, however, the number of electrons in the conduction band is not related to the lattice periodicity, so the CDW wavelength could be any fraction of the lattice constant a .

When the ratio of the CDW wavelength λ and lattice constant a is an irrational number, the CDW state is said to be incommensurate. Then the CDW floats around and it is not affected by the lattice until pinned down by a defect; a defect acts like a pot-hole in which the CDW state gets stuck. On the other hand, when the ratio of the CDW wavelength λ and lattice constant a is a rational number, the CDW is commensurate with the lattice periodicity, and then it is hard to get it moving, as it is more likely to be pinned to the lattice. This is the reason why incommensurate CDWs show a variety of interesting physical properties.

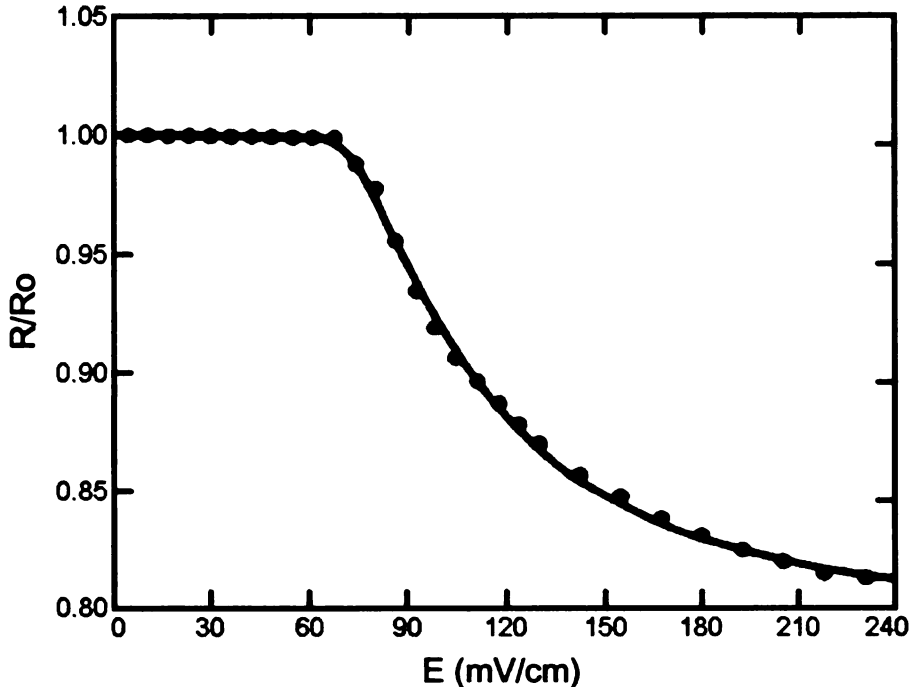


Figure 3.4: The normalized resistance $R/R_0 = (1/R_0)dV/dI$, versus applied external electric field, E , in NbSe_3 [17]. V represents voltage, I is current, and R_0 is the value of R at $V = 0$. For the low values of E the system obeys Ohm's law, $R/R_0 = 1$. Above certain threshold field ($E_0 = 117\text{mV/cm}$ in case of NbSe_3), the incommensurate CDW starts sliding, thus opening a second conduction channel, resulting in a decreased resistance $R/R_0 < 1$.

The single-particle energy diagram is suggestive of CDW conductors being semi-conductors: they have a band of filled states which is separated by an energy gap from a band of empty states. However, like superconductors, CDW conductors have a collective charge transport mode. When an external electric field is applied, the CDW can slide relative to the lattice. The lattice atoms oscillate back and forth, producing a traveling potential, and the conduction electrons move with this potential, producing a current. However, the CDW conductors are not superconductors, since various mechanisms damp the collective motion at nonzero temperature, leading to finite resistance. This is one of the most interesting properties of the incommensurate CDW: the nonlinear conductivity, as has been found in several CDW compounds [16]. For example, in NbSe_3 in the CDW state, non-linear electrical conductivity has been

observed by Fleming [17]. When an external electric field is applied, for low values of the electric field, NbSe₃ obeys Ohm's law, as seen in Figure 3.4. Typically the sliding will not begin until a depinning threshold field is exceeded where the wave can escape from a potential well caused by a defect. Once the threshold is reached, a new conduction channel occurs due to the sliding of the CDW that results in enhancement of the conductivity. Hence the resistance drops below that given by Ohm's law. This property can be utilized for potential applications, such as extremely sensitive detectors of electromagnetic radiation if the applied field is tuned to drive the CDW close to the depinned state, where small changes in electric field cause abrupt changes in material's conductivity.

3.4 Methods of detection of CDWs in materials

The charge density wave state in materials can be observed and studied using various experimental methods that are sensitive either to the charge distribution, or associated lattice deformation, or some other physical property that is affected by the presence of the CDW. Here I provide a brief overview of some selected techniques and means by which these are used to detect the CDW state in materials.

Angle resolved photoemission spectroscopy (ARPES) is a surface probe and is a commonly used method for studying the electronic structure of complex systems [43]. It represents the technique of choice in order to assess with high resolution the energy and momentum phase space of the electrons. It is based on the photoelectric effect, and involves measurements of the kinetic energy and angular distribution of the electrons photoemitted from a sample illuminated with high-energy photons. The ARPES technique allows for deduction of information on energy band dispersion and Fermi surface of materials. It has been successfully used to study and characterize the transition to a CDW state in materials, such as that in quasi-two-dimensional KMo₆O₁₇ [44], where partial CDW gap opening, as well as nesting of the Fermi

surface were observed. This study revealed that in this material below T_{CDW} the carriers are removed from the Fermi surface, and transferred to higher binding energy states (those that are below the gap) [44]. ARPES can be used to estimate the nesting vector $q_{CDW} = 2k_F$.

Scanning tunneling microscopy (STM) is a surface probe that provides information about local density of electronic states at the Fermi level [14, 45]. STM allows the mapping of regions of high and low electron density and hence the observation of the CDW on the surface of the material directly [46]. In the spectroscopic mode, the technique can measure the size of the CDW gap as it opens when the material undergoes the transition from its normal to the CDW state. STM has been widely used to characterize the CDW state of variety of materials, such as $K_{0.9}Mo_6O_{17}$, where spectroscopic measurements revealed a strong decrease of the density of electronic states near the Fermi energy, indicating suppression of a fraction of the material's Fermi surface at temperatures below T_{CDW} [47].

The CDW state can be detected through transport measurements, where transport properties exhibit anomalous behavior. For example, in one of the most thoroughly studied CDW materials, $NbSe_3$, two distinct CDWs occur, at two transition temperatures. Figure 3.5 shows dc resistivity of $NbSe_3$, as obtained by Ong and Monceau [48], where two anomalous bumps are observed indicating formation of two independent CDWs in this system at 144 K and 59 K. Similarly, in KMo_6O_{17} resistivity measurements show a metal-metal transition at around T_{CDW} , seen as a bump in the resistivity curve, which reflects Peierls transition to a CDW state. This is due to a change of mobility of the charge carriers and to a decrease in the density of states at Fermi level, as the CDW gap opens up [44].

Diffraction based methods, utilizing x-rays [49], neutrons [50], or electrons [51] as a probe, provide information about the positions of the atoms, and are not particularly sensitive to the details of the charge distribution. However, these methods provide

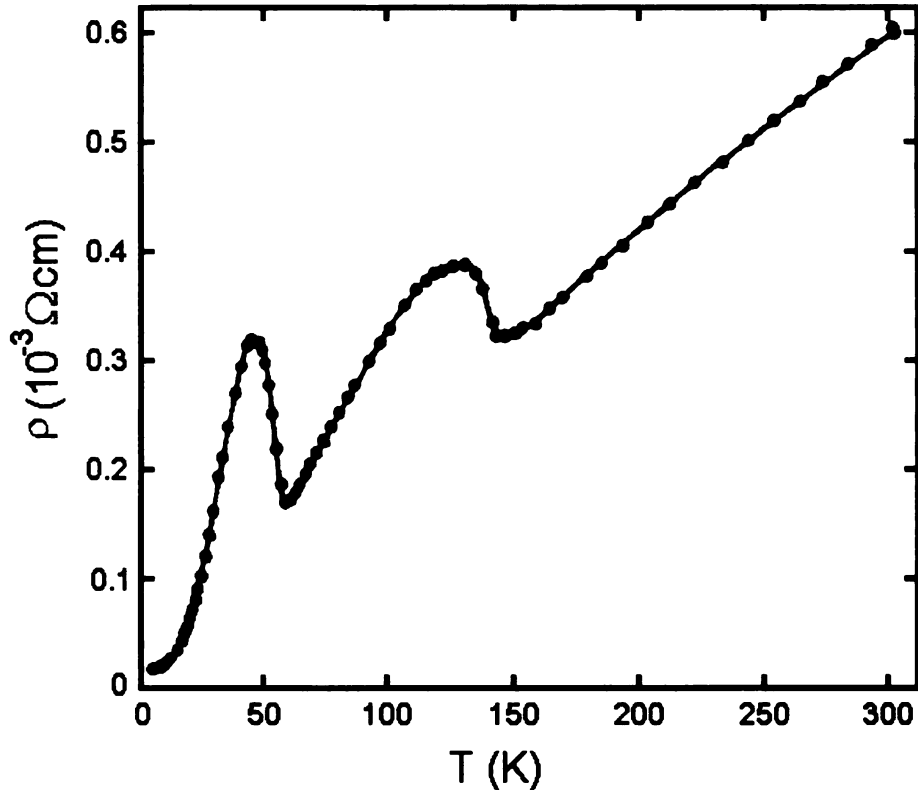


Figure 3.5: Anomalous transport properties of NbSe₃, as observed by Ong and Monceau [48]. Large increases of the dc resistivity appear at 144 K and 59 K, indicating the formation of two independent CDWs in this system.

valuable information related to the underlying periodic lattice deformation associated with the CDW. The periodicity \mathbf{q} of the periodic lattice deformation is responsible for the occurrence of additional Bragg reflections, known as superlattice reflections, in the diffraction patterns at satellite positions $\pm\mathbf{q}$ around each Bragg reflection of the underlying basic structure [42]. For example, single crystal electron and x-ray diffraction studies on KMo₆O₁₇ [52] demonstrated that periodic lattice distortions occur at low temperature and the diffraction patterns exhibit superlattice reflections below T_{CDW} .

The CDW state can also be studied using various spectroscopic methods, such as nuclear magnetic resonance (NMR) and Raman spectroscopy. Detailed account of these techniques is beyond the scope of this review. In a simplified view, the NMR

method utilizes a strong magnetic field to align the magnetic nuclei in the structure under study, splitting the energy levels of the magnetic nuclei. An energy-variable electromagnetic field is then applied to the sample. For characteristic values of this field, that match the energy splitting caused by the magnetic field, resonance occurs. The result of the experiment is an NMR signal as a function of frequency [53]. It provides detailed information on the topology, dynamics and three-dimensional structure of magnetic species, spin density (NMR) and charge density (NQR) distribution in materials. In NbSe_3 , the nature of CDW occurring at 144 K was studied using NMR spectroscopy [54]. This study revealed the nature of different Nb sites in this material in the normal state. Below T_{CDW} the NMR spectra gave line shapes that are broadened due to presence of a CDW, indicating that the CDW is incommensurate [54]. Raman spectroscopy provides information about vibrational, rotational, and other low-frequency phonon modes in solids [55]. It utilizes inelastic (or Raman) scattering of monochromatic laser light, typically in the visible, near infrared, or near ultraviolet range. The laser light interacts with phonons in the sample, which causes shifts in the energy (increase or decrease) of the laser photons. The shift in energy provides information about the phonon modes present in the system. Upon transition from normal to a CDW state in materials, changes occur in the spectrum indicating presence of the CDW state. For instance, in 1T-TaS_2 a CDW state is achieved at temperatures below 200 K. Hirata and Ohuchi studied Raman spectra from this material as a function of temperature between 48 K and 297 K using unpolarized laser light [56]. The study demonstrated that high-frequency modes in the spectra exhibit significant changes towards lower wavenumbers (and therefore lower energies) when T_{CDW} is approached on cooling.

3.5 Examples of CDW materials

Characterizing in detail the nature of the charge density wave state [57] as one of the possible broken symmetry and competing low-temperature ground states [58, 59] of low dimensional electronic systems is extremely important for understanding the physics of these materials [60]. It may also provide important insights into the nature of other competing states, such as high temperature superconductivity [28, 59, 61, 62]. Intensive research has been carried out on various layered systems, including $(\text{TaSe}_4)_2\text{I}$ [63, 64, 65, 66, 67], NbSe_3 [17, 68, 69, 70, 71], 1T-TaS_2 [72, 73, 74, 75, 76, 77], and 1T-TaSe_2 [78, 79, 80, 81] among many others. These systems, due to their low dimensionality, exhibit rich CDW behavior caused by the intrinsic electronic instability. For example, 2H-NbSe_2 exhibits an incommensurate CDW state below 33.5 K and remains in that state down to at least 5 K [78]. In 1T-TaSe_2 a commensurate CDW was observed, and is stable for a wide range of temperatures [82]. In 2H-TaSe_2 below 122 K an incommensurate CDW state was observed, and the CDW locks to a commensurate state at 90 K temperature [78]. Various CDW phases characterize 1T-TaS_2 over a wide temperature range [73, 83]. Above 543 K this material is in the normal phase [83]. It exhibits an incommensurate CDW for $353 \text{ K} < T < 543 \text{ K}$ [84, 85]. The nature of the CDW phase between $200 \text{ K} < T < 353 \text{ K}$ had been controversial for quite some time, and the suspected characters were nearly commensurate (NC) [86, 87] and domain-like discommensurate (DC) structures [73, 88]. In the NC state the CDW is characterized by uniform amplitude and phase, while the corresponding lattice distortion is rotated with respect to the atomic lattice by 12° . On the other hand, in the DC model hexagonal domain-like structure is proposed such that the CDW is commensurate within domains that are $\approx 67 \text{ \AA}$ in size, separated by domain walls in which the CDW amplitude decreases and the CDW phase changes. The STM study of Wu and co-workers demonstrated that the DC model is the right one for describing the CDW state of 1T-TaS_2 at room

temperature [73]. Below 200 K, 1T-TaS₂ is in a commensurate CDW state [75].

Chapter 4

Study of the charge density wave in CeTe_3

4.1 Introduction

Recently, the family of layered RETe_3 materials, where RE is a rare-earth element (RE = La, Ce, Pr, Nd, Sm, Gd, Tb, Dy, Ho, Er, Tm), has been recognized to belong to a class of two-dimensional CDW materials [89, 90, 91]. This class of materials exhibits two-dimensional square-net motifs composed of Te atoms in the structure. Such square-net arrangements have been considered theoretically (e.g. by Tremel and Hoffmann who performed electronic band structure calculations for such systems) [92] and were found to be unstable and prone to CDW formation. On the experimental side, results of transport measurements indicate that coupling between layers in RETe_3 is rather weak [93, 94]. Studies on different RE compounds revealed that for the electronic structure the rare earth is of minor importance [95]. This, in turn, suggests that the tellurium planes play a key role in determining the electronic properties of RETe_3 . In this system, a CDW forms in tellurium layers that contain a square net of Te-atoms. However, the exact nature of the CDW in the RETe_3 family has not been resolved to date, and there is still an ongoing debate regarding

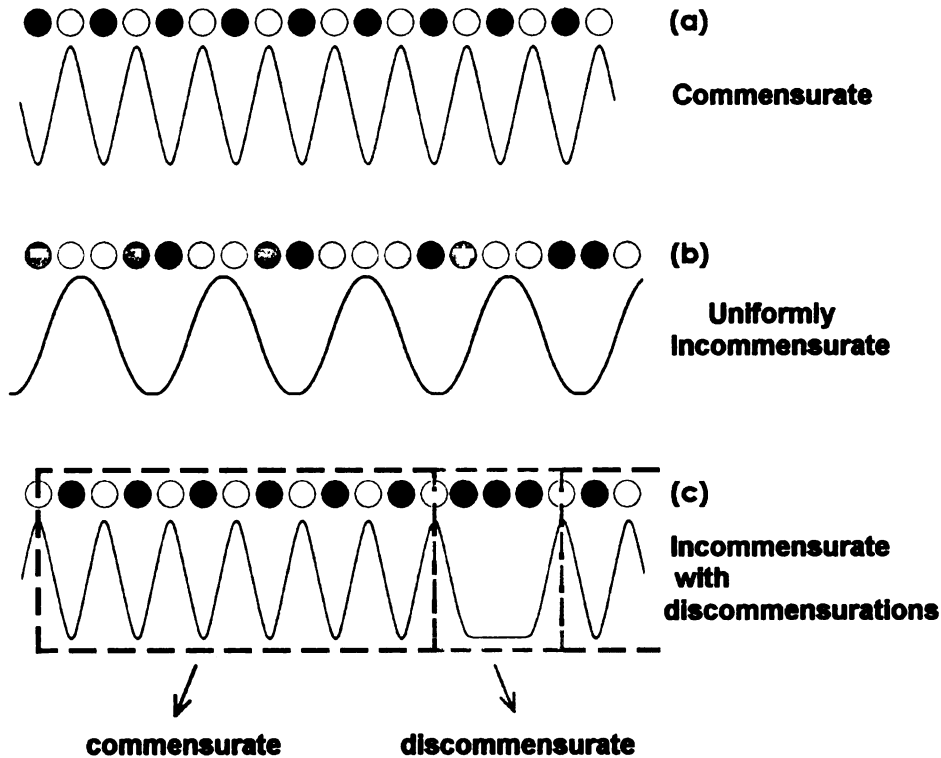


Figure 4.1: Schematic illustration of charge density waves along one-dimensional chains of atoms (circles and dots). The shading of each atom indicates its apparent magnitude with respect to an STM measurement, with white corresponding to a relatively high signal and black indicating a relatively low signal. Depending on the ratio of the CDW wavelength λ and atomic lattice a , the CDW can be (a) commensurate with λ/a rational, or (b) incommensurate with λ/a irrational. Part (c) shows the discommensurate case, for which an incommensurate CDW is locally commensurate - or locked in with the atomic lattice - with discommensurations (domain walls) preserving the average CDW wavelength.

whether the incommensurate CDW in RETe_3 is uniformly incommensurate or discommensurated as discussed below [96, 97]. Resolving this issue is of importance for better understanding of the physical properties, such as determining the strength of electron-lattice interaction.

In general, an incommensurate CDW state can take two forms depending on the nature of the CDW-lattice interaction. It could be uniformly incommensurate for which the CDW and the lattice modulations are simply superimposed. Alternatively, it is possible to achieve a state which is considerably more subtle, where the lattice

and the CDW become locally commensurate within domains and undergo phase slips at the domain walls. The phase slips are called discommensurations and their role is to preserve the average incommensurate periodicities, as shown schematically in Figure 4.1. Discommensurations have been found in a variety of complex systems such as ferroelectrics [98], semiconducting monolayer surfaces [99], graphite compounds [100] and CDW dichalcogenide compounds [101].

One of the goals of this study is to look for evidence of discommensurations in the systems of interest. In this work we used STM and STS methods to characterize the CDW state of CeTe_3 and closely related YTe_3 at 300 K and 77 K temperature, and to determine the value of the CDW energy gap. To the best of our knowledge, these measurements yielded the first atomically-resolved STM data on these materials.

4.2 CDW and structure of CeTe_3

4.2.1 Ideal crystallographic structure of CeTe_3

Crystallographic structure of CeTe_3 , shown in Figure 4.2, is of NdTe_3 [102, 103] type, weakly orthorhombic and described within the space group $Cmcm$. It is a layered structure that consists of two building blocks: double layers of $[\text{Te}]^-$ square-nets, and puckered ionic $[\text{Ce}_2^{3+}\text{Te}_2^{2-}]^{2+}$ double layers that are placed between the nets. Three-dimensional structure is composed of slabs of these structural motifs. The atoms within slabs are covalently bonded, while bonds between the slabs are weak van der Waals, allowing the crystals to cleave easily between the Te layers where the CDW forms, making them suitable for STM measurements. It should be noted that this structural view is an idealized representation, and is strictly speaking incorrect, as I further discuss.

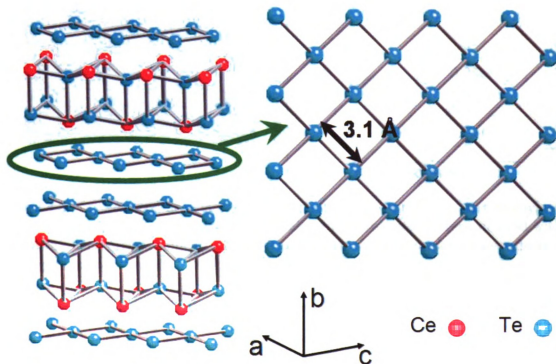


Figure 4.2: (This figure is presented in color.) The average crystal structure of CeTe_3 consisting of corrugated CeTe slabs, and Te layers, where Te atoms are separated by 3.1 \AA in a square-net. The figure is courtesy of H.J. Kim.

4.2.2 CDW detection and revised structure of CeTe_3

In the initial crystallographic structural interpretation perfect square nets of Te atoms separated by $\sim 3.1 \text{ \AA}$ were assumed. However, recent more careful studies involving electron diffraction, superstructure and super space group approaches revealed that this is only an average representation, and that the real structure is more complicated, containing distorted tellurium nets [90]. These experimental observations confirmed theoretical predictions of square net arrangements being unstable, and prone to CDW formation [92], as mentioned.

The existence of a unidirectional CDW in tritellurides was first detected in transmission electron microscopy study of series of RETe_3 by DiMasi and collaborators [89]. They identified superlattice reflections in the electron diffraction pattern corresponding to a single incommensurate modulation wave vector with a magnitude of q_{CDW}

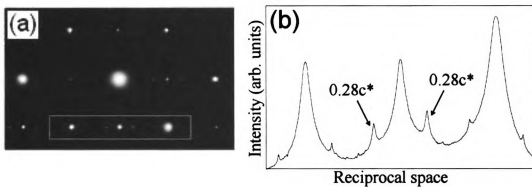


Figure 4.3: (a) Selected area electron diffraction pattern of CeTe_3 , and (b) selected intensity scan along the c^* direction of the electron diffraction pattern marked with a box in (a). The arrows indicate the positions of the observed superlattice reflections. The figure is courtesy of C. Malliakas [91].

$\approx 2/7 \times 2\pi/c$. This indicated the presence of incommensurate distortions in the Te layer planes. The incommensurate superstructure was solved within space group $Ama2$ for RE = Ce, Pr, and Nd by Malliakas and collaborators using single crystal x-ray diffraction [91]. Figure 4.3 shows the electron diffraction pattern of CeTe_3 featuring superlattice reflections. This study quantified distortions in the Te net, and revealed that a distribution of planar Te-Te distances exists, with a minimum value of $\sim 2.95 \text{ \AA}$ and a maximum value of $\sim 3.24 \text{ \AA}$.

This was further qualitatively confirmed by means of the atomic pair distribution function (PDF) method, based on a total scattering approach, which gives structural information in direct space. A small shoulder (Figure 4.4) at $\sim 2.9 \text{ \AA}$ is evident to the left of the principal PDF peak at around 3.1 \AA , which is due to the short Te-Te bonds.

Further detailed local atomic structural study of Kim and co-workers [96] on CeTe_3 utilizing the PDF method showed that local atomic distortions of the Te nets due to the CDW are larger than those observed crystallographically [91]. Distinct short (2.83 \AA) and long (3.36 \AA) Te-Te bonds are found to be present in the structure, consistent with bimodal bondlength distribution. The discrepancy between the local and crystallographic model has been interpreted in terms of the discommensurated

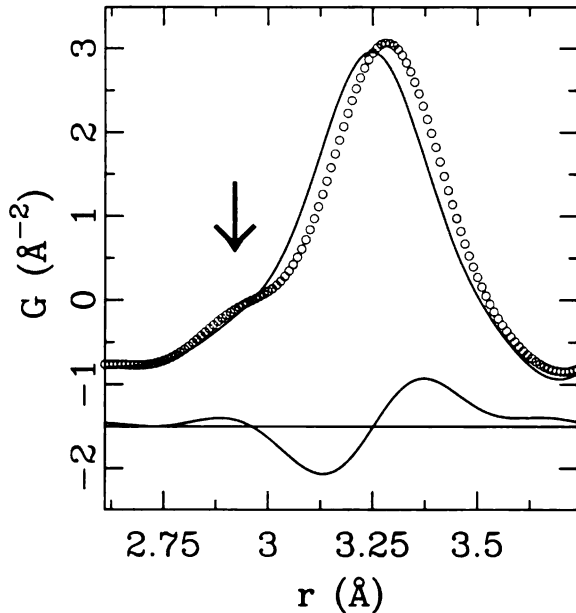


Figure 4.4: The experimental atomic PDF of CeTe_3 (symbols) up to 3.7 Å, featuring a shoulder that corresponds to ~ 2.9 Å Te-Te distance, indicated by the arrow. The solid line represents the $Cmcm$ model that assumes an undistorted Te net, and the difference curve is offset below. This model clearly does not explain the data. The data are courtesy of H.J. Kim [91].

nature of the CDW in CeTe_3 . While the PDF is sensitive to the local displacements within the commensurate regions, the crystallographic result provides the same information averaged over many discommensurated domains. The PDF study estimated the commensurate domain size to be about 27 Å [96].

4.3 Electronic properties of RETe_3

Due to the large lattice constant along the b-direction (~ 25 Å), as shown in Figure 4.2, the Brillouin zone of RETe_3 is squashed (plate-like) and slightly orthorhombic [104]. Strong anisotropy has been observed in their transport properties [89, 94]. For CeTe_3 this is shown in Figure 4.5, featuring low-temperature resistivity, as obtained by Ru and Fisher [94]. This reflects the nearly two-dimensional nature of the system originating from the weak hybridization between the Te layers and the RETe slabs. Electronic structure for tellurium planes is rather simple. The electronically

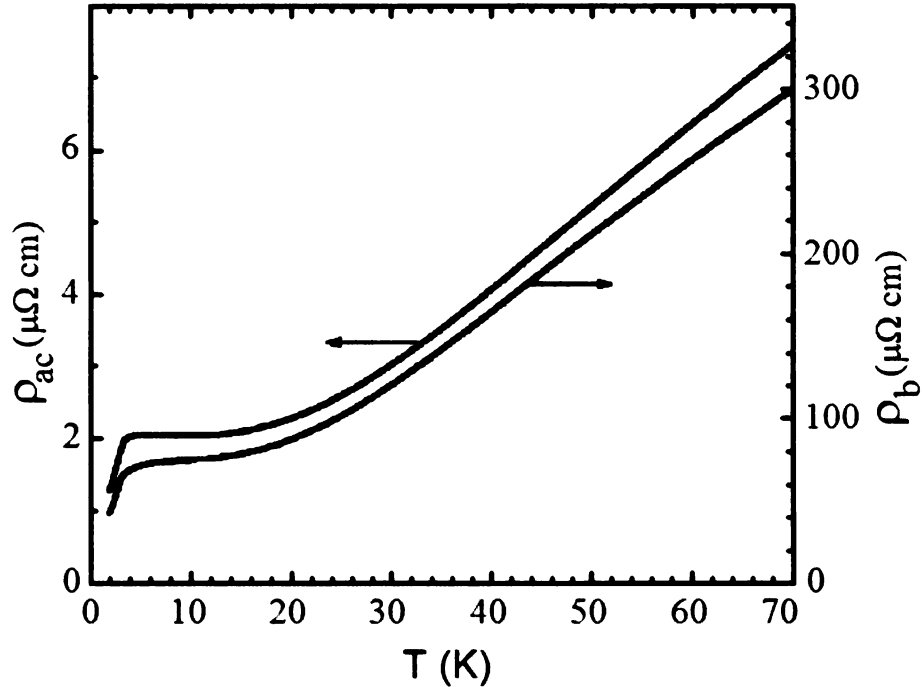


Figure 4.5: Low-T resistivity of CeTe_3 , as obtained by Ru and Fisher [94], for current flowing within Te layers and along the direction perpendicular to it. Arrows indicate corresponding ordinates. Note the degree of anisotropy: at ~ 45 K the in-plane resistivity is about 50 times smaller than that corresponding to the out-of-plane direction.

active valence band consists predominantly of $5p$ orbitals of the Te atoms from the Te planes. The only significant role is played by the perpendicular chains of in-plane $5p_x$ and $5p_y$ orbitals, since the energy of completely filled $5p_z$ is pushed below the Fermi level as indicated by the first principle band structure calculations [105, 106].

After it was first detected in RETe_3 from TEM studies [89], the CDW state was also observed in this family of materials by other experimental techniques. More recently observation of a CDW in CeTe_3 was made by ^{125}Te NMR studies on single-crystal sample [107]. The NMR spectrum showed three split lines, an indication of spatial modulations of the magnetic shifts and the electric field gradients at Te nuclear positions, consistent with the presence of an incommensurate CDW.

ARPES, which is the most direct technique to visualize the dispersion of the

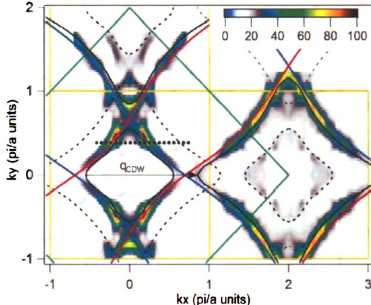


Figure 4.6: Contour plot in reciprocal space of ARPES spectral weight for CeTe_3 at 25 K, representing a Fermi energy intensity map, as obtained by Brouet and collaborators [95]. The arrow indicates characteristic nesting vector \mathbf{q}_{CDW} .

occupied bands, found a rather large CDW gap in the optimally nested regions of the Fermi surfaces of SmTe_3 ($\sim 280\text{meV}$) [108] and of CeTe_3 ($\sim 400\text{meV}$) [95, 104]. If these values are substituted in the mean-field calculations, transition temperatures to a CDW state are estimated to be around 1500-2000 K [109], values that are beyond the melting point of these materials. Large suppression of mean-field values is therefore expected and observed [109, 110]. In Figure 4.6 a Fermi energy intensity map of CeTe_3 at 25 K is shown [95], indicating that the CDW wave vector nests large portions of the Fermi surface. The Fermi surface is gapped, with the gap value as indicated. This strongly supports the idea that the CDW phenomenon is driven by Fermi surface nesting [108, 104, 95]. While optimally nested regions are gapped, the other sections of the Fermi surface with poorer nesting remain ungapped, which explains why the material shows metallic behavior in the CDW phase.

Accurate values of T_{CDW} are typically obtained from either detailed diffraction studies, where superlattice peak intensities corresponding to the CDW order are monitored in the diffraction patterns as a function of temperature, or from transport

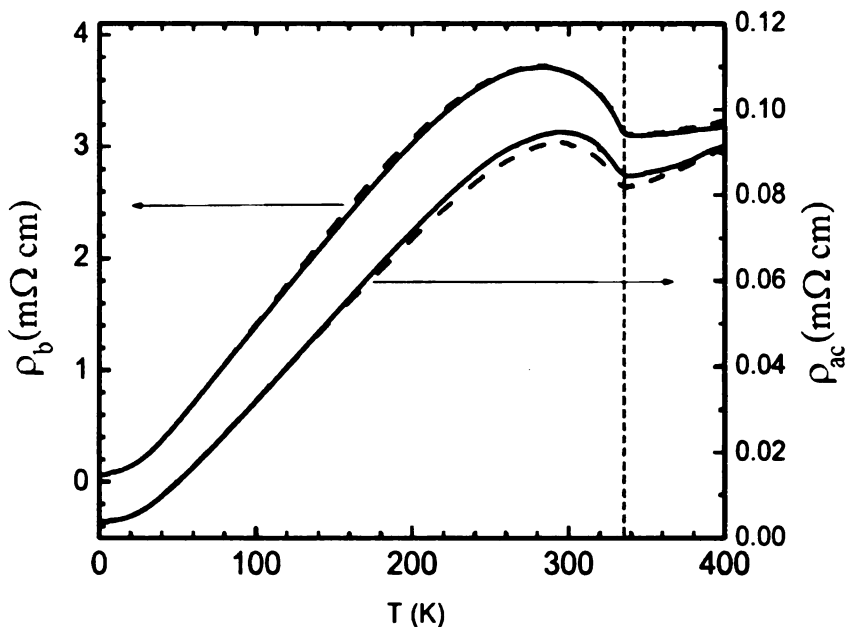


Figure 4.7: Temperature dependence of the anisotropic resistivity for TbTe₃, as measured by Ru and co-workers [110]. Arrows indicate corresponding ordinates for the in-plane and perpendicular directions. A characteristic change in resistivity is present around $T_{CDW} = 336$ K, as indicated by the vertical dashed line.

measurements where distinctive kinks are observed in the temperature-dependent data. For the RETe₃ family, T_{CDW} varies from about 240 K in TmTe₃ to values above 400 K in SmTe₃ and other members with lighter RE [110]. For CeTe₃ the transition temperature has not been determined to date, as transport measurements were carried out up to 400 K. Based on the mean-field predictions using measured values of the CDW band gap, that predicted T_{CDW} of 1600 K for TbTe₃ while the observed value was over 4 times smaller [109, 110], we can use the mean-field T_{CDW} value of over 2000 K for CeTe₃ and project the expected measured value to be above 500 K. Due to the lack of transport data for CeTe₃ that show the CDW transition, I show the temperature dependence of TbTe₃ resistivity, Figure 4.7, as obtained by Ru and collaborators [110]. Again we see highly anisotropic transport properties, as expected, and we also see a distinct change in resistivity at the transition temperature which is indicated by the vertical dashed line. Interestingly, the kink is present

RETe₃	$q_{CDW}/(2\pi/c)$ at 300K	CDW gap (meV)	T_{CDW} (K)
CeTe₃	0.2801	400	> 500
NdTe₃	0.2827	-	> 450
SmTe₃	0.2874	280	415
TbTe₃	0.2957	240	336
TmTe₃	N/O	-	240

Table 4.1: Characteristics of some of the rare-earth tritellurides. The table shows q_{CDW} component, approximate maximum size of the CDW gap, and the CDW transition temperature. q_{CDW} components were measured by C. Malliakas. CDW gap values are based on ARPES measurements [95, 108]. CDW transition temperature values are based on resistivity measurements [110].

in both in-plane and out-of-the-plane resistivity curves, suggesting that the coupling between the layers may be stronger than originally thought. Another possible explanation may be that the out-of-plane resistivity is highly correlated with the electronic state of the planes containing Te nets.

Several CDW-related properties of some of RETe₃ (RE = Ce, Nd, Sm, Tb, Tm) that are known at present are summarized in Table 4.1.

4.4 Sample synthesis and experimental details

Single crystals of CeTe₃ are prepared by a halide flux method. Stoichiometric amounts of cerium (~ 0.3 g) and tellurium (0.82 g) were loaded into quartz tubes under nitrogen together with a double amount (~ 2 g) of halide flux (0.42:0.58 molar mixtures of RbCl and LiCl). All manipulations were carried out under dry nitrogen atmosphere in a Vacuum Atmospheres Dri-Lab glovebox. The tubes were sealed under vacuum ($<10^{-4}$ torr) and heated to 650 °C over 12 hours and kept there for 6 days. The tubes were then cooled down to room temperature at a rate of 4 °C per minute. The halide flux was dissolved in water and the crystals were washed with acetone and dried under nitrogen environment. The morphology of the crystals is that of thin plates with a brown (copper-like) color. Electron microprobe energy dispersive spectroscopy (EDS)

was performed on several crystals of the compound and confirmed the 1:3 ratio of the cerium to tellurium and the absence of other elements of the flux. The compound is found to be x-ray pure and moisture sensitive after exposure to air for a few days. The single crystal samples were prepared and characterized by C. Malliakas. Other samples used in this study were prepared using similar synthesis routes.

STM experiments were performed on several single crystals of CeTe_3 . The crystals were carefully prepared by cleaving them with an adhesive tape so that the exposed layers were tightly packed without loose flakes. The cleaved crystals were about 2x2 mm in size, and with thickness of approximately 200 μm . The measurements were carried out at 300 K and 77 K in the constant current mode of STM and in the STS mode. Data were acquired with a bias voltage of 100 mV and with a tunneling current of 0.6 nA. The experimental data were analyzed in both direct and reciprocal space. Fourier transforms (FT) of the STM images were generated using commercially available image analysis and processing software for nano- and micro scale microscopy, "Scanning Probe Image Processor (SPIP)" [111].

In the experiments carried out in this study, slow drift effects tended to shift the apparent position of the atoms after several scans. Therefore, simple averaging of many scans did not always improve the signal to noise ratio in the data. With this in mind, we processed our data using the following approach: a set of multiple STM images were averaged together, after which the Fourier transform from the average was obtained. This procedure was then repeated several more times for the next sets of images. As phase information is not included in the FT image, we eliminated the drift effects that could otherwise obscure the results.

4.5 Results of STM measurements on CeTe_3

4.5.1 Room temperature data and the nature of the CDW

Initial STM experiments on the exposed Te net of a freshly cleaved single crystal of CeTe_3 were performed at 300 K. These measurements have successfully resolved the CDW. A real-space STM image, showing both the atoms of the Te net (dark yellow features) and the CDW modulations (bright yellow features) oriented at $\sim 45^\circ$ to the net, is shown in Figure 4.8. The areas of low intensity correspond to interatomic spacing. On the expanded image the network of Te distances is superimposed as a guide to the eyes. This image represents a first direct observation of CDW in CeTe_3 , and is a result of the average of eight images that were obtained consecutively at a scan range of 27 nm x 27 nm. This was the maximum scan range used that was still providing images with atomic resolution. Moreover, the images shown in Figure 4.8 were Fourier filtered to eliminate the angstrom-scale scatter artifacts and obtain a clearer image. This procedure was carried out by Fourier transforming the raw data to reciprocal space, eliminating the longest wave-vector component that corresponds to the shortest wavelength features in the real space, and then back Fourier transforming the data, resulting in the image shown in Figure 4.8. This filtering process is routinely performed on STM images spanning wide range that involve large numbers of atoms. I direct interested readers to inspect for comparison the 77 K data image (Figure 4.12) where this procedure was not carried out.

Results of the atomic PDF method based on x-ray experiments showed that there is a bimodal bond-length distribution in Te nets with distinct short and long Te-Te bonds in the structure, as detailed in Section 4.2.2 [96]. Such bimodal bond-length distribution indicates the commensurate CDW. In case of a uniformly incommensurate CDW, the Te-Te bondlength distribution is expected to be Gaussian, which was not observed experimentally in the local structure. Since it is known that CDW

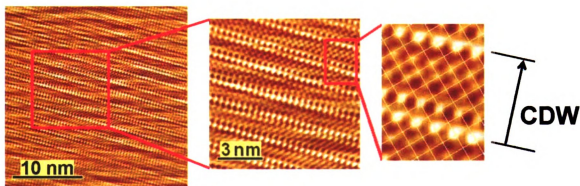


Figure 4.8: (This figure is presented in color.) A representative room temperature STM image of the Te net, showing both Te atoms and the CDW modulations oriented at 45° to the net. The image, obtained at a scan range of $27 \text{ nm} \times 27 \text{ nm}$, has been Fourier filtered. On the expanded image, the network of Te distances is superimposed. Lines indicate locations of high charge density due to the CDW, while the arrow marks the CDW direction.

modulation is incommensurate on average, this may indicate that the structure consists of commensurate domains separated by discommensurations. The PDF analysis involving variable r -ranges showed that as the distance range in the PDF refinements is increased, the bimodal distribution crosses over to the crystallographic distribution (Gaussian like) at around 27 \AA . This defines the characteristic lengthscale in this interpretation for commensurate domains as seen by the PDF method.

Since the STM is also a local probe, we sought an analysis method of STM data to address this important issue. It should be noted that the CDW displacements are typically rather small; the atomic displacements are about 5 % of the interatomic spacing, while the conduction electron density varies by several percent. While such small atomic displacements cannot be noticed from the STM image by naked eye, the density variations are easily observed in the real space. Further, analyses of the real-space STM images are inadequate to distinguish between locally commensurate states with discommensurations and uniformly incommensurate states [112]. Fortunately, it has been shown that one possible method for determining the nature of the CDW system from STM experiments is to examine the Fourier transform of

the STM images. As demonstrated by Thompson and coworkers, satellite peaks in the FT of the STM images observed in the vicinity of the principal CDW peaks, represent direct experimental evidence of discommensurations and domain structure in 1T-TaS₂ [113]. Moreover, from the Fourier transform of STM images, one can estimate the characteristic size of the domains through analysis of the wave vectors.

Here I provide a summary explaining the origin and significance of satellite peaks in the FT of STM data. In the case of 1D discommensurate CDWs, the wavefunction of the CDW can be written as the product of a uniformly incommensurate CDW and a modulation envelope [114],

$$\psi_{CDW}(x) = \psi_{IC}(x)M(x). \quad (4.1)$$

Function

$$\psi_{IC}(x) = \psi_0 \exp(ik_{IC}x) \quad (4.2)$$

is the wavefunction of the uniformly incommensurate CDW, where k_{IC} is the incommensurate wave vector and $M(x)$ is a modulation envelope. Assuming that the modulation envelope is periodic with periodicity $\lambda=2\pi/k_D$, we can express it as a Fourier series in the modulation wave vector k_D

$$M(x) = \sum_n f_n \exp(ink_D x). \quad (4.3)$$

The first two terms in modulation envelope are important since they are much larger than the higher-order terms. Thus equation

$$\psi_{CDW}(x) = f_0 \psi_{IC}(x) + f_1 \psi_{IC}(x) \exp(ik_D x) + \dots \quad (4.4)$$

has terms in the Fourier expansion at k_{IC} and at $k_{IC} \pm k_D$. The term at k_{IC} is the fundamental incommensurate CDW peak in FT, and terms at $k_{IC} \pm k_D$ are the satel-

lite peaks which are the signature of modulation due to the domain structure [113].

Hence the difference in wave vectors of the main peak and the corresponding satellite provides information about the domain size. We can understand this as a beating pattern of two waves with nearly the same wave vector. For example, closely spaced wave vectors k_1 and k_2 result in beats with wave vector $k = k_1 - k_2$. With respect to this discussion, the separation in k-space is k_D , which corresponds to a wavelength for the beating pattern of $\lambda=2\pi/k_D$. These ideas can be applied directly to STM data to characterize the nature of CDW and its relationship to the lattice.

The corresponding two-dimensional FT of the raw STM data collected at 300 K, is shown in Figure 4.9. This FT image represents information from a total of 24 STM images, and is obtained by averaging three FTs of the STM images that are themselves averages of eight scans. The unprocessed transform image shows enhanced noise along the vertical axis, which is an experimental artifact due to the scan direction, that was setting a color scale of the FT image in such a way that all the features of interest close to the origin were hard to see. To better see the peaks near the origin, we applied a line-by-line correction to remove this noise. This creates the dark line along the y axis, as seen in Figure 4.9. Horizontal and vertical axes are wave vector components k_x and k_y . The peaks are labeled for easier identification.

The square Te net gives rise to four distinct peaks (L). Peaks at 45° to the Te net are along the direction where we expect to see the CDW peaks. The direction of the CDW is indicated by the arrow. We now identify the peaks of interest for the analysis, where all labels refer to these in Figure 4.9. The fundamental CDW peak (nesting vector with magnitude $q_{CDW} \approx 2/7 \times 2\pi/c$) [89] and the first harmonic $\lambda/2$ are labeled 1 and 3, respectively. We think that peak 5 corresponds to the underlying Ce atoms, which form a square lattice below the surface oriented at 45° to the Te-net, i.e., along the CDW direction. Hence we conclude that, under the conditions of this measurement, the surface Te atoms and subsurface Ce atoms have comparable

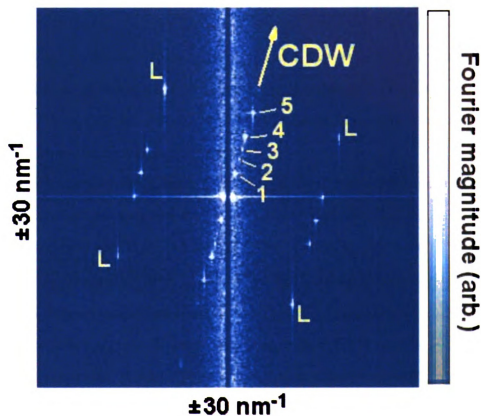


Figure 4.9: (This figure is presented in color.) The two-dimensional Fourier transform of the room temperature STM data. The unprocessed transform image shows enhanced noise along the vertical axis, an artifact due to the scan direction. To better resolve the peaks near the origin, we applied a line-by-line correction to remove this noise. This creates the dark line along the y axis. Horizontal and vertical axes are wave vector components k_x and k_y . The square Te net gives rise to four distinct peaks (L). Peaks related to the CDW are oriented at 45° to Te net peaks, as indicated by the arrow. The fundamental CDW peak and the first harmonic are labeled 1 and 3, respectively. Peaks 2 and 4 are in close proximity to peak 3, and peak 5 corresponds to the underlying structure.

tunneling matrix elements. It is likely that the Ce f-electrons hybridize with Te conduction states (with large amplitude at the surface) giving rise to a density of states enhancement near the Fermi level [115]. This is further supported by the results of a simulation of STM image shown in Figure 4.10. STM results were simulated using electronic structure calculations based on density functional theory [116, 117, 118, 119]. The image is obtained from calculations in a slab geometry by calculating the charge density in an energy range 0.05-0.1 eV at a plane 3 Å above the surface Te atoms. The simulation shows that the subsurface Ce atoms should contribute significantly to the surface tunneling signal.

Peak 4 is separated from peak 5 by the fundamental CDW wave vector, the magnitude of which corresponds to the position of peak 1. This indicates that the subsurface lattice is also distorted by the CDW. Following the work of Thomson *et al.* (Ref. [113]) a satellite peak needs to be identified in order to establish if the CDW is in a discommensurated state. The only peak along the CDW direction that remains unidentified is peak 2. Since this peak is in close proximity to peak 3, and based on the discussion given above, it could be interpreted as a satellite to peak 3. This is then supporting the idea that the CDW in the Te-net is discommensurated. The characteristic size of the commensurate domains, or the distance between discommensurations, can then be estimated from the differences in the wave vectors k_D , as described above. From the separation of peaks 2 and 3, we find a characteristic domain size of $\lambda=2\pi/k_D \approx 38(2)$ Å.

However, there are some concerns with this interpretation. In general, based on Eq. 4.4, one would expect peak 3, at around 7.5 nm^{-1} , to have *two* satellites at $k_{IC} \pm k_D$, the first satellite being peak 2 at 6.0 nm^{-1} . Indeed, our data show peak 4 in close proximity to peak 3, to the right of it, but this peak is *not* at the correct position in order to be considered as a second satellite to peak 3, equivalent to the satellite peak 2. This is shown explicitly in Figure 4.11. Figure 4.11(a) shows a line

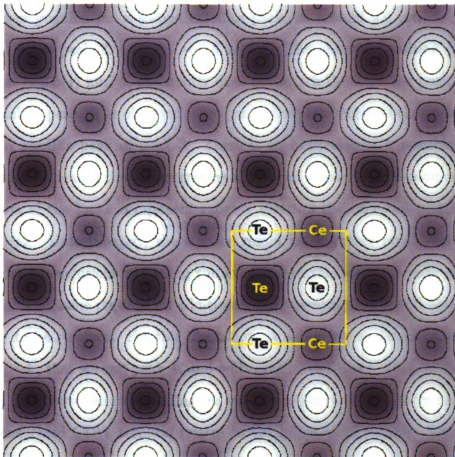


Figure 4.10: Simulated STM image of CeTe₃ from theoretical calculations. The image is simulated by calculating the charge density in the plane 3 Å above the surface Te layer, obtained for an energy range between 0.05 eV and 0.1 eV above the Fermi level. The first atomic layer below the surface Te layer is Ce layer. The color scale denotes charge density changes: light color denotes large charge density, while dark color denotes small charge density. The square marks one unit cell along the *a* and *c* directions, with a lattice parameter of 4.4 Å. Simulation courtesy of Z. Rak.

cut of the data from the Fourier transform Figure 4.9 taken along the direction of the CDW. The line cut starts from the origin, and goes through the peaks in the CDW direction. Figure 4.11(b) shows the same data on an expanded scale, focusing on peaks 2, 3, and 4, to better determine the peak positions. The red arrow indicates the expected position for a second satellite peak, at around 9.0 nm^{-1} , given our interpretation of peak 2, and $k_D = 1.5 \text{ nm}^{-1}$. The observed position of peak 4, however, at $\sim 9.5(1) \text{ nm}^{-1}$, apparently does not match the expected position of the second satellite peak. The observed discrepancy therefore suggests that peak 4 is *not* the second satellite peak of peak 3. There is an indication of a possible shoulder at low- k side of peak 4 that is suggesting that peak 4 may be two-component, and the position of the low- k component roughly matches the expected position of the satellite peak. Unfortunately, the k -space resolution is rather poor, and does not allow to draw conclusions regarding the existence of this shoulder peak with great confidence. This issue requires an additional measurement that would allow for this ambiguity to be resolved. For this discussion we are going to assume that there is only one peak, that we call peak 4, and will come to this again when 77 K data are discussed. Another concern regarding the interpretation of the results in terms of the discommensurated CDW scenario relates to the intensity of peak 4. The intensity of peak 4, if considered as a satellite peak to the CDW peak, is actually greater than the intensity of the CDW peak itself, while we expect satellite peaks to have always smaller intensity than the principal peak. In addition, it can be noted that the fundamental CDW peak is lacking its satellites, which were considered in the original work of Thomson and co-workers to estimate the commensurate domain size. This leads to a conclusion that our hypothesis about the nature of peak 2 should be re-examined.

Another possibility, within Thomson's interpretation, is to consider peak 2 as a satellite to the principal CDW peak 1. In such case, the second satellite of peak 1

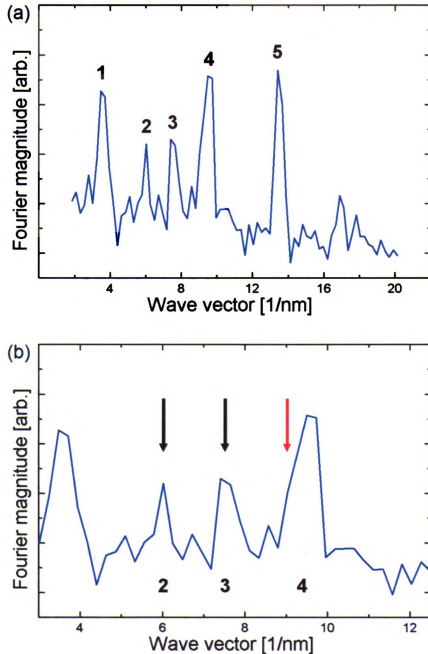


Figure 4.11: (This figure is presented in color.) Part (a) shows a line cut of the data from Figure 4.9 starting from the origin in the direction of the CDW. Part (b) shows the same data with an expanded scale. The red arrow indicates where we would expect to find a 2^{nd} satellite peak, given our interpretation of peak 2 (as a satellite peak).

would be positioned to its left, toward the origin in Figure 4.11. This is not observed due to enhanced noise near the origin. The satellite peaks of the first harmonic, peak 3, are in this view not observed as these would be sufficiently small and buried in the background. An estimate of commensurate domain size can then be made based on the difference between the positions in peaks 2 and 1, which is about $k_D = 2.5(2) \text{ nm}^{-1}$. This yields a characteristic domain size of $\lambda = 2\pi/k_D \approx 25(2) \text{ \AA}$. This is then much closer to the value obtained from PDF analysis than the estimate using peak 2 as a satellite to peak 3. However, this interpretation has no explanation for peak 4, which is one of the most prominent features.

4.5.2 Results of STM at 77 K

Here I present results of scanning tunneling microscopy measurements of the CeTe_3 surface obtained at 77 K temperature. Compared to the room temperature measurements [96] where, due to drift effects, data were noisier, measurements at 77 K provide data of better quality. The peaks in the Fourier transform of the real-space data obtained at 77 K are sharper allowing for the new analyses. A representative atomic resolution real-space STM image is shown in Figure 4.12. In some sections of the image the complete net of Te atoms is clearly visible, while in other sections only every other atom appears brighter. CDW modulation is oriented at 45° to the Te net, as in room temperature data.

Analysis of the Fourier transform of the real space data was performed in the same way as for the room temperature data. Figure 4.13 shows a Fourier transform of the 77 K temperature real-space data obtained at a scan range of 24 nm x 24 nm. The FT image contains information from a total of 16 STM images, by averaging four FTs of the STM images that are averages of four scans each. The Te square lattice peaks are labeled L. Peaks related to the CDW are oriented at 45° to the square lattice peaks. In order to resolve peak positions we again take a line cut along the CDW direction

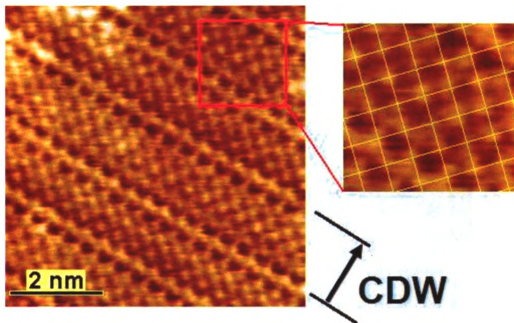


Figure 4.12: (This figure is presented in color.) A real-space STM image of the Te net obtained at 77 K, showing both Te atoms and CDW modulations oriented at 45° to the net. The image is the average of four images that were obtained consecutively at a scan range of 10.2 nm x 10.2 nm, with just a line-by-line correction. Here we show the biggest area without substantial contamination, although some contamination is present as seen in the upper left corner. The approximate size of the displayed area is 6.5 nm x 6.5 nm. Lines indicate locations of high charge density due to CDW, while the arrow marks the CDW direction.

in Figure 4.14. The CDW peak $q_{CDW} \approx 2/7 \times 2\pi/c$, where $c=\sqrt{2}a$ and a is the Te-Te separation of 3.1 Å, at around 3.9 nm^{-1} is the first prominent peak, as labeled. Peak q , at 14.3 nm^{-1} , corresponds to the underlying structure closest to the surface, in this case the Ce atoms, which form a square lattice below the surface oriented at 45° to the Te-net. Again, as in the room temperature case, four additional peaks can be clearly observed. The data are of better quality and less noisy than that obtained at room temperature.

The first observation we make is that the peak corresponding to peak 4 in the linecut along the CDW direction of the room temperature data (Figure 4.11) this time does *not* contain a shoulder at low- k side. This removes the ambiguity that was present in the room temperature data.

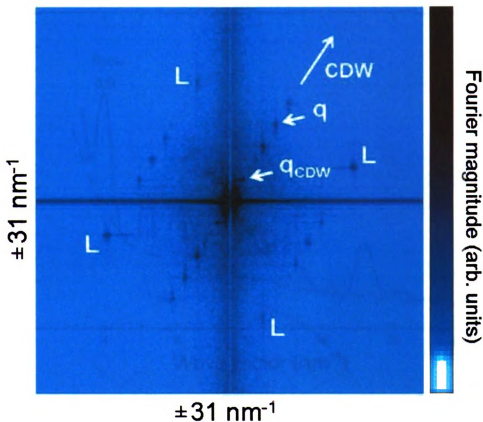


Figure 4.13: (This figure is presented in color.) The Fourier transform of the low temperature STM data. Enhanced noise along the vertical axis is an artifact due to the scan direction. Horizontal and vertical axes are wave vector components k_x and k_y . The square Te net gives rise to four distinct peaks (L). Peaks at 45° to Te net are consistent with the CDW peaks. The CDW peak q_{CDW} , as well as peak q related to underlying Ce atoms, are labeled.

4.5.3 Wave vector mixing

Observation of satellite peaks in the vicinity of the principal CDW peak in the FT of the STM data, as discussed earlier, would be evidence of a discommensurated CDW. However, it is hard to unambiguously establish if the extra peaks observed in the FT of the STM data are indeed satellite peaks. We shall, therefore, explore another origin of the peaks observed in the FT. In real-space images it is not uncommon to observe contributions to the STM signal due to the subsurface layer, and measurement conditions, such as the exact configuration of the STM tip can

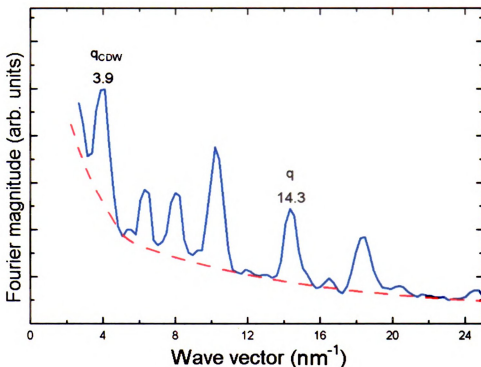


Figure 4.14: (This figure is presented in color.) Subset of the data from the Fourier transform along a path from the origin in the direction of the CDW. Noise in the Fourier transform becomes significantly larger near the origin. This is due to the impurities present in the real-space data. As the guide to the eye, the red dashed line indicates the background noise.

lead to non-sinusoidal atomic signals. In the case of a uniformly incommensurate CDW, ideally it is expected to give only two peaks in the FT of the STM data in the CDW direction, one corresponding to the incommensurate CDW, and the other due to the underlying lattice. In real space this corresponds to a superposition of two sinusoidal signals. However, if appreciable non-sinusoidal components are present, then the two waves may resemble a product, as illustrated in Figure 4.15. Algebraically, the product of two sine waves can be expressed as a sum and a difference: $\sin(A)\sin(B) = \frac{1}{2}\cos(A-B) - \frac{1}{2}\cos(A+B)$. This effect can lead to extra peaks in the Fourier transform. In order to demonstrate this, we carried out a series of simulations to mimic the effect of non-sinusoidal artifacts and explore the effect that this has on the FT of the real space image. We start from an undistorted superposition

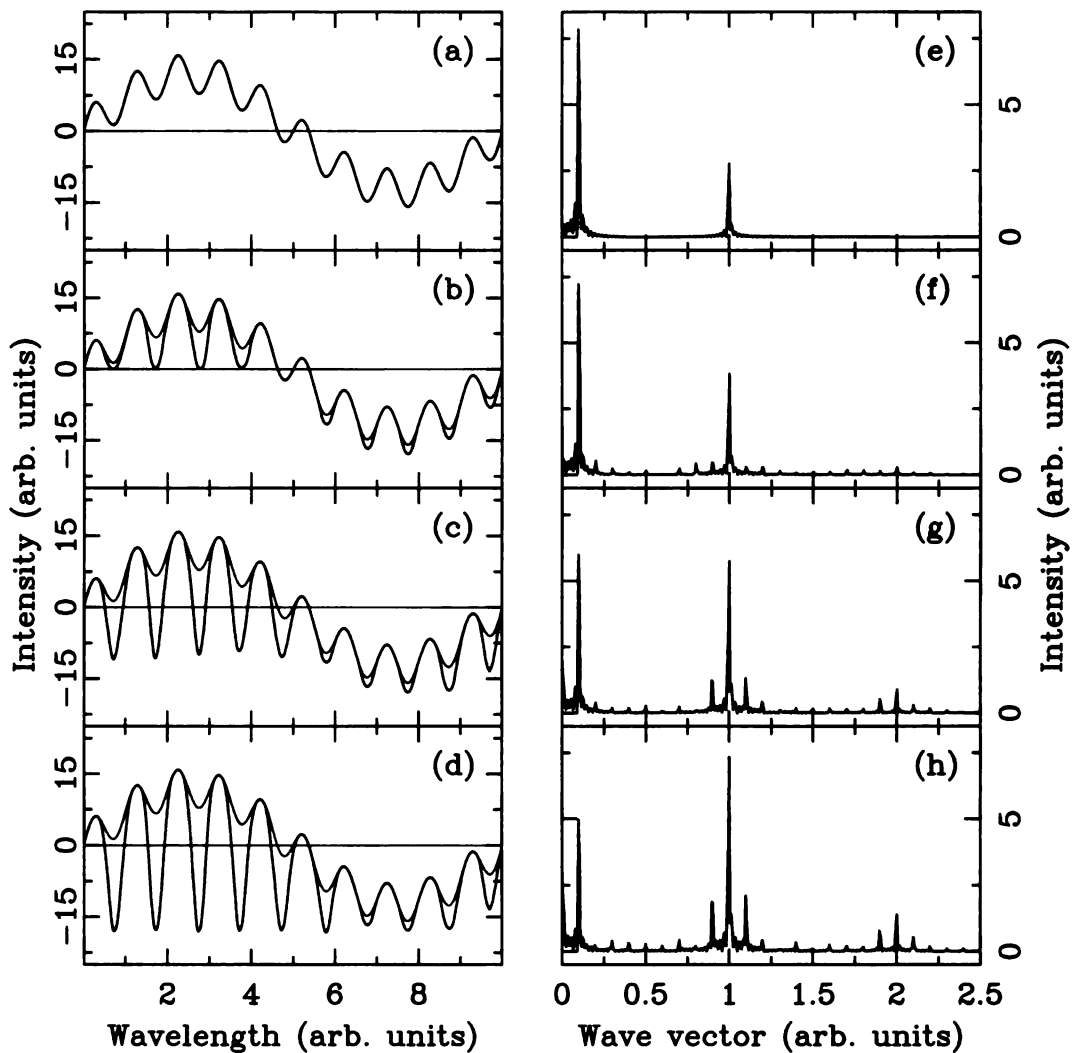


Figure 4.15: (a) Simulated one-dimensional STM signal representing the superposition of two sine waves: the short wavelength represents lattice effects, while the long wavelength represents CDW. The corresponding Fourier transform is shown in panel (e). Non-sinusoidal distortions to the simulated STM signal of various magnitudes were considered in (b)-(d), with the original signal shown as a gray curve for comparison. The corresponding Fourier transforms are given in panels (f)-(h). Additional peaks appear at special positions in the Fourier transform as the distortion is introduced. See text for details.

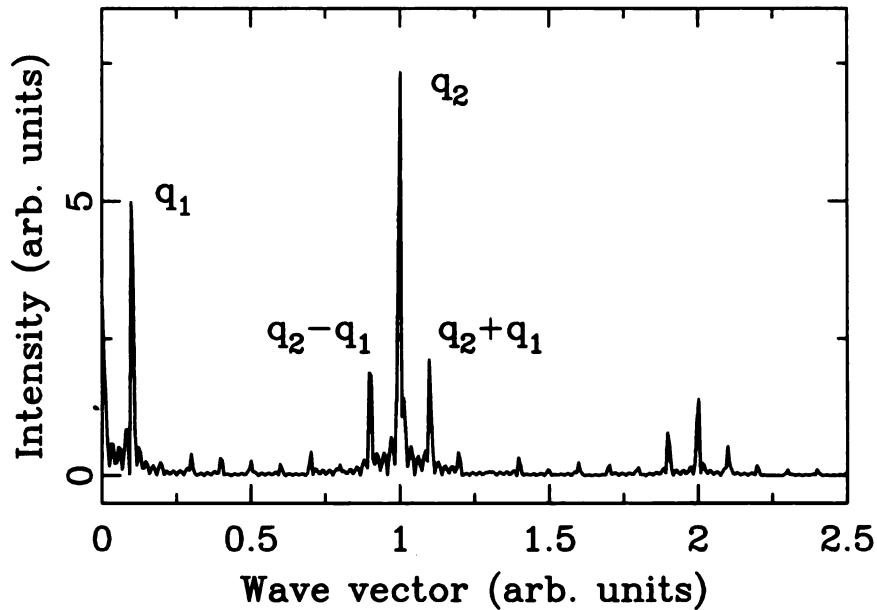


Figure 4.16: Fourier transform of the distorted signal from Figure 4.15(h). While in the Fourier transform of undistorted signal only peaks labeled with q_1 and q_2 appear, as they correspond to the two superposed waves in the direct space, additional peaks are observed in the case when distortions are present. These additional peaks occur at $q_2 - q_1$, $q_2 + q_1$, $2q_2$, $2q_2 - q_1$, $2q_2 + q_1$, and other linear combinations.

of two sinusoidal signals, one with large and another with small wavelength, λ_1 and λ_2 , respectively, representing the CDW and the underlying lattice, Figure 4.15(a). The Fourier transform of this superposition consists of two peaks at positions $q_1 = 2\pi/\lambda_1$ and $q_2 = 2\pi/\lambda_2$, as shown in Figure 4.15(e), that represent the two Fourier components in this Fourier decomposition. A series of distortions with various magnitudes is then introduced to the superposition, to observe their effect on the Fourier transform. These distorted signals are shown in Figure 4.15(b)-(d), with the undistorted signal superimposed for comparison (gray curve). The corresponding Fourier transforms, shown in Figure 4.15(f)-(h), contain additional peaks that appear at special positions, and which originate from the distortions that are introduced to the original signal. These additional peaks, reproduced for clarity in Figure 4.16, occur at positions corresponding to various linear combinations of q_1 and q_2 , such as $q_2 - q_1$ and $q_2 + q_1$, where q_1 and q_2 are the Fourier components of the original undistorted

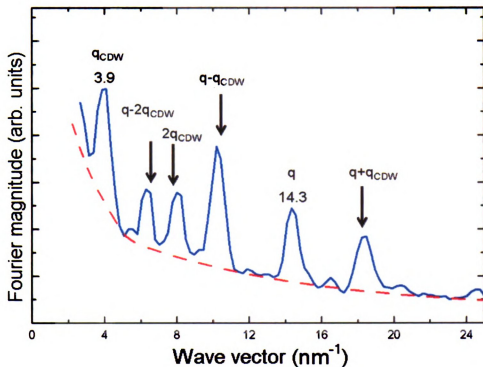


Figure 4.17: (This figure is presented in color.) Subset of the data from Fourier transform along path from the origin in the direction of the CDW. Noise in the Fourier transform becomes significantly larger near the origin. This is due to the impurities present in the real-space data. As the guide to the eye, the red dashed line indicates the background noise.

signal.

Having this in mind, the interpretation of additional peaks in the FT of our STM data on CeTe₃, shown in Figure 4.14, can then be given as follows. In the case of ideal STM measurements and a uniformly incommensurate CDW we expect to observe only peaks at q and at q_{CDW} along the CDW direction, coming from the periodicity of underlying structure below the surface and from the CDW periodicity, respectively. Due to the distortion effects in the STM measurements, wave vector mixing is present and the additional peaks occur, as shown in Figure 4.17. They are a linear combination of the CDW wave vector q_{CDW} , and the wave vector q . In the figure, the peaks are labeled in the increasing order as follows: $q-2q_{CDW}$, $2q_{CDW}$, $q-q_{CDW}$, $q+q_{CDW}$. This analysis is similar to analysis given by Fang *et al.* to

explain the FT of the STM data of TbTe₃ [97]. An important difference between the analysis of Fang and the one presented in this work is that we identify the first peak as the CDW wave vector, whereas Fang and co-workers use equivalent wave vector corresponding to $q_{CDW} \approx 5/7 \times 2\pi/c$. As a result, subsequent structure in our case can be explained well without invoking unresolved wave vectors, while Fang *et al.* invoked wave vector $2q$ corresponding to a wavelength which is even shorter than the lattice spacing. In this view, the STM data of CeTe₃ can be seen as consistent with a uniformly incommensurate CDW.

4.6 Scanning tunneling spectroscopy of CeTe₃

Formation of the CDW state in a material, as described in section 3.2.1, is associated with an energy gap opening up at the Fermi level. Using the point spectroscopy mode we can probe the CDW gap at different locations of the sample surface and estimate its size. STS measurements on CeTe₃ were performed at a temperature of 77 K at various locations of the tip above the surface of the exposed Te plane. Sweeping the bias voltage V in ranges of ± 300 mV and ± 400 mV, we have measured the tunneling current I as a function of the voltage. Differentiation of $I(V)$ data with respect to V gives the local density of states (DOS), as has been explained in the Scanning Tunneling Spectroscopy Section 2.2.2. The determination of the gap size from STS measurements is often hard due to the presence of the subgap states. In this work, under such circumstances, the gap has been determined by linear extrapolation of the STS signal before it changes slope due to the subgap states. The assigned size of the gap is then the approximate value obtained between the two intercepts of extrapolated lines with the zero dI/dV base line.

Curves of different shapes are obtained for the local density of states in spectroscopic measurements at different positions of the Te plane, indicating the local nature of the measurement. Here I show representative spectra of two kinds, one obtained

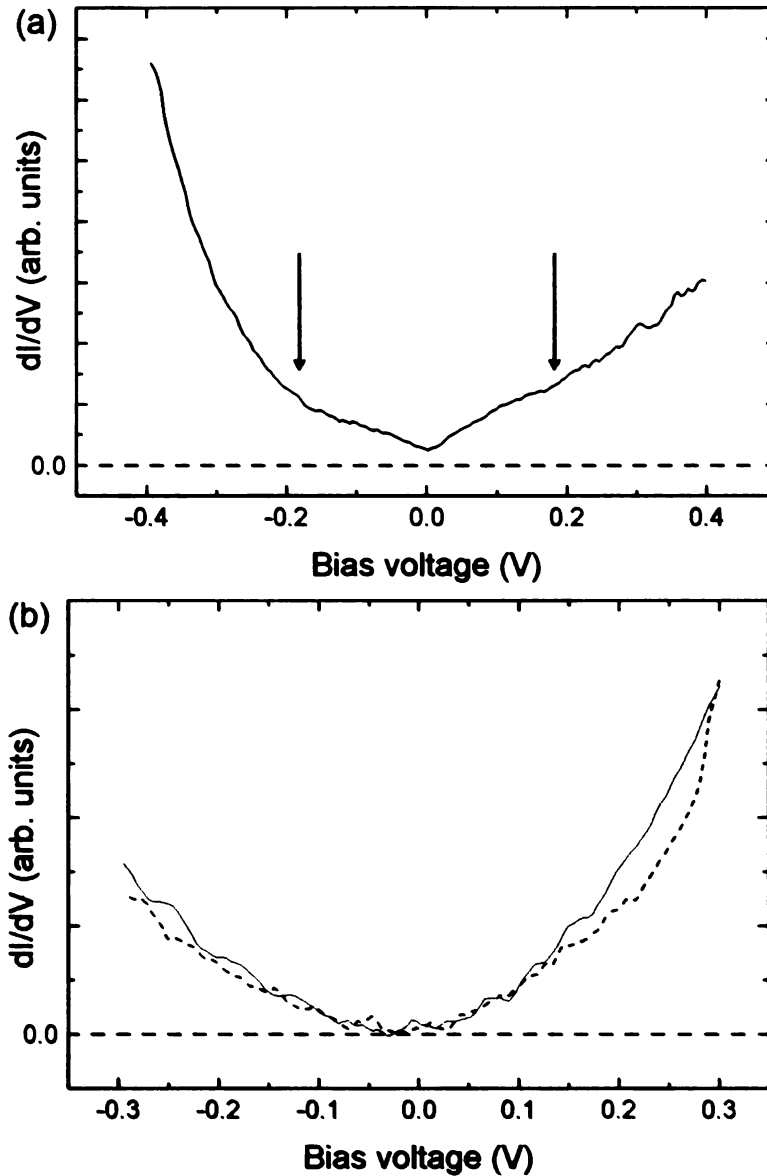


Figure 4.18: Local DOS around the Fermi level for CeTe₃. The Fermi level corresponds to zero bias voltage. The estimated CDW gap size in CeTe₃ is about 360 meV, as indicated by vertical arrows. The spectroscopy was carried out when the tip was located directly above a Te atom (a), and when the tip position was above the center of a Te plaquette (b). In the later case the data were collected above two adjacent plaquettes, shown as two curves, one above Ce and another above Te subsurface atoms. See text for details.

with the tip positioned directly above a Te atom, and another with the tip position between Te atoms, in the center of the plaquette consisting of four Te atoms. Figure 4.18(a) shows the characteristic density of states as obtained when the tip is at the top of a Te atom. The data represent an average of 168 measurements performed over the same spot consecutively. The Fermi level corresponds to zero bias voltage. From these data the value of the CDW gap is estimated to be 360 meV, in good agreement with the ARPES results [95]. The effect of thermal smearing of the data is approximately $3.5 k_B T \approx 25$ meV at 77 K temperature. The local density of states has a shape that is suggestive of subgap states. This is characterized by an enhanced density of states when going towards the edges of both conduction and valence bands. There is noticeable asymmetry in the density of states in the conduction band (right from the Fermi level) and valence band (left from the Fermi level), with steeper rise in the valence band. The characteristic spectra obtained for the tip above the center of the Te plaquette is shown in Figure 4.18(b), for two adjacent plaquettes, one centered above Te subsurface atom, and another centered above Ce subsurface atom, therefore sampling different subsurface atoms. The data are averages of 69 and 15 measurements respectively, performed over the same spots consecutively. In this case, there is opposite asymmetry in the density of states in the conduction and valence bands, with a steeper rise in conduction band. We speculate that the solid line data in Figure 4.18(b) correspond to the STS measurement carried out over a plaquette centered above a Ce atom, where 4*f* states of Ce atom contribute to the density of states in the conduction band, giving rise to an apparent increase of DOS in that region. If this is the case, then the dashed line data correspond to the case of a plaquette centered above a Te atom.

It is expected that the tip location will affect the outcome of the measurement simply because areas with different spatial distribution of electronic density are probed for these different tip positions. However, the exact reason for the change of the shape

of the density of states is still not fully understood. Our STS measurements suggest that there are contributions to the observed DOS that originate from one layer below the probed Te layer, most probably when the subsurface atom is Ce. However, more work is required to better understand, both qualitatively and quantitatively, the exact origin of the observed effects. Theoretical calculations exploring the local electronic band structure of CeTe₃ are being conducted in collaboration with Z. Rak and Dr. Mahanti to better understand this system [116]. By comparing our measurements to these calculations, we hope to get a complete picture of the local electronic structure.

4.7 STM and STS measurements on other RETe₃

We have attempted measurements on two other members of the RETe₃ family of materials, particularly YTe₃ and GdTe₃. Here I provide a brief summary of these attempts. Measurements on both materials were done at room temperature. Experiments on GdTe₃ were not successful, as we were not able to obtain the STM data with atomic resolution.

Measurements on YTe₃ were done in STM and STS modes, and the results are as follows. The STM measurements were of sufficiently good quality to allow for the atoms in the Te plane to be seen, but unfortunately the CDW was barely observed. We believe these problems originate from a slightly more chemically reactive surface.

Figure 4.19(a) shows one of the STM data sets obtained at the scan range of 5.2 nm × 5.1 nm, with bias voltage of 100 mV and tunneling current of 0.6 nA. Streaky features that are originating from the noise in the data are clearly visible, particularly at the top of the scan. For comparison I refer to Figure 4.8 and Figure 4.12, STM images of CeTe₃, that are of much better quality.

Figure 4.19(b) shows the Fourier transform of the STM data obtained at 8.4 nm × 8.1 nm, with bias voltage of 100 mV and tunneling current of 0.6 nA. Due to the bad

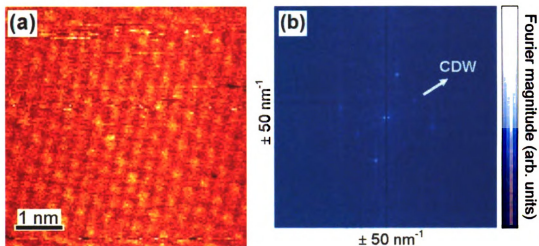


Figure 4.19: (This figure is presented in color.) (a) STM real-space image and (b) Fourier transform of YTe_3 . STM data are obtained at the scan range of $5.2 \text{ nm} \times 5.1 \text{ nm}$, with bias voltage of 100 mV and tunneling current of 0.6 nA . The Fourier transform shown is that of the STM data with scan range $8.4 \text{ nm} \times 8.1 \text{ nm}$, obtained at bias voltage of 100 mV and tunneling current of 0.6 nA . These data are of poor quality, hence no conclusions related to the CDWs could be made.

quality of the STM data, the peaks in the CDW direction in the Fourier transform, which are of our interest, are insufficiently resolved and cannot be analyzed. For comparison, better quality Fourier transforms were obtained for CeTe_3 , as shown earlier in Figure 4.9 and Figure 4.13. The results of the STM measurements of YTe_3 at room temperature are consistent with the presence of CDW in the system, as CDW-like features are observed in the scans. However, due to poor data quality no further conclusions could be drawn.

Spectroscopic test measurements of the CDW gap in YTe_3 were also carried out at room temperature. These measurements were partially successful, but the measurements were again prone to noise. In Figure 4.20 a representative local density of states curve obtained from these measurements is shown. Local DOS around the Fermi level clearly shows a CDW gap. A very rough estimate of the size of the gap yields value of about 320 meV , as indicated by the dashed lines in Figure 4.20. As described in Section 2.2.2, the measurements of local density of states at room tem-

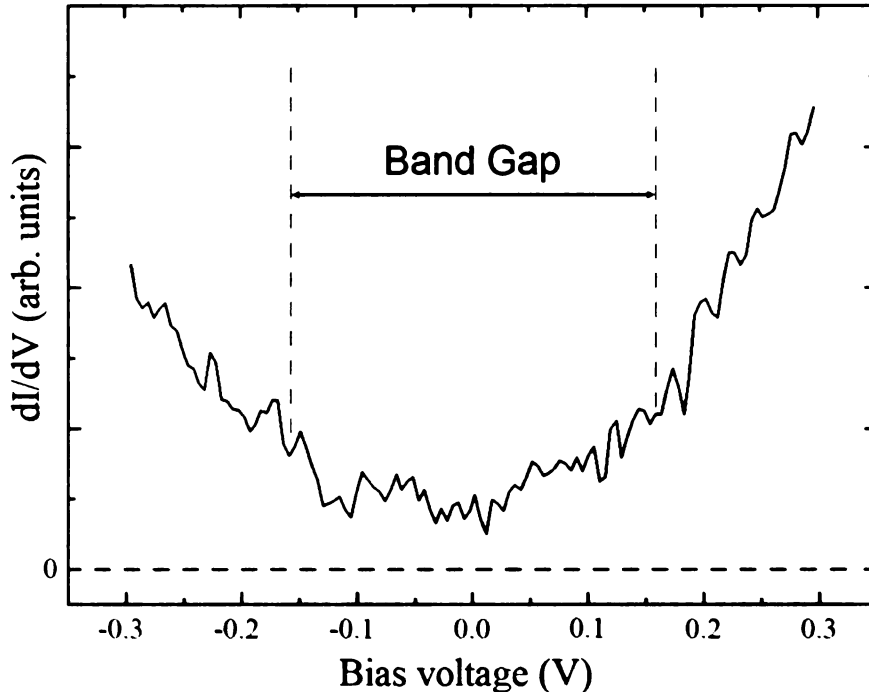


Figure 4.20: Local DOS around Fermi level for YTe_3 . dI/dV curve was obtained from I vs. V data measured by sweeping the bias voltage in range $\pm 300\text{mV}$. The data is very noisy, but it gives hints on the size of CDW gap. Dashed vertical lines are guides for the eyes. Our estimate for the CDW gap size in YTe_3 is about 320 meV .

perature are smeared out, an effect estimated to be approximately 90 meV , which represents an additional uncertainty of the gap size. To the best of our knowledge, one other measurement of the CDW gap size of YTe_3 has recently been performed by Brouet and collaborators using ARPES, that gave the gap size of 335 meV [120].

4.8 Summary

STM and STS measurements of the CeTe_3 at room temperature and 77 K and YTe_3 at room temperature were performed. The one-dimensional CDWs are observed on the surfaces of CeTe_3 and YTe_3 . In the Fourier transform analysis of the STM images of CeTe_3 , we observed a peak at $q_{CDW} \approx 2/7 \times 2\pi/c$, as well as several additional peaks. We explored several possible interpretations concerning these peaks,

in an attempt to characterize the nature of the CDW in CeTe_3 . Our FT analysis cannot unambiguously differentiate between the discommensurated and uniformly incommensurate CDW. The principal reason for this is lack of a reliable criterion that would allow us to distinguish whether these extra peaks are satellite peaks to the CDW peak, which would suggest the discommensurated nature of the CDW, or the peaks originate from the artifacts of STM measurement. In the interpretation that supports discommensurated picture we obtained the commensurate domain size that agrees reasonably well with the estimate made by the atomic PDF study [96]. However, we believe the extra peaks in our FT data can be better explained within a wave vector mixing picture, that does not invoke discommensurations.

There are two possibilities for reconciliation of PDF and STM observations. As I have shown, subsurface effects affect STM signal which gives extra peaks in FT. First, the intensity of the satellite peaks is possibly weak compared to these extra peaks. A hint that this could be a case is found in the case of FT of 77 K data (Figure 4.14, small peak at position $\sim 5.5 \text{ nm}^{-1}$). Second, the domain size obtained from the PDF study is possibly underestimated. Larger domain size would result in satellite peaks closer to the fundamental peaks in FT, and would not be resolved in our STM data.

We also measured the local density of states using the STS mode at 77 K, and obtained the CDW gap at various places on the surface of the sample. The gap size obtained in measurements directly above the Te atoms is $\sim 360 \text{ meV}$, in good agreement with the ARPES result [95]. The data obtained from measurements on YTe_3 were not of sufficient quality to perform the FT analysis. The CDW gap in YTe_3 obtained from room temperature STS was estimated to be roughly 320 meV.

Chapter 5

Characterizing electronic structure of β -K₂Bi₈Se₁₃ thermoelectric using STS

5.1 Introduction

One of the technologically important and scientifically challenging subjects of contemporary condensed matter physics is the field of thermoelectricity. Thermoelectricity is a phenomenon that involves induction of electric potential across a system whose ends are exposed to a temperature gradient, and conversely, generation of a temperature gradient in a sample across to which an electric voltage is applied [121, 18, 122, 123]. Good thermoelectric materials should have their thermal conductivity minimized, and at the same time should have their electric carrier transport maximized [19], as discussed below. It has been a challenge in the past few decades to search for and engineer new thermoelectric materials suitable for commercial applications. In the mid 1950's it was recognized that semiconductors can be superior thermoelectric materials over metals [124, 122]. This comes about due to the fact that in metals the ratio of thermal to electrical conductivity is proportional to temperature (Wiedemann-Franz

law). In contrast, semiconductors can have a higher ratio of electrical to thermal conductivity, and can also be doped to allow for this ratio to be tuned to optimize thermoelectricity. More recently, it has also been recognized that structural disorder plays an important role in promising bulk thermoelectric materials. An important part of the process of optimization is proper characterization of the properties of these materials, including the assessment of precise information regarding their electronic structure. Here I present results of STS characterization of one such promising material, $\text{K}_2\text{Bi}_8\text{Se}_{13}$.

5.2 Fundamentals of thermoelectrics

5.2.1 Historic highlights

Thermoelectricity has its foundations in three mutually related phenomena, namely the Seebeck, Peltier, and Thomson effects. Thomas Johann Seebeck in 1821 first discovered the thermoelectric phenomenon, when he noticed that a temperature gradient placed across a metal sample caused a potential difference (thermoelectric electromotive force) across the sample. If two opposite ends of such a sample are placed in contact with high and low temperature surfaces respectively, then the charge carriers in the conductor move in the direction from the hot end towards the cold end. This current will flow until a voltage builds up at the metal ends to cancel the thermoelectric voltage. The same effect is observed in a closed loop, called a thermocouple, formed of two metals or semiconductors, if their junctions are exposed to different temperatures. This effect is described mathematically as

$$E = \frac{dV}{dr} = S \frac{dT}{dr} = S \nabla T, \quad (5.1)$$

where T is temperature, V is the thermoelectric voltage, E is the resultant electric field, which is proportional to the temperature gradient along direction r , and S is the Seebeck coefficient or the thermopower. The thermopower is characteristic of a material, and depends on the material's average temperature, and crystal structure.

The Peltier effect, which is the reverse of the Seebeck effect, was observed by Jean Peltier in 1834. It represents generation of heat difference as a result of applied voltage difference across the sample (typically a junction of two different materials, metals or semiconductors), and is often used for thermoelectric cooling. Essentially, as the electric current runs through a sample, heat flows from one part of the sample to another. In one such setup, when current passes through a circuit of two different conductors, a thermal effect is found at the junctions. The temperature at the junction would increase or decrease depending on the direction of the current flow. The rate of heat flow dQ/dt is then proportional to the magnitude of the current I through the sample,

$$\frac{dQ}{dt} = \Pi I, \quad (5.2)$$

where Π represents the Peltier coefficient that determines how much heat is carried per unit charge through a material. More insight into these phenomena was brought by work of William Thomson in 1854, who determined the thermodynamic relationships behind the effects. This work described the coupling between thermal and electrical currents:

$$J = \sigma [E - S\nabla T], \quad (5.3)$$

and

$$Q = (\sigma TS)E - \kappa\nabla T, \quad (5.4)$$

where J is the electrical current density, σ is the electrical conductivity, Q is the heat current density, and κ is the thermal conductivity. It has been shown that the Peltier coefficient and the thermopower are related through $\Pi = ST$, which is known

as the Kelvin relation. Thermoelectric materials are often discussed in terms of their thermopower rather than their Peltier coefficient simply because S is easier to obtain from experiments [125].

Both electron and hole transport determine the net thermopower in a material, such that:

$$S_{net} = \frac{\sigma_e S_e + \sigma_h S_h}{\sigma_e + \sigma_h}, \quad (5.5)$$

where S_e and σ_e , and S_h and σ_h are the thermopower and electrical conductivity of the electrons and holes respectively. Because metals have partially-filled bands, they typically have small thermopowers. At finite temperature some electrons are thermally excited above the Fermi energy, leaving the holes below the Fermi energy. Since electrons and holes contribute in opposite ways (S_e is negative, whereas S_h is positive), they cancel each other's contribution and make S_{net} small. In contrast, semiconductors can be doped with an excess amount of electrons (n-type) or holes (p-type). Therefore, semiconductors can have large positive or negative values of S_{net} depending on the charge of the excess carriers. In order to determine which charged carriers dominate the electric transport in both metals and semiconductors, one can determine the sign of S_{net} in an experiment. Semiconductors with energy gaps of the order of $10k_B T_{max}$, where k_B is the Boltzmann constant, and T_{max} is the maximum operating temperature represent good candidates as thermoelectric materials [125] suitable for thermoelectric devices to be used for cooling or generation of electricity directly from a heat source.

5.2.2 Thermoelectric figure of merit and good thermoelectric materials

Good thermoelectric materials require a combination of electrical and thermal properties. The dimensionless figure of merit ZT provides a measure of efficiency of a

thermoelectric material as a function of temperature:

$$ZT = \frac{\sigma S^2 T}{\kappa_L + \kappa_e}, \quad (5.6)$$

where κ_L and κ_e represent lattice and electron contributions to the net thermal conductivity. A material is characterized as a better thermoelectric if ZT has a higher value. In order to achieve high ZT , the material must simultaneously possess high σ , high S , and low κ . Manipulating the thermal conductivity of a material is one of the essential parameters in optimizing properties of new promising bulk materials for thermoelectric applications [19]. In particular, the lattice component, which is the phonon thermal conductivity, can be reduced appreciably by increased phonon scattering in systems with considerable structural disorder. Present efforts in developing high-performance thermoelectric materials are focused on engineering various superlattices and nanowire systems, some of which utilize nonequilibrium effects to decouple electron and phonon transport, to increase S and reduce κ [122].

As the key to the commercial applicability is high efficiency of a thermoelectric material reflected in a high ZT [19], a large body of work is focused on searching for materials with enhanced thermoelectric properties.

Material classes that are intensively studied at present as prospective thermoelectrics, where thermal conductivity can be appreciably reduced, include chalcogenides [126, 127, 128] with complex structures, metal oxides [129, 130, 131], or skutterudites [132, 133, 134] that incorporate large "rattler" atoms in their cage-like structures, acting as phonon-scattering centers. β - $\text{K}_2\text{Bi}_8\text{Se}_{13}$ studied in this work belongs to the class of complex chalcogenides, containing "rattlers", and is promising for thermoelectric applications due to highly anisotropic structure with low symmetry, having low thermal conductivity.

Three parameters relevant for optimizing ZT , σ , S and κ_e , are determined by the details of the electronic properties including the size and structure of the semiconduc-

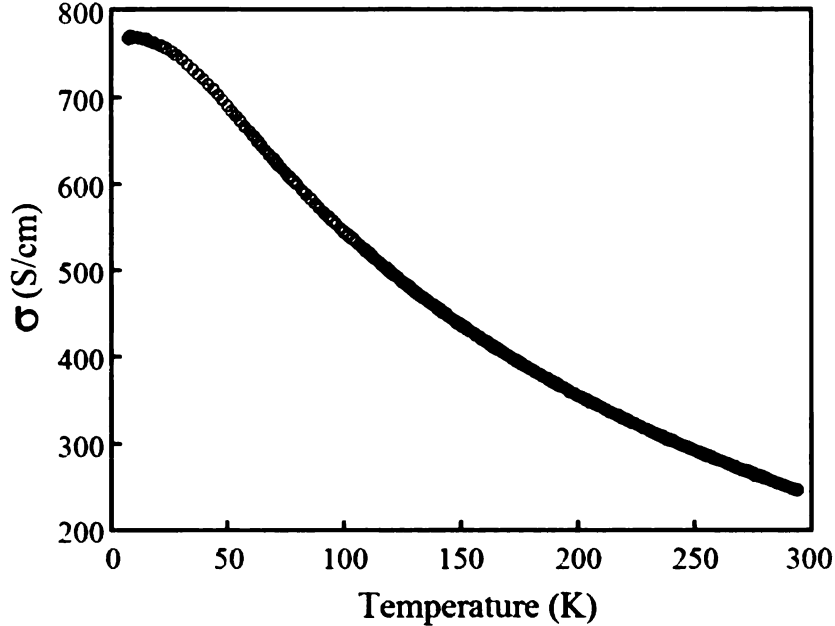


Figure 5.1: Electrical conductivity of single crystal β - $\text{K}_2\text{Bi}_8\text{Se}_{13}$ sample [20].

tor band gap and scattering of charge carriers by defects and impurities. Therefore, understanding the electronic structure of thermoelectric materials is key to optimizing their thermoelectric properties. Scanning tunneling spectroscopy is a powerful tool capable of providing important information on the electronic structure of materials.

5.3 $\text{K}_2\text{Bi}_8\text{Se}_{13}$

5.3.1 Properties

One of the promising candidates for room temperature thermoelectrics is the complex chalcogenide $\text{K}_2\text{Bi}_8\text{Se}_{13}$ [20], which crystallizes in two distinct phases, α - $\text{K}_2\text{Bi}_8\text{Se}_{13}$ and β - $\text{K}_2\text{Bi}_8\text{Se}_{13}$. The α -phase contains no structural disorder, it is a wide band-gap (~ 0.76 eV) semiconductor, and is not a good thermoelectric, as it has rather low electrical conductivity of 2 S/cm at room temperature. On the other hand, the β -phase is structurally disordered [135, 136], it is a narrow band-gap semiconductor and shows great promise for room temperature thermoelectric. Its room temperature

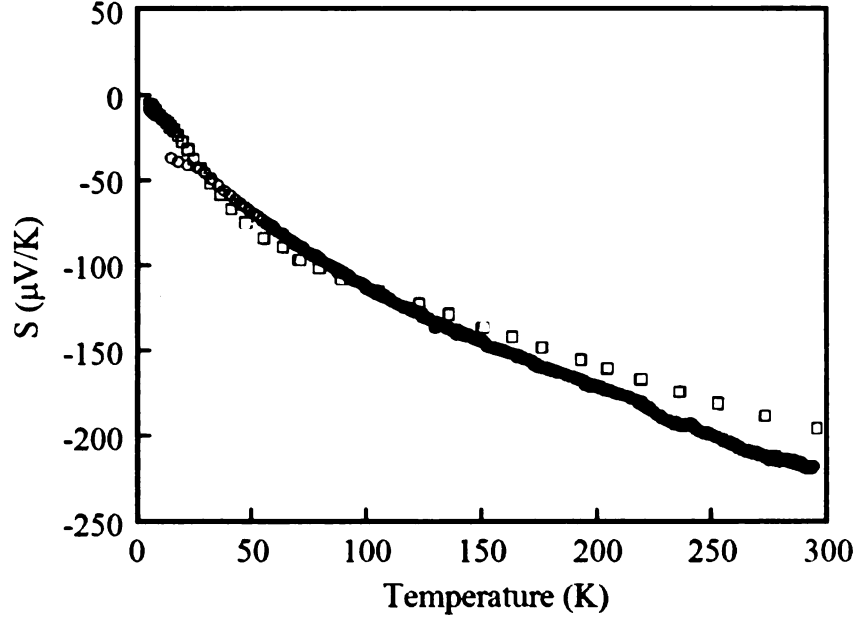


Figure 5.2: Seebeck coefficient of β - $\text{K}_2\text{Bi}_8\text{Se}_{13}$ for single crystal (open circles) and powder (open squares) samples [20].

electrical conductivity is about 250 S/cm (Figure 5.1), it has a Seebeck coefficient of $-200 \mu\text{V/K}$ (same as in the α -phase) (Figure 5.2), and thermal conductivity of 1.28 W/m·K [20]. The negative sign of the Seebeck coefficient indicates that the charge carriers are electrons. The corresponding unitless thermoelectric figure of merit, ZT , is shown in Figure 5.3. The β -phase has a crystal and electronic structure that can lead to a high Seebeck coefficient. It also has a low thermal conductivity that arises from a large, low-symmetry unit cell and weakly bonded K^+ ions, occupying space in tunnels present in the structure that act as "rattlers" [137] and hence phonon-scattering centers. The thermopower is given by the Mott formula

$$S = \frac{\pi^2 k_B^2 T}{3e} \frac{d \ln \sigma(E)}{dE}, \quad E = E_F \quad (5.7)$$

where $\sigma(E)$ is the electrical conductivity, whose logarithmic derivative with respect to energy is taken at Fermi energy E_F [138, 139]. If the scattering of charge carriers is independent of their energy E , then $\sigma(E)$ is proportional to the density of states

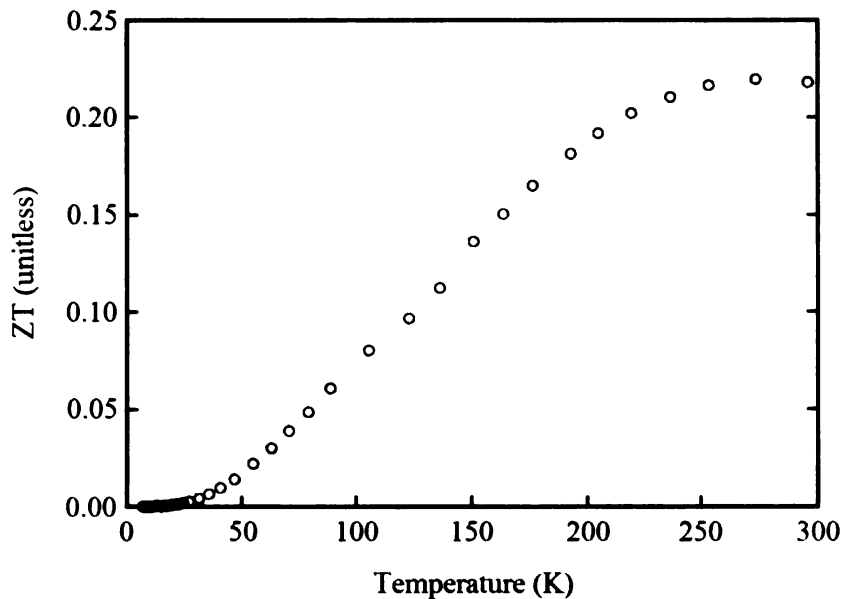


Figure 5.3: ZT of single crystal β -K₂Bi₈Se₁₃ sample [20].

at E [20], and the carrier velocity. As the thermopower S depends on the change of $\sigma(E)$ across the Fermi surface via the logarithmic derivative, manipulation of the density of states near the Fermi level will affect the energy dependence of $\sigma(E)$; hence both electrical conductivity and thermopower can be changed.

5.3.2 Crystal and electronic structure of β -K₂Bi₈Se₁₃

β -K₂Bi₈Se₁₃ has a complex low-symmetry structure described within a monoclinic space group with 46 atoms in the unit cell. The lattice parameters are $a=17.492\text{\AA}$, $b=18.461\text{\AA}$, $c=4.205\text{\AA}$, and $\gamma=90.49^\circ$. Its highly anisotropic structure results in needle-like morphology along the c crystallographic axis. While the structure shown in Figure 5.4 is rather complex, of interest for this work are some specific features, and I am going to focus our attention on these. The structure includes two different interconnected types of Bi/Se building-blocks and K⁺ ions in chains between these blocks. The two different Bi/Se blocks are connected to each other at special mixed occupancy K/Bi sites, circled in Figure 5.4 and labeled K1/Bi9 and Bi8/K3. The original crystallographic study [20] found that these sites, forming chains along the c

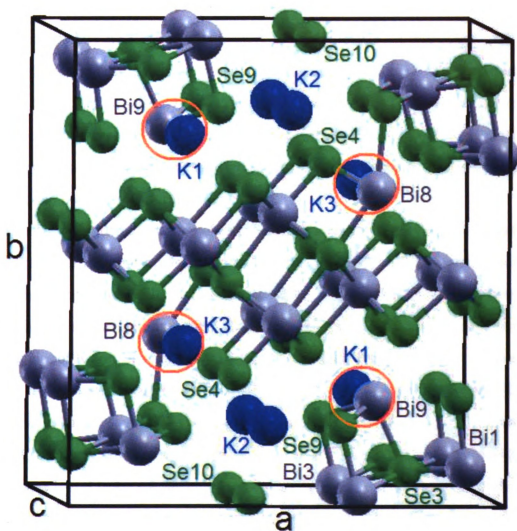


Figure 5.4: (This figure is presented in color.) Crystal structure of $\beta\text{-K}_2\text{Bi}_8\text{Se}_{13}$ [20]. The structure shown represents the unit cell doubled in the c direction. Large blue spheres represent K atoms, large gray spheres denote Bi atoms, while small green spheres show Se atoms. K/Bi sites of interest for this study that form chains in the structure along c direction are circled. See text for details. Figure courtesy of D. Bilc.

direction, have mixed occupancy, K1/Bi9 containing 62% K and 38% Bi, and Bi8/K3 containing 62% Bi and 38% K. Mixing of K and Bi on these crystallographic sites appears to be crucial in defining the electronic structure near the Fermi level, and consequently governing the electronic properties [20]. This is further supported by the results of *ab-initio* electronic band structure calculations on this compound [135]. These calculations are based on density functional theory, using the same methods introduced in Section 4.5.1. These calculations indicated that the mixed occupancy is crucial for the system to be semiconducting, because Bi atoms at the mixed sites stabilize the $4p$ orbitals of nearest-neighbor Se atoms by lowering their energy, hence allowing the band gap to form.

In order to understand the role that chemical disorder plays in the electronic structure, three different models were considered by D. Bilc and coworkers [135]: two corresponding to chemically homogeneous chains, and one that involves heterogeneous chains, as further discussed. Two different ordered structures with extreme occupancies of K and Bi atoms at the mixed sites were considered. In configuration I, the Bi8/K3 site was occupied solely by Bi, while the K1/Bi9 site contained K only. The other homogeneous configuration, configuration II, was the opposite of configuration I, with a K atom on the Bi8/K3 site, and a Bi atom on the K1/Bi9 site. The system was found to be a semi-metal for both homogeneous structures, in contrast to the experimental fact that the system has semiconducting behavior, with a semiconducting band-gap of 0.56 eV as observed in infrared diffuse reflectance spectra [20]. Therefore, further theoretical considerations had to involve $1 \times 1 \times 2$ super-cell containing 92 atoms per cell, in order to accommodate alternative occupancy of K and Bi atoms at the mixed sites (configuration III). As opposed to the case of homogeneous chains, where Se9 and Se4 atoms (see Figure 5.4) had either K or Bi as nearest neighbors, in the model involving chains of alternating K and Bi atoms, Se9 and Se4 atoms had both K and Bi as nearest neighbors. Results of the band structure calcu-

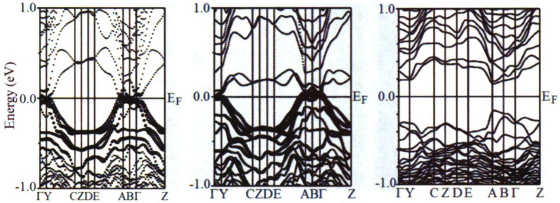


Figure 5.5: Band structure of $\beta\text{-K}_2\text{Bi}_8\text{Se}_{13}$ as obtained from theoretical considerations for three different configurations of atoms along K/Bi chains. See text for details. Figure adapted from D. Bilc *et al* [135].

lations showed that the system is an indirect band gap semiconductor, with the band gap value of about 0.41 eV. Figure 5.5 summarizes these theoretical findings. From left to right, this figure shows a sequence of calculated electronic band structures of $\beta\text{-K}_2\text{Bi}_8\text{Se}_{13}$ for configurations I, II, and III, with the band-gap clearly observed in the last case.

Hence, we see that the Bi/K disorder in $\beta\text{-K}_2\text{Bi}_8\text{Se}_{13}$ has a profound effect on the band structure near the Fermi level, and has been suspected to reduce thermal conductivity [20]. Depending on the position of the atoms in the mixed sites, either narrow band gap semiconducting or semi-metallic behavior is found [135]. The calculated band gap, however, is smaller than the measured value of 0.56 eV.

In order to clarify the reasons behind the mismatch between the theoretical and experimental band gap value, as well as to understand the electronic band structure of this material in greater detail, I used scanning tunneling spectroscopy to assess the electronic structure of $\beta\text{-K}_2\text{Bi}_8\text{Se}_{13}$ at low temperature. This provides an important experimental reference allowing for more substantial theoretical considerations to take place, aimed to differentiate various types of disorder and their role in electronic structure.

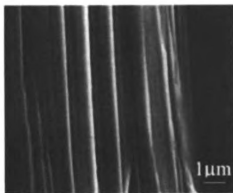


Figure 5.6: SEM image of needle-like structure of $\beta\text{-K}_2\text{Bi}_8\text{Se}_{13}$. Figure courtesy of T. Kyratsi.

5.4 Scanning tunneling spectroscopy of $\beta\text{-K}_2\text{Bi}_8\text{Se}_{13}$

5.4.1 Sample synthesis

$\beta\text{-K}_2\text{Bi}_8\text{Se}_{13}$ sample used in this study was prepared by T. Kyratsi and was obtained by reacting stoichiometric combination of elemental K, Bi, Se as follows. All manipulations were carried out under a dry nitrogen atmosphere in a Vacuum Atmospheres Dri-Lab glove-box. A mixture of 0.282 g of K, 6.021 g of elemental Bi, and 3.697 g of elemental Se was loaded into silica tube, which was subsequently flame-sealed at a residual pressure of $<10^{-4}$ Torr. The mixture was heated to 850 $^{\circ}\text{C}$ over 12 hours and kept there for 1 hour, followed by slowly cooling to 450 $^{\circ}\text{C}$ and kept there for 48 hours, and cooling to 50 $^{\circ}\text{C}$ at a rate of -15 $^{\circ}\text{C}/\text{h}$. The product was annealed at 450 $^{\circ}\text{C}$ for 48 hours to ensure phase purity of $\beta\text{-K}_2\text{Bi}_8\text{Se}_{13}$. Metallic black needles of $\beta\text{-K}_2\text{Bi}_8\text{Se}_{13}$ were obtained by isolation in dimethylformamide and washing with diethyl ether. A quantitative microprobe analysis with electron microprobe energy dispersive spectroscopy (EDS) was performed on several crystals of the compound to verify the stoichiometry. Scanning electron microscope (SEM) images of the sample confirms a highly oriented needle-like morphology of $\beta\text{-K}_2\text{Bi}_8\text{Se}_{13}$, as shown in Figure 5.6.

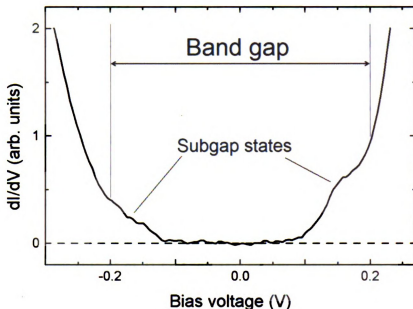


Figure 5.7: Local density of states of β -K₂Bi₈Se₁₃ as obtained by the STS measurements at 1.6 K. From the data, a band-gap of ~ 0.4 eV is estimated, in agreement with theoretical prediction [135] based on configuration III that assumes alternating K/Bi chains. In addition, subgap states are observed. See text for details.

5.4.2 Results and discussion

Using the STM point spectroscopy mode, the energy band gap at the sample surface was probed and its size was estimated. The STS measurements on a cleaved surface of β -K₂Bi₈Se₁₃ were performed at 1.6 K temperature for various positions of the probing tip above the surface of the sample. Sweeping the bias voltage V over a range of ± 300 mV, I have measured tunneling current I as a function of the ramped voltage. Differentiation of $I(V)$ data with respect to V gives the local density of states, as has been explained in the STM spectroscopy Section 2.2.2. The measurements for a given tip position were repeated 100 times, and averaged, in order to improve signal to noise ratio.

Measured local density of states of β -K₂Bi₈Se₁₃ at 1.6 K temperature is shown in Figure 5.7. The data clearly indicate the presence of the band gap. The magnitude of the observed gap of ~ 0.4 eV agrees reasonably well with the calculated value based

on configuration III described earlier, that assumes chains with alternating K/Bi atoms [135]. The discrepancy between our STS result for the band gap size, and that of ~ 0.56 eV obtained from optical measurements [20] can be understood if the band gap in β -K₂Bi₈Se₁₃ is indeed indirect [135], as the bottom of the conduction band and the top of the valence band would be offset along the momentum axis. The key difference between the optical and tunneling measurements of the band gap is that optical measurements are sensitive to wave vector \mathbf{k} , while tunneling measurements are not. Hence optical measurements can get larger gap values. According to theoretical calculations by Bilc *et al.* [135] the band gap in β -K₂Bi₈Se₁₃ is almost direct, in which case results of tunneling and optical measurements should approximately agree.

We should note that the surface of the sample exhibited relatively rough texture and was not easily cleavable. Due to the surface roughness and as a result of the coarse approach of the sample with slight sideways motion, the tip became blunt on the atomic scale, and the atomic STM resolution necessary to obtain real space surface topography was not achieved. Consequently, the density of states obtained in our measurements is not truly local, but rather represents a spatial average over several atomic sites on the sample surface.

As can be seen in Figure 5.7, the STS data indicate the presence of subgap states, seen as an enhancement of the density of states in the gap region near the top of the valence band and bottom of the conduction band. One possible explanation of the origin of these states could be the presence of disorder. More specifically, “less mixed” segments along the chains composed of Bi₈/K₃ sites and of K₁/Bi₉ sites may shift the energy states into the gap, making it narrower.

It is indeed plausible that in the real material there exist regions close to configurations I and II, which may create such subgap states, which are not predicted by configuration III. It is of particular importance to verify if this is really the case,

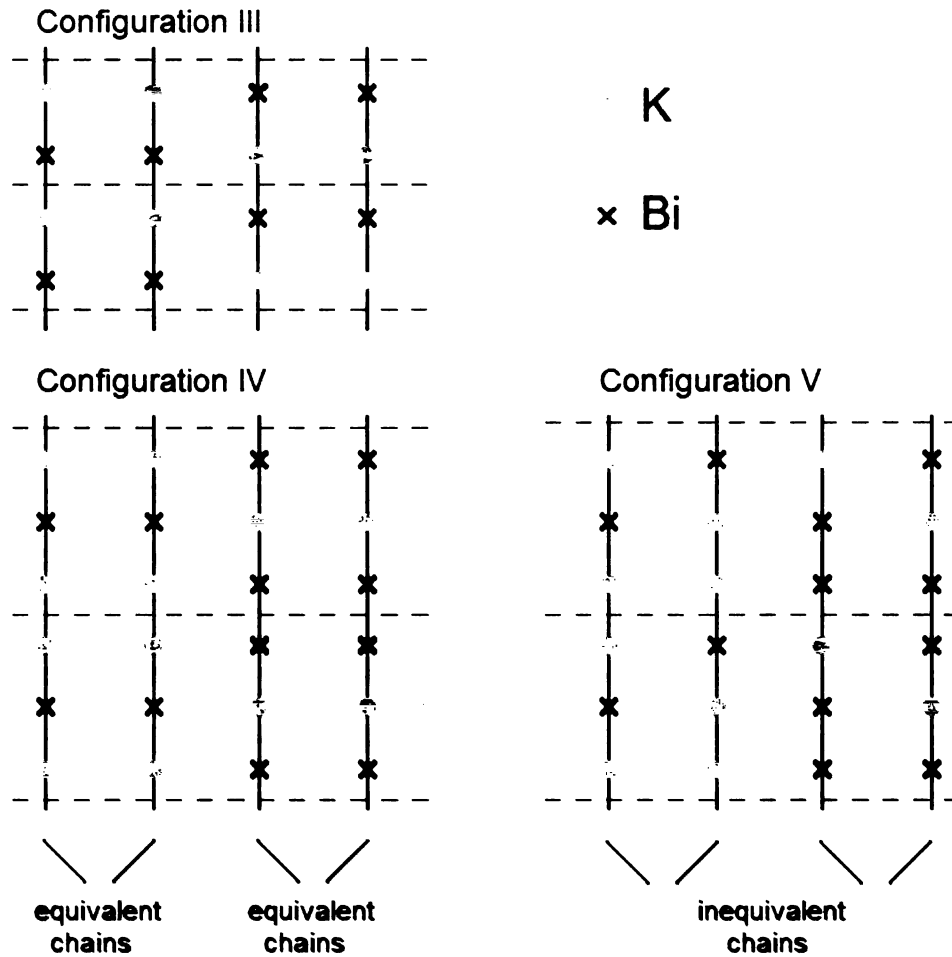


Figure 5.8: Schematic representation of various configurations of the K/Bi chains considered in theoretical calculations. K atoms are represented with solid circles, while Bi atoms are represented with cross-marks. There are four K/Bi chains of interest in the original unit cell, however there are only two inequivalent chain types, K1/Bi9 and Bi8/K3. Configuration III requires unit cell doubling along the chain direction and assumes chains of alternating K and Bi, such that two inequivalent chains have opposite ordering phase. Configuration IV requires unit cell tripling along the chain direction, with K1/Bi9 chain type having K-Bi-K sequence, while Bi8/K3 type features Bi-K-Bi sequence. Configuration V also requires tripling of the unit cell, and is closely related to configuration IV, except that all four chains are now made inequivalent, by offsetting the phase along the equivalent chains.

as these states would change the density of states near the Fermi level, and would contribute to the charge transport, raising the values of electrical conductivity and thermopower [135]. If the nature of the observed subgap states could be characterized through electronic band structure calculations, this would also provide an information of possible structural motifs involved along the disordered K/Bi chains.

In collaboration with group of Dr. Mahanti, and motivated by the observation of the subgap states, further theoretical calculations have been carried out by K. Hoang using various configurations along K/Bi chains. These configurations are shown in Figure 5.8, representing several different variants of K/Bi interchain disorder. We note here that within the unit cell of β -K₂Bi₈Se₁₃ there are four K/Bi chains of interest in the original unit cell; however there are only two inequivalent chain types, K1/Bi9 and Bi8/K3. Configuration III requires unit cell doubling along the chain direction and assumes chains of alternating K and Bi, such that two inequivalent chains have opposite ordering phase. Configuration IV assumes interchain disorder and requires unit cell tripling along the chain direction, with K1/Bi9 chain type having K-Bi-K sequence, while Bi8/K3 type features Bi-K-Bi sequence. Configuration V also requires tripling of the unit cell, and is closely related to configuration IV, except that all four chains are now made inequivalent, introducing intrachain disorder between previously equivalent chains by offsetting the phase along the equivalent chains.

The resulting DOS obtained in preliminary electronic band structure calculations are shown in Figure 5.9 for all three configurations considered. Since the theoretical calculations did not include spin-orbit interaction, the size of the theoretical band gaps are overestimated [21]. The results of the calculations allowed for the following observations to be made. On going from configuration III to configuration IV, the band gap size decreases. In addition, Se9 states that occur near the top of the valence band get redistributed towards lower energies, as these states are strongly affected by the structure of neighboring K1/Bi9 chains. Se9 has the K1/Bi9 chain atoms as

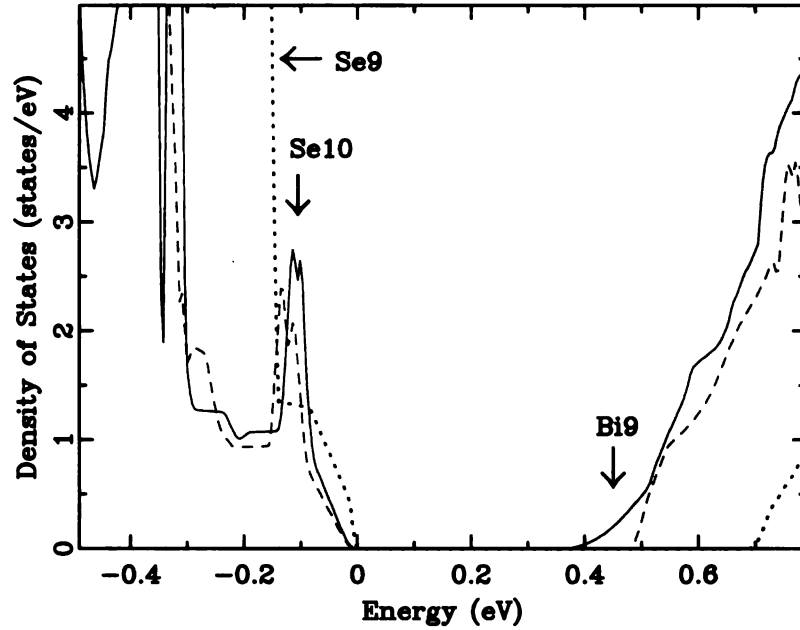


Figure 5.9: DOS obtained from the electronic band structure calculations considering three different configurations along the K/Bi chains: configuration III (dotted line), configuration IV (dashed line), and configuration V (solid line). Arrows indicate specific features discussed in the text.

nearest neighbors. The energy range of our STS measurements was not sufficiently wide to involve region where Se9 states occur.

On the other hand, Se10 states that are also near the top of the valence band do not get affected by the changes in the chains, since Se10 atoms are sufficiently far from the chains. On going from configuration IV to configuration V, the following observations are made. Se10 states near the valence band top do not change, as expected. However, changes occur near the bottom of the conduction band, that may be significant in understanding the subgap states observed by STS. According to the results of electronic band structure calculations for configuration V [140], the bottom of the conduction band is filled with states related to K/Bi chains. In particular, it has been found that these states are predominantly of Bi9 character, and relate to chains where Bi9 atoms are sandwiched between K1 dimers. In other words it is Bi atoms within the disordered chains that give rise to the DOS at the bottom of the

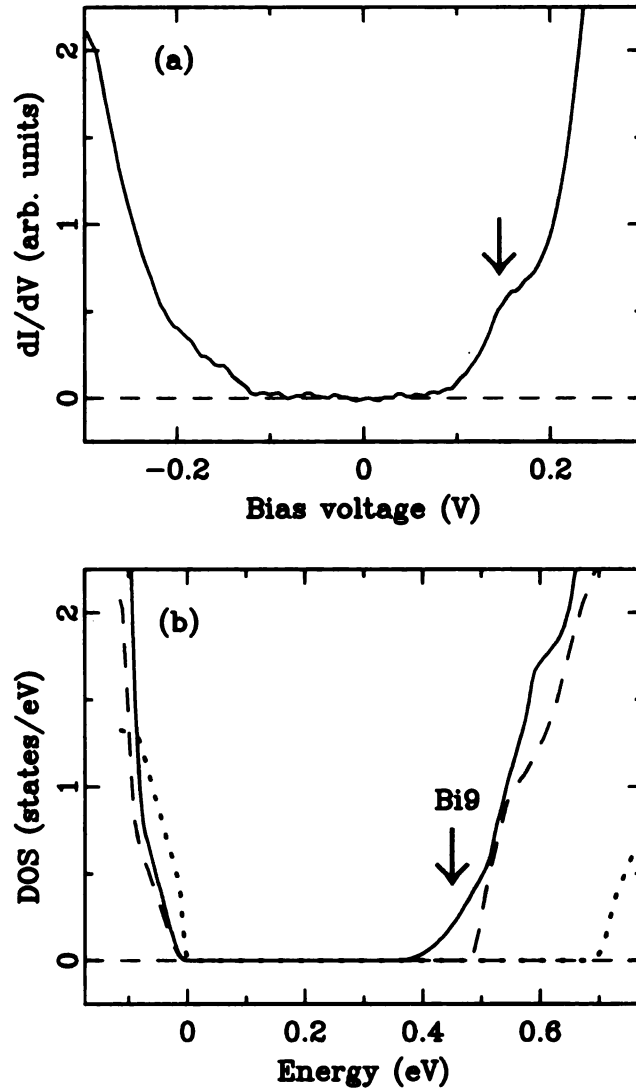


Figure 5.10: (a) STS data for DOS near the Fermi level of β -K₂Bi₈Se₁₃, at 1.6 K. (b) DOS obtained from the electronic band structure calculations considering three different configurations along the K/Bi chains: configuration III (dotted line), configuration IV (dashed line), and configuration V (solid line). The arrows in both panels indicate features of interest discussed in text.

conduction band. On the other hand, the contribution to the subgap states from Bi8/K3 chains, where Bi8 dimers are sandwiched between K3 atoms, is not appreciable. A comparison of density of states obtained experimentally and theoretically is shown in Figure 5.10, with notable similarity of the experimental curve and the calculated one for configuration V in the energy range of the measurement.

5.5 Summary

The local electronic structure near the Fermi level of β -K₂Bi₈Se₁₃, a promising thermoelectric material, was studied using scanning tunneling spectroscopy. This material is a narrow band gap semiconductor, and the STS experiment at 1.6 K temperature revealed a gap of approximately 0.4 eV, in good agreement with results of theoretical calculations. Further, the STS study revealed the presence of subgap states that, according to recent electronic band structure calculations exploring several K/Bi chain configurations, represent a signature of disorder along K1/Bi9 and Bi8/K3 chains. This disorder significantly influences the electronic structure and narrows the band gap. This further suggests that the subgap states near the bottom of the conduction band are predominantly of Bi9 character. On the other hand, the subgap states near the top of the valence band can be attributed to Se10. The disorder in β -K₂Bi₈Se₁₃ could play an important role for its thermoelectric properties, by changing the density of states near the band gap and perhaps increasing the thermopower.

Chapter 6

Concluding remarks

6.1 Summary

Scanning tunneling microscopy and spectroscopy represent important tools providing valuable information about electronic structure of complex materials, allowing for better understanding of their physical properties. In this work we studied the electronic structure of samples belonging to two different classes of complex materials, one exhibiting incommensurate CDW, and another that is a promising high-performance thermoelectric. Both of these studies highlight the importance of knowing the details of the electronic structure near the Fermi level for the respective phenomena.

6.1.1 CeTe_3 and YTe_3

The charge density wave (CDW) state is one of the competing ground states in anisotropic, low-dimensional materials. CeTe_3 as a cleavable, layered system featuring tellurium layers where a stable one-dimensional incommensurate CDW forms, is a model system for incommensurate CDW studies. Scanning tunneling microscopy is a powerful technique to study surface topography and local electronic structure of complex materials. We applied STM and STS to study the electronic properties of the CDW within Te-layers of CeTe_3 and related YTe_3 . STM and STS measurements

of the CeTe₃ at room temperature and 77 K and YTe₃ at room temperature were performed. The one-dimensional CDWs were observed on the surfaces of CeTe₃ and YTe₃. In Fourier transform analysis of the STM images of CeTe₃, we observed the $q_{CDW} \approx 2/7 \times 2\pi/c$ peak, as well as several additional peaks. We explored several possible interpretations concerning these peaks and their relation to the CDW. Our FT analysis cannot unambiguously differentiate between the discommensurated and uniformly incommensurate CDW. The principal reason for this is lack of reliable criterion that would allow us to distinguish whether these extra peaks are satellite peaks to the CDW peak, which would suggest discommensurated nature of the CDW, or the peaks originate from the artifacts of the STM measurement. In the interpretation that supports the discommensurated picture we obtained the commensurate domain size that agrees reasonably well with the estimate made by the atomic PDF study [96]. However, the extra peaks in our FT data can also be explained within the wave vector mixing picture, that does not invoke discommensurations. The local density of states near the Fermi level has also been obtained using the STS mode at 77 K. We obtained the CDW gap at various places on the surface of the sample. The CDW gap size obtained in measurements directly above the Te atoms was ~ 360 meV, in good agreement with ARPES result [95]. The data obtained from measurements on YTe₃ were not of sufficient quality to perform the FT analysis. The CDW gap in YTe₃ obtained from room temperature STS was estimated to be roughly ~ 320 meV.

6.1.2 β -K₂Bi₈Se₁₃

The local electronic structure near the Fermi level of β -K₂Bi₈Se₁₃, a promising thermoelectric material, was studied using STS. This material is a narrow band gap semiconductor, and the STS experiment at 1.6 K temperature revealed a gap of approximately 0.4 eV, in good agreement with results of theoretical calculations. Our STS study also revealed the presence of subgap states. According to recent electronic

band structure calculations exploring several K/Bi chain configurations, the subgap states represent a signature of disorder along the chains. This disorder significantly influences the electronic structure and narrows the band gap. The experimental results of this work, together with the results of the electronic band structure calculations support the idea of K/Bi disorder being present in the system. The disorder in β -K₂Bi₈Se₁₃ could play an important role for its thermoelectric properties.

6.2 Future work

On the CDW side, a natural extension of this work would be to study the details of the electronic structure in a systematic way of a broad class of Rare-Earth tritellurides (RETe₃ with RE = La, Ce, Pr, Nd, Sm, Gd, Tb, Dy, Ho, Er, Tm). While all of them exhibit the CDW state with different critical temperatures, very few of these materials have their electronic properties fully characterized. It would be therefore beneficial to assess the sizes of the band gaps across the series, for example, and see how this important parameter varies with different RE. Another possible STM study in this class of materials would involve HoTe₃, which exhibits two CDW transitions, one present at room temperature, and another below 110 K [110]. At low temperature two CDWs with mutually perpendicular CDW wave vectors are expected. The experiments aimed in assessing the CDW surface structure as well as spectroscopy would be carried out in both CDW states at room temperature and at 77 K, to investigate the electronic structure in this material.

Another direction for this research follows from the magnetic properties, as it has been demonstrated that CeTe₃ is a Kondo lattice material [94]. The Kondo effect arises from the interactions between a magnetic atom and the conduction electrons in an otherwise non-magnetic metal. In this case, the magnetic state is the 4*f* level of the cerium ions. The Kondo temperature is roughly 10 K and the system stays in that state down to 2.8 K. Repeating the topographic measurements at liquid helium

temperature (4.2 K) and then acquiring spectra with the tip positioned above Ce atoms, the electronic structure of the Kondo lattice system would be resolved with scanning tunneling spectroscopy. Our cryogenic STM system achieves the resolution expected to be necessary to resolve the Kondo features in the local density of states. Theoretical density of states exhibit the basic predicted spectroscopic features using a model system. By comparing the measurements to theory, the study will explore questions of the Kondo lattice system and the interplay with the charge density wave.

Additional experiments could also be carried out on the thermoelectric material β - $\text{K}_2\text{Bi}_8\text{Se}_{13}$, to further investigate the details of the electronic structure using STS. In the present study, the band gap and the subgap states have been observed. However, the energy range probed was insufficiently broad to assess the part near the top of the valence band where, according to the electronic band structure calculations, Se9 states are observed to rearrange dramatically, which could be used as an important indicator in more reliable distinction between various different types of disorder along K/Bi chains.

Bibliography

- [1] M. Vershinin, S. Misra, S. Ono, Y. Abe, Y. Ando, and A. Yazdani, *Science* **303**, 1995 (2004).
- [2] J. C. Loudon, S. Cox, A. J. Williams, J. P. Attfield, P. B. Littlewood, P. A. Midgley, and N. D. Mathur, *Phys. Rev. Lett.* **94**, 097202 (2005).
- [3] D. Bilc, S. D. Mahanti, E. Quarez, K.-F. Hsu, R. Pcionek, and M. G. Kanatzidis, *Phys. Rev. Lett.* **93**, 146403 (2004).
- [4] J. W. Lynn, D. N. Argyriou, Y. Ren, Y. Chen, Y. Mukovskii, and D. Shulyatev, *cond-mat* , 0701001 (2007).
- [5] H. J. Kim, E. S. Božin, S. M. Haile, G. J. Snyder, and S. J. L. Billinge, *Phys. Rev. B* **75**, 134103 (2007).
- [6] H. Lin, E. S. Božin, S. J. L. Billinge, E. Quarez, and M. G. Kanatzidis, *Phys. Rev. B* **72**, 174113 (2005).
- [7] E. S. Božin, S. J. L. Billinge, H. Takagi, and G. H. Kwei, *Phys. Rev. Lett.* **84**, 5856 (2000).
- [8] X. Qiu, S. J. L. Billinge, C. R. Kmetz, and J. F. Mitchell, *J. Phys. Chem. Solids* **65**, 1423 (2004).
- [9] S. Cox, J. Singleton, R. D. McDonald, A. Migliori, and P. Littlewood, *cond-mat* , 07054310 (2007).
- [10] G. C. Milward, M. J. Calderon, and P. B. Littlewood, *Nature* **433**, 607 (2005).
- [11] A. Mourachkine, *Supercond. Sci. Technol.* **13**, 1378 (2000).
- [12] J. M. Tranquada, B. J. Sternlieb, J. D. Axe, Y. Nakamura, and S. Uchida, *Nature* **375**, 561 (1995).
- [13] H. A. Mook, P. C. Dai, S. M. Hayden, G. Aeppli, T. G. Perring, and F. Dogan, *Nature* **395**, 580 (1998).
- [14] G. Binnig, H. Rohrer, C. Gerber, and E. Weibel, *Appl. Phys. Lett.* **40**, 178 (1982).
- [15] G. Binnig, H. Rohrer, C. Gerber, and E. Weibel, *Phys. Rev. Lett.* **49**, 57 (1982).

- [16] G. Grüner, *Density waves in solids*, Addison Wesley, Reading, MA, 1994.
- [17] R. M. Fleming, Phys. Rev. B **22**, 5606 (1980).
- [18] G. S. Nolas, J. Sharp, and H. J. Goldsmid, *Thermoelectrics: basic principles and new materials developments*, Springer-Verlag, 2001.
- [19] G. S. Nolas, J. Poon, and K. G. Kanatzidis, Mater. Res. Soc. Bull. **31**, 199 (2006).
- [20] D. Y. Chung, K. S. Choi, L. Iordanidis, J. L. Schindler, P. W. Brazis, C. R. Kannewurf, B. Chen, S. Hu, C. Uher, and M. G. Kanatzidis, Chem. Mater. **9**, 3060 (1997).
- [21] D. Bilc, *Electronic structure and thermoelectric properties of narrow band gap chalcogenides*, Ph.D. Thesis, Michigan State University, 2005.
- [22] J. A. Stroscio and W. J. Kaiser, *Scanning Tunneling Microscopy*, Academic Press, Boston, 1993.
- [23] M. Tinkham, *Introduction to superconductivity*, Robert. E. Krieger Publishing Company, Malabar, Florida, 1980.
- [24] E. Stoll, A. Baratoff, A. Selloni, and P. Carnevali, J. Phys. C: Solid State Phys. **17**, 3073 (1982).
- [25] K. Besocke, Surface Sci. **181**, 145 (1987).
- [26] D. Tománek, S. G. Louie, H. J. Mamin, and D. W. Abraham, Phys. Rev. B **35**, 7790 (1987).
- [27] J. M. Carpinelli, H. H. Weitering, E. W. Plummer, and R. Stumpf, Nature **381**, 398 (1996).
- [28] J. A. Wilson, F. J. DiSalvo, and S. Mahajan, Phys. Rev. Lett. **32**, 882 (1974).
- [29] J. M. Tranquada, D. J. Buttrey, V. Sachan, and J. E. Lorenzo, Phys. Rev. Lett. **73**, 1003 (1994).
- [30] V. Sachan, D. J. Buttrey, J. M. Tranquada, J. E. Lorenzo, and G. Shirane, Phys. Rev. B **51**, 12742 (1995).
- [31] S. Mori, C. H. Chen, and S.-W. Cheong, Nature **392**, 473 (1998).
- [32] T. Hanaguri, C. Lupien, Y. Kohsaka, D.-H. Lee, M. Azuma, M. Takano, H. Takagi, and J. C. Davis, Nature **430**, 1001 (2004).
- [33] S. Komiya, H.-D. Chen, S.-C. Zhang, and Y. Ando, Phys. Rev. Lett. **94**, 207004 (2005).
- [34] M. I. Salkola, V. J. Emery, and S. A. Kivelson, Phys. Rev. Lett. **77**, 155 (1996).

- [35] R. E. Thorne, *Physics Today* **5**, 42 (1996).
- [36] S. Brown and G. Grüner, *Scientific American* **4**, 50 (1994).
- [37] R. E. Peierls, *Quantum theory of solids*, Clarendon Press, Oxford, 1955.
- [38] H. Akamatu, H. Inokuchi, and Y. Matsunaga, *Nature* **173**, 168 (1954).
- [39] L. B. Coleman, J. A. Cohen, A. F. Garito, and A. J. Heeger, *Phys. Rev. B* **7**, 2122 (1973).
- [40] P. W. Anderson, P. A. Lee, and M. Saitoh, *Solid State Commun.* **13**, 595 (1973).
- [41] M. J. Rice and S. Strässler, *Solid State Commun.* **13**, 1389 (1973).
- [42] S. van Smaalen, *Acta Crystallogr. A* **61**, 51 (2005).
- [43] A. Damascelli, *Physica Scripta* **T109**, 61 (2004).
- [44] M. A. Valbuena, J. Avila, S. Drouard, H. Guyot, and M. C. Asensio, *J. Phys. Chem. Solids* **67**, 213 (2006).
- [45] C. J. Chen, *Introduction to Scanning Tunneling Microscopy*, Oxford Science Publications, Oxford, 1993.
- [46] N. Magonov and M.-H. Whangbo, *Surface analysis with STM and AFM*, VCH Publishers, Weinheim, 1996.
- [47] P. Mallet, K. M. Zimmermann, P. Chevalier, J. Marcus, J. Y. Veuillen, and J. M. G. Rodriguez, *Phys. Rev. B* **60**, 2122 (1999).
- [48] N. P. Ong and P. Monceau, *Phys. Rev. B* **16**, 3443 (1977).
- [49] B. E. Warren, *X-ray diffraction*, Dover, New York, 1990.
- [50] G. E. Bacon, *Neutron diffraction*, Oxford University Press, Oxford, 1975.
- [51] B. Fultz and J. M. Howe, *Transmission Electron Microscopy and Diffractometry of Materials*, Springer-Verlag, Berlin, 2002.
- [52] P. Foury and J. P. Pouget, *Int. J. Mod. Phys. B* **7**, 3973 (1993).
- [53] D. D. Laws, H. L. Bitter, and A. Jerschow, *Angew. Chem. Int. Edit.* **41**, 3096 (2002).
- [54] J. H. Ross, Z. Wang, and C. P. Slichter, *Phys. Rev. B* **41**, 2722 (1990).
- [55] D. J. Gardiner, *Practical Raman spectroscopy*, Springer-Verlag, Berlin, 1989.
- [56] T. Hirata and F. S. Ohuchi, *Solid State Commun.* **117**, 361 (2001).

- [57] G. Grüner, *Rev. Mod. Phys.* **60**, 1129 (1988).
- [58] A. H. C. Neto and C. M. Smith, *Charge Inhomogeneities in Strongly Correlated Systems, in "Strong Interactions in Low Dimensions", D. Baeriswyl and L. Degiorgi Edts., Kluwer, Dordrecht, The Netherlands, 2004.*
- [59] A. M. Gabovich, A. I. Voitenko, and M. Ausloos, *Phys. Rep.* **367**, 583 (2002).
- [60] H. H. Weitering, J. M. Carpinelli, A. V. Melechko, J. Zhang, M. Bartkowiak, and E. W. Plummer, *Science* **285**, 2107 (1999).
- [61] T. Valla, A. V. Fedorov, P. D. Johnson, P. A. Glans, C. McGuinness, K. E. Smith, E. Y. Andrei, and H. Berger, *Phys. Rev. Lett.* **92**, 86401 (2004).
- [62] A. H. C. Neto, *Phys. Rev. Lett.* **86**, 4382 (2001).
- [63] R. J. Cava, P. Littlewood, R. M. Fleming, R. G. Dunn, and E. A. Rietman, *Phys. Rev. B* **33**, 2439 (1986).
- [64] W. G. Lyons and J. R. Tucker, *Phys. Rev. B* **38**, 4303 (1988).
- [65] A. Terrasi, M. Marsi, H. Berger, G. Margaritondo, R. J. Kelley, and M. Onellion, *Phys. Rev. B* **52**, 5592 (1995).
- [66] J. Voit, L. Perfetti, F. Zwick, H. Berger, G. Margaritondo, G. Grüner, H. Höchst, and M. Grioni, *Science* **290**, 501 (2000).
- [67] N. Shannon and R. Joynt, *Solid State Commun.* **115**, 411 (2000).
- [68] S. Sridhar, D. Reagor, and G. Grüner, *Phys. Rev. Lett.* **55**, 1196 (1985).
- [69] S. van Smaalen, J. L. de Boer, A. Meetsma, H. Graafsma, H.-S. Sheu, A. Darovskikh, P. Coppens, and F. Levy, *Phys. Rev. B* **45**, 3103 (1992).
- [70] J. Schäfer, E. Rotenberg, S. D. Kevan, P. Blaha, R. Claessen, and R. E. Thorne, *Phys. Rev. Lett.* **87**, 196403 (2001).
- [71] Y. S. Hor, Z. L. Xiao, U. Welp, Y. Ito, J. F. Mitchell, R. E. Cook, W. K. Kwok, and G. W. Crabtree, *Nano Lett.* **5**, 397 (2005).
- [72] T. Haga, Y. Abe, and Y. Okwamoto, *Phys. Rev. Lett.* **51**, 678 (1983).
- [73] X. L. Wu and C. M. Lieber, *Science* **243**, 1703 (1989).
- [74] R. V. Coleman, V. V. McNairy, and C. G. Slough, *Phys. Rev. B* **45**, 1428 (1992).
- [75] T. Pillo, J. Hayoz, H. Berger, M. Grioni, L. Schlapbach, and P. Aebi, *Phys. Rev. Lett.* **83**, 3494 (1999).
- [76] Y. Toda, K. Tateishi, and S. Tanda, *Phys. Rev. B* **70**, 33106 (2004).

- [77] L. Perfetti, T. A. Gloor, F. Mila, H. Berger, and M. Grioni, *Phys. Rev. B* **71**, 153101 (2005).
- [78] D. E. Moncton, J. D. Axe, and F. J. DiSalva, *Phys. Rev. Lett.* **34**, 734 (1975).
- [79] K. Horiba, K. Ono, J. H. Oh, T. Kihara, S. Nakazono, M. Oshima, O. Shiino, H. W. Yeom, A. Kakizaki, and Y. Aiura, *Phys. Rev. B* **66**, 073106 (2002).
- [80] T. Valla, A. V. Fedorov, P. D. Johnson, J. Xue, K. E. Smith, and F. J. DiSalvo, *Phys. Rev. Lett.* **85**, 4759 (2000).
- [81] M. Bovet, D. Popović, F. Clerc, C. Koitzsch, U. Probst, E. Bucher, H. Berger, D. Naumović, and P. Aebi, *Phys. Rev. B* **69**, 125117 (2004).
- [82] B. Giambattista, C. G. Slough, V. V. McNairy, and R. V. Coleman, *Phys. Rev. B* **41**, 10082 (1990).
- [83] S. C. Bayliss, A. M. Ghorayeb, and D. R. P. Guy, *J. Phys. Chem.* **17**, L533 (1984).
- [84] B. Burk and A. Zettl, *Phys. Rev. B* **46**, 9817 (1992).
- [85] M. Arita, H. Negishi, K. Shimada, F. Xu, A. Ino, Y. Takeda, K. Yamazaki, A. Kimura, S. Qiao, S. Negishi, M. Sasaki, H. Namatame, and M. Taniguchi, *Physica B* **351**, 265 (2004).
- [86] J. A. Wilson, F. J. DiSalvo, and S. Mahajan, *Adv. Phys.* **24**, 117 (1975).
- [87] C. B. Scruby, P. M. Williams, and G. S. Parry, *Philos. Mag.* **31**, 255 (1975).
- [88] A. Yamamoto, *Phys. Rev. B* **27**, 7823 (1983).
- [89] E. DiMasi, M. C. Aronson, J. F. Mansfield, B. Foran, and S. Lee, *Phys. Rev. B* **52**, 14516 (1995).
- [90] R. Patschke and M. G. Kanatzidis, *Phys. Chem. Chem. Phys.* **4**, 3266 (2002).
- [91] C. Malliakas, S. J. L. Billinge, H.-J. Kim, and M. G. Kanatzidis, *J. Am. Chem. Soc.* **127**, 6510 (2005).
- [92] W. Tremel and R. Hoffmann, *J. Am. Chem. Soc.* **109**, 124 (1987).
- [93] E. DiMasi, B. Foran, M. C. Aronson, and S. Lee, *Chem. Mater.* **6**, 1867 (1995).
- [94] N. Ru and I. R. Fisher, *Phys. Rev. B* **73**, 033101 (2006).
- [95] V. Brouet, W. L. Yang, X. J. Zhou, Z. Hussain, N. Ru, K. Y. Shin, I. R. Fisher, and Z. X. Shen, *Phys. Rev. Lett.* **93**, 126405 (2004).
- [96] H. J. Kim, C. D. Malliakas, A. Tomic, S. H. Tessmer, M. G. Kanatzidis, and S. J. L. Billinge, *Phys. Rev. Lett.* **96**, 226401 (2006).

- [97] A. Fang, N. Ru, I. R. Fisher, and A. Kapitulnik, *Phys. Rev. Lett.* **99**, 046401 (2007).
- [98] H. Bestgen, *Solid State Commun.* **58**, 197 (1986).
- [99] A. B. McLean, R. M. Feenstra, A. Taleb-Ibrahimi, and R. Ludeke, *Phys. Rev. B* **39**, 12925 (1989).
- [100] R. Clarke, J. N. Gray, H. Homma, and M. J. Winokur, *Phys. Rev. Lett.* **47**, 1407 (1981).
- [101] C. H. Chen, J. M. Gibson, and R. M. Fleming, *Phys. Rev. Lett.* **47**, 723 (1981).
- [102] W. Lin, H. Steinfink, and E. J. Weiss, *Inorg. Chem.* **4**, 877 (1965).
- [103] B. K. Norling and H. Steinfink, *Inorg. Chem.* **5**, 1488 (1966).
- [104] H. Komoda, T. Sato, S. Souma, T. Takahashi, Y. Ito, and K. Suzuki, *Phys. Rev. B* **70**, 195101 (2004).
- [105] A. Kikuchi, *J. Phys. Soc. Jpn.* **67**, 1308 (1998).
- [106] J. Laverock, S. B. Dugdale, Z. Major, M. A. Alam, N. Ru, I. R. Fisher, G. Santi, and E. Bruno, *Phys. Rev. B* **71**, 085114 (2005).
- [107] H. Chudo, C. Michioka, Y. Itoh, and K. Yoshimura, *Phys. Rev. B* **75**, 045113 (2007).
- [108] G.-H. Gweon, J. D. Denlinger, J. A. Clack, J. W. Allen, C. G. Olson, E. DiMasi, M. C. Aronson, B. Foran, and S. Lee, *Phys. Rev. Lett.* **81**, 886 (1998).
- [109] H. Yao, J. A. Robertson, E.-A. Kim, and S. A. Kivelson, *Phys. Rev. B* **74**, 245126 (2006).
- [110] N. Ru, G. Y. Margulis, K. Y. Shin, M. F. Toney, and I. R. Fisher, *cond-mat* , 0610319 (2006).
- [111] www.imagemet.com.
- [112] B. Burk, R. E. Thomson, A. Zettl, and J. Clarke, *Phys. Rev. Lett.* **66**, 3040 (1991).
- [113] R. E. Thomson, B. Burk, A. Zettl, and J. Clarke, *Phys. Rev. B* **49**, 16899 (1994).
- [114] K. Nakanishi, *J. Phys. Soc. Jpn.* **43**, 1509 (1977).
- [115] S. Urazhdin, D. Bilc, S. H. Tessmer, S. D. Mahanti, T. Kyratsi, and M. G. Kanatzidis, *Phys. Rev. B* **66**, 161306 (2002).
- [116] Z. Rak, A. Tomic, S. D. Mahanti, and S. H. Tessmer, unpublished (2008).

- [117] P. Hohenberg and W. Kohn, *Phys. Rev.* **136**, B864 (1965).
- [118] D. J. Singh, *Plane Waves, Pseudopotentials and the LAPW Method*, Kluwer Academic Publishers, Boston, 1994.
- [119] J. P. Perdew, K. Burke, and M. Ernzerhof, *Phys. Rev. Lett.* **77**, 3865 (1996).
- [120] V. Brouet, unpublished (2007).
- [121] D. M. Rowe, editor, *CRC Handbook of Thermoelectrics*, Chemical Rubber Press, Boca Raton, FL, 1995.
- [122] M. G. Kanatzidis, S. D. Mahanti, and T. P. Hogan, *Chemistry, Physics, and Materials Science of Thermoelectric Materials: Beyond Bismuth Telluride*, Kluwer Academic/Plenum Publishers, 2002.
- [123] T. M. Tritt and M. A. Subramanian, *MRS Bulletin* **31**, 188 (2006).
- [124] A. F. Ioffe, *Poluprovoduikovy Termoelementy*, Moskow-Leningrad (1956).
- [125] F. J. DiSalvo, *Science* **285**, 703 (1999).
- [126] B. Wolfing, C. Kloc, J. Teubner, and E. Bucher, *Phys. Rev. Lett.* **86**, 4350 (2001).
- [127] K. Kurosaki, A. Kosuga, H. Muta, M. Uno, and S. Yamanaka, *Appl. Phys. Lett.* **87**, 061919 (2005).
- [128] M. G. Kanatzidis, *Acc. Chem. Res.* **38**, 359 (2005).
- [129] K. Fujita, T. Mochida, and K. Nakamura, *Jpn. J. Appl. Phys.* **40**, 4644 (2001).
- [130] S. Lambert, H. Leligny, and D. Grebille, *J. Solid State Chem.* **160**, 322 (2001).
- [131] I. Terasaki, Y. Ishii, D. Tanaka, K. Takahata, and Y. Iguchi, *Jpn. J. Appl. Phys.* **40**, L65 (2001).
- [132] G. S. Nolas, M. Kaeser, R. T. Littleton, and T. M. Tritt, *Appl. Phys. Lett.* **77**, 1855 (2000).
- [133] Y. Miyazaki, X. Y. Huang, and T. Kajitani, *J. Solid State Chem.* **178**, 2973 (2005).
- [134] J. Y. Son, B. G. Kim, and J. H. Cho, *Appl. Phys. Lett.* **86**, 221918 (2005).
- [135] D. I. Bilc, S. D. Mahanti, T. Kyratsi, D.-Y. Chung, M. G. Kanatzidis, and P. Larson, *Phys. Rev. B* **71**, 085116 (2005).
- [136] T. Kyratsi, E. Hatzikraniotis, K. M. Paraskevopoulos, C. D. Malliakas, J. S. Dyck, C. Uher, and M. G. Kanatzidis, *J. Appl. Phys.* **100**, 123704 (2006).
- [137] M. G. Kanatzidis, *Semicond. Semimet.* **70**, 51 (2001).

- [138] N. F. Mott and H. Jones, *Theory of the properties of metals and alloys*, Oxford University Press, London, 1936.
- [139] P. L. Taylor, Phys. Rev. B **6**, 1197 (1973).
- [140] K. Hoang and S. D. Mahanti, private communications (2007).

MICHIGAN STATE UNIVERSITY LIBRARIES



3 1293 02956 5904